UNIVERSITÀ DEGLI STUDI DI TRIESTE

XXXII CICLO DEL DOTTORATO DI RICERCA IN

SCIENZE DELLA TERRA E MECCANICA DEI FLUIDI

Zircon dating and trace element content of transparent heavy minerals in sandstones from the NE Alps and Outer Dinarides flysch basins

Settore scientifico-disciplinare: Geo/06 Mineralogia

DOTTORANDO / A
MATTEO VELICOGNA

COORDINATORE
PROF. PIERPAOLO OMARI

SUPERVISORE DI TESI
PROF. FRANCESCO PRINCIVALLE

CO-SUPERVISORE DI TESI
PROF. DAVIDE LENAZ

ANNO ACCADEMICO 2018/2019

UNIVERSITA' DEGLI STUDI DI TRIESTE

Department of Mathematics and Geosciences

Ph. D. course in Earth Sciences and Fluid Mechanics

Zircon dating and trace element content of transparent heavy minerals in sandstones from the NE Alps and Outer Dinarides flysch basins

Ph. D. student:

Dott. Matteo Velicogna

Supervisor:

Prof. Francesco Princivalle

Co-supervisor:

Prof. Davide Lenaz

XXXII Cycle 2016-2019

Contents

Introduction

The Flysch basin is a typical product of orogenic events and is represented by clastic wedges that consist of a thick assemblage of turbiditic sediments that have been eroded from a fresh formed orogeny and deposited landward. These are often divided in two members: i) the flysch that represent the turbiditic unit deposited in moderate/deep marine environment that generally is the product od submarine landslides, and ii) the molasse that occurs during the final stages of an orogeny and it is generally represented by shallow water deposits. Mineralogical studies are often performed on sedimentary bodies to have constraints about the source/s lithology and provenance area/s helping the geodynamic reconstructions of a region.

These turbiditic basins are well suited for provenance studies, since their nature allow to collect important volume of sediments, supporting multimethodological and multiparametrical approaches. In particular the Cretaceous-Eocenic sedimentary basins of the North Eastern Part of the Adria Plate have been filled by two main sources, the first that derive by the disgregation of a huge carbonatic platform existed dering the Mesozoic and wich remains are exposed widely in the studied region, and a second siliciclastic fraction that derive from the near orogenies. The latter is extremely interesting since it could contain by stable (i.e spinel, garnets) and superstable minerals (zircon, rutile, tourmaline; ZTR group) that are resistant to physical and chemical alteration. These latter are the mostly used for provenance studies since they can preserve their genetic information also after the experiencing of light metamorphic conditions.

The extension, kinematics and position of the Adria Plate during the evolution of the Pangea and after its break-up are still matter of debate. However, it is known that it was one of the Peri-mediterranean regions that played an active role during the rearrangements of the plates and microplates in the Mesozoic and Cenozoic, which led to the formation of the Dinaric and Alpine orogenies. The Dinaric orogeny led to the formation of several turbiditic basins that have an elongated shape and are with NW-SE direction subparallel to the Dinaric chain. These are distributed from the Italian-Slovenian

border at north west (i.e. Bovec) until the North Dalmatia (i.e. Zadar Region) in the south-east. Taking in account the stratigraphy, thickness and exposition of the sedimentary rocks, in this work four nearly coeval turbiditic basins located at the north-eastern part of the Adria Plate have been selected. These four are the Julian (JB), Brkini (BK), Istrian (IB) and North Dalmatian Flysch Basins (ZB), which age of deposition varies between Late Cretaceous (Maastrichtian) for JB to Late Eocene in Pag Island (IB). In the past it has been suggested that these basins were filled in sequence, starting from the oldest one (JB) and following with BK and IB. This theory suggested that the new basin will open only when the previous one was filled. Furthermore, previous studies on heavy minerals (e.g. spinel, pyroxenes, and amphiboles) gave hints about the siliciclastic fraction provenance, but not in a definitive way.

The aims of this work are mainly three: i) to better understand the provenance of the siliciclastic sediment that filled the basins, ii) to find out the relation among the studied basins, if there is any and iii)to give constraints about the geodynamical evolution of the Perimeditteranean region between the end of the Cretaceous and the Middle Eocene.

The selected approach is to use three different mineral phases that are complementary with those that have been already used in the previous works. In particular, it has been identified two heavy superstable minerals such as zircon and rutile together with the garnet as perfect candidates. The three minerals are present in the all the basins, but in different concentration. In particular, zircon resulted the rarer phase, while the garnet was commonly found in all the samples. Notably, the zircon is commonly crystallized in acid magmas, while rutile and garnets represent mostry mafic and metamorphic sources.

The zircon resulted highly versatile since it contains high amount of radiogenic and trace elements that are used to have constraints about their crystallization age and the genetic information of the source. The isotopic methodology used in this work is the uranium-lead system that is particularly useful for dating minerals with ages between 5 to 5000 Ma and stable in zircon minerals. However, minerals and rock are often disturbed by physical and chemical alteration and behave as isotopically

open systems. In addition, zircon can be recycled during several magmatic/metamorphic events that could product magmatic acresciments that register the different age of growth of the mineral or isotopic omogenizzation, with the partial loss of meaning of the age data. For these reasons, the data must require a careful interpretation. In this work, theU/Pb isotopes have been used to confirm their magmatic origins (together with their chemistry) using the Concordia plot together with the chemistry of the zircon (Th/U ratio). Furthermore, the age relative probability spectra have been built for every basin and could be considered as a fingerprint of the sedimentary basin. This latter identifies peaks of age in wich there has been a crustal accretion and so an intense magmatic phase. Since they are characteristic of the basin, it has been possible to directly compare the spectra among the studied basins to verify their relation, furthermore it has been possible to compare the spectra with other coeval basins located in the Perimediterranean region.

Generally, garnet and rutile in sedimentary rocks preserve their original chemistry that is useful to define their source rocks. In particular, it has been used both major and trace elements diagrams and classifications that allow to discriminate between magmatic-metamorphic crystals, and among the different kind of metamorphic and magmatic source rocks. Furthermore, the content of Zr in rutile is also used to calculate the temperature of crystallization of the mineral. In particular, in this work two geothermomethers are used for comparison that are based on different sperimental curves. The data help to better define the metamorphic facies in which the rutiles have been crystallized, helping to circumscribe possible source area.

Similar approaches are also used for coeval basins that are located close to those studied in this work. Among these, the Bosnian Flysch basin is often put together to JB due to their similar age, mineralogy and their geographical proximity, while the coeval North West Dinaric basins are considered separated. Geochronological and chemical comparison among the mineral phases of the here studied basins and the literature data will be performed to have constraints about their possible sharing of sediment sources and the possible relation among each other. This information could help to better understand the regional arrangements of the source areas that indirectly give constraints about the

position of relative position of the microplates and their relation. Furthermore, these data could improve the understanding of the geodynamical evolution of the Primediterranean area helping the geodynamical reconstructions.

.

Geological Setting

The Adria problem

In literature, Adria and Apulia Plate terms are often used as synonymous, and it is possible to find both. However, the extension and the geodynamic evolution together with its role in the Mediterranean area are still strongly debated.

There exist several definitions of Adria or Apulian Plate. Channel & Horvát (1976) and Anderson & Jackson (1987), taking in account geophysical and geological features, defined the Adriatic subplate as the stable foreland partially submerged by the Adriatic Sea confined by the surroundings orogenic chains (Apennines, Southern Alps, Dinarides and Hellenides). This undeformed lithospheric subplate acted as a rigid intender during the Alpine and Dinaric orogens (e.g. Channel et al., 1979; Placer et al., 2010). Other authors (i.e. Stampfli, 2000, 2005; Stampfli et al., 2001, 2006) are partially in agreement, suggesting that the Adria Plate were divided in two parts, Adria and Apulia s.s., which welded together and formed the Greater Apulia (or Adria), a plate that existed during the Mesozoic and incorporated the autochtonous portion of Greece and Bay-Daglary of southwest Turkey. Later, this increased plate has been reduced to the present day Apulia-Adria dimension after subduction-shortening events occurred as testified by the Hellenides-Dinarides-Balkan transect of ophiolites. Others, (i.e. Schmid et al. 2008 and references therein) consider as “Apulia Plate” the group of all the continental terranes that were southward of the Alpine Tethys and north of the Neotethys. Among the comprised terranes there are the Austroalpine and the Southern Alps, which are divided by the Periadriatic Line, which is considered active since the Palaeozoic times. Schimd et al. (1989) pointed out two phases, the first dextral transpression occurred during the Cretaceous and a second sinistral movement during the Oligocene, in agreement with the movement of the Defereggen-Anterselva/Antholz-Valles/Vals fault (DAV Line) in Eastern Alps (Mancktelow et al., 2001).

The second issue regards the paleoposition and the drifting of the Adria Plate and in particular its movement compared to those of the Africa one. During the last decades the researchers suggested many different theories supported by geological and/or geophysical evidences.

In particular, several authors suggested that, on a large scale, the Adria could be considered as an African Plate promontory and that both of them moved together from the Early Jurassic to the Cenozoic (e.g. Channel & Horvát, 1976; Schettino & Turco, 2009), or from the Late Paleozoic (e.g. Muttoni et al., 2003; Rosenbaum et al. 2004; Fig. 1). Wortmann et al. (2001) pointed out the "space problem" of Adria, the authors observed that starting from the common Adria Jurassic paleoposition (common in most of the paleoreconstructions), a coherent rotation with the African plate led Adria in a final position located much eastward than the actual one, in overlapping with Iberia. Their final model relocate the Adria Plate and assumed that there exists a rigid connection between the two plates suggesting that during Jurassic and Cretaceous times, the two moved coherently. However, the authors stated that, a connection between the two plates in the Mesozoic are possible but not necessary for the plate reorganizzation. A possible solution is to divide Adria in two independent microplates (Adria and Apulia s. s.) divided along an E-W boundary around the Gargano latitude (Stampfli et al., 2006; Schettino & Turco, 2011 and reference therein; Fig. 2). This hypothesis seems to be agreed by GPS field studies that suggest two different kinematics for north and south Adria (Adria s.s and Apulia s.s.; e.g. Mantovani et al., 2015).

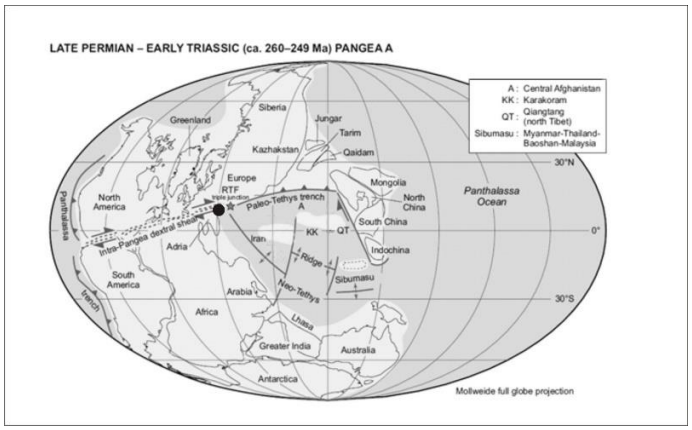

Fig. 1. Paleoposition of the Adria Plate during the Late Permian-Early Triassic following the reconstruction of Muttoni et al. (2009, modified)

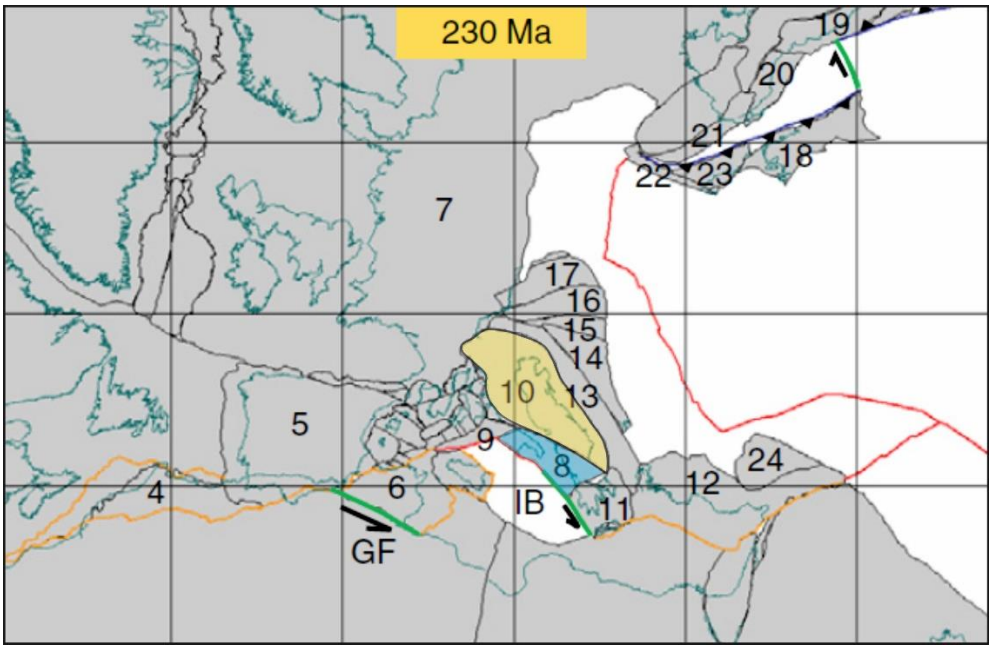

Fig. 2. Paleoreconstruction of the Perimediterranean Region during the Triassic following Schettino & Turco (2011) modifiedThe areas in grey represent the continental lithosphere, the white ones the oceanic domain. The areas affected by the first rifting events are bounded by orange lines. Transform faults are shown in green. Dark-red line is an incipient spreading center. GF—Gafsa fault; IB—Ionian Basin; 1—North Africa, 4—Morocco; 5—Iberia; 6—Tunisia; 7—Eurasia; 8 (blue)—Apulia; 9—Panormide platform; 10 (Yellow)—Adria; 11—southern Greece;12—Menderes-Taurides platform; 13—Eastern Dinaride platform; 14—Eastern Dinaride accretionary wedge; 15—southern Pannonian Basin; 16—Tisza; 17—Pelso; 18—Sakarya; 19—East Pontides; 20—West Pontides; 21—Strandja; 22—Serbia-Macedonia; 23—Rhodope; 24—Kirşehir.

Even though Africa and Adria showed similar motions since the Palaezoic times, recent paleomagnetic studies show that the coeval paleopoles of Istria (Croatia) and Africa differ in Late Jurassic times, suggesting that during that period, Adria moved independently from the African Plate (Márton et al., 2017). These movements could be due to the opening of the Ionian Ocean that started to form during Late-Middle Jurassic and stopped with the opening of the Alpine Tethys (Tugend et al., 2019). Successive polar shifts suggest two mains rotationally movements, the first occurred during the Late Cretaceous (clockwise), in which Africa and Adria probably definitely separated, and a second happened after the Eocene, probably closing to the end of the Miocene (anticlockwise) (Márton et al., 2008; 2010). In agreement with the actual separation of the two plates, historical seismicity, fault-plane solutions, and young tectonic structures as well as the geodetic measures suggest that Adria is actually separated from Africa, and recently acted as an independent microplate (Anderson & Jackson, 1987; Battaglia et al., 2004; Fig. 3). However the data supported by Márton et

al. (2008; 2010; 2019) are considered not reliable by Ustawezski et al (in print) because of their sampling.

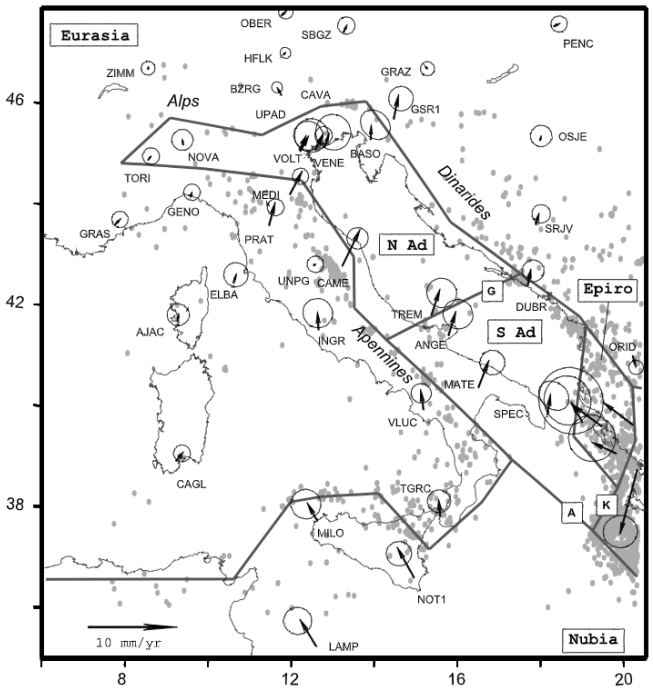

Fig. 3. Gps velocities of the [N Ad] North Adria, [S Ad] South Adria, [G] Gargano-Dubrovnik fault zone, [K] Kefallinia fault zone and [A] Apulia escarpment segments.The black lines represent the block separations (Battaglia et al., 2014)

Finally, the paleomagnetic and geodetic studies seem to agree with the Schettino & Turco (2011) and Stampfli et al. (2006) reconstructions, where the Adria Plate has been divided in two independent fragments. The Ionian Ocean is located south of the Apulia s.s. and there are no geological evidences of Jurassic basins between Adria and Apulia s.s. microplates, suggesting that the two were welded and moved together since the Early Jurassic. For what concerns this work, Adria Plate will be referred as the group of terranes that behave as rigid intender during the Alpine and Dinaric orogeny formed by both Adria s.s. and Apulia microplates.

Evolution of the Adria Plate and of the Mediterranean Region

The Mediterranean Region occupied the central part of the Pangea super continent but the story of its evolution recorded in the sedimentary basins started earlier. The first trace of the Adria plate could be associated to the drifting of the Armorica Terranes Assemblage (ATA) during the Palaeozoic that followed the detachment of Avalonia. The ATA formed a promontory that has been divided by the forming of Saxo-Thuringian and Galicia-Moldanubian narrow oceans detaching the Franconia-Turingia and Iberia-Armorica-Boemia terranes. The Paleo-Adria is supposed to comprise Galicia-Moldanubian allochthons on the Mediterranean flank of the Variscides, exposed in north-east-Iberia, south France (including western parts of the Maures-Tanneron-Corsica/Sardinia assemblage) and the southern Alps remained in contact with the northern edge to the Gondwana (Franke et al., 2017 and reference therein; Fig. 4a-h). During the Devonian, the Rehic Ocean and all the basins between Laurussia and Gondwana continents started to close, embedding all the detached terrain between the two continents and in the Middle Carboniferous the Pangea super continent was formed (Fig. 4e-h). The contact between the two occurred mainly between the northwestern edge on the Africa and North America. This event led to the formation of the Variscan orogeny, which remnant extends from the North America (Ouachita and Appalachian chains) to Poland. In particular, in the Mediterranean Region it is possible to find part of this huge orogeny in Sardinia, Corsica and South Iberia. After the Pangea formation there were still two small oceans between Gondwana and Laurussia, the Paleotethys and Theic oceans, at east and west of the collision, respectively (Matte et al., 2001). A clockwise rotation of the Gondwana in the Early Permian closed the Theic and widened Paleotethys.

Several authors suggest that, during the Permian (e.g. Golonka, 2004; Stampfli & Kozur, 2006), the northward subduction of the Palaeotethys under the southern part of the Laurussia formed a mechanism that detached a ribbon like terrane from the northern Gondwana, resulting in the opening of the Neothetys. The subduction rollback created several oceanic ridges, generally considered NW-

SE elongated, i.e., Meliata, Maliac, Pindos (Stampfli et al., 2002) or Vardar and Pindos (Csontos & Vörös, 2004). In particular, the Meliata rift may have affected also the continental plate from the Balkans to northern Italy (Ivrea) where Permian basic magmatism is widespread (e.g., Zanetti et al. 2013).

On the contrary, Schmidt et al. (2008), Bortolotti & Principi (2005), Maffione & Hinsbergen (2018) and Muttoni et al. (2009) suggest that the Triassic Eastern Tethys was formed only by one branch (Fig. 4). The former authors use the term "Neotethys" to describe all oceanic realms located in an area southeast of the Alpine Tethys and the future Western Alps that opened during and after the Permian to Triassic closure of the Paleotethys.

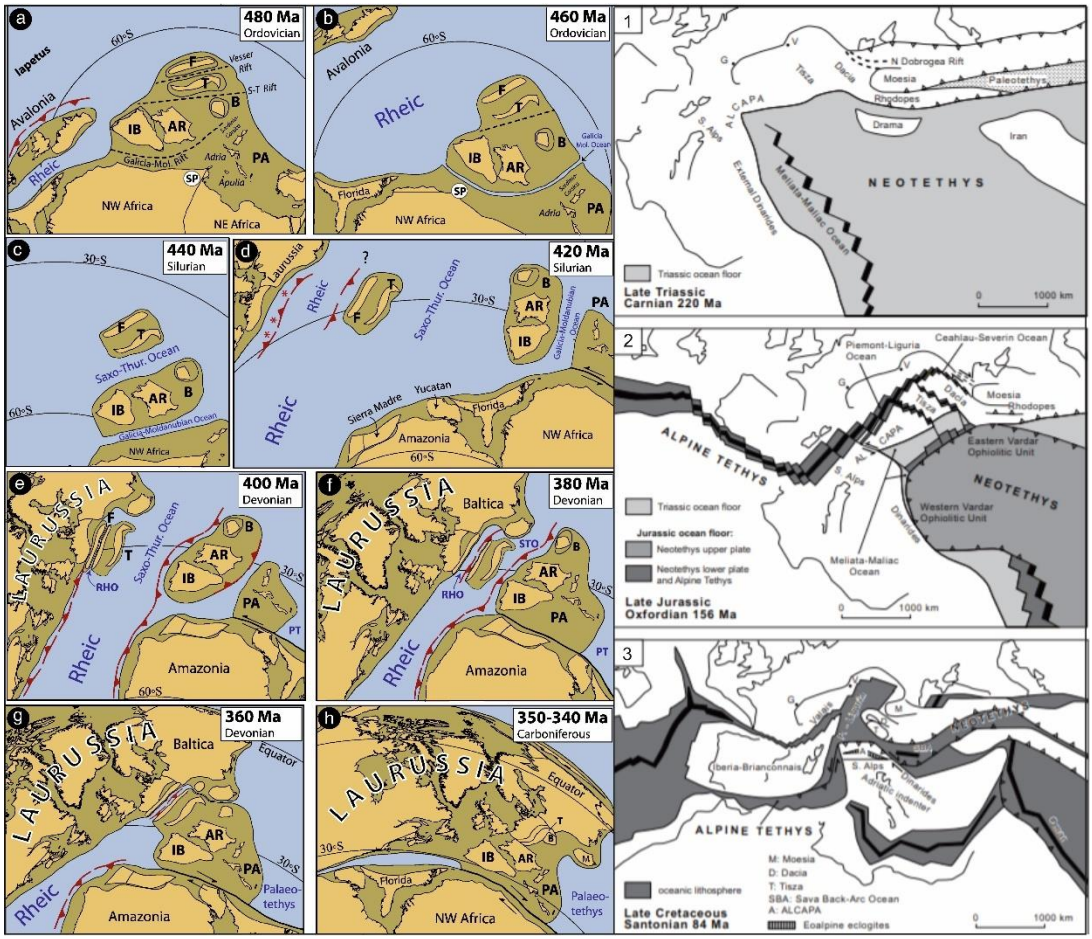

Fig. 4. On the left the paleoreconstruction of the Variscan and surrounding areas from the Early Ordovician (Tremadocian: 480 Ma) to the Early Carboniferous (a-h) as suggested by Franke et al. (2017). PA, Palaeo-Adria; PT, Palaeotethys; AR, Armorica; B, Bohemia; F, Franconia; IB, Iberian Peninsula; RHO, Rheno-Hercynian Ocean; SP, South Pole; S-T Saxo-Thuringia; STO, Saxo-Thuringian Ocean; T, Thuringia. On the right the schematic palinspastic sketches of the Perimediterranean area as suggested by Schmid et al. (2008) from the Late Triassic to the Late Cretaceous (1-3).

During the Late Triassic the spreading of the Vardar Ocean compensated the subduction of Neotethys and Paleotethys, making stay stable the amount of total oceanic lithosphere (Schettino & Turco, 2011). The reconstruction of Schettino & Turco (2011) suggests that the spreading of the Neotethys was linked with the extensional system of the Central Pangea with a triple point, similar to the triple point suggested by Muttoni et al. (2009 Fig. 1) that connected Neothethys, Paleotethys and Intrapangea Dextral Shear.

The breakup of the Pangea occurred in the Late Triassic-Early Jurassic and could be due to the restart of the extension in the Ionian basin, which linked the Atlantic and Atlas extensional system with the rifting of the Anatolide-Tauride platform (Schettino & Turco, 2011 and reference therein). The opening of the Atlantic Ocean started during the Early Jurassic (Toarcian; Stampfli & Hochard, 2009) and led to a rotation of the Adria Plate with respect to the Euroasian terranes, determining a spreading with northwest-southeast direction between the two, while the Vardar zone ridge segments were constrained by the Cimmeria alone. The difference in movement between the Adria and Vardar plates suggested a new extension formed along the Gondwana that led to the formation of several basins: the Hallstatt Trough corresponds to the western continuation of the Meliata Ocean and separated the Austroalpine from the Southalpine realm (Sölva et al., 2015; Channell et al., 1992) or/and the Tisza (or Tisza) terrane (showing a mixed Adria-Europe affinities) from Europe (Golonka, 2004), positioning the latter in a paleogeographic area comparable to those of the Southern Alps (Schmid et al, 2008), the Belluno Trough located in the Venetian Dolomites (North Italy; Stefani et al., 2007), the Bosnian Trough in the External Dinarides and the Inner Tauride Ocean (Schettino & Turco, 2011 and reference therein). It is worth noting that in the literature the Bosnian Basin contain all the basins considered in this study and extend from the Julian Alps to the Bosnian Flysch Basin. All these basins have been filled by syntectonic flyschoid sediments during Late Cretaceous-Middle Eocene.

During the Middle-Late Jurassic the Vardar Plate welded with Europe, and the spreading of the Atlantic Ocean led to the subduction of the western Tethys under the Vardar. The new oceanic branches opened between the Eurasia and Adria are the Ligurian Tethys, which was

paleogeographically located south of the Briançonnais continental fragment, and Alpine Tethys, which was its northeastern continuation (Schmid et al., 2019; Schettino & Turco, 2011). The second cannot be traced in the Western Carpathians because it has not found relics of basalts, gabbros or serpentine, while the Meliata ophiolite fragments represents the remnants of the northern branch of the Neotethys (Schmid et al., 2019).

In the beginning of the Cenozoic Africa and Eurasia convergence stopped, freezing all the subductions in Alps and Pyrenees domains, while in the Vardar zone a slow convergence still continued. This standstill moment probably induced a gravitational collapse of the orogeny with the formation of local extensional structures (Marton et al., 2017).

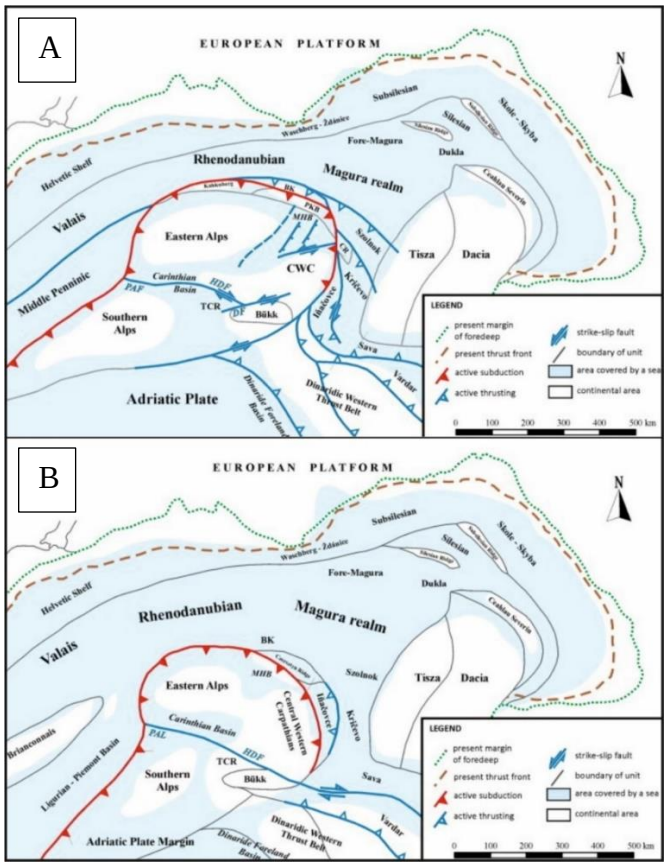

Fig. 5. Early-Middle Eocene (A) and Early Paleocene (B) models of the Perimediterranean Region as suggested by Kováč et al. (2016).

At the end of the Cretaceous-Early Plaeocene the Perimediterranean Realm and the actual Central Europe were formed by several microplates separated by small oceanic domains (Fig. 5A); Kovac et al., 2016). Hemipelagic material and turbiditic systems have been instaurated in the Subsilesian and

Skole basins at the edge of the European Platfrorm, as well as in the Magura ocean and its continuation, the Northern Penninic Rhenodanubiam–Valais domain located in the foreground of the Eo-Alpine thrust system of the Alps (Kovac et al., 2016 and reference therein). The Paleocene movement of the Adria Plate toward the north generated a build-up of compression in the Alpine, Western Carpathian and Dinaridic orogenic systems (e.g., Dercourt et al., 1986; Albarello et al., 1995; Rosenbaum et al., 2002, 2004; Rosenbaum and Lister, 2005), triggering the westward to south-westward propagation of the Dinaridic orogenic wedge. The evolution of the orogenic system occurred simultaneously with a dextral shear NW–SE oriented along the easternmost segment of the Periadriatic Fault, which separates the Central Western Carpathians and units of the Northern Pannonian (Kovac et al., 2016)

Even though, during the Paleocene-Eocene a transpressional regime controlled the tectonic of the Perimediterranean region, the Lutetian lateral movements of individual segments of the Eastern Alpine-Western Carpathian orogenic system generated also widespread extension (Kovac et al., 2016). In particular, the northward movement af the Eatsern Alps and the northeasteward one of the Central Western Carpathians affected their junction zones, and the development of a marine connection among the Magura, South Penninic and the Dinaridic foredeep occurred (Fig 5B). Early and Middle Eocene were also characterized by the reactivating of the Alpine and Pyrenees low speed convergent structures, together with the left lateral strike slip fault between Adria and Apula s.s. and the right lateral fault zone within the Dinaric domain (Schettino & Turco, 2011). The two are responsible of the north-western drift of the Adria Plate and its subduction beneath the Pannonian blocks. These strike slip motion within the Dinarides is supposed to have doubled the Vardar ophiolite belt. (Schettino & Turco, 2011).

In Paleocene-Eocene Periods connection among the Northern Hungaria-Slovenian Paleogene and Dinaric foredeep basins is sustained by similar fossils findings. The close position of the Transdanubian and Southern Alpine Units is also sustained by their affinity and it is possible to suggest their northern position respect the Adria Plate together with the Dinaridic foredeep basin (e.g

Kovac et al., 2016; Tari et al., 2000).In the Middle Eocene, Valais and the Alpine Tethys were already almost totally subducted under the Pyrenean Fault and the Western Alps Trench, respectively, while south Ligurian and Ionian Oceans were still opened.

During the Late Eocene the lateral movement among Adria, Apula and Dinarides areas stopped, and the first two reached their actual position respect each other. Coevally, a compressional deformation occurred within the Dinarides zone, registering the main deformation of the orogeny. During this phase, the basins were extensively filled by flyschoid sediments.

Adria represent a continental plate where shallow-deep marine carbonates were deposited almost continuously from the Mesozoic to the Tertiary (Carminati & Doglioni, 2012 and references therein).

The Dinaric orogeny

The Dinarides are an orogenetic belt, 700 km long, generally characterized by SW verging structures with main tectonic lines that are oriented NW-SE, and are part of the Alpine orogenic system. Historically the chain is divided in External and Internal Dinarides, taking in account tectonostratigraphic elements belonging to the passive and active Tethyan continental margins, respectively (Palinkaš et al., 2008). Schmid et al. (2008), suggest the Drina-Ivanjica unit as structural divisor between the two areas, taking in account the two sub-parallel ophiolites located west and east of the suggested divisor unit. The External Dinarides are formed by the Adriatic Carbonate Platform (AdCP) and carbonate-clastic formations of the passive continental margin (Bosnian Flysch), while the Internal ones are composed by ophiolite units and active continental margin lithologies, olistostrome mélange (Palinkaš et al., 2008).

The geodynamic evolution of the Adria plate and the Dinaric domain started during the Mesozoic, but the exact kinematics that involved the formation of the Dinarides are still strongly debated, in particular regarding the number and shape of carbonate platform/s. There are two main paleogeographic models which try to suggest possible solutions: the first involves a unique Carbonated Platform called Adriatic-Dinaric Carbonate Platform (ADCP; Pamić et al., 1998; Korbar, 2009; Fig.6) or Adriatic Carbonate Platform (AdCP; e.g. Vlahović et al., 2005) and the second suggests two carbonate platforms separated by a deep water basin (e.g, Tari, 2002; Schmid et al. 2008).

The two models differ in interpreting the kinematics for the shortening of the formation of the Dinarides, and so the Tertiary geodynamic evolution of the region. The first involves folding and faulting along steep reverse faults while the second suggests a predominant thrust stacking. Notably, the seismic and borehole data do not show consistent evidences of inter-platform underthrust unit (Korbar, 2009; Fig. 6).

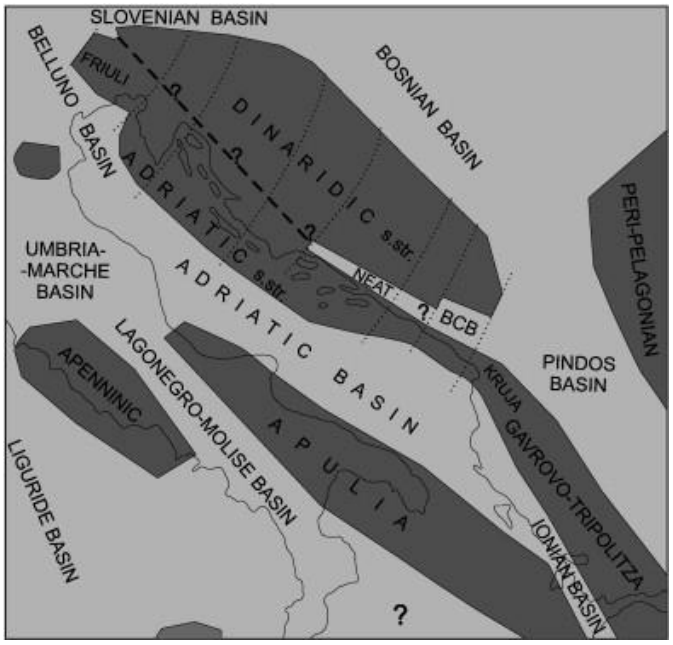

Fig.6. Paleogeographic map of the Adriatic region for the Late Cretaceous time (some present-day geographic lineaments are indicated, as suggested by Korbar (2009). The Adriatic–Dinaridic carbonate platform (s. l.) is split into the Dinaridic and Adriatic platforms (s. s.) by the supposed continuous NE Adriatic trough (NEAT, thick dashed lines). Hypothetical transform faults (thin dotted lines). Basins on the continental and oceanic crust — light grey. Carbonate platforms and shelves — dark grey. BCB — Budva–Cukali Basin.

Vlahović et al. (2005) suggested that the ADCP could have been part of a huge separated platform in Southern Tethyan realm, the Southern Tethyan Megaplatform, whose relics can be found in the area of Italy, Austria, Hungary, Slovenia, Croatia, Bosnia and Herzegovina, Serbia, Montenegro, Albania, Greece and Turkey (Fig. 7). Due to tectonic forces, this huge platform framed, forming several carbonate platforms (e.g. Apennine and Adriatic Carbonate Platforms; Vlahović et al., 2005; Velić et al., 2015) with a shared basement.

The oldest part of the Palaeozoic basement represent the Variscan basement, while from the Carboniferous to lower Triassic prevailed the deposition of mixed carbonate-siliciclastic material, since the entire area was still an epeiric platform along the northern Gondwana margin (Pamić et al., 1998; Vlahović et al., 2005). The youngest part of the basement is made by thick sequence of shallow-water limestones punctuated and intruded by volcanics, volcanoclastic rocks and bauxites (Vlahović et al., 2005).

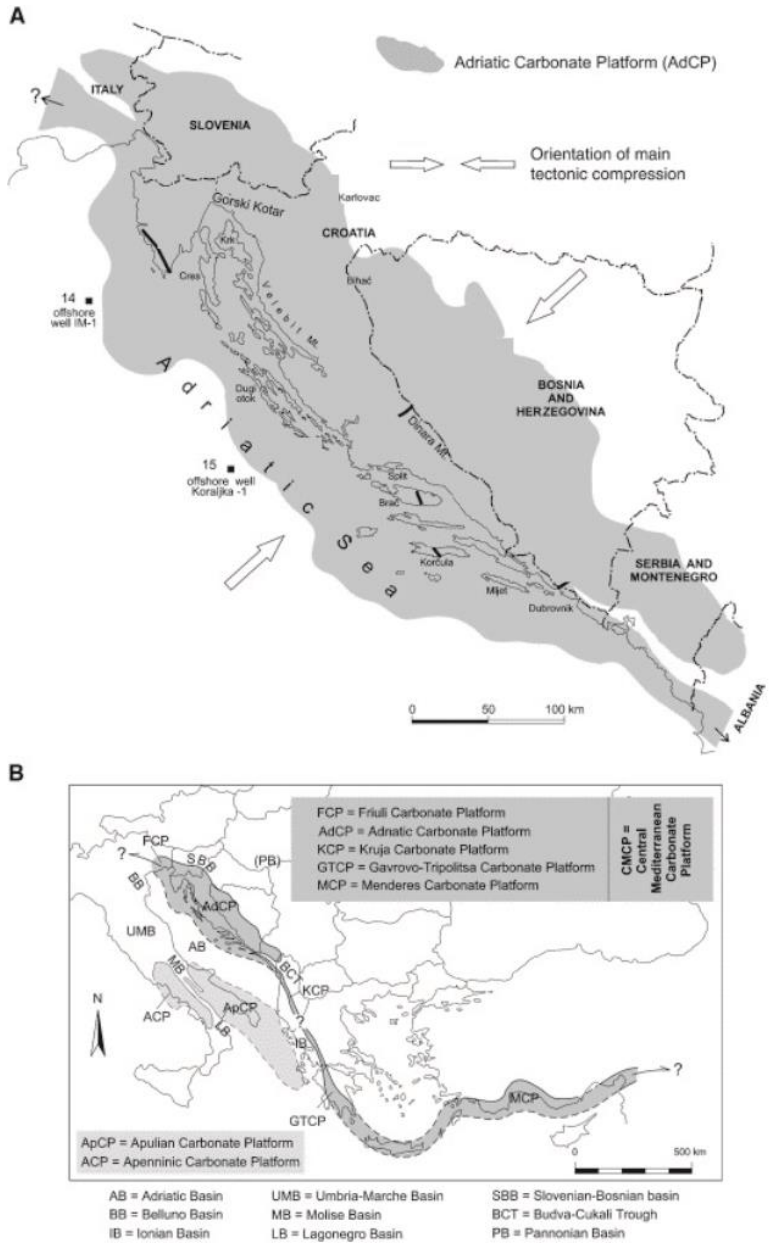

Fig. 7. Simplified geological maps showing the present distribution of Adriatic Carbonate Platform (AdCP) deposits on the basis of outcrops and off-shore (A) and the recent distribution of the carbonate platform deposits in the central Mediterranean (B) as suggested by Vlahovic et al. (2005).

The volcanic occurrences could be referred to the initial rifting phases due to the incipient instability of the Pangea. In Triassic times, the rifting accelerated as a consequence of the high magmatic activity and culminated with the opening of the Dinaric Ocean. During Late Triassic-Early Jurassic, the continental slope of AdCP started to develop and it has been supplied until the Late Cretaceous with carbonate detritus by the Adriatic platform, and siliciclastic materials coming from northern sources as turbidity currents (Pamić et al., 1998). During the Jurassic, the north-western seafloor spreading

triggered the subduction of the Tethys along the eastern promontory of the Adria plate generating a magmatic arc, while sedimentation of the Bosnian flysch continued its Apulian passive margin in the south (Pamić et al., 1998). The Cretaceous- Paleogene times were characterized by strong tectonic movements, which affected all the sedimentary Dinaric and Tethyan areas. Flysch basins mainly represent the remnants of little elongated troughs which appeared during the Late Cretaceous emergence near the NE ADCP platform margin and during Middle Paleogene due to the extensional tectonics of the area. The strongest deformation events occurred during Paleogene because of the closure of the Dinaric Tethys, producing the uplift of the Dinarides, which separated the Tethys into the Mediterranean and Paratethys branches. This generated several larger and smaller intramontane basins inside the emerged Dinarides.

The studied basins

The area investigated in this work is located in the northeastern part of the Adria plate and cover an area including Italian, Slovenian and Croatian terranes. The sedimentary basins considered for this work are four in total: the Julian Basin (JB), the Brkini Basin (BK), the Istrian Basin (IB) and the North Dalmatian/Zadar Basin (ZB). They are located in the External Dinarides Area and more precisely in the S-Alpine Apenninic and Dinaric foreland, High Karst unit and Dalmatian and Kruja zones (Fig. 8B).

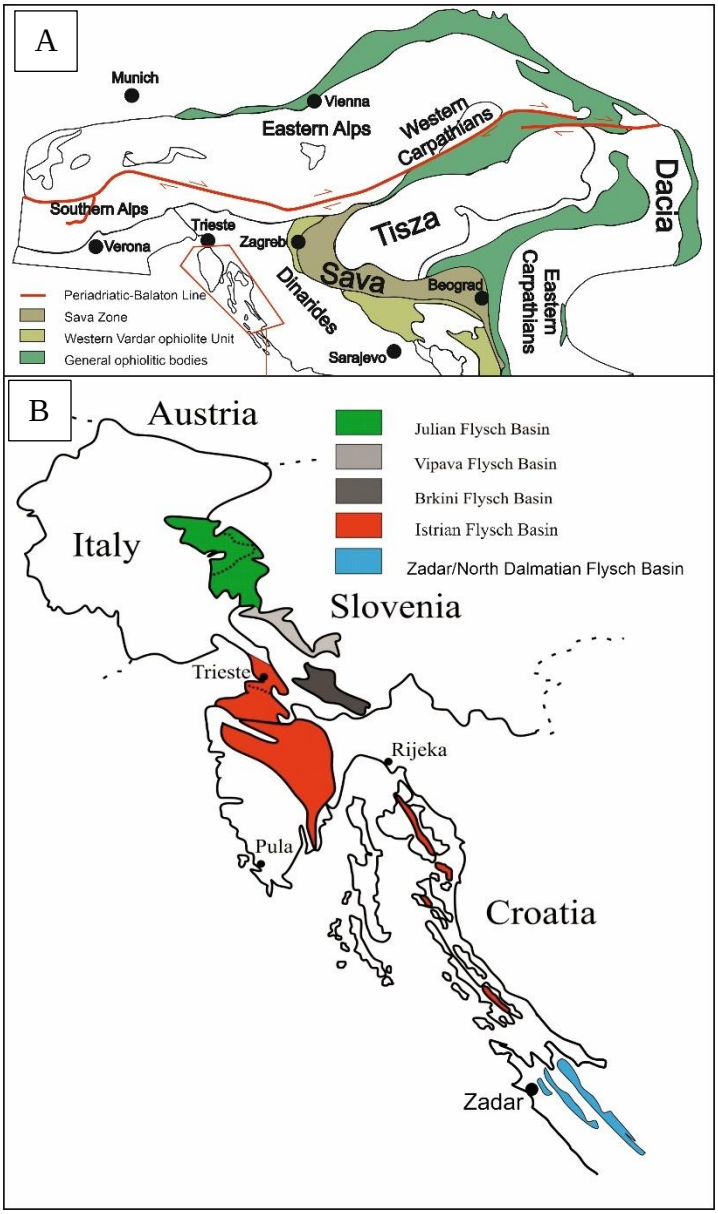

Fig. 8. Simplified geological map after Ustaszweski et al. (2010, modified) indicating the main geological units, the main ophiolitic bodies and the sampled area (A). In B the inset showing the investigated flysch basins and their relative positions (Lenaz et al., 2000, modified).

Generally, the basins show an elongated and narrow form body (i.e. Tunis & Venturini, 1992, 1996 and references therein) that recall the deep-sea trough of submarine tunnels. Their age spans from the Santonian-Campanian to the Middle Eocene, with a general rejuvenation trend that start from the northwest (JB) to the southeast (ZD). Several authors (i.e. De Min et al., 2014 and references therein) suggested that the filling of the basins occurred in a sequential way, thus the start of a new filling started only when the previous one was completely filled.

The samples of JB, IB and BK used in this work belong partially to an old sampling campaign and they have been selected taking in account the previous works of Lenaz (2008), Lenaz & Princivalle (1996; 2002 and 2005), Lenaz et al. (2000; 2001 and 2003) and De Min et al., (2014). While, ZB samples have been collected in a recent sampling campaign and firstly studied in this work.

Julian Basin

The Julian Basin (or Slovenian basin for the Slovenian authors) represents a sedimentary basin which has been active from the Jurassic to the Middle Eocene. JB extends in an area that comprehends the Julian Prealps, Tolmin Mts., Natisone Mts., the western part of the Banjška Plateau and the Vipanska Dolina (Fig.9). The basin shows a narrow-elongated body that has been often tectonically active (Tunis & Uchman, 1996). The southern boundary of the sedimentary basin is represented by the Friulian Carbonatic Platform, which correspond to the maximum northwestern extension of the Dinaric Platform (Tunis & Uchman, 1996), while the northern border is located in the Bovec area.

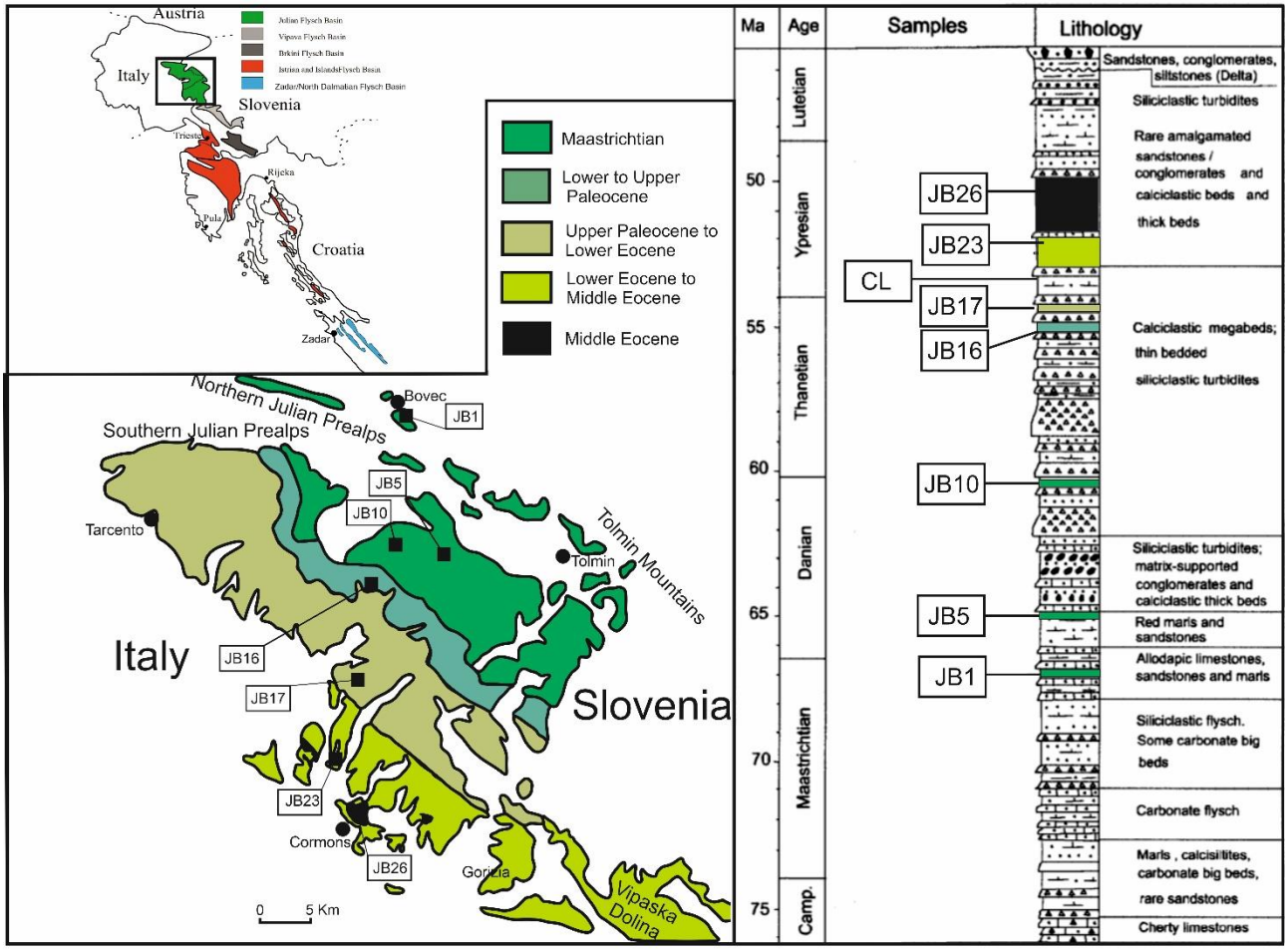

Fig. 9. Simplified geological map of the Julian Flysch basin, after Tunis & Uchman, (1996 modified) and its stratigraphical column (Lenaz et al., 2000).

The northern area of the basin (in particular north of Mataiur Mt.) has several paleokarstic structures that have been formed presumably in the Early Jurassic, suggesting that one or more emersion events occurred in the area, probably due to some platform block tilting (Venturini et al., 1991). On the contrary, in the southern part of the basin similar emersion structures are rare and are supposed to have been formed only at the end of Early Jurassic and limited in a small area (Pirini et al., 1986). The latter suggests a different subsidence history between the northern and southern part of the Julian Basin.

During the Middle Jurassic, in the Mataiur Mt. area the sedimentation reactived forming a series of oolitic calcarenites embedded with pelagic limestones (Tunis & Venturini, 1984), probably related to a strong subsidence. It is worth noting that in the southern area of the Mataiur Mt. the thickness of these levels appears strongly reduced (Pirini et al., 1986) or absent (Miklavić & Rožić, 2008).

In the Late Jurassic, a strong south-western retreat of the Carbonatic platform increases the subsidence of the area, transforming it in a continental slope. The coeval main deposits were composed by carbonatic breccia, which show a decrease of thickness from southwest to northeast. Furthermore, in this part of the basin several lacunas have been observed, probably due to tilting movements of the slope blocks.

During the Early Cretaceous the platform talus moves toward northeast, but several sedimentation lacunas occur, that have probably been formed due to slope paleocurrents established in middle of the period. At the end of the Early Cretaceous a strong subsidence occurred, increasing sedimentation rates. The Matajur Mt. behave as a relative high, stopping the material, while in the Colovrat Region the fluxes reached the Tolmin trough (Tunis & Venturini, 1984). After this period of strong sedimentation, the basin does not register new deposits until the Late Campanian and Maastrichtian, probably due a sea regression as testified by the presence of bauxitic levels near Trieste (Italy), which suggest an emersion moment (Gregorič et al., 1998). During the Maastrichtian a new tectonic phase occurred and in this series of events, the Tomin trough axis, the platform margin and the meridional

slope moved toward southwest. From this moment to the Middle Eocene there will occur the main turbiditic deposition that reaches the maximum thickness of 4000 m.

During the initial stages of this event, the material coming from the collapsing of the carbonatic platform formed a breccia, which thickness locally reached 130 m (Miklavić & Rožić, 2008). Successively, the sediments originated by the erosion of this basal breccia have filled the topographic lows located in the eastern part of the basin.

Only at the end of this phase and coevally with the emersion of the northern territories, the deposition of the distal emipelagic strata with siliciclastic composition started. Occasionally, the siliciclastic turbidites are alternated with carbonatic strata that have been transported by gravitative fluxes from the Dinaric Carbonate Platform in regression (Miklavić & Rožić, 2008). These carbonatic levels could be quite thick and considered as megabeds deposited in a system of transverse intrabacinal ridges, which seem to have been structurally controlled and representing relative paleobathymetric highs that isolate intra-platform and intra-slope basin systems (Ogata et al., 2019). The most probable trigger mechanism invoked for the emplacement of the carbonatic megabeds is the seismic shock, but several pre-conditioning factors must be taking in account, which could be directly or indirectly related to major climatic shifts occurred in the area at that times (Ogata et al., 2019). However, the two carbonatic megabeds cropping out in Matajur Mt. area seem to suggest a westward relocation of the carbonatic source (Miklavić & Rožić, 2008). Regarding the provenance of the siliciclastic strata of JB flysch, & Tunis & Venturini (1992) suggested that a possible souce could be located in the nearby north and northeast areas of the basin, probably in the South Alpine area, implying longitudinal paleocurrents. In the Bovec area, rare igneous rock clasts have been found in the Maastrichtian flysch (De Min et al., 2007), showing tholeiitic affinities with a strong arc-type signature, which source area has been located in the Internal Dinarides and belonging to the Vardar-arc system.

The stratigraphy of the Julian basin have been studied in detail through the years by several authors (e.g. Tunis & Venturini 1984, 1992; Venturini & Tunis, 1991), it is informally divided in 8 main units from the oldest to the youngest:

a) Drenchia Unit (Lower Maastrichtian) that crops out from the Drenchia village to Nacucu Mt (Tunis & Venturini, 1984), it begins with an erosion breccia followed by siltites and calcarenites.
b) Clodig Flysch (Lower Maastrichtian) is 250 m thick and it is characterised by calcarenites and calcilutites with carbonate and marls interbedded. The unit crops out from the Iudrio Valley to Obranche (Tunis & Venturini, 1984). Sandstones are rarely present in the lowest part of the sequence, but they are more frequent in the higher part. Slumps are generally numerous in all the sequence.
c) Iudrio Flysch (Lower Maastrichtiano - Upper Maastrichtian) that is generally composed by sandstones, marls, calcarenites and calcirudites. Carbonatic strata are frequently present with thickness that varies from 20 to 400 cm (Tunis & Venturini, 1984)
d) Brieka Flysch (Middle Maastrichtian-Upper Maastrichtian) is ~40m thick and mainly crops out in the Mt. Brieka area. It is mainly constituted by sandstones and marls, embedded with calcarenites and calcilutites strata that show a thickness <20 cm.
e) Calla Flysch (Lower Paleocene – Middle Paleocene) is characterised by reddish and greenish marls, carbonate level marls and thin sandstones levels. Calcarenites and calcilutites are rarely present in the western outcrops (Loanaz Mt.), becoming more frequent in the eastern ones. The thickness varies between 120 m near Loanaz Mt. to 170m east of Natisone Valley (Rodda area).
f) The "Flysch di Masarolis" (Middle Paleocene-Upper Paleocene) mainly crops out in the central-eastern sector of the Natisone Valleys and extends to the Banjšice Plateau region (Trušnje) in western Slovenia. This unit is characterized by predominant medium-thick siliciclastic turbidites consisting of a sequence of quartz-litharenite and gray marl beds.

Carbonate proximal turbidites and, occasionally, paraconglomerates rich in chert pebbles are interbedded within the siliciclastic turbidites (Tunis and Venturini, 1992).

g) A thick megabed marks the start of the “Flysch del Grivo" unit (Upper Paleocene-Lower Eocene), characterized by several types of megabeds that gradually become thinner and less frequent in the upper part of the section (Ogata et al., 2019). Siliciclastic-carbonate turbidites, hybrid sandstones, massive calcarenites and conglomerates (debrisflow) are generally present among the megabeds. The "Flysch del Grivo" extends from the West to the East from the Mt. Faeit-Zimor T. area, across the Natisone valleys and the Goriška Brda as far as the Banjšice Plateau (Anhovo region).

h) Cormons Flysch (Lower-Middle Eocene) where a progressive decrease in paleobathimetry is recognised in good agreement with the vertical changes of the sedimentary structures (Venturini and Tunis, 1991). The succession shows the entire evolution from epibathial turbidites to a delta plane facies, which is probably related to tectonic and eustatic forces (Venturini and Tunis, 1991).

Ten representative sandstones have been selected (JB1, JB5, JB10, JB16, JB17, JB21, JB26, Nim and CL), where JB1 and JB26 represent the bottom and the top of the stratigraphic column (Fig. 9). The samples are classified as lithic greywackes and are mainly composed by quartz, calcite, plagioclase, clay minerals, dolomite and fine grained lithic fragments of dolostones, limestones, radiolarites, cherts, diabases, siltstones, quartzites, micaschist and phyllite. Rarely, K-feldspars (microcline) and phyllosilicates (muscovite, biotite and chlorite) occur. Cr-spinel, garnet, tourmaline, zircon, pyrite, amphibole, pyroxene and staurolite constitute the heavy mineral assemblage (Tunis & Venturini; 1992; Lenaz e al., 2000, 2003; De Min et al., 2014).

Brkini Basin

The Brkini Basin (BK) is formerly a synclinal located in the south western Slovenia, which show an elongated NW-SE shape (Fig. 10). The sedimentation was active from the Late Paleocene and in particular flyshoid and molassic material filled the basin during the Eocene for a thickness of about 1000m (Tunis & Venturini, 1986). Along the northeastern margin, it is possible to observe the smooth transition that occur from the limestone to the deep-sea sediments, while this results much more rough in the south-western part, probably induced by tectonics (Wasser et al., 2008).

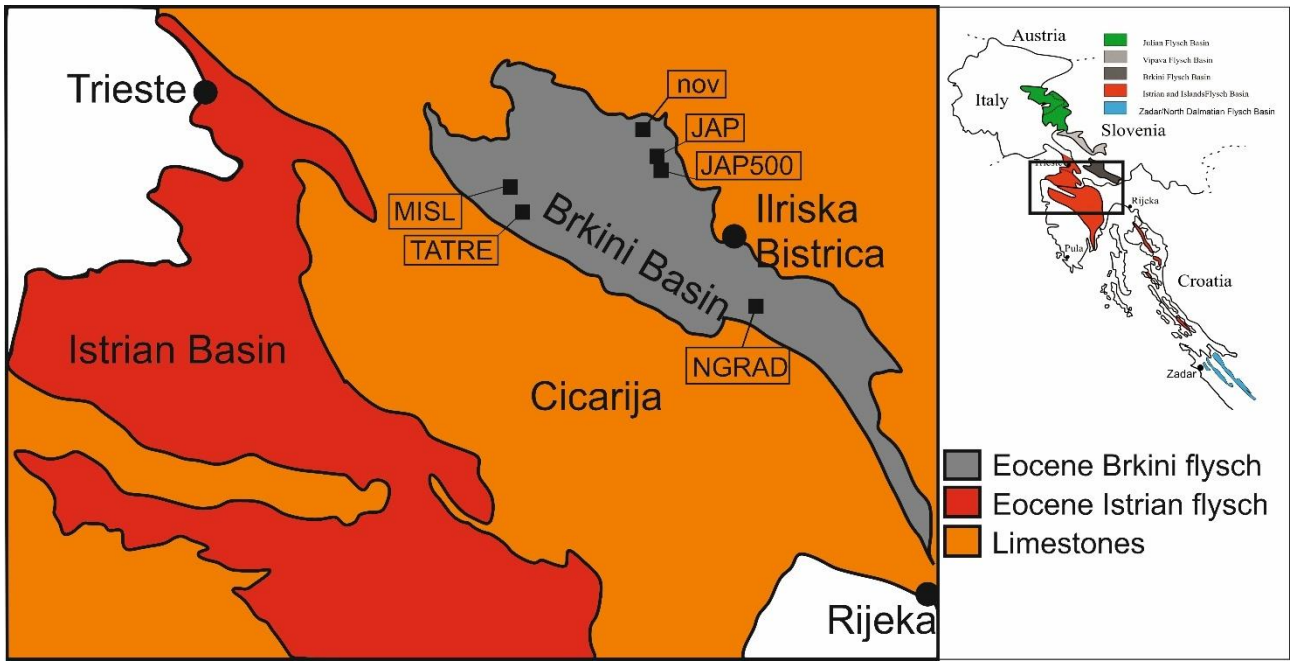

Fig. 10. Semplified geological map of the Brkini Flysch basin area.

In literature, the Brkini succession has never been described as a whole. The basal part has been considered by Orehek (1972), while Tunis & Venturini (1996) focused on its continuation that is composed mainly by siliciclastic turbiditic strata. The stratigraphy of BK has been divided in several segments. The basement strata is composed by an underwater landslide which could be related to a large calciruditic-calcarenite block that crops out south of Ruttars, representing the only re-sedimentation episode of the coeval Cormons flysch (JB; Tunis & Venturini, 1996). The stratigraphy continues with terrigenous turbiditic deposits (with the presence of large calcareous blocks)

embedded with calcarenite strata that show a fining upwards granulometry, becoming marls with strata thickness of over 10 m. The third segment is composed by an alternating of fine sandstones and marls. Then, follows a marl-arenaceous flysch rich in bioturbation with the insertion of frequent hybrid turbiditic strata and bio-calcarenites (Tunis & Venturini, 1996, and references therein). The fifth segment (Jap-Brdo) is composed by conglomerates related mainly to distal terrigenous turbidites and hybrid turbiditic strata. A series of distal terrigenous turbidites lie above rarely interrupted by thin calcarenite strata (6^{th} segment). Petrological studies indicate the Middle Eocene as the time of formation for this segment. The upper portions of the basin (7^{th} segment) shows a thickening of the arenaceous fraction with the presence of the first thick conglomeratic sandstone strata. The basin ends with grey-yellowish siltitic strata and siltous-marls, which are overlain by thin poorly cemented sandstones with a thickness of ~100 m.

The studies of Orehek (1972; 1991) indicates signals of paleocurrents with main north-west and partially west flow direction, suggesting the basement rocks buried in the Adriatic and Gorski Kotar areas as possible sediment sources. On the contrary, Tunis & Venturini (1996) observed several flute casts suggesting opposite directions, similar to those measured in the Cormons area, Dornberk (Slovenia) and Ajdovščina (Slovenia). The two authors are in agreement with possible paleogeographic link among the Brkini Basin and those located in the nearby western area.

Six samples have been selected (JAP, TATRE, MISL, NGRAD, JAP500, and NOV) from BK and classified as lithic geaywackes. Generally, quartz and calcite are the main components, while plagioclase, clay minerals and dolomite are minor abundant. Makes exception NOV (Nova Vas) that is from the molasse segment and differs from the others for the presence of the dolomite instead of calcite. However, all the samples show rare K-feldspar (microcline) and micas (biotite, muscovite and chlorite) are also present. Furthermore, in thin section, clasts of dolostones, limestones, radiolarites, cherts, diabases sandstones, quartzites, gneisses and low grade scists have been identified (Tunis & Venturini; 1992; Lenaz e al., 2000, 2003). In the Brkini Basin, Orehek (1972) indicates in

the flysch the presence of pyrite (15.5 %), rutile (7.1 %), zircon (4.1 %), tourmaline (3.3 %), garnets (22.3 %) and an abundance of opaque minerals (47.7 %). Later on Lenaz et al. (2001; 2003) found orthopyroxene and showed that the opaque minerals observed by Orehek (1972) were Cr-spinel and ilmenite.

Istrian Basin

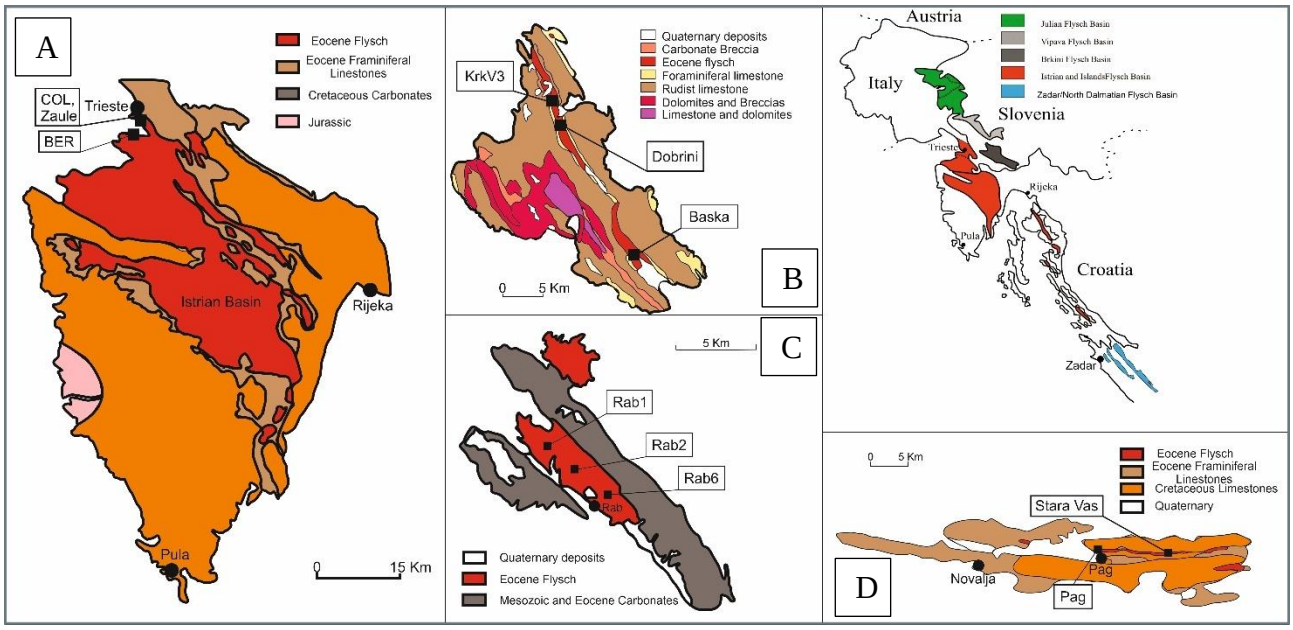

Fig. 11. Simplified geological maps of the Istrian Basin in A) Istria peninsula (modified), B) Krk (Benac et al., 2013, modified), C) Rab (Marjanac T. & Marjanac L., 1991 modified) and D) Pag (Magaš, 2000, modified) islands.

The Istrian Basin (IB hereafter) is formally composed by three different members, the Trieste-Koper, the Pazin and the Kvarner Island Basins (Fig.11). The first is mainly composed by the Trieste Province area, in particular the zone just below the High Karst Plateau, together with the San Dorligo della Valle and Muggia and Koper areas. The Pazin Basin extends all over the north-northeast Istrian Peninsula while the Kvarner Island Basin is represented by Krk, Rab and Pag islands. IB show an elongated form body that suggests that it filled a narrow deep foreland basin. This has been filled from the Middle to Late Eocene as testified by the studies of macrofossils, nummulites and the planktonic foraminiferal biostratigraphy (Babić et al., 2007; Živkovic & Glumac, 2007). The Istrian Flysch basin is composed by the alternation of gravity flow deposits with hemipelagic marls. The low ratio between sandstone and marls thickness suggests that the flysch has been deposited in a distal foredeep. The turbidite thickness seems to be quite homogeneous between the Trieste-Koper and Pazin members. Marinčić et al. (1996) suggest a maximum thickness of about 350 m for the first, while Babić et al. (2007) suggest that the Pazin Member could reach about 450 m. Taking in account

that the second work considers also the basement of Globigerina Limestones, which thickness is valued about 50 m, it is possible to state that the two thickness are similar with a small increase from northwest to southeast direction.

Medium-fine grainsize turbidites dominate the lower section of the stratigraphy, but are often intercalated with several thick megabeds composed by (generally from 0.5 to 5 m but also 10 m) carbonate breccias, conglomerates, bioclastic arenites/siltites and marls (OUGSME Geotrip 2007). Notably, these megabeds have been found also in the Julian Basin (i.e. Tunis & Venturini, 1992) and the Central Dalmatian Basin (Marianač et al., 1991). Towards the top of the stratigraphy the granulometry tends to increase (De Min et al., 2014).

In the Krk Island (Fig. 11B), the Paleogene flysch mainly fill the central depression of the island, and outcrops along the north-eastern and south-western coast as small stretched bodies and in Baška area to the south. The sedimentation of the clastics (marls and sandstones) occurred during the Eocene, filling deep basins (NW–SE elongated) formed during the tectonic movements that resulted in the Dinarides uplift. The clastics of the Rab Island (Fig. 11C) have been dated as Middle-Late Eocene (Magaš, 2000), outcropping along the central body of the island and are better exposed in the Lopar peninsula. The sedimentary rocks can be divided in two units, the upper one consists of marls and sandstones, while foraminiferal limestones compose the lower one (Marjanac & Marjanac 2007). The clastics have been interpreted as flysch deposits and shallow tidal-marine sediments (Marjanac & Marjanac, 2007 and references therein). The siliciclastic mineral composition of the sandstones indicate a provenance from the outside of the Dinaric area, probably in the Alps Region (Marjanac & Marjanac, 2007). The Middle and Upper Eocene flysch of Pag Island (Fig. 11D) is mainly located in the syncline beds of the Pag valley, Vlašići and Povljana fields, and at Smokvica. Generally it is covered by Quaternary sediments, while in Barbat area, it is possible to find separated Mid-Miocene complexes (Magaš, 2000).

Different directions have been suggested for the main paleocurrent suppliers, in particular Magdalenić (1972) stated that the siliciclastic material had a northwestern provenance and so its origin should be searched in the Alps. On the other hand, Marinčić et al. (1996) measuring the direction of the flute casts suggested that the material mainly derived from the near exposed northeastern area, and a minor one with southeast direction that carried material from the Alps. In agreement, Žickovic & Glumac (2007) found particular sedimentary intervals that could testify high sedimentation flux and low oxygenation features that could be the result of the action of secondary paleocurrents that arrived from distant places, connecting the IB with other basins (i.e. Belluno Basin). In the southeastern part of the Istrian Basin, it is also possible to notice rare calciruditic-calciarenites intercalations. Babić & Zupanić (1996) suggest that these carbonatic strata could be originated through gravitational fluxes with north-northeast direction due to the sudden rising of the carbonatic platform located just southward of the basin. These currents could be the announcement of the start of the disaggregation of the Adriatic Carbonatic Platform.

Several authors studied the mineral composition of the Istrian turbidites (e.g. Malaroda, 1947; Wiesender, 1960; Woletz, 1960; Lenaz & Princivalle 1996, 2005; Pavšič & Peckman, 1996; Lenaz et al., 2003; Lenaz, 2008) suggesting that the sandstone is generally composed by quartz, plagioclase (often altered) orthoclase, opale (rose and brown-rose), rare microcline and phyllosilicate (e.g. chlorite, muscovite and biotite).

Regarding the heavy minerals it has been observed ilmenite, zircon, tourmaline, apatite, rutile, Cr-spinel, monazite, anatase and garnets. Furthermore, the presence of rare titanite, staurolite, epidote, zoisite, brookite, cloritoids, glaucophane and other clinopyroxenes is reported. Chemical analyses pointed out that the calcite increases from West to East (Malaroda, 1947), while Marinčič et al. (1996) suggest an increase of the garnet fraction from north-east to south-west, similary to the independent data of Sparica cited in Bonazzi et al. (1996).

Eleven samples have been selected among Trieste, Istrian and Islands units. In particular, two sandstones of Trieste (CONT, ZAULE and BER), three from Krk and Rab (Krkv3, Baska and Stara Vas; Rab1, Rab2 and Rab6; respectively) and two from Pag (Pag and Dobrinj). All these samples can be classified as lithic graywackes-arenites. In some cases the calcareous part is predominant and they can be classified as calcarenites.

North Dalmatian flysch basin

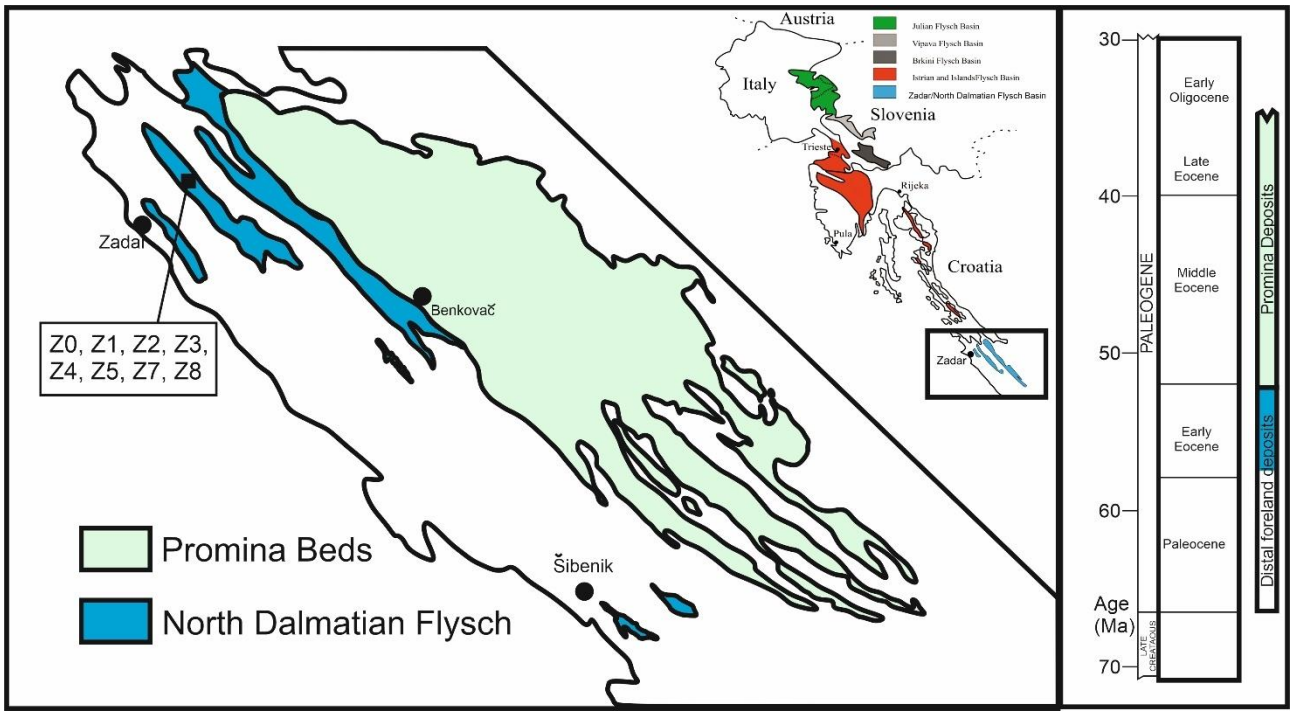

Fig. 12. Sketch map representing the North Dalmatian Flysch Basin and the Promina Beds as suggested by Vlahović et al. (2012, modified).

During the Middle Eocene, the Dalmatian Flysch filled the foredeep zone of the foreland basin that occurred during the compressional tectonic deformation of the Dinaric orogenic phase together with the collapse and drowning of the Adriatic Carbonate Platform. The turbidite succession is about 900 m thick, showing slump features and in the upper part, occasional paleochannels. The directions of the turbidite paleocurrent seem to be mainly towards southeast without radial pattern dispersal, suggesting that the basin floor was inclined southwestward. The flysch is overlain by the Promina Beds that is a Late-Middle Eocene shallow-marine ramp deposit (Vlahovic et al., 2012; Fig. 12). These two formations took part in a complex scenario composed by a deep water distal foreland in which the turbidites accumulated, and a shallower water proximal foreland was filled by the Promina Beds. The formation of blind thrust folds resulted in a proximal foreland with strong lateral and vertical differences in thickness and facies, which reflects a compartmentation-like behavior. Later, the basin has been divided in two smaller and semi-isolated basins by the advance of a large fan delta

(the Gradina Unit) that are referred as Korlat and Ostrovica sub-basins. As the orogenic thrusting continue, the orogeny crustal loading increased the bulk subsidence with the result of the drowning of the delta-fan system and the merging of the two sub-basins. The braidplane formed contained several smaller fan-deltas characterizing local units. Since when the system were uplifted during the Oligocene, the delta system prograded into a terminal lake zone. The deposits were then eroded and spread.

The Dalmatian Flysch has been divided mainly in four units by Babić and Zupanič (2008) that correspond to four lithozone and together with the Promina Beds show at least two transgressive system tracts, two regressive system tracts and one lowstand system tract with two maximum regression surfaces, two maximum flooding surfaces, one major and three minor surfaces of forced regression and ten flooding surfaces.

The four units are:

1) The massive sandstone and mudstone unit is about 220 m thick and correspond to the base of the turbidite formation. The sandstones are massive with common mud clasts and plant debris and rare mollusks and nummulites. Their beds are commonly several meter thick and are intercalated by mudstone intervals. The mudstone isrich in planktonic foraminifera and are rarely intercalated with thin sandstones.
2) The laminated sandstones unit is about 200 m thick. The sandstones laminae show a thickness between several centimeters to 1 meter and are characterized by laminated ripples. They are rich in plant remains and are often muddy. Slumps and slides are commonly present, while slide scars are present only in the upper part. There are intervals decimeters thick where the alternation of sandy mudstones and muddy sandstones predominate.
3) Sheeted Sandstones and Channel-Fills are about 450 m thick and contain three facies. The first is the sandbodies that show a thickness that may reach 30 m and are up to 1km wide in section transverse or diagonal to the main paleotransport currents, showing both sheet-like or lensoid

bodies. They may be flat or graded laminated and can contain nummulites stripes, pebble interbeds and mud clasts. Bioturbation and plant remnants presence are common. The channel fills are the second facies, and are 2-13 m thick and up to 50 m wide with a northeast-southwest elongation. They generally appear as flat laminated sandstones with south-southwest directed flutes and occasionally display a rippled top, similar sandstones with bioclastic basal portion, and scour-filling conglomerates. The third unit is composed by thin bedded sandstones and mudstones dominated sequences.

4) The mudstones correspond to the top of the succession and show about 50 m of thickness, sandstones intercalations are very rare. They may contain mollusks and smaller benthic and planktonic foraminifera. This unit represents an offshore deposition that is the result of a relevant transgressive event due to the sea level rise.

The ZB samples were collected from an outcrop that emerges on the side of D8 state road near the crossing with 6011 street (N 44° 8’ 58.7’’; E 15° 19’ 46.9’’). The outcrop consists of a stratified tilted wall ~50 m long composed mainly by yellow-brownish sandstones with few intercalations of thin marls strata and belonging to the first unit. Seven samples (Z0, Z1, Z2, Z3, Z4, Z5 and Z8) have been collected along the entire column where Z0 and Z8 are the bottom and the top of the outcrop, respectively. The seven samples show similar mineralogy and similar fine granulometry and have been classified as lithic greywackes. The main minerals are quartz and calcite with the presence of dolomite, micas (muscovite and chlorite), K-feldpars (microcline and orthoclase) and clay minerals. The lithic fragments are quite abundant and have been identified as clasts of cherts and limestones. Makes exception Z4 showing a coarser granulometry and the presence of abundant bioclasts.

In this work, the first detailed heavy mineral separation has been performed for the North Dalmatian Flysch Basin. It has been recognize Cr-spinel, garnet, zircon, pyrite, rutile, ilmenite and tourmaline.

Heavy minerals in the studied basins

Heavy minerals of the here studied sedimentary basins have been detailed during the last decades for better understanding the provenance of the siliciclastic fraction of the turbiditic material. In particular, Lenaz et al. (2000, 2003 and 2005) studied the crystallography and chemistry of Cr-spinels and their fluid inclusions in spinels of the JB, BK and IB. Also the clinopyroxene of the Istrian Basin (Lenaz, 2008) and high-pressure amphiboles and clinopyroxenes of the Julian Basin have been investigated (Lenaz & Princivalle, 2002). Regarding the North Dalmatian Basin, the first informations about the heavy minerals compare in this work.

In the Julian Basin, Cr-spinel resulted the most abundant phase among the heavy minerals, displaying according to Kamenetsky et al. (2001) classification, peridotitic and volcanic affinities. Lenaz et al. (2000) showed that in this basin there are peridotitic spinels with both harzburgitic and lherzolitic affinity that were, accordingly, assigned to Internal and External Dinarides, respectively. Lherzolitic spinels have been found only in most recent layers (post 56Ma). The chemistry of the volcanic spinels indicates provenance from MORB or MORB-type backarc rocks, subduction related backarc or continental rifting, plume-related intraplate basalts and island-arc tholeiites or boninites. In this basin, amphibole and pyroxene have been recognize only in the Early Eocene part of the stratigraphy. In particular, Mg-hornblende and actinolite, barroisite, glaucophane and omphacite occur suggesting that the source could be represented by metabasites in eclogite-bluschist facies, experienced retrometamorphic and greenschist facies overprint events. These metamorphic rocks could be the result of uplift and exhumation of the ancient subducted slab occurred 56 Ma in the Dinarides (Lenaz & Princivalle, 2002).

The detrital Cr-spinel found in the quartzolithic sandstones in BK and IB show a predominant peridotitic population (about 85%). In particular, the crystals mainly show transitional Type II and

Type III peridotitic affinities, while all the volcanic ones show backarc-related characteristics. Similarly for the Julian basin, the origin of these types of spinels have been identified in the Internal Dinarides. The remnant peridotitic crystals are better represented in the IB than the BK and show Type I (lherzolitic) features, which are similar to those found in the External Dinarides (Lenaz et al., 2003). Only in the IB detrital pyroxenes with augitic and pigeonitic composition occur. These have been related to within-plate tholeiites/calcalkaline basalts crystallized at a pressure between 0 and 5 Kbar and the sources suggested are the basaltic andesites of Ljubač or the tholeiites that outcrops in the Požeška Mountains. However, in the dinaric area, the presence of pigeonite is also reported in the Banija Ophiolite complex, related to the presence of high Mg andesites and boninites arc (internal Dinarides; Bernardini et al., 2009), and the Triassic Mid-Adriatic Volcanic Islands (Balogh et al., 1994; Palinkaš et al., 2010) .

Finally, Cr-spinels, pyroxenes and amphibole suggest that the main supply area of the siliciclastic fraction of the Maastrichtian-Eocenic turbidites should reside in the Internal Dinarides. The authors identified the suprasubduction zone of the ancient Vardar Ocean as the main source rocks for the detrital Cr-spinel. These supplied detritus acted since the beginning of the sedimentation in the Julian and Brkini Basins. During the Early Eocene, a second input of similar material filled both JB, BK and IB, while only by the Middle Eocene the lherzolite-like spinels have been transported from the External Dinarides into the Brkini and Istrian Basin. Furthermore, the presence of the clinopyroxene only in the IB suggest that the basins probably have different supply areas depending on the time of deposition and the location of the trough.

The heavy minerals data appear in agreement with the reconstruction of the paleocurrents suggested by Tunis & Venturini (1992), Vlahovic et al (2012) and Marinčić et al. (1996) among all.

Methods

Rocks were firstly crushed in a mortar, then zircon, rutile and garnet were concentrated by standard sieving, magnetic separation, heavy liquids (1,1,2,2 Tetrabromoethane; 2.97 g/mL) and finally handpicked using an optical microscope. The selected crystals were then mounted in epoxy resin and polished.

The garnets have been analyzed by using a Cameca Camebax hosted in the CNR Institute for Geosciences and Georesources at the Department of Geosciences (University of Padua) in standard operating conditions (accelerating voltage: 15 kV; current: 10 nA; acquisition time for each element: 10 s; acquisition time on background: 5 s). Natural and synthetic standards were used for the calibration, and the PAP correction procedure was followed. Analytical measurements are affected by a relative uncertainty of 1% for the major elements (>5 wt %) and 3% for the minor elements (<5 wt %).

Trace element concentrations of the garnets were determined by LA-ICP-MS on all the same grains, using a Thermo-Finnigan ELEMENT XR, a high resolution double focusing magnetic sector inductively coupled plasma mass spectrometer (HR-ICP-MS) coupled to a GEOLAS 193 nm Excimer laser ablation system, at Memorial University of Newfoundland (MUN, St. John's, Newfoundland, Canada). A laser spot size of 40 μm was used with energy density of approximately 4 J/cm^2 with a laser repetition rate of 10 Hz. Time-resolved intensity data were acquired by peak-jumping in a combination of pulse-counting and analogue modes, depending on signal strength, with one point measured per peak.

The SiO_2 concentrations determined by the EMPA analyses for garnet were used as internal standard to normalise counts to concentrations for the trace element analyses. For calibration, NIST 612 glass (Pearce et al., 1997) and BCR-2G glass (Morishita et al., 2005) were used. The LA-ICP-MS data were reduced using the MUN's in-house developed CONVERT and LAMTRACE spreadsheet programs according to van Achterbergh et al. (2001) allowing selection of representative signal

intervals, background subtraction, and internal standard correction for ablation yield differences, instrument sensitivity drift during the analytical session, and perform calculations converting count rates into concentrations by reference to the standards.

The Renishaw InVia Raman Spectometer (objective 50x with 0.75 NA, 1,200 lines/mm grating, 576 pixel CCD detector) hosted by the Department of Engineering and Architecture of the University of Trieste has been utilized to recognize the rutiles among the TiO_2 polymorphs. The excitation was a near-infrared diode laser at 785-nm excitation, delivering 16 mW at the sample surface, focused on a spot of approximately 10 μm2. After the deconvolution of the Raman spectra and their parameter, the Grams AI (Thermo Galactics) program has been used to fit the spectra with a set of pseudo-voigt peak functions.

In situ chemical analyses performed on zircons and rutiles and U-Pb analyses have been performed with a LA-ICPMS (Laser Ablation Ion Coupled Plasma Mass Spectometer) hosted by the Department of Physics and Geology of the University of Perugia. The laser ablation device is a Teledyne/Photon Machine G2 (ATL-I-LS-R solid state-triggered excimer 193 nm laser) equipped with a two-volume ANU (Australian National University) HelEx 2 cell. The spectrometer is a quadrupole-based Thermo Scientific iCAP Qc ICP-MS. The analytical setup and relative figures of merit (precision, accuracy, and detection limits) are described in Petrelli et al. (2016a, 2016b). The spot size for all the analyses has been set at 12 μm and Helium has been used as carrier. The rutile trace elements (^{24}Mg, ^{27}Al, ^{29}Si, ^{42}Ca, ^{51}V,^{53}Cr, ^{55}Mn, ^{57}Fe, ^{85}Rb, ^{89}Y, ^{90}Zr, ^{93}Nb, ^{123}Cs, ^{137}Ba, ^{139}La, ^{140}Ce, ^{141}Pr, ^{146}Nd, ^{147}Sm, ^{153}Eu, ^{157}Gd, ^{159}Tb, ^{163}Dy, ^{165}Ho, ^{166}Er, $^{16}{}_{9}$Tm, ^{173}Yb, ^{175}Lu, ^{178}Hf, ^{181}Ta, ^{182}W, ^{208}Pb, ^{232}Th and ^{238}U) and zircon trace elements (^{31}P, ^{42}Ca, ^{47}Ti, ^{55}Mn, ^{57}Fe, ^{71}Ga, ^{85}Rb, ^{89}Y, ^{90}Zr, ^{93}Nb, ^{118}Sn, ^{137}Ba, ^{139}La, ^{140}Ce, ^{141}Pr, ^{146}Nd, ^{147}Sm, ^{153}Eu, ^{157}Gd, ^{159}Tb, ^{163}Dy, ^{165}Ho, ^{166}Er, ^{169}Tm, ^{173}Yb, ^{175}Lu, ^{178}Hf, ^{181}Ta, ^{208}Pb, ^{232}Th and ^{238}U) have been analyzed using the USGS standard reference QC-BCR2G (USGS, 2009) and following the method suggested by Longerich et al. (1996). In situ U-Pb zircon analyses have been calibrated using the standards STD 91500 and Ples-20. Raw data were corrected for common Pb using the data reduction software ICPMSDataCal (Lin et al., 2016) and then processed

using the ISOPLOT 3.0 software (Ludwig, 2003) to calculate isotopic ratios and ages of $^{207}Pb/^{206}Pb$, $^{206}Pb/^{238}U$, $^{207}Pb/^{235}U$ and $^{206}Pb/^{238}U$, respectively.

Results

Garnets

Major elements

About 250 garnets of JB, BK and IB have been selected and analyzed (Tables 1a, 1b, 2a, 2b, 3a, 3b). All the crystals have been classified using the triangular diagram (Alm+Sp-Gr-Py) suggested by Morton et al. (2004). The crystals with low pyrope content and Alm+Sp from 0 to 45 mol% are well represented in all the basins, falling in the type B field (Fig. 13). Type B field is further discriminated in two subdivisions according the Ca fraction content (Fig. 13), type Bi (X_{ca}<10%) garnets are considered amphibolite facies metasediments derived, while type Bii (X_{ca}>10%) represent granitoids-metasediments derivation (Mange & Morton, 2007). JB and IB show a slight majority of Bii garnets with respect to Bi, while the BK garnets displays a strong Bi type preference. Garnets with higher pyrope content fall in the C type field (Fig. 13), which similarly to B type is divided in two sub areas. Ci suggest a high grade mafic metamorphic protolith and is represented by garnets with X_{Mg}<40%, while Cii is represented by the population with X_{Mg}>40%, suggesting a high grade ultramafic metamorphic derivation (Mange & Morton, 2007).

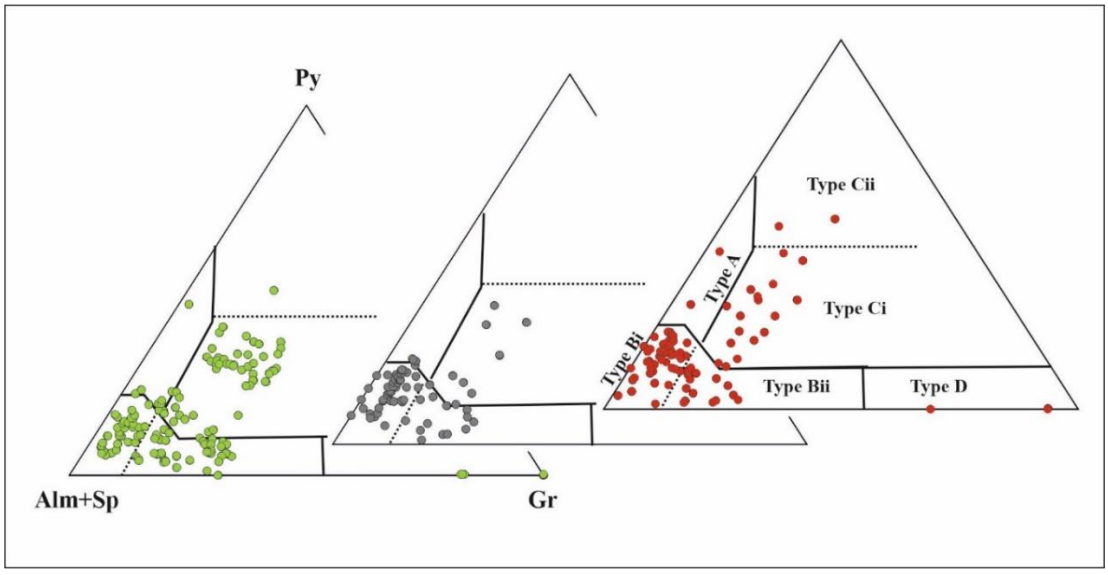

Figure 13. Alm+Sp – Py – Gr diagram of the garnets from, left to right, Julian (green), Brkini (grey), Istrian (red) basins. Alm: almandine; Sp: spessartine; Py: pyrope; Gr: grossulare. A- , Bi-, Bii-, Ci-, Cii-, D- fields according to Morton et al. (2004).

All the basins are represented in Ci area that generally show a number of crystals higher than Cii, where BK garnets lack (Fig. 13). Very few crystals of JB and IB show high Py and low grossularia content, falling in the A type area or very high grossular-andradite contents falling in the D-type field (Mange & Morton, 2007). The first is characterized by crystals derived from high grade granulite-facies metasediments, charnokites or intermediate-acidic igneous rocks, while the second represent crystals derived from metasomatic rocks, very low grade metabasic rocks, or from ultrahigh temperature metamorphosed calc-silicate granulites (Mange & Morton, 2007).

Trace elements

Titanium is the most abundant trace element with values between 12.5 and 9800 ppm. Yttrium (3.52-4570 ppm), Cr (0.21-828 ppm), V (0.86-745 ppm), P (2-1205) and Sc (1.48-232 997 ppm) are elements where it is possible to reach hundreds of ppm. Zinc (0.42-165.9 ppm), 233 Co (0.93-94.3 ppm), Ge (1.3-78.4 ppm) and Ga (2.36-112 ppm) are the less abundant (Tables 1a, 1b, 2a, 2b, 3a, 3b).

REE

There few A-type garnets in the studies population are characterized by a strong ΣREE content difference, ranging from 8 to 542 ppm (Tables 4, 5, 6). The chondrite normalized patterns show that the Eu anomaly is present only in four patterns, while in others is missing (Fig. 14). The Eu/Eu* ratio ranges from 0.0.2 to 3.7, while the $(Gd/Lu)_N$ is comprised between 0.15 and 6.8.

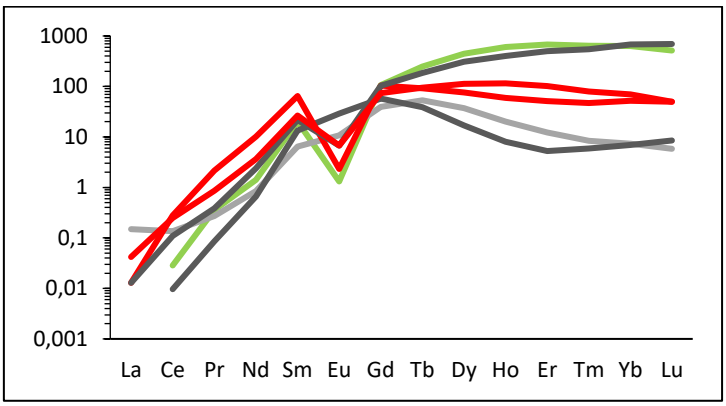

Fig. 14. Selected REE patterns of the A-type detrital garnets. Colours as in Fig. 13

In order to avoid a large number of overlapping lines in standard spidergrams, we prefer to plot the data in the diagram $(Gd/Lu)_N$ vs. Eu/Eu*, where it is possible to locate each single garnet and where differences from garnets belonging to the same type are evidenced (Fig. 15).

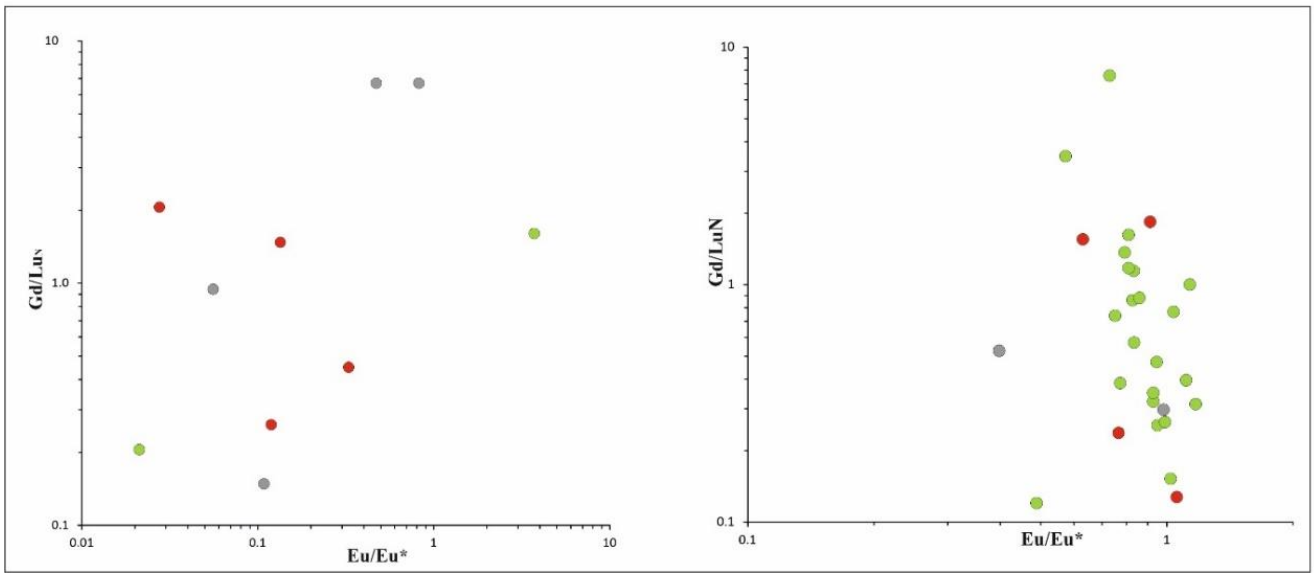

Figure 15. Gd/Lu_N vs. Eu/Eu* in A-type garnets on the left and in C-type garnets on the right. Colours as in Fig. 13.

In Ci-type garnets the ΣREE content ranges from 10 to 121 ppm, the Eu/Eu* from 0.4 to in 241 the diagram $(Gd/Lu)_N$ vs. Eu/Eu*, where it is possible to locate each single garnet and reveal differences from garnets belonging to the same type (Fig. 15).

In Bi-type garnets the ΣREE content ranges from 14 to 1858 ppm, the Eu/Eu* ratio from 0.004 and 1.7, while the $(Gd/Lu)_N$ ratio lies between 0.001 and 70.5 (Fig. 16A, 16C, 16E). Diagram $(Gd/Lu)_N$ vs. Eu/Eu* shows that garnets from different basins behave in a different way. In addition, garnets from sample BK41 overlap the field of JB garnets, as well as those from Kvarner Islands (KVI). Other garnets from BK and those from IB fall in a separate field. Moreover, garnets from the Rab and Krk flysches (KVI) plot in two different regions of the diagram, those from Rab usually showing higher Eu/Eu* ratios. In Bii-type garnets the ΣREE content ranges from 5 to 864 ppm, the Eu/Eu* ratio from 0.1 and 3.3, and the $(Gd/Lu)_N$ ratio between 0.0009 and 176.7. In a $(Gd/Lu)_N$ vs. Eu/Eu* diagram garnets mostly overlap (Fig. 16B, D, F). It is, however, possible to recognise different fields for BK41 and BK30 garnets, while those from the Krk and Rab flysches mostly differ from those of IB.

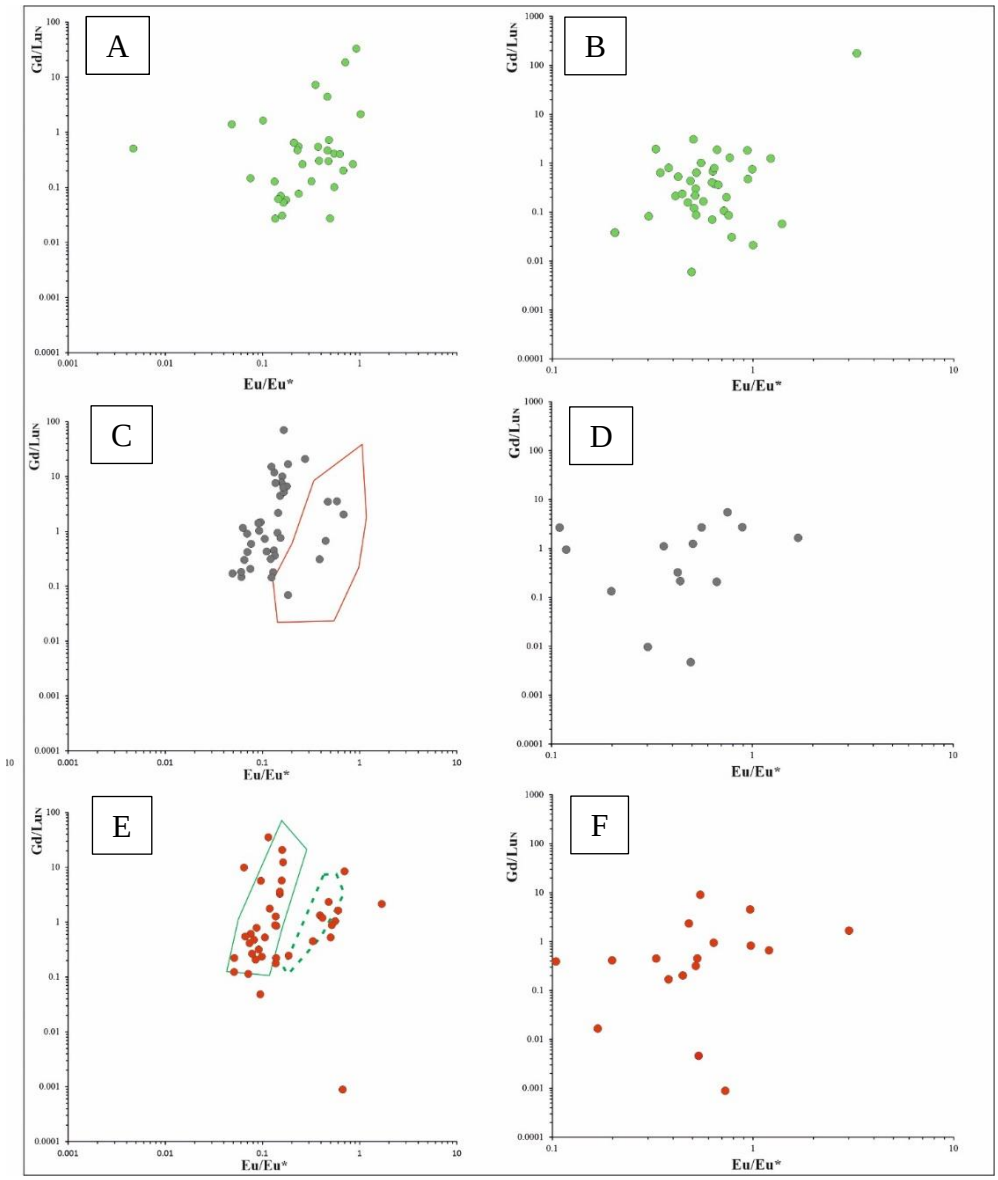

Figure 16. Gd/Lu_N vs. Eu/Eu* in Bi-type (left row, A-C-E) and in Bii-type garnets (right column, B-D-F). Colours as in Fig. 13.

Rutile

A total of 133 rutiles have been found and subsequently analyzed for trace element composition from JB, BK and IB. More precisely, we selected 86 crystals from the JB (Table 7), 5 crystals from Nova Vas (BK; Table 8), and 42 from the IB (including the Kvarner Islands; Table 9). Generally, the rutiles are 63 to 150 µm long and appears dark brown-brown rounded crystals. Only few rutile crystals from BK have been analysed, because, even if rutile is present in all the samples, all these crystals were lost during polishing. No ZB rutiles have been analysed due to sample preparation problems.

The Cr vs Nb diagram (Fig. 17B) shows that 55% and 89% of the crystals of the JB and IB respectively are metapelitic in origin (Meinhold et al., 2010), as well as all the rutile of the BK. The content of Cr in the three basins range between 7 and 3030 ppm (JB), 13 and 2779 ppm (IB) and 13-410 (BK), while the Nb span between 117 and 5650 (JB), 199 and 9180 (IB) and 1279 and 2970 (BK). In JB the magnesium and Al content vary between 81-4000 ppm and 14-24100 ppm, respectively, so that, by using the diagram suggested by Smythe et al. (2008) 77 % of the rutiles have a crustal derivation (Fig. 17A). In the same diagram, 93% and all the rutiles of IB and BK show crustal affinities, with Al ranging between 97-570 and 24-1530 ppm and Mg 15-15100 and 17-84 ppm respectively.

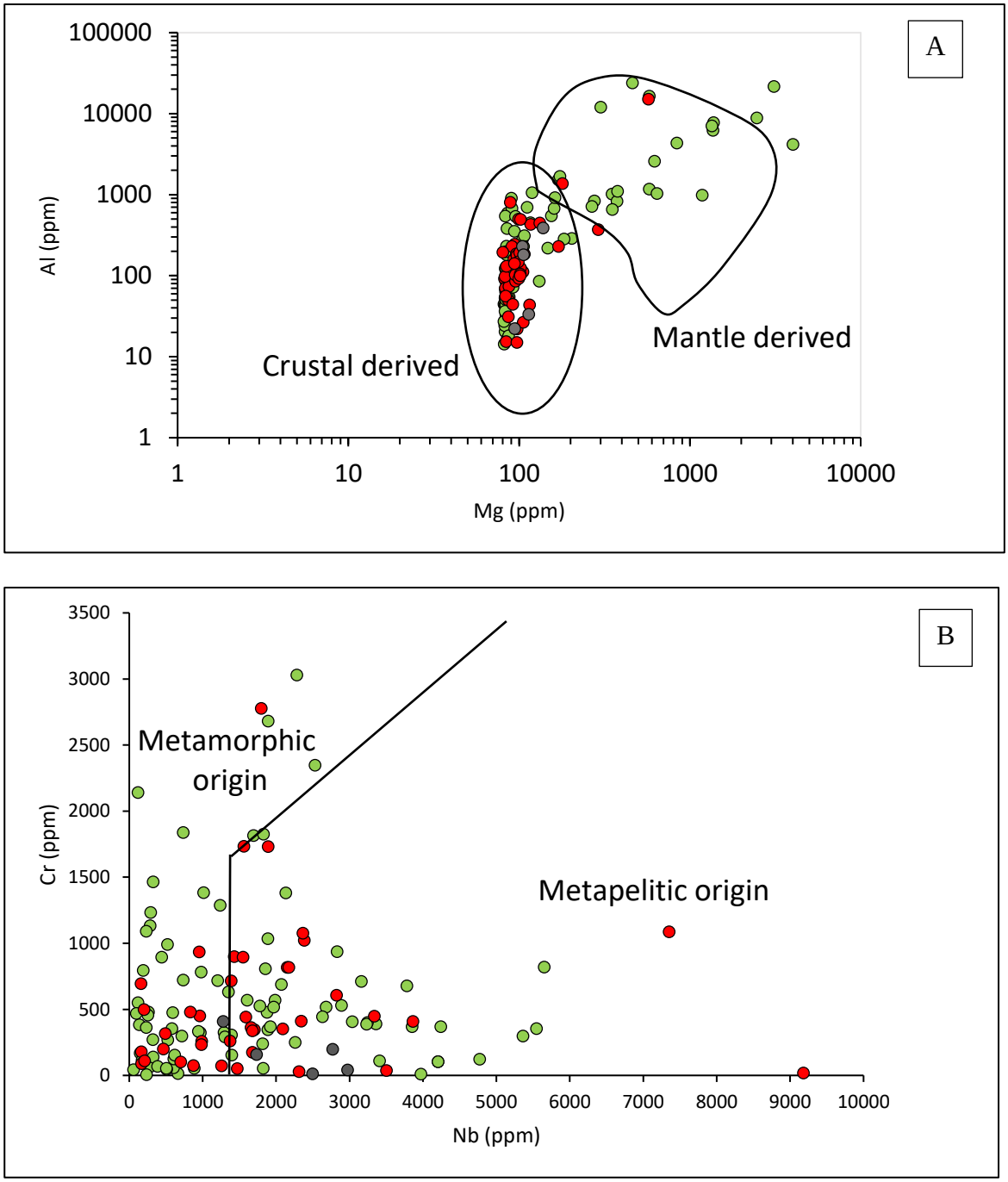

Fig. 17. Al vs Mg (A) and Cr vs Nb (B) diagrams suggested by Smythe et al. (2008) and Meinhold et al., (2010) respectively. Colours as in Fig.13.

According to Zack et al. (2004) and Watson et al. (2006) the Zr in rutiles geothermometers suggested temperatures of crystallization varying between -22-1064°C and 331-932 °C, respectively (Table 7, 8, 9). Considering the three basins, JB (Zr = 2.34-4474 ppm), IB (Zr = 8-887 ppm) and BK (Zr = 6-482 ppm) show temperatures between -22-1064, 253-922°C, 212-780°C (Zack et al., 2004) and 332-930°C, 498-793°C and 404-683°C (Watson et al., 2006).

Generally, the two methods show good agreement for intermediate temperatures (Fig. 18), while major differences appear in the extremes. The Watson et al. (2006) geothermometer shows more conservative results, while the formula suggested by Zack et al. (2004) shows more spreads. Furthermore, the latter shows a crystallization temperature of -22 °C (JBxxx), which is clearly uncorrect, suggesting that the geothermometer of Watson et al. (2006) is the more reliable for the rutile with low Zr. For these reasons the geothermometer suggested by Zack et al. (2004) will be not taken in account.

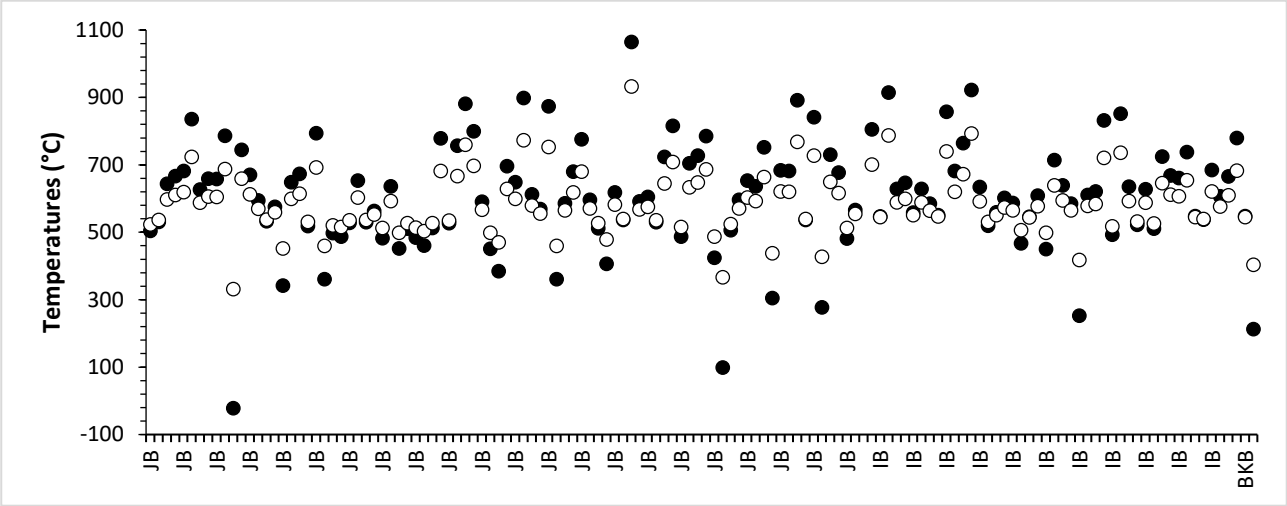

Figure 18. Comparison between the Zr-in-rutile geotermomethers suggested by Watson et al. (2006; white circles) and Zack et al. (2004; black circles).

Most of the crystals of JB, BK and IB show temperature in line with metamorphic condition of the amphibolite facies (80%, 80% and 93%, respectively), while the 14%, 10% and 5% of the rutiles seem to have crystallized in the upper greenschist facies, the lasts (6%, 10% and 2%) show crystallization temperatures above 750°C suggesting a granulite facies affinity (Table 7, 8, 9).

The temperature distribution spectra built for JB, IB and BKB show that the highest peaks are comprised between 500 and 650°C, suggesting that most of the rutiles crystallized in amphibolite-eclogite facies temperature. In particular, JB show peaks at 530, 572 and 610 °C, IB at 543 and 588°C, and BKB only one peak at 574, probably due to its small number of analyses. Furthermore, important lower temperature peaks are shown at 450 by JB, 419 by IB and 406 by BKB, while at

higher temperature these have values of 687-766, 735 and 680 for JB, IB and BKB, respectively. Finally, in the here studied basin it is possible to discriminate mainly three populations, the most important one that span from 500 to 650 °C, a second with higher temperatures (650-800 °C), and the minor one with an average value at about 400 °C. Only JB shows highest temperature with a peak at 938 °C.

Nb and Ta are often used to obtain constraints about the rock sources and their geodynamical implication, in particular their ratio (Nb/Ta; e.g. Cave et al., 2015; Meyer et al., 2011; John et al., 2011). The IB rutiles show the Nb highest spread (78-9180 ppm; Table 7) followed by the JB ones (56-5650 ppm; Table 8) and finally the BK crystals (1279-2970 ppm; Table 9). The Ta content span between 6 and 849 ppm, 4 and 2427 ppm and 34 and 560 ppm for IB, JB (showing the highest spread) and BK, respectively (tables 7, 8, 9). Due to their strong affinity with Ti, Nb and Ta (both Ti vicarious) are particularly abundant in the rutile, in its polymorphs and, more in general, in all the other Ti-rich phases like Sphene or Ilmenite. This occur in crystals like in blasts. However, Ti bearing magmatic silicates like HTi clinopyroxenes, hornblende and biotite-phlogopite series show a general depletion in Ti-Nb-Ta during metamorphic or subsolidus recrystallization (eg. Rosset et al., 2007). Probably this also encourage the formation of rutile, very common in all the metamorphic rock types. Therefore for the minerals rich in Ti like rutile, the fractionation of Nb and Ta could be roughly expressed by the ratio between the two distributions coefficient ($D_{Nb\ mineral\text{-}melt}$ and $D_{Ta\ mineral\text{-}melt}$) and results as $D_{Nb}/D_{Ta} \leq 1$ (Klemme et al., 2005). For these reasons, the Nb/Ta ratio of rutiles can be interpreted as the ratio of the bulk rock, and equal or slightly lower than that of the protolith and coexisting partial melts with low Nb content and high Nb/Ta (Stepanov and Hermann, 2013; Luvizotto et al., 2009; Sengun & Zack, 2016). Continental crust and depleted mantle show sub-chondritic values (8-14 and 11-16 respectively), while mantle xenoliths eclogites and migmatites obtained by intracrustal differentiation of TTG show supra-chondrites ones (19-37; 22-42 respectively) (Hoffman et al., 2011; Rudnick et al., 2000; Stepanov & Hermann, 2013).

The studied rutiles show high variable Nb/Ta ratio (Fig. 19), spanning between 2 and 80. In particular, the JB and IB values show spread behaviors with ratio between 2 and 38 and 5 and 8 respectively, while the BK crystals show values between 5 and 46, plotting in two zones. One falls in the subchondritic section with a mean value of 5.5 and the second in the suprachondritic field (mean 38). This ratio does not show a linear correlation with Nb or Ta concentration, nor the calculated temperature. In fact, the largest difference is due to crystals from Istrian basin with similar crystallization temperature (540 vs 545 °C).

Hafnium is also often considered since its high partitioning coefficient (similar to those of zirconium; $HfD_{Ru/L}$= 3.9-14.8 and $ZrD_{Ru/L}$=2.7-13.1 Xiong et al., 2005 and references therein) between melt and rutile and generally show a positive correlation with its vicarious Zr (e.g. Brenan et al., 1994; Meyer et al., 2011; Kalfoun et al., 2002; John et al., 2011). However, the two elements are not characteristic of the protolite, since they show quite high partitioning coefficients also with the clinopyroxenes (Brenan et al., 1994). All the basins trendlines show a good R^2 (JB = 0.94, BK = 0.98 and IB = 0.90; Fig. xxx), with BK and IB line equation displaying similar slopes, while JB one differs by 0.02. The inset of the Zr vs Hf diagram (Fig. 20) shows three trendlines with Zr/Hf ratio of 10, 20 and 40. Julian, Brkini and Istrian basins show that most of their crystal fall along the 20 ratio line, a small amount of JB and IB on the 10 one and only few JB and BKB crystals along the line with the higher ratio (40). The Zr/Hf show quite broad values in all the basins, JB = 4-54 (Hf = 0.051-48 ppm), BKK = 15-31 (Hf = 0.39-15.7 ppm) and IB = 8-48 (Hf = 0.68-66 ppm). Most of the rutile of all the basins falls in the subchondritic area (JB = 93%, BKB = 100 and IB = 5%), while only JB and IB show suprachonditic values, 7% and 5%, respectively (Fig. 19).

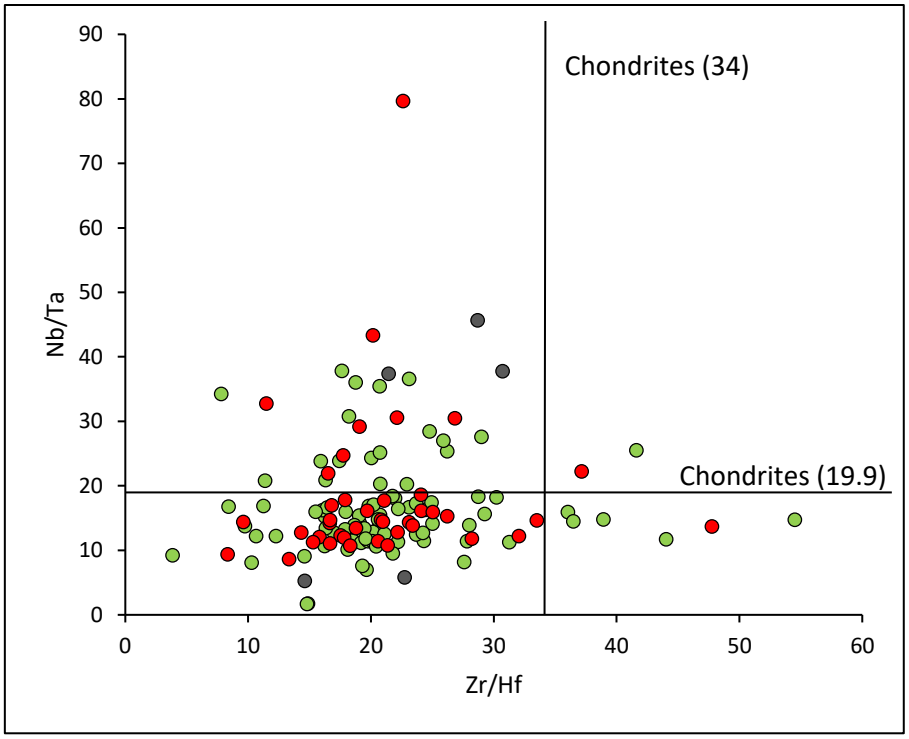

Figure 19. Nb/Ta vs Zr/Hf diagram, the chondritic values have been calculated taking in account the data of Boynton et al. (1984). Colours as in Fig. 13.

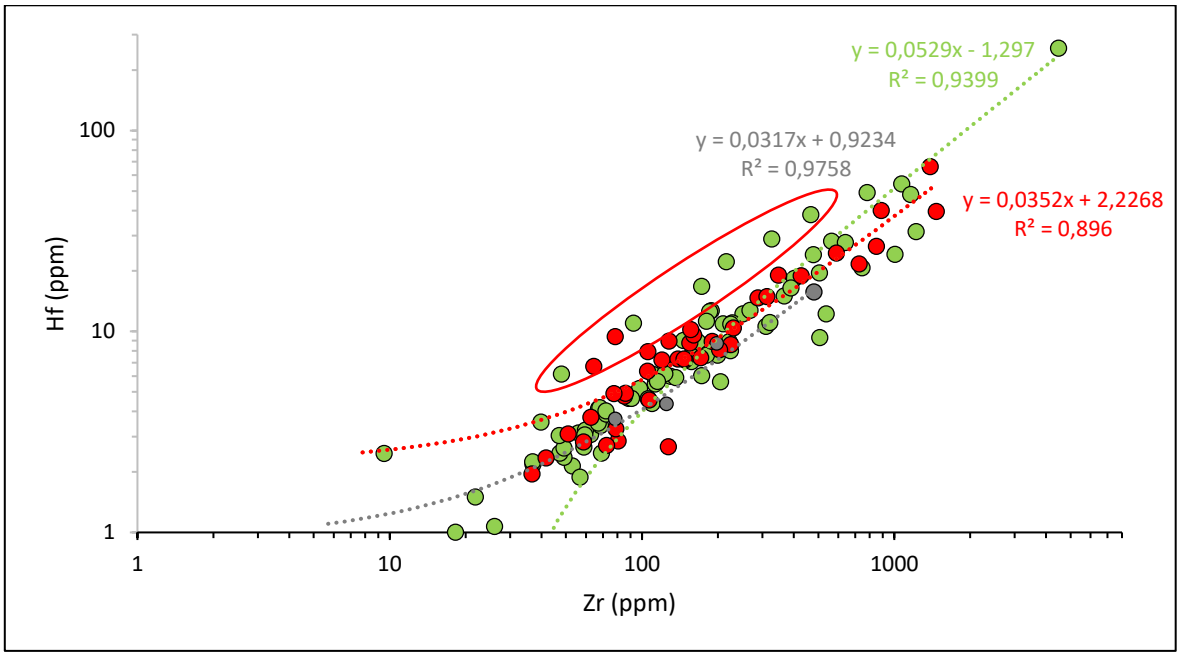

Fig. 20. Hf vs Zr diagram for rutile with JB (green dotted line), BK (grey dodded line) and IB (red dotted line) trendlines. Colours as Fig.19.

Other abundant trace elements are Fe (322-10900 ppm), V (72-5440 ppm) and W (0.22-444 ppm)

Zircon

The 254 selected detrital zircons are generally fragments of crystals, most of them euhedral to sub-euhedral, pale rose in color, and show a size between 63 and 150 μm. Among them, 93 are from the JB, 43 from the IB, 86 from the BK and 32 from the ZB. Cathodoluminescence (CDL) analyses generally show crystals with a well-defined core with isomorphic overgrowths, typical of magmatic crystals. Some of them only an overgrowth. Rarecrystals present no isomorphic overgrowth. Where possible, according to their size, both cores and rims analyses have been chemically and isotopically analyzed in zircons from BK and IB for a total of 11 points, which will be discussed in separated chapter.

The Th/U ratio is commonly used to discriminate magmatic from metamorphic zircon (Fig. 21), generally it is accepted that Th/U=0.1 is the upper limit for the metamorphic zircons and the lower one for the magmatic ones (e.g. Hoskin & Shaltegger, 2003; Hoskin, 2005; Kirkland et al., 2015; McKay et al., 2018). In recent years, it has been demonstrated that metamorphic crystals from high and ultrahigh temperature could show a Th/U ratio above 0.1 (Rubatto et al., 2017, and references therein), and that monazite presence could increase this ratio of several times (Yakymchuk et al., 2018). Eight (9%), 3 (3%), 1 (1%) and 2 (6%) zircons of JB, BKB, IB and ZB respectively, show a Th/U ratio below 0.1 suggesting their metamorphic affinity, while the others having a Th/U ratio above 0.1 seem to be crystallized in a magmatic environment (Th/U_{JB} = 0.1-1.4; Th/U_{BKB} = 0.1-2.0; Th/U_{IB} = 0.1-0.8; Th/U_{ZB} = 0.2-0.9).

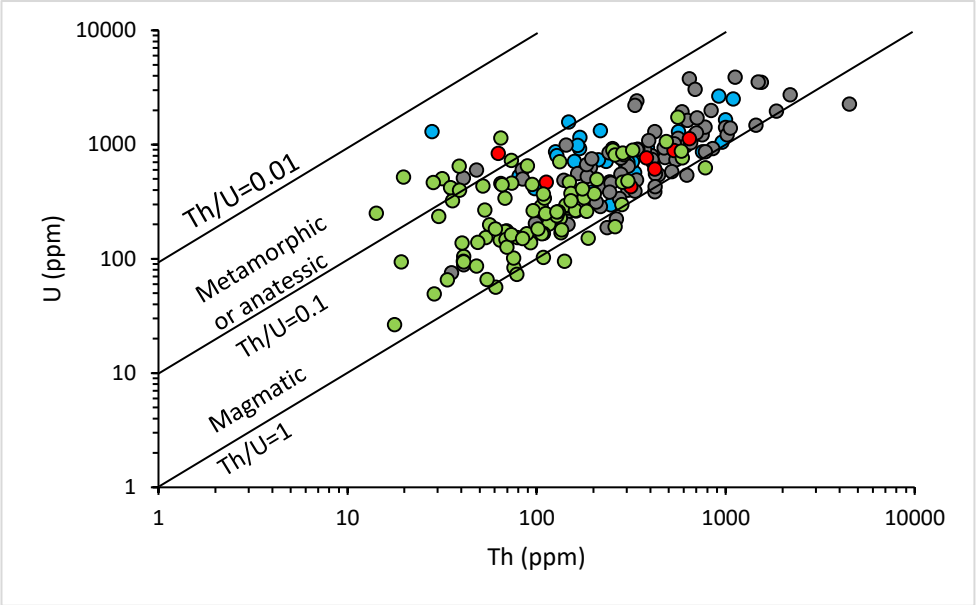

Figure 21. Th vs U zircon discrimination driagram. Colours as in as fig. 13, blue circles: ZB.

The Hoskin classification (2005) divides magmatic and hydrothermal zircon taking in account La vs $(Sm/La)_N$ and $(Sm/La)_N$ vs Ce/Ce* diagrams (Fig. 22). Most of the crystals fall out of the areas, but it is possible to suggest that generally they show an affinity that is more magmatic than the metamorphic. In particular the JB show only 32 crystals able to be classified because of the small La content present in the zircons. Among them, in the first diagram (Fig.22A) 14 fall in the magmatic field (44%) and two near the Xinger granite zircon, while the others plot outside of the drawn areas and far of the granite crystals. The second diagram (Fig. 22B) shows 16 crystals (50%) in the magmatic field, 3 plots near the Xinger granite zircon, 2 in the hydrothermal field and close to the Xinger granite zircon, while the others plot outside the area and far the granite. In the Brkini Basin, 82% of the crystals can be classified in both diagrams, showing that 36% of the zircons fall in the magmatic area and 5 plot close to the Xinger granite.

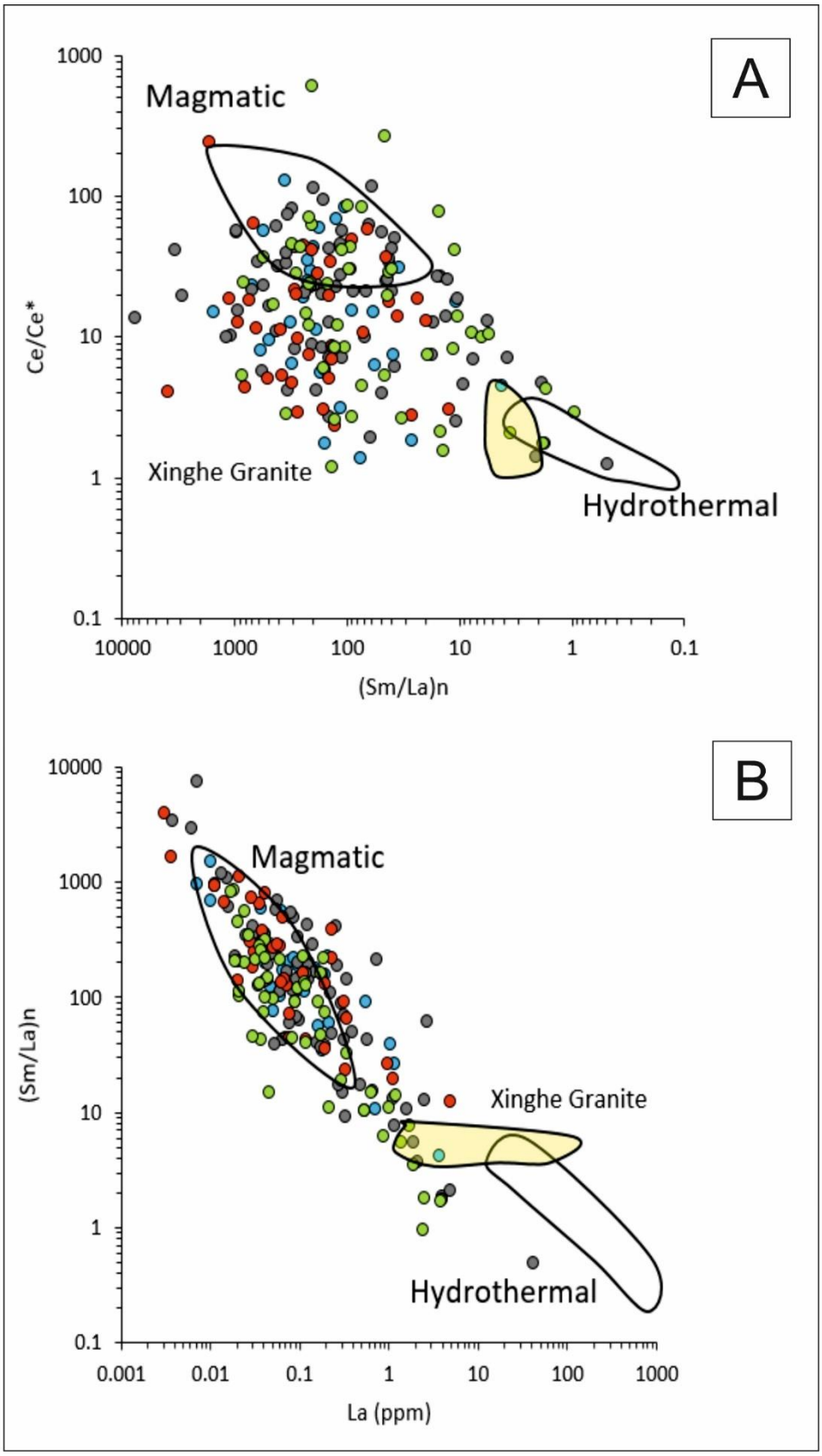

Figure 22. $(Sm/La)_N$ vs La (A) and Ce/Ce* vs $(Sm/La)_N$ (B) zircon classification diagrams that divide magmatic from hydrothermal crystals (Hoskin, 2005). Colours as in Fig. 21.

The others plot outside from the fields and far the granite in the La vs $(Sm/La)_N$ diagram, while in the (Sm/La)n vs Ce/Ce* one (Ce*= (La+Pr)/2), two crystals fall in the hydrothermal field, while the others are not classified. Among the IB zircons the 42% are not classifiable (Fig. 22). In the first diagram 95% of the crystals show magmatic affinity while one plot close to the magmatic field, while in the second diagram most of them fall outside the considered fields (75%). No hydrothermal crystals can be found for IB. Among the 33 crystals of the ZB, 97% of them have been classified. 8 and 10 (25% and 31%, respectively) zircons fall in the magmatic area in the first and second diagram, respectively, one (3%) plot close the Xinger granite in both, and the others fall outside the fields.

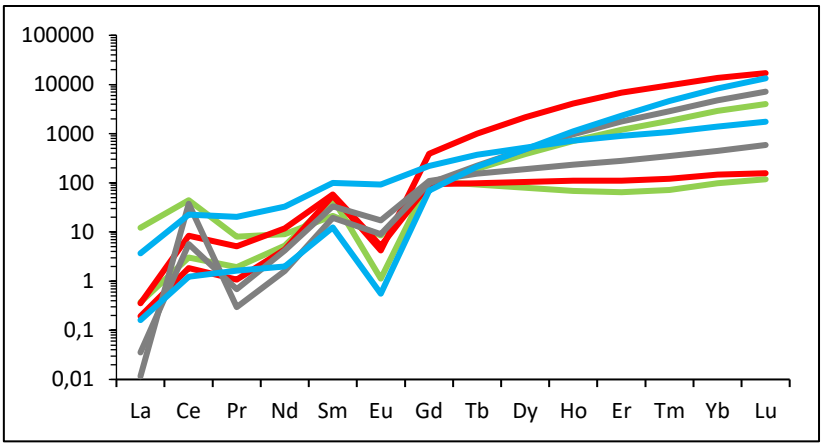

Fig. 23. REE patterns of the detrital zircon, it has been selected two crystals for basin, one showing a flat HREE pattern and a second showing a magmatic one. Colours as Fig. 21.

The REE patterns normalized to chondrites (Boynton et al., 1984; Fig. 23) suggest that 95% of the studied crystals show a magmatic pattern and according to Belousova et al. (2002), Grimes et al. (2009), Schulz et al. (2006) partially confirm the chemical classification.

The other zircons (JB=4, BK=4, IB=2 and ZB=3) show a pattern with flat HREE, probably due to the coeval crystallization of garnets, suggesting a granulitic affinity (Rubatto et al., 2017). Figure 24 put in relation the HREE pattern (Gd/Lu normalized to chondrite) and Y, an element more compatible in garnet than in zircon. The diagram shows that for a $(Gd/Lu)_N > 0.50$ the Y content is quite low, but comparable with lower ratio values (0.01-0.02), partially agreeing with Rubatto et al. (2017).

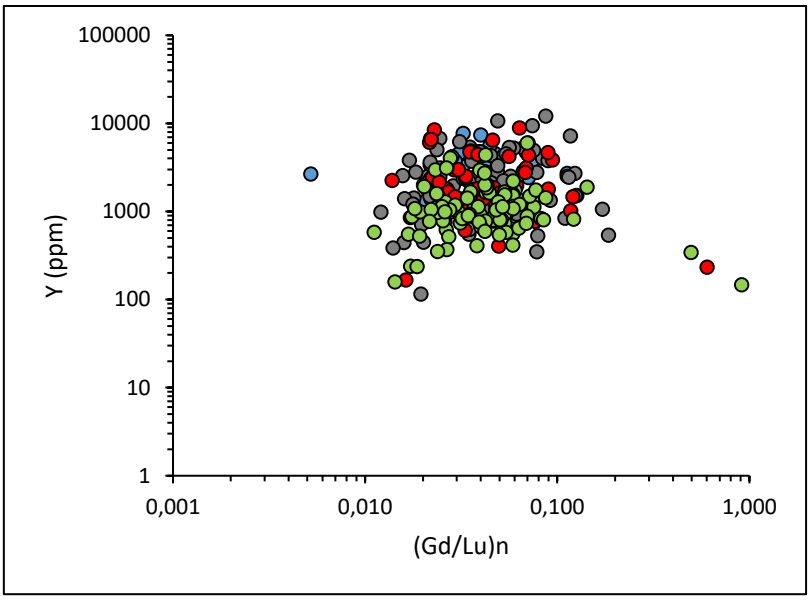

Fig. 24. Y vs $(Gd/Lu)_N$ diagram of the detrital zircon. Symbols as Fig. 21.

However, the REE patterns alone are not sufficient to discriminate properly the magmatic source/s because many of them show a high overlap, with only carbonatite and kimberlite host zircons generally show unique patterns (e. g. Grimes et al., 2007). Belousova et al. (2002) suggested two tree patterns to classify the magmatic zircon, a long and a short version, which take in account the content of several trace elements. In their classification, the crystals have been divided in metamorphic (MET; Th/U<0.1), crystallized in granitoids with silica content of less than 65%, between 70 and 75% and more that 75% (GR65, GR70 and GR/75%, respectively), basaltic (BAS), carbonatitic (CARB), doleritic (DOL) and syenitic-monzonitic (SYE). Generally, most of the crystals show granitoid affinities with different abundances in the studied basins (Fig. 25). In particular, 67% (JB), 30% (BK), 41% (IB) and 31% (ZB) show GR65 characteristics, 13% (JB), 39% (BK), 43% (IB) and 38% (ZB) GR70 ones, while only BK (13%) and ZB (6%) show zircon with GR75 features. Metamorphic and doleritic crystals are present in all the basins (JB=9%, 8%; BK=4%, 4%; IB=1%, 10%; ZB=6%, 3%), while carbonatitic only in JB (2%), BK (2%) and IB (7%). Basaltic and syenitic/monzonitic are represented by JB (2%) and BK-ZB (8%, 19%) respectively.

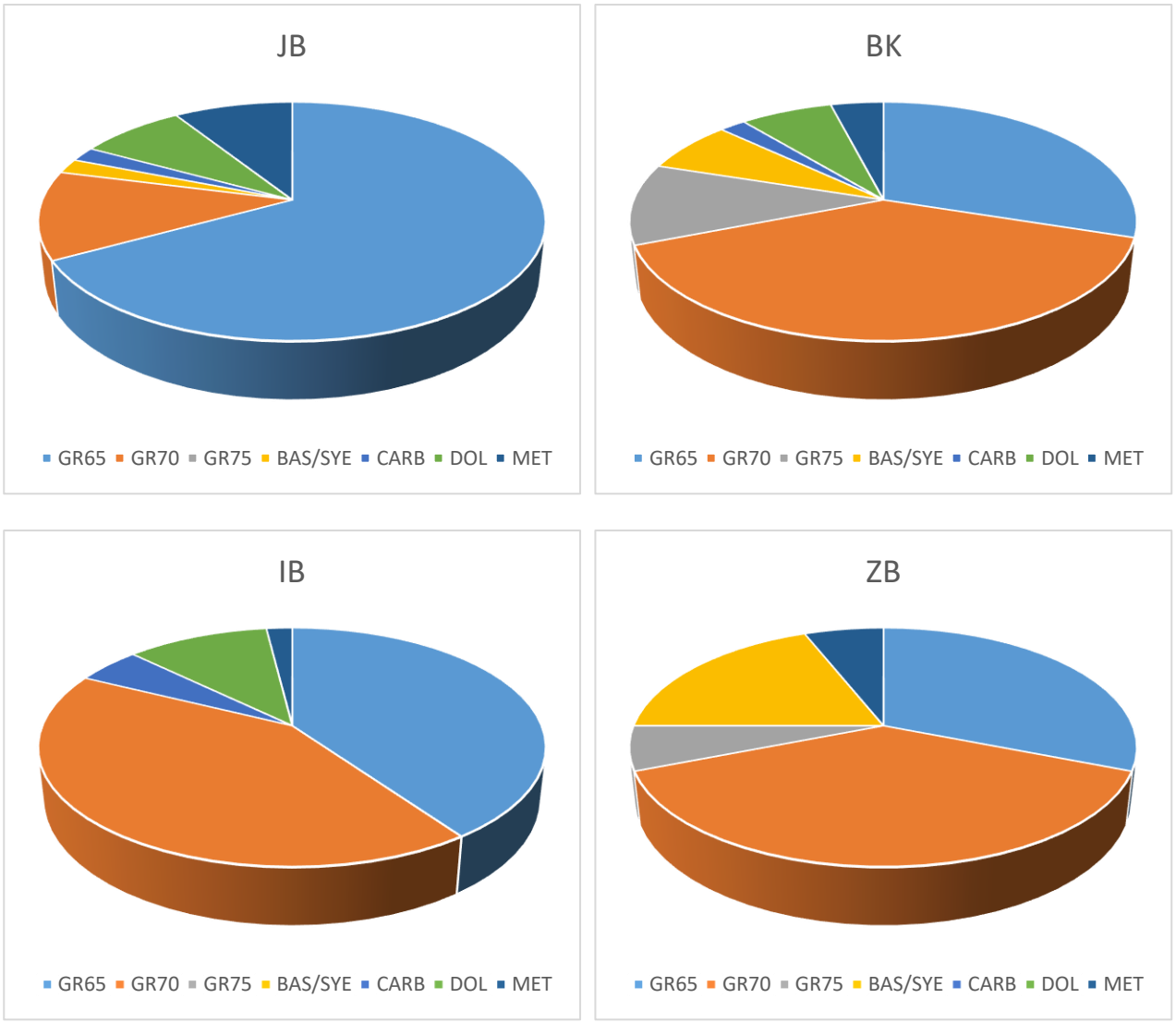

Figure 25. Pie chart representing the zircon host-rock affinity percentage for every basin.

The REE patterns of the zircons crystallized by the different protoliths generally show differences in REE content/ratio, Ce and Eu anomalies, confirming that the crystals originated from several sources.

In particular the GR65 zircon generally shows a higher Eu anomaly (Eu/Eu*= 0.06-0.79) than Gr65 and Gr75, Eu/Eu*= 0.02-0.43 and Eu/Eu*= 0.02-0.54, respectively, with comparable Ce values (Ce/Ce*= 2-169; Ce/Ce*= 186-5; Ce/Ce*= 119-4; respectively). The LREE ratio is higher for the dolerite zircons (mean=0.085), than for the Gr65 and Gr75 ones (La/Gd= 0.002 and La/Gd= 0.003 respectively) while the mean of the HREE is more similar for three kinds of protolith, Gd/Lu= 0.009,

Gd/Lu= 0.007 and Gd/Lu= 0.005 respectively. Notably, the zircons crystallized in dolerites show the highest variability in REE patterns.

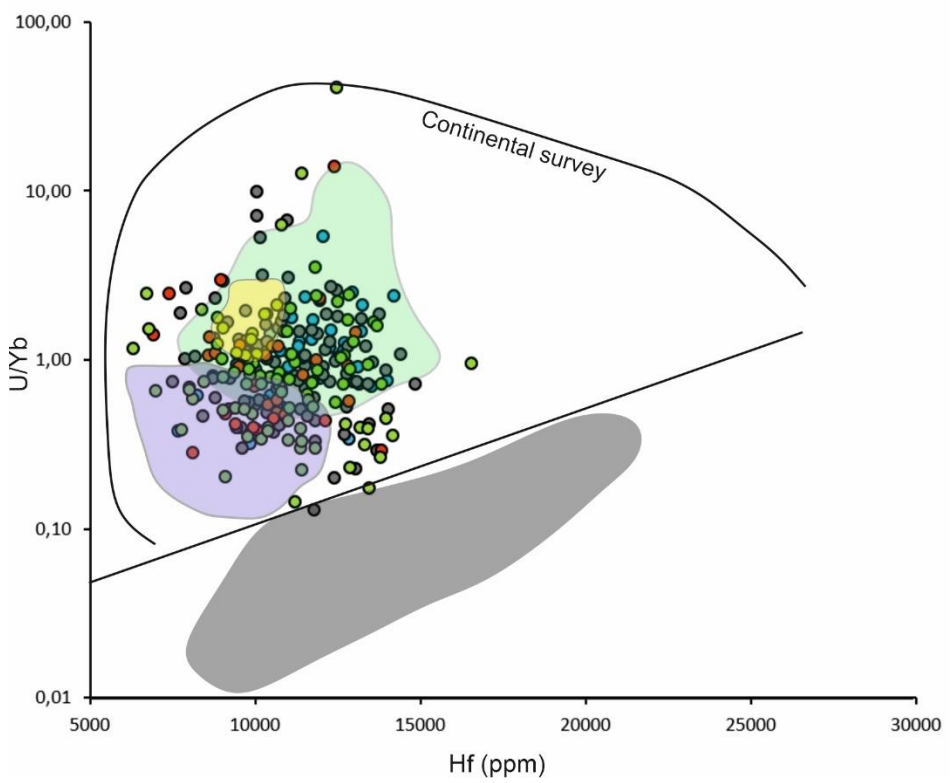

Fig. 26. U/Yb vs Hf zircon discrimination diagram (Grimes et al., 2015, modified) with continental-arc (green field), post-collisional (yellow field), Iceland OI-type (lilac field) Mor-type (grey field) zircons. Colours as Fig. 21.

Grimes et al. (2015) used the trace elements to define the tectonomagmatic affinity of the zircon. In particular, in this work it has been used the U/Yb vs Hf (Fig. 26), U/Yb vs Nb/Yb (Fig. 27A) and the log10 (U/Yb) vs log10 (Nb/Yb) diagrams (Fig. 27B), which discriminate continental from MOR zircons, continental and mantle arrays and Continental Arc Type, MOR type (mid-ocean ridge) and OI type (ocean-island; plume influenced) affinities (Fig.26, 27). In Fig. 26 it is possible to see how all the samples fall in the continental survey field, overlapping the continental arc, post-collisional and Iceland OI-type fields. In the U/Yb vs Nb/Yb the here studied zircons can be mainly found in the magmatic arc array (97%), falling in the continental arc, post-collision, OI-type and partially MORB type fields (Fig. 27A). The few that fall in the mantle array belong to JB and BK and generally fall at

the interception of Continental, and Iceland areas. Partially in agreement, in the log_{10}(U/Yb) vs log_{10}(Nb/Yb) diagram, most of the samples fall in the Continental Arc Type, but the overlapping is rather strong (Fig. 27B).

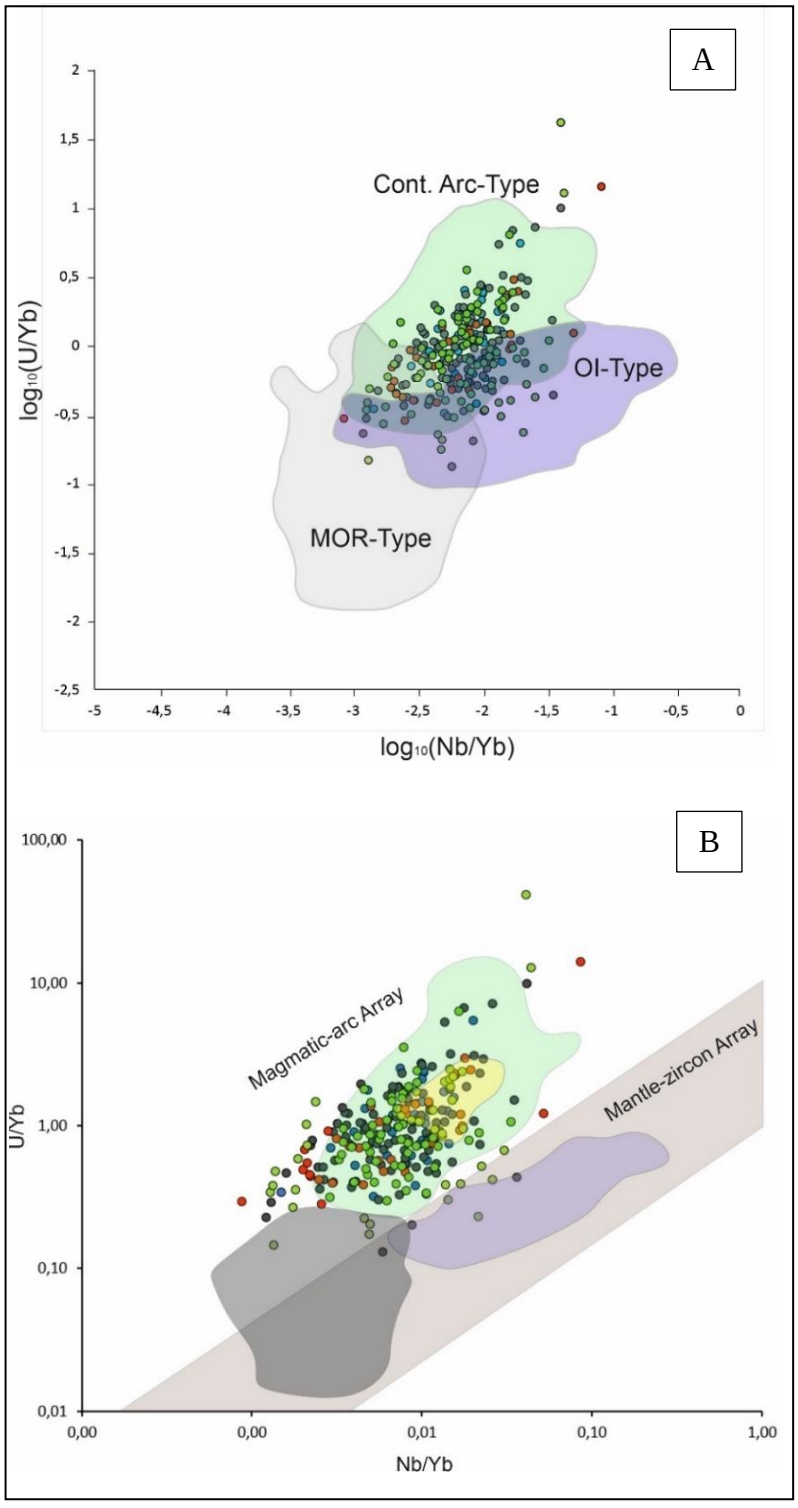

Fig. 27. (A) log_{10}(U/Yb) vs log_{10}(Nb/Yb) (A) and (B) U/Yb vs Nb/Yb (B) zircon discrimination diagrams (modified after Grimes et al. 2015). Continental-arc (green field), post-collisional (yellow field), Iceland OI-type (lilac field) MOR-type (grey field) zircons. Symbols as in fig. 19.

Zircon geochronology

A total of 265 LA-ICP-MS age measures have been performed. Zircons from JB (95), BK (91; including 85 rims and 6 cores), IB (49; 43 rims and 6 cores) and ZB (33) have been analyzed. Generally, the difference between core-rim ages are rather small and show similar values, the highest gap belongs to Rab1-4 with 26 Ma.

The 265 analyses show a wide range of Pb^{206}/U^{238} age values, which span from Archean to Cretaceous times (Tables 15, 16, 17, 18). Among all the analyzed crystals, 90% (n=240) fall on the concordia line (Fig. 28A, 29A, 30A, 31A). About 4% (n=11) of JB and BK zircons and 2% (n=5) of ZB zircons below the Concordia suggesting their metamorphic overprint.

The detrital zircon population have been divided following the main tectonothermal events: Mesozoic-Dinaric (250-80 Ma), Variscan (280-380 Ma), Caledonian (400-500 Ma), Cadomian-Pan African (550-750 Ma), Greenvillian (900-1300 Ma). Ages older than 1.3 Ga are not included in any orogenic event and will be indicated just with the period name

Rims

Julian Basin

The JB zircons show the largest span of crystallization ages from 180±3.4 Ma to 3286±43 Ma (Table 15). Among the 95 ages obtained, 88 have been used in the Concordia diagram and distribution specters (Fig. 28). The Palaeozoic Era is the most represented (40 zircons). Among them Permian and Carboniferous are the more abundant. Then Precambrian (35), where Neoproterozoic is the richest Period and Mesozoic (12), occur. Almost all the Mesozoic ages are represented by Triassic zircons (11).

The Concordia that take in account only the first billion of years show that the age are quite well distribute, but it is possible to recognize three main assemblages that spans from 180 to 500 Ma, from

560 to 710 Ma, and from 800 to 1000 Ma (fig. 28B). It is worth noting that no Cretaceous crystals have been found in this basin, and that there is only one Jurassic zircon.

The Age distribution spectra show that the main peaks are related to Mesozoic and Caledonian phases (Fig. 28C). The Mesozoic and Variscan phases show the highest density of peaks (n=8) with the highest one at 232 Ma followed by other four important peaks with similar height at 264, 297, 332 and 346 Ma. The Caledonian phase show the second highest peak of the whole spectra at 446 Ma, together with two at 460 and 497 Ma. Cadomian-Pan African and Grenvillian phases are also represented with minor peaks at 563-710 Ma and 915-978 Ma respectively. Proterozoic Era also shows several small peaks located both in Mesoproterozoic and Paleoproterozoic times, the most significative are at 1414, 1825 and 2100 Ma.

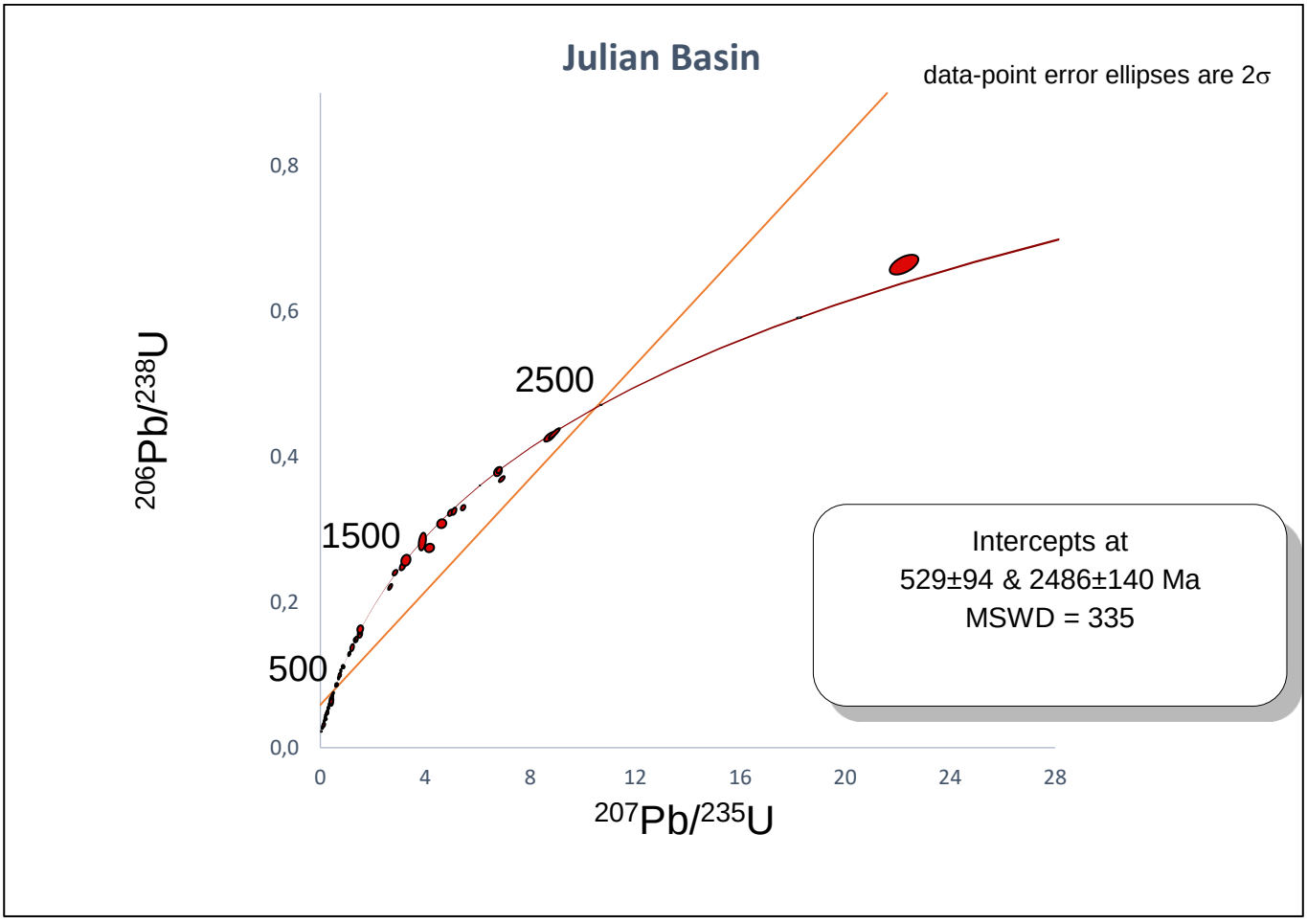

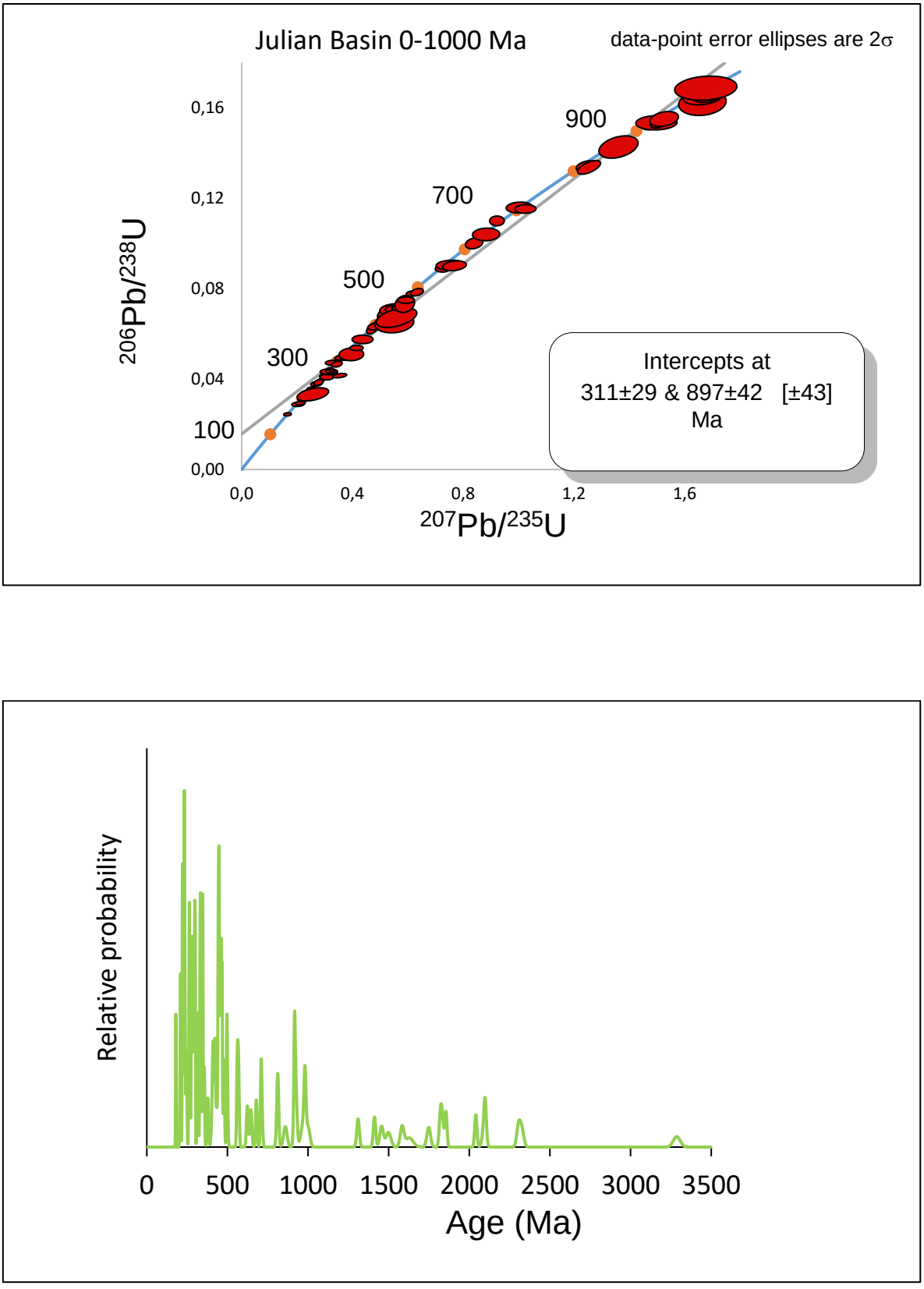

Fig. 28. Concordia plot of JB showing the whole zircon polulation (A) and the Cretaceous-Neoproterozoic interval (B). Data point error ellipses are 2σ. In C, the same analyses are plotted in relation to the relative age-probability curve. The curve is based on $^{238}U/^{206}Pb$ ages up to 1.5 Ga and $^{207}Pb/^{206}Pb$ ages for older ages.

Brkini Basin

Eighty-three analyses of the BK zircons fall on the Concordia line, showing ages that span from 86±3 to 2787 ±64 Ma (Fig. 29A). Similarly to JB, Palaeozoic Era is the most represented (n=36) followed by the Proterozoic (n=24), Mesozoic (n=18) and Archean (n=5). Neoproterozoic, Permian and Triassic Periods show the major number of age of crystallization with 14, 14 and 12 measures, respectively. Other significative Periods are Devonian (n=8), Carboniferous (n=8), Paleoproterozoic (n=7) and Cretaceous (n=6).

In the Concordia diagram, it is possible to recognize seven groups of ages, the first spans from 86 to 96 Ma, representing a Cretaceous magmatic event, while a second spans from 225 Ma to 700 Ma. The other groups extend from 860 Ma to 890 a, from 990 Ma to 1090 Ma, from 1850 Ma to 1950 Ma, from 2100 Ma to 2400 Ma and from 2600 to 2800 Ma (Fig. 29A). Taking in account the Concordia built with the data of the first billion years, the largest group could be divided in three sub-groups whith age intervals 225-330 Ma, 370-500 Ma, and 550-700 Ma (Fig. 29B).

The highest peak of the age distribution line is Cretaceous in age with a value of 87 Ma (fig. 29C). It is followed by peaks belonging to the Mesozoic and Variscan phases with age of 231 Ma, 277 Ma and 312 Ma. Caledonian and Cadomian-Pan African phases are represented by minor peaks at 390-462 Ma and 600-637 Ma, respectively. Grenville, Proterozoic and Archean ages show small maximums at 990-1037 Ma, 1947-2090 Ma and 2624 Ma, respectively. It is curious that the general height of the peaks diminishes with the increase of the age.

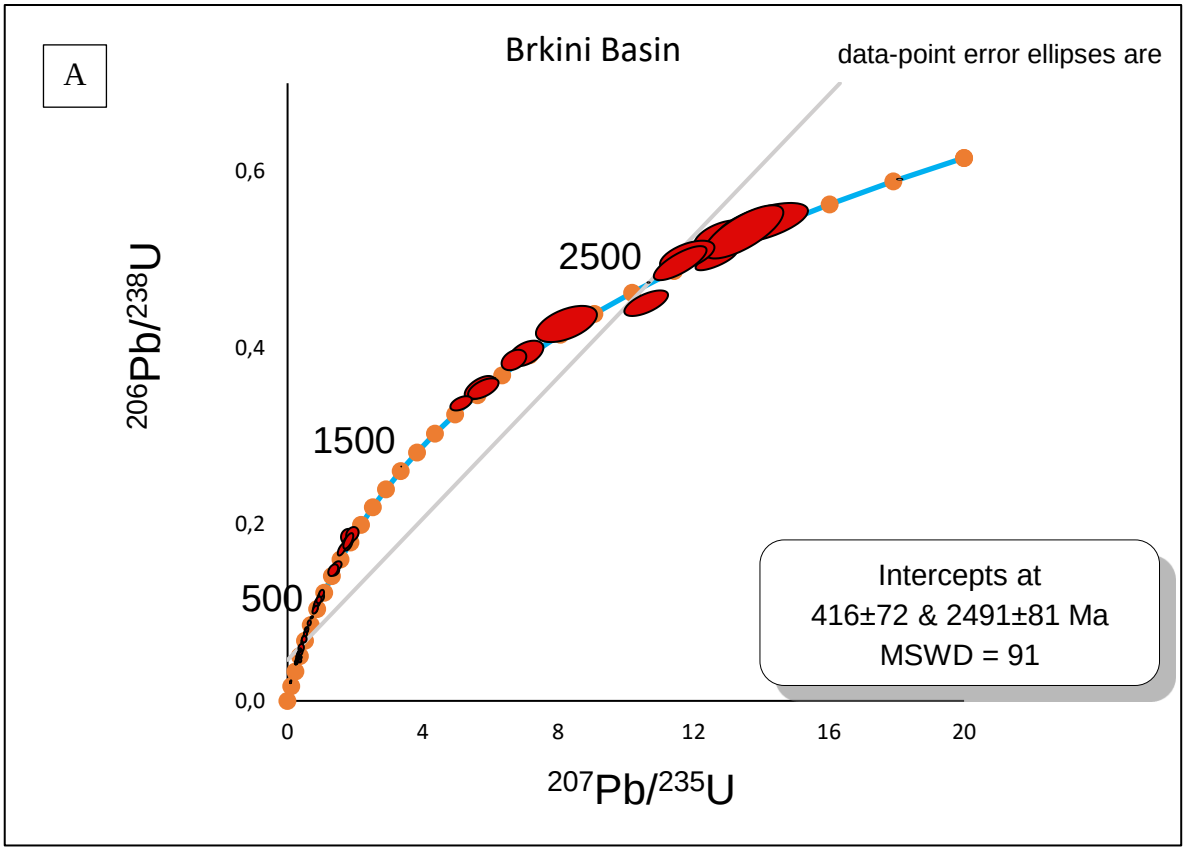
A
Brkini Basin
data-point error ellipses are
0,6
0,4
0,2
0,0
2500
1500
500
Intercepts at
416±72 & 2491±81 Ma
MSWD = 91
0
4
8
12
16
20
206Pb/238U
207Pb/235U

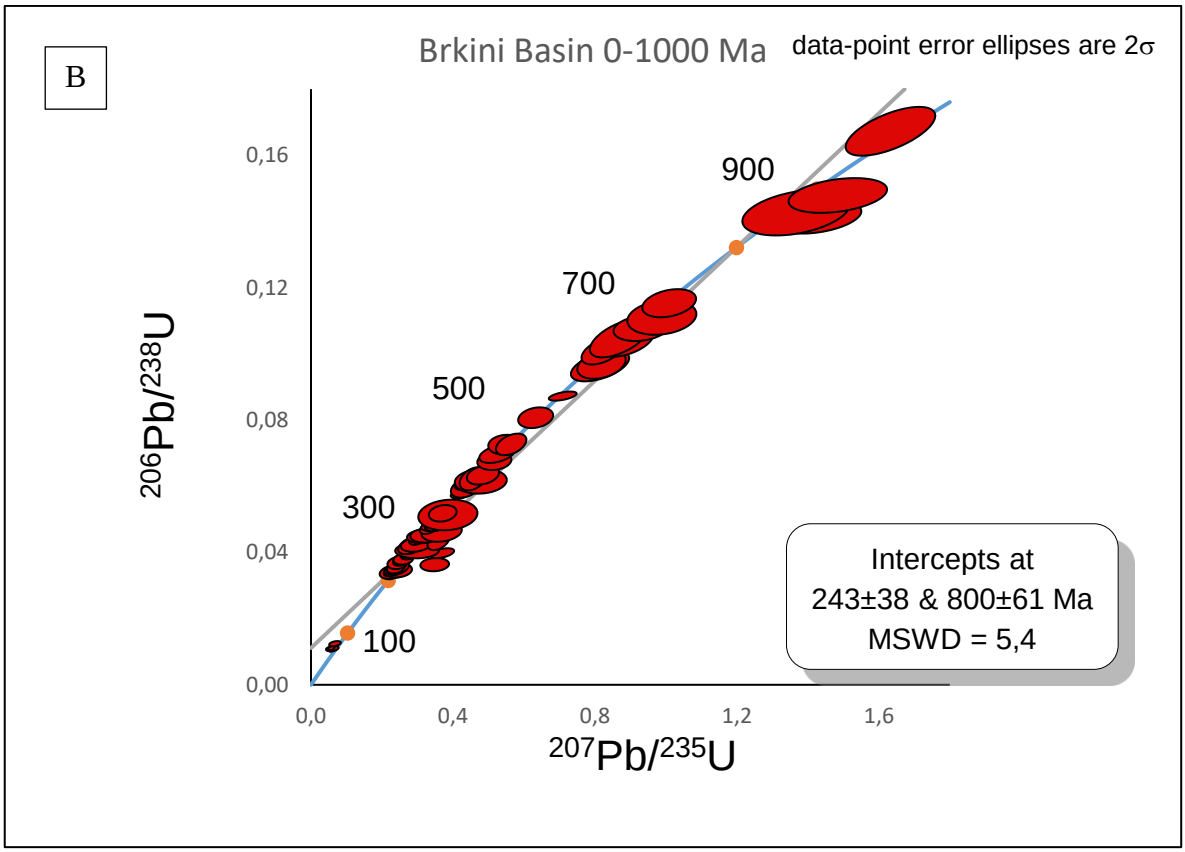
B
Brkini Basin 0-1000 Ma
data-point error ellipses are 2σ
0,16
0,12
0,08
0,04
0,00
900
700
500
300
100
Intercepts at
243±38 & 800±61 Ma
MSWD = 5,4
0,0
0,4
0,8
1,2
1,6
206Pb/238U
207Pb/235U

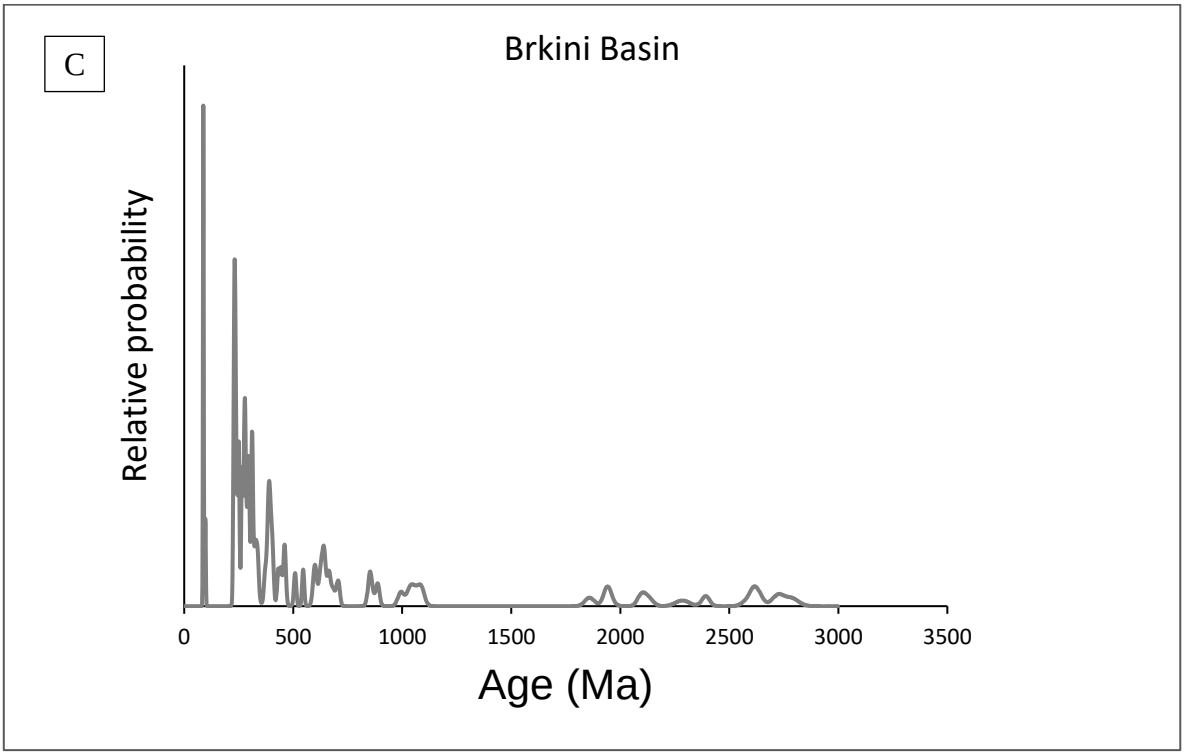

Fig. 29. Concordia plot of BK showing the whole zircon polulation (A) and the Cretaceous-Neoproterozoic interval (B). Data point error ellipses are 2σ. In C, the same analyses are plotted in relation to the relative age-probability curve. The curve is based on $^{238}U/^{206}Pb$ ages up to 1.5 Ga and $^{207}Pb/^{206}Pb$ ages for older ages.

Istrian Basin

The IB shows the smallest age interval among the basins, spanning from 97±6 to 2568±37 Ma (Fig. 30), and the smallest number of point analyses considered (n=40). As for the BK the zircon ages are better represented in Palaeozoic (n=22), followed by Proterozoic (n=15), Mesozoic (n=3) and finally the Archean with only two ages (Neoarchean). It differs from BK for the age distribution in the Palaeozoic, in fact Devonian (n=6), Silurian (n=3) and Permian (n=5) are the periods with more crystallization ages. In Proterozoic Era, 9 crystals are Neoproterozoic, 4 are Paleoproterozoic while Mesoproterozoic shows one data.

Even though this basin presents a low amount of data, the reduced Concordia shows four small clusters of ages, 250-380 Ma, 416-435 Ma, 470-490 Ma and 650-675 Ma (fig. 30B).

The age distribution highest peak show an age of 98 Ma Variscan and Caledonian phases are well represented, showing 3 (277, 246 and 309 Ma) and 4 peaks (417,480, 490 and 358 Ma) with similar heights, respectively. Cadomian-Pan African, Grenvillian and Proterozoic phases are poorly represented, counting only minor peaks at 677, 1075, 1950 and 2570 Ma (Fig. 30C).

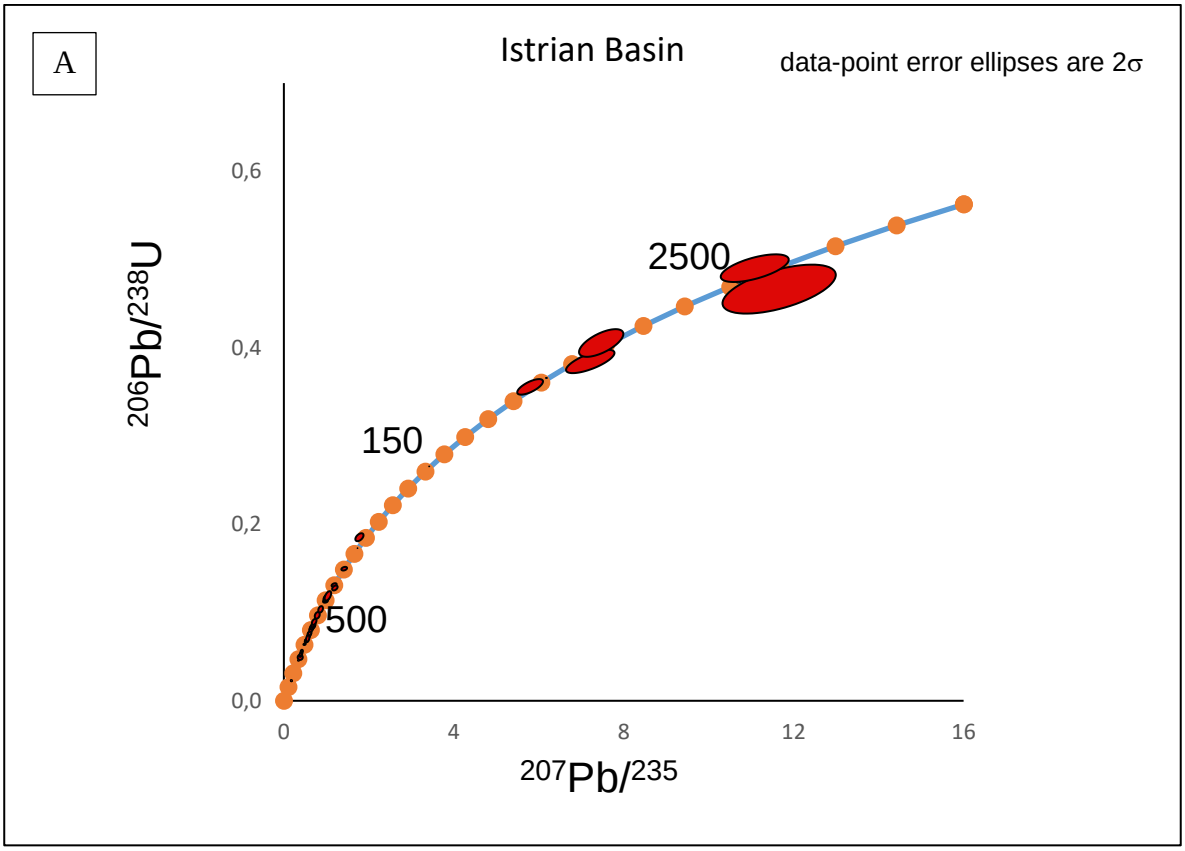

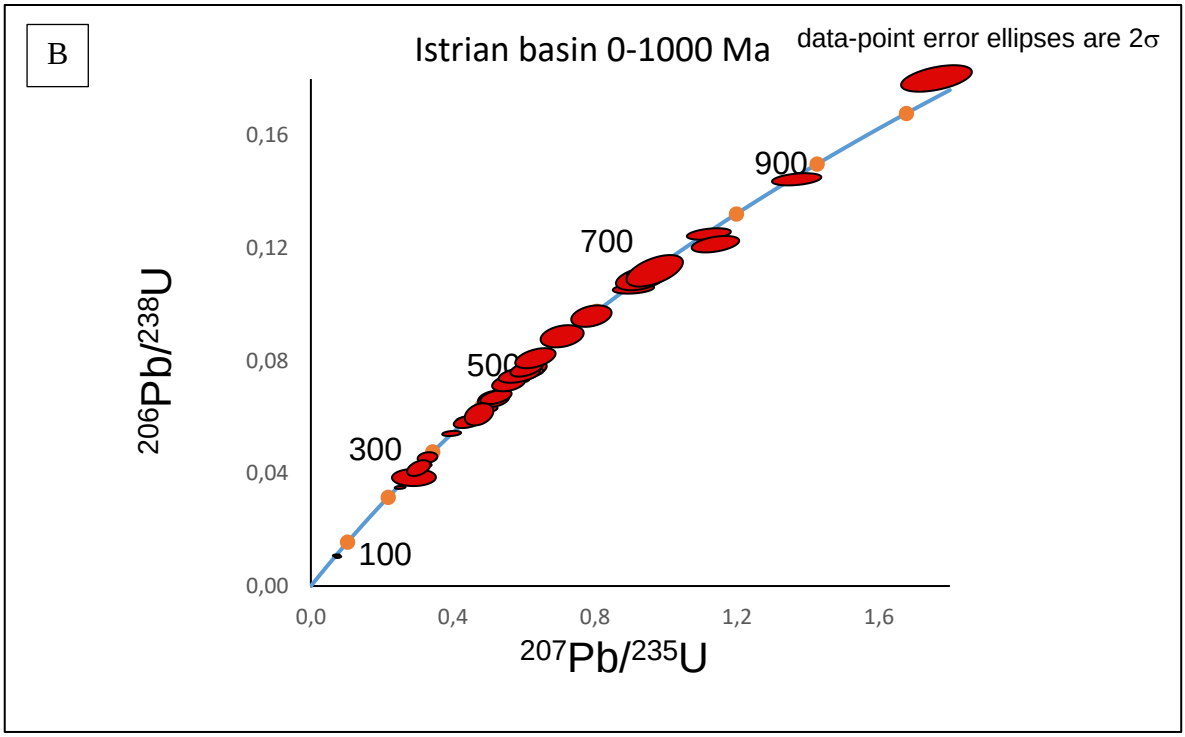

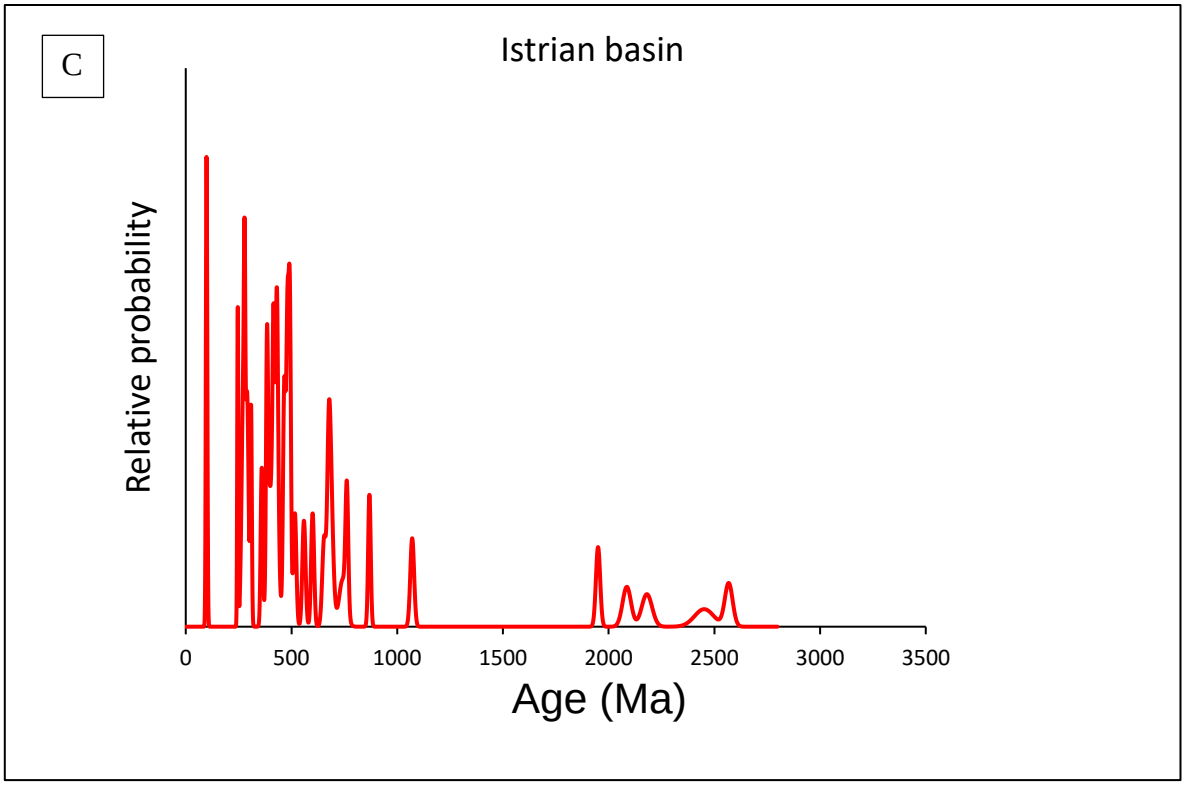

Fig. 30. Concordia plot of IB showing the whole zircon polulation (A) and the Cretaceous-Neoproterozoic interval (B). Data point error ellipses are 2σ. In C, the same analyses are plotted in relation to the relative age-probability curve. The curve is based on $^{238}U/^{206}Pb$ ages up to 1.5 Ga and $^{207}Pb/^{206}Pb$ ages for older ages.

North Dalmatian Basin

Thirty-two zircon of the North Dalmatian Basin have been selected for the Concordia diagram, showing crystallization ages between 81±4 and 2908±100 Ma (fig. 31A). Similarly to BKB and IB, there are more zircons crystallized during the Paleozoic (n=15), with Permian, Ordovician and Cambrian represented by 4 crystals each, followed by Proterozoic (n=12) where the Neoproterozoic is the most represented (n=7), Mesozoic (n=4) with 3 Cretaceous data and the Archean (n=1) are scarcely present.

The Concordia diagram built with the whole zircon population shows that generally the measures are concordant, with the exception of the oldest crystal and Z8-1 (Fig. 30A). Taking in account a reduced Concordia it is possible to notice three main gathering of data, which occur at 85, 240-290 and 460-520 Ma (Fig. 30B). Furthermore, a Discordia has been traced for three crystals with an upper interception at 841±100 Ma, a lower one at 219±99 Ma, and a MSWD of 6.9.

The ZB age distribution line is similar to those of IB, but with a major difference among Cretaceous and other peaks. The highest one show age of 83 Ma, while the second most significative peak belong to the Variscan phase (284 Ma). The Caledonian phase is well represented by the presence of three peaks at 396, 435 and 460 Ma. Cadomian, Greenville and Proterozoic phases show only minor peaks at 614-684-722 Ma, 888-1000-1100 Ma and 1524-1854-1929 Ma, respectively (Fig. 31C).

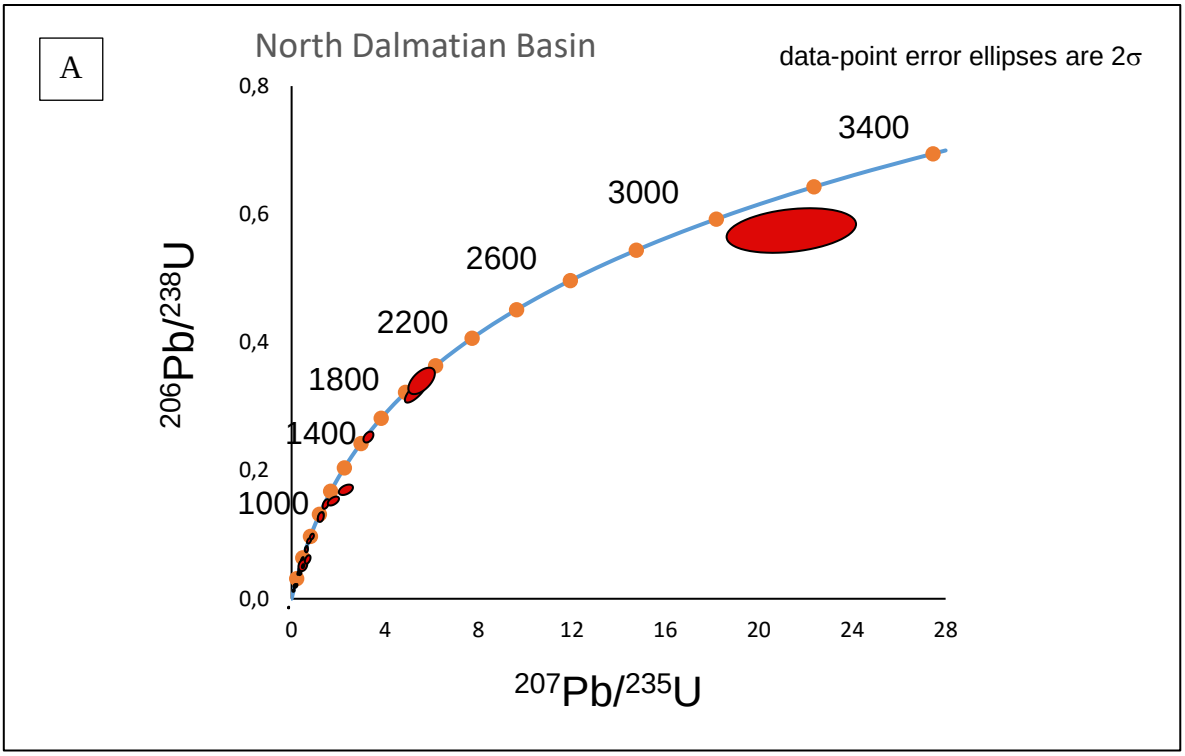
A
North Dalmatian Basin
data-point error ellipses are 2σ
0,8
0,6
0,4
0,2
0,0
206Pb/238U
3400
3000
2600
2200
1800
1400
1000
0
4
8
12
16
20
24
28
207Pb/235U

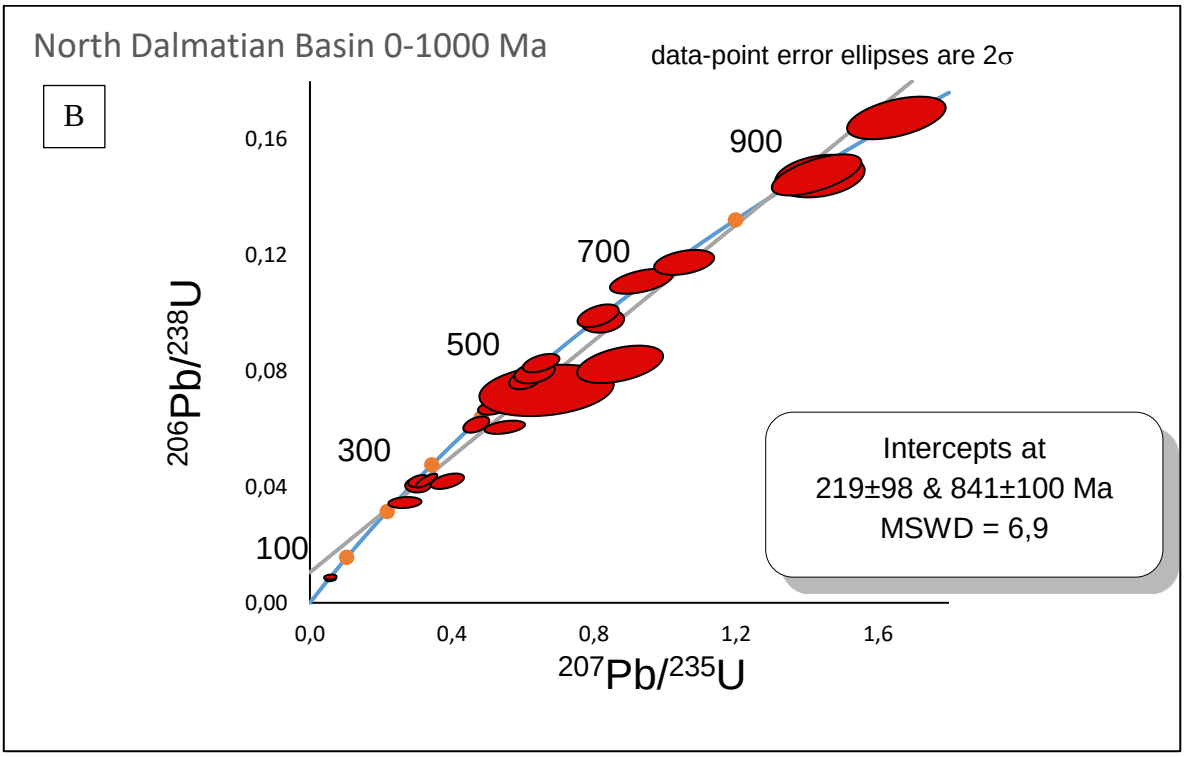
North Dalmatian Basin 0-1000 Ma
data-point error ellipses are 2σ
B
0,16
0,12
0,08
0,04
0,00
206Pb/238U
900
700
500
300
100
0,0
0,4
0,8
1,2
1,6
207Pb/235U
Intercepts at
219±98 & 841±100 Ma
MSWD = 6,9

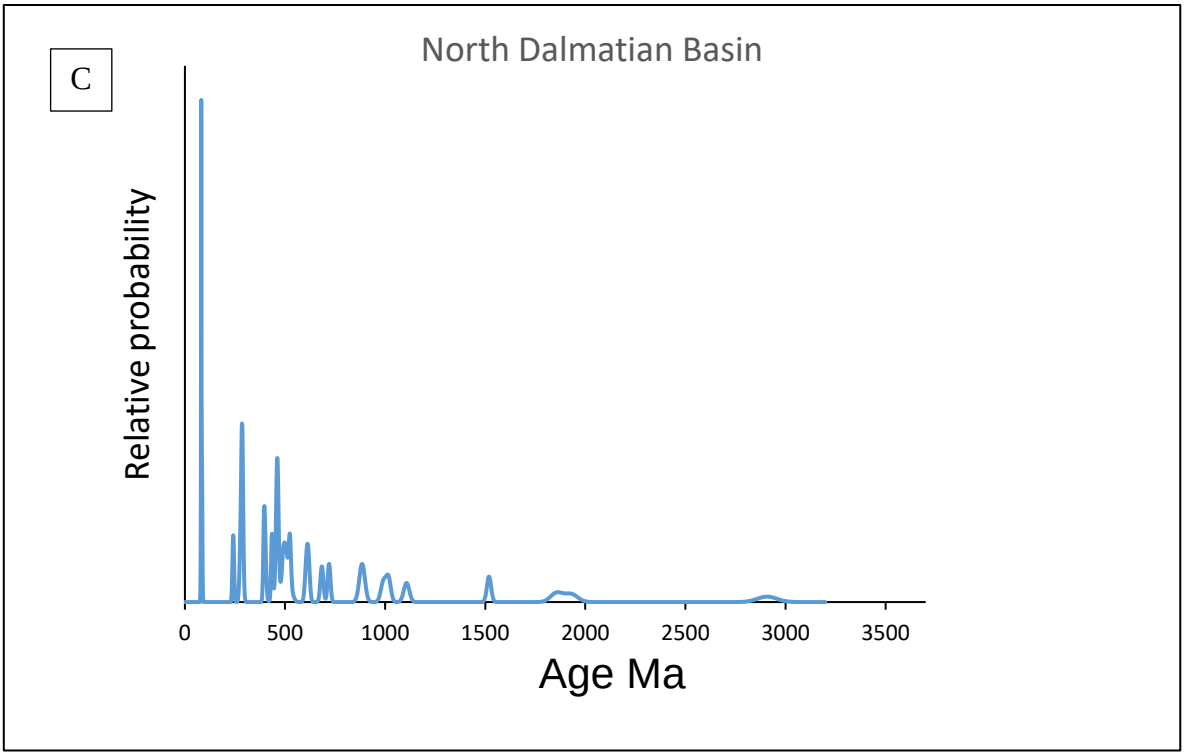

Fig. 31. Concordia plot of ZB showing the whole zircon polulation (A) and the Cretaceous-Neoproterozoic interval (B). Data point error ellipses are 2σ. In C, the same analyses are plotted in relation to the relative age-probability curve. The curve is based on $^{238}U/^{206}Pb$ ages up to 1.5 Ga and $^{207}Pb/^{206}Pb$ ages for older ages.

Cores

Three and five cores of IB and BK have been analysed. Both the basins show ages that span form the Early Permian (Asselian), 297±11 and 293±8 respectively, to the Neoproterozoic (Ediacaran), 550±11 and 628±12 respectively. The Variscan and Caledonian phases are the better represented orogeny, both showing one and two cores of IB and BK, respectively. In both the basins, one crystal belonging to the Cadomian-Pan African cycle is present. It is noteworthy that no Grenvillian or oldest phases have been found among the cores analyzed (Tables 16, 17).

Discussion

Several authors studied the mineralogy and petrography of the Upper Cretaceous-Paleogene External Dinarides flysch basins (e.g. Lenaz & Princivalle, 1996, 2002, 2005; Lenaz et al., 2000, 2001, 2003; De Min et al., 2007, 2014; Mikes et al., 2008; Lužar-Oberiter et al., 2009) to define the sedimentary provenance and to contribute to the geological evolution of the area. The heavy minerals collection of the basins generally comprehends ZTR family (zircon, tourmaline and rutile), garnets and volcanic/peridotitic spinels, suggesting a coheval erosion of continental and ophiolitic rocks. Lenaz et al. (2000, 2003) studied the chemistry of Cr-spinels suggesting a mixing of Internal and External Dinaric origin for this kind of minerals. The Internal Dinarides are supposed to be the supplier of the peridotitic spinels, more present in the Julian basin, while the main supply area suggested of the volcanic ones are the External Dinarides, better represented in the Istrian and Krk basins. Lužar-Oberiter et al. (2009) studied the Upper Cretaceous clastic formations located in the Medvednica Mountains and nearby areas. According to the chemistry of Cr-spinels of these basins, the authors suggest a possible common provenance and a palaeogeographic connection between the Julian and Vivodina (NW Croatia).

Garnets

Several garnet-bearing rocks outcrop in the Dinarides and the surroundings, which have been considered by several Authors as the sources for the flysch deposits (Magdalenić, 1972; Lužar-Oberiter et al., 2012; Mikes et al., 2008b among the others). It is worth noting that garnet in amphibolite (Pamić et al., 1973; Milovanović, 1984) is commonly Alm- and Py-rich with Gr ranging between 15 and 25 mol. %, while in the Variscan amphibolite from Moslavacka Gora, garnet composition is about $Gr_{82}And_{11}Alm_{7}$. These values are similar to those of some garnets found in IB although andradite content is different. Pre-Variscan Barrovian garnet found in micaschist, paragneiss and amphibolite of the Slavonian Mts. (Balen et al., 2006) are similar to Bi-Bii (B-type) garnets here studied.

Recently, Lužar-Oberiter et al. (2012) observed that most of the garnets of the Cretaceous northwestern Dinaric basins belong to the B-type, suggesting a source composed by greenschist-amphibolite facies metasediments. Bistra and Glog formations (both of Medvednica Mts, Upper and Lower Creatceous, respectively), and moderately the Vivodina one (Upper Cretaceous), show garnets with low Mg, low Ca but high Mn contents, which suggest that intermediate-acidic igneous sources have played a role. Type A and C garnets are subordinate populations of all the basins, indicating a small contribute of high-grade granulite facies metasediments and medium-high grade metabasic rocks sources, respectively. The Authors suggested that in Lower Cretaceous these flexural basins have been filled by the detritus of obducted oceanic lithosphere with hazburgitic composition, which constituted an extended nappe complex, together with exhumed continental lithologies. Successively, in Upper Cretaceous, Vivodina and Glog formations received a mixed ophiolitic-continental and purely continental detritus supply, respectively. The two have been suggested to have formed in a pro-wedge and wedge top setting, testifying a change in detrital provenance. Similarly, Mikes et al. (2008) studied the Bosnian Flysch, forming a rather uniform belt comparable to those cropping out to the NW of Central Bosnia, in the Zrinska Gora and in the JB (Aubouin, 1973; Cousin, 1972; Babić

and Zupanič, 1976; Bušer, 1987; Hrvatović, 1999; Rožič, 2005). In this basin, trench sedimentation was controlled by the sub-ophiolitic high-grade metamorphic basement and from the distal continental margin of the Adriatic plate. In fact, after the obduction onto Adria, from the Jurassic–Cretaceous transition onwards, a vast clastic wedge developed at the front of the leading edge. The following mid-Cretaceous deformation caused migration towards SW and increasing amounts of redeposited carbonate detritus released by the Adriatic Carbonate Platform margin with subordinate siliciclastic source components. These facts indicated a change in the source rocks with ophiolites supplying a lower amount of material. Even in this basin, the B-type garnets occur from the Tithonian to the Maastrichtian in the Vranduk and Ugar Formations while type C garnets are well represented in the Dinaride Ophiolite Zone melange, in particular those with a spessartine content >5%mol.

The Late Cretaceous-Eocene Gosau Group show detrital heavy minerals assemblage indicating that during the evolution of the basin the supply area changed. The garnets are usually rich in almandine (Alm_{mean}=63 ± 9 %, Alm_{Max}= 85 %), with moderate grossular content (Gr_{mean}=18 ± 9 %) and pyrope that vary between 0 and 46 % with (Py_{mean}=12 ± 7 %). Low spessartine proportions are characteristic (6 ± 6 % in average), while andradite and uvarovite component is almost lacking (Stern & Wagreich; 2013). Using the triangular classification suggested by Morton et al. (2004), the Maastrichtian, Paleocene and Eocene sediments show crystals that fall mainly in the Bi-Bii and rarely in Ci-A fields (Stern & Wagreich; 2013), suggesting that the supply area of the Gosau Group and northeast Adria flysch is not the same.

The data obtained for the studied garnets seem in agreement with the literature data of coeval and slightly older basins located in the Dinarides. (Mikes et al., 2008; Lužar Oberiter et al. 2012). The Alm + Sp – Py – Gr triangular diagram suggested by Morton et al. (2004) shows that the crystals have mainly Bi-, Bii- and Ci-type features, but also A-, Cii- and D-types affinities and several sources must be taken in account. Furthermore, the triangular diagram show that there are only small changes of sources from the Upper Cretaceous to the Eocene. This is testified by the quite constant type B/type

C ratio among the studied basins, and the small changes of the minor garnet type represented. However, considering also the trace elements some differences can be noticed even among garnets of the same typology, in particular the Eu anomaly (Eu/Eu*) and the $(Gd/Lu)_N$ ratio (Fig. 15, 16). Schwandt et al. (1993) argued that Eu anomaly in garnet might reflect the temperature and fO_2 conditions of the fluid in which the precursor phases precipitated. In systems where REE-bearing phases are present the negative Eu anomaly in garnet has been interpreted as the preferential partitioning of Eu into feldspars (Heimann et al., 2011). An important factor for the REE re-distribution during metamorphism is the presence of accessory phases, and breakdown or significant molar reduction of major phases. Konrad-Schmolke et al. (2008) showed that a progressive HREE depletion can be determined by continuous extraction of HREE from the matrix, due to garnet crystallization, limited REE liberation from matrix phases such as chlorite and constant modal amounts of epidote and increasing modal amphibole. A reduction in the amounts of these phases would result in a change of the REE patterns in the associated garnet due to the liberation of predominantly medium to HREEs. In particular, Konrad-Schmolke et al. (2008) showed that epidote breakdown determines an abrupt increase of Dy, Ho and Er in the growing garnet, and REE patterns with MREE higher than HREE. Consequently, it is quite clear that differences in the $(Gd/Lu)_N$ and Eu/Eu* ratios reflect different sources even in garnets of the same typology.

Analyzing composition of the Bi and Bii type garnets, it is then possible to recognize at least two possible sources for Julian, Istrian and Brkini basins for each type. The first one should be a feldspar-free source, while in the second one garnet possibly co-crystallized with feldspars, determining lower Eu/Eu* values (Fig. 15, 16). Furthermore, Ge vs Ga diagram points out that Bi population can be divided in other two groups that show different Ga for comparable Ge contents (fig. 32). Ge and Ga content remains constant during prograde metamorphism due to the large stability of their host minerals, while a small part of Ga is lost during retrograde metamorphism, probably due to the breakdown of hydrous minerals. On the other hand, for Ci garnets, only a feldspar free source is here proposed.

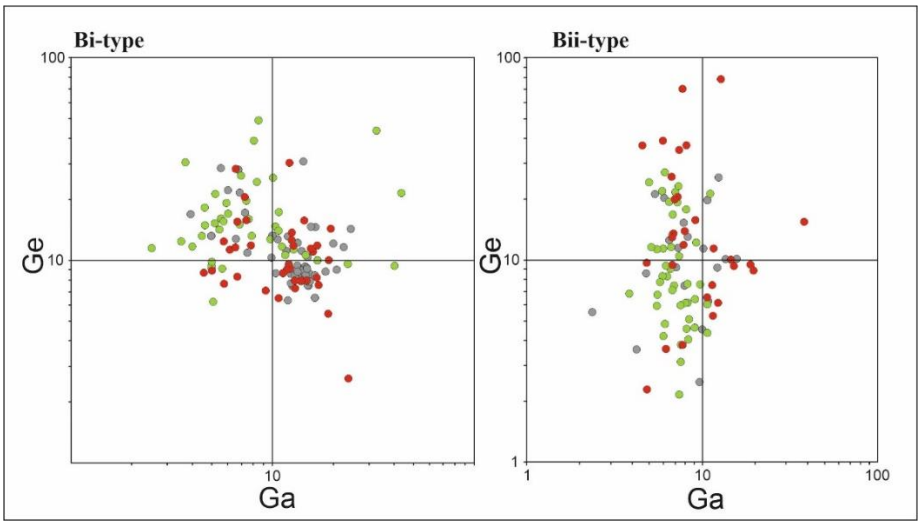

Fig. 32. Ge vs. Ga in Bi- and Bii-type garnets. Colours as in Fig.21.

Finally, the main affinities of Bi, Bii and Ci types content and their relative abundances suggest a primary source composed by amphibolite-facies metasediments. This kind of source is here preferred since the population fall both in Bi and Bii fields, but it is not possible to exclude that a portion of the garnets could be derived from intermediate-acidic igneous rocks. Taking in account also the trace elements, it is possible to suggest that the garnets that falls in Bi and Bii field could be crystallized in rocks both feldspar-free and feldspar-bearing. Furthermore, Bi type garnets could be divided in those that experienced prograde or retrograde metamorphism. The crystal plotting in Ci area suggest a secondary source composed by high-grade metabasic rocks. Minor suppliers could be high grade granulite-fies metasediments or charnokites, ultramafics and metasomatic rocks (e.g. skarn, low grade metabasic rock, ultrahigh metamorphosed calc-silicate granulites).

Rutiles

The trace elements analyses performed by LA-ICPMS suggest that the 82% of the rutiles have a crustal origin and 51% show metamorphic affinities (Fig. 17), with crystallization temperatures between 212 and 932 °C (using Watson et al., 2006 geothermometer; Fig. 18). Most of the crystals show amphibolite-eclogite-facies crystallization temperature (77%; Tc=500-750 °C), with Nb/Ta and Zr/Hf ratios that varies between 2-46 and 8-55, respectively (Fig.19). Among these, 79 (77%) and 98 (95%) crystals show sub-chondritic Nb/Ta and Zr/Hf values ($Ch_{Nb/Ta}$ =19.9; $Ch_{Zr/Hf}$=34.3; Münker et al., 2003). While 17 (13%) and 13 (10%) rutiles crystallized at greenschist- and granulite-facies temperature (<500 and >750 °C), with Nb/Ta values of 9-33 and 11-80 and Zr/Hf of 4-31 and 17-37, respectively (Fig. 19).

The difference in Nb/Ta ratio in rutile could be due to the growth of the rutile together with titanite and ilmenite during the prograde metamorphism in amphibolite-eclogite and granulite facies conditions (Luvizotto et al., 2009; Luvizotto & Zack, 2009; Meyer et al., 2011; Stepanov and Hermann, 2013; Şengün et al., 2017). In particular, subchondritic values (9-19) are related to mineral dehydration during eclogitization. Otherwise, the trigger for such differences is the breakdown during HP metamorphism of Ti-rich minerals as biotite that is responsible for the diffusion of elements such as Zr, Nb, Ta and Ti during the crystals re-equilibration. Between the two elements, Nb is more compatible in rutile than in the other phases, while Ta prefers ilmenite/titanite/biotite, suggesting that the first rutiles that crystallize should have a higher Nb/Ta ratio than the last ones. Furthermore, the ratio could also depend by the amount of reacting Ti-rich minerals hosted by the source-rock. Finally, aqueous solution with high Nb/Ta ratio could derive by the breakdown of hydrous minerals, such as phengite, in which Nb is more compatible than Ta during HP metamorphism (Zheng et al., 2011; Şengün, 2017). These supercritical fluids could be also responsible of little core-rim zonation within the grains (Şengün et al., 2017 and references therein).

In the rutiles analyzed, Nb/Ta and Zr/Hf ratios seem to be mainly controlled by the decrease of Ta and the increase of Zr. The first is generally in agreement with literature (i.e. Şengün, 2017; Schmidt et al., 2009; Gao et al., 2014), which suggest the metamorphic dehydration in subduction zones as main trigger for the ratio increase as well as for rutile formation. On the other hand, Zr/Hf seems to be controlled mainly by the Zr content, rather than the Hf. However, the bilogaritmical Zr vs Hf diagram shows a quite good linear correlation between the two. Brkini and Istrian Basins trendlines shows similar angular coefficients (0.0317-0.0352, respectively; Fig. 20), while the JB appear to have a steeper line with 0.0529 value, suggesting that BK and IB could share similar rutile rock sources. Furthermore, two crystals of IB and 6 of the JB, form a line that is parallel to the main trend suggesting a possible secondary source for these two basins.

Due to their geochemical importance in rutile, the ternary diagram in Fig. 33 correlates Nb, Zr and Ta. Here it is possible to see how the BK rutiles tend to have more Ta-rich compositions. More in detail, it is possible to see how the first group is composed by JB, BKB and IB crystals, showing the highest number of crystals with high Nb (>80%) and relatively low Zr-Ta content. The high Nb content suggests metapelitic-felsic nature and the wide range of Nb/Ta ratio can be assigned to the different nature of the protolites that suffered both prograde and retrograde metamorphism. Rutiles studied by Hart et al. (2016) crystallized in metapelitic garnet–glaucophane micaschists of the Val Sesia that have undergone blueschist- to eclogite-facies metamorphism and metasomatic pyrope-bearing of the Dora Massif plot in the same area, suggesting a similar nature.

A second shows Nb relative content from 80 to 30 %, Zr from 15 to 70% and Ta <10%. This group seems to have a rather good linear relation, in which an increase of Zr correspond to a decrease in Nb/Ta ratio and could be divided in three main subgroups. One corresponds to an assemblage of analyses between 80 and 70% of Nb and it is constituted by JB, BK and IB, while the others are formed only by JB and IB crystals. It is worth noting that the 8 crystals forming the subgroup with Nb=40-30% correspond to those that plot parallel to the main trend in the bilogaritmic Hf vs Zr

diagram, suggesting they possibly derive from a different source. Generally, it is possible to suggest that the rutiles of the second group derive from mafic protolithes that probably have suffered medium-high prograde metamorphism (low Nb/Ta ratios), suggesting an amphibolite-eclogitic nature (e. g. Șengün, 2017; Șengün et al., 2017; Pereira et al., 2019). In the group 2 area (Nb=50-70%) there are also the metamafic products of the Syros Island that are composed by metasomatized metabasalt, metagabbro in eclogite-facies and metaigneous glaucophane scist in bluschyst-facies (Hart et al., 2016b), together with the hornblendite of the Bougmane arc complex (Anti-Atlas, Morocco; Triantafillou et al., 2018), metagabbro of Kazdağ Massif collected in an ophiolite suite (NW Turkey; Șengün & Zack, 2016) and paragneiss in granulite facies (Bracciali et al., 2013).

The third group show the highest Zr (Zr=90-70%) relative content and are constituted by three rutiles with very high temperature of crystallization (831-921 °C), suggesting granulitic facies, and two with amphibolitic-eclogitic facies temperatures. These last two are characterized by low Nb and Ta rather than high Zr content, but similar sub-chondritic Nb/Ta ratio (Nb/Ta=15-16), suggesting a mafic protolite with low Nb-Ta content that suffered a quite strong prograde metamorphism. The rutiles in garnet-bearing hornblende gabbro of the Bougmane arc complex (Anti-Atlas, Morocco; Triantafillou et al., 2018) plots near two crystals with T_c of 831 and 851 °C and Nb relative content of about 20%, while no data are available in literature for those with less Nb relative content.

Lastly, a group formed by BK and JB crystals, with Nb=80-60%, Ta=15-40% and Zr<10%, which show crystallization temperatures between 537 and 605 °C and very low Nb/Ta ratio (2) due to the high Ta content. No similar literature data have been found, but high Ta is characteristic of crystals formed in a Ta-rich pegmatite.

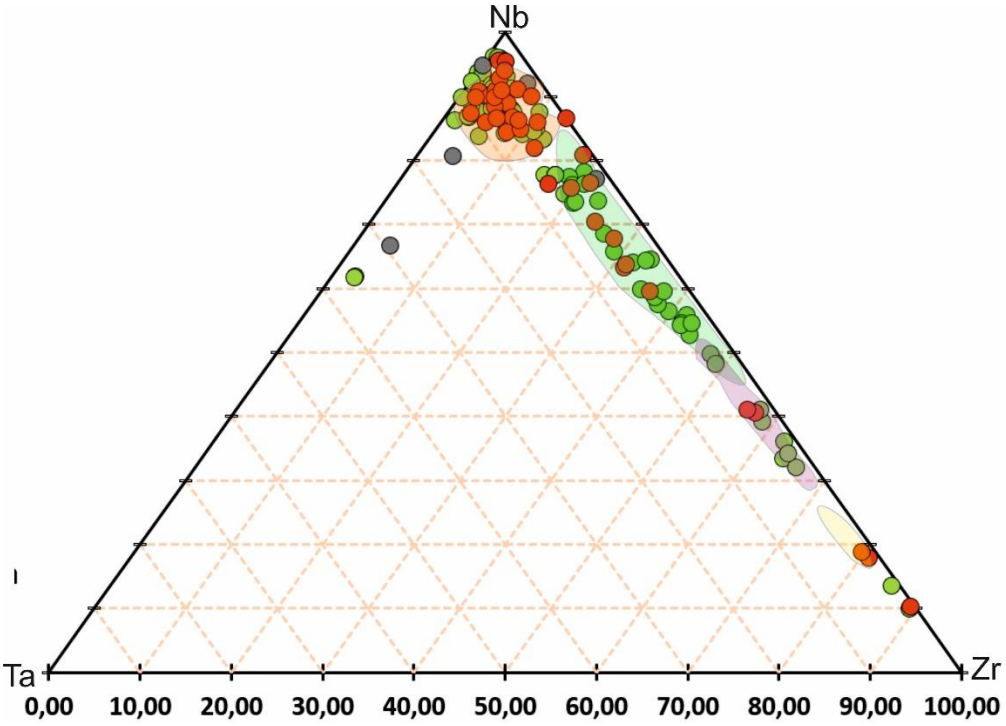

Fig. 33. Nb-Ta-Zr rutile ternary diagram. The orange area represents micaschist-quartzite protoliths (Hart et al. (2016), the green and purple ones represent mafic protoliths that underwent amphibolitic-facies metamorphism (Şengün, 2017; Şengün et al., 2017; Pereira et al., 2019, Hart et al., 2016, Triantafillou et al., 2018, Şengün & Zack, 2016, Bracciali et al., 2013) and the yellow area are drawn using the gabbro data of Triantafillou et al. (2018).

In the works of Lužar-Oberiter et al. (2009; 2012) about the Cretaceous basins in NW Dinarides, rutiles are not debated. According to Mikes et al. (2008), the metapelitic rutiles are between 60 and 80%, depending on the basin considered. When calculating the crystallization temperature, these authors considered only metapelitic rutiles obtainig two populations (650-860 and 500-650) for the DOZ mélange and a single one for the flysch formations (Vranduk and Ugar formations) with a mode between 550-700 °C.

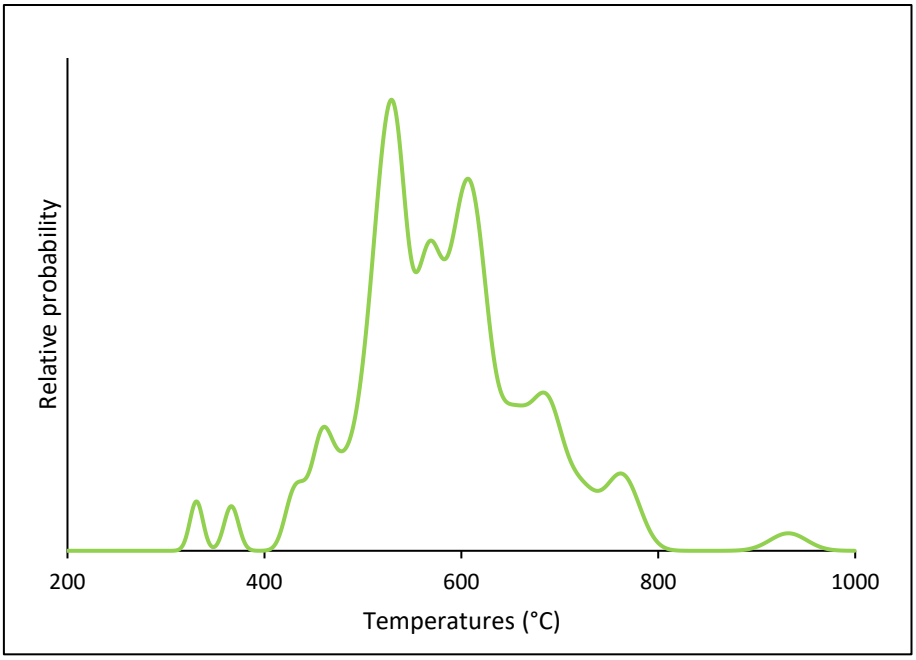

Fig. 34. Rutile crystallization temperature of JB crystals obtained using the Zr-in geotermomether of Watson et al. (2006) plotted against the relative probability.

The here studied basins are more similar to the DOZ formation with three populations, the main one that temperature spans from 500 to 650 °C, a second with the limits of 650 and 800 °C and the less important at about 400°C. Julian and Istrian basins main population is formed by three (530, 572 and 610 °C) and two peaks (543 and 588 °C), respectively (Fig. 34, 35A). Considering only those positioned at 530-543 and 610-588 (the highest two), it is possible to observe that they show a different ratio. In JB the most important peak is at 530°C, on the contrary IB highest peak is that at 588 °C, suggesting that the sources of the rutiles partially differ. Notably, 550-630 °C are the temperature calculated for the metamorphism event occurred in Late Cretaceous during the Sava-Adria collision (Usteszwesti et al., 2010).

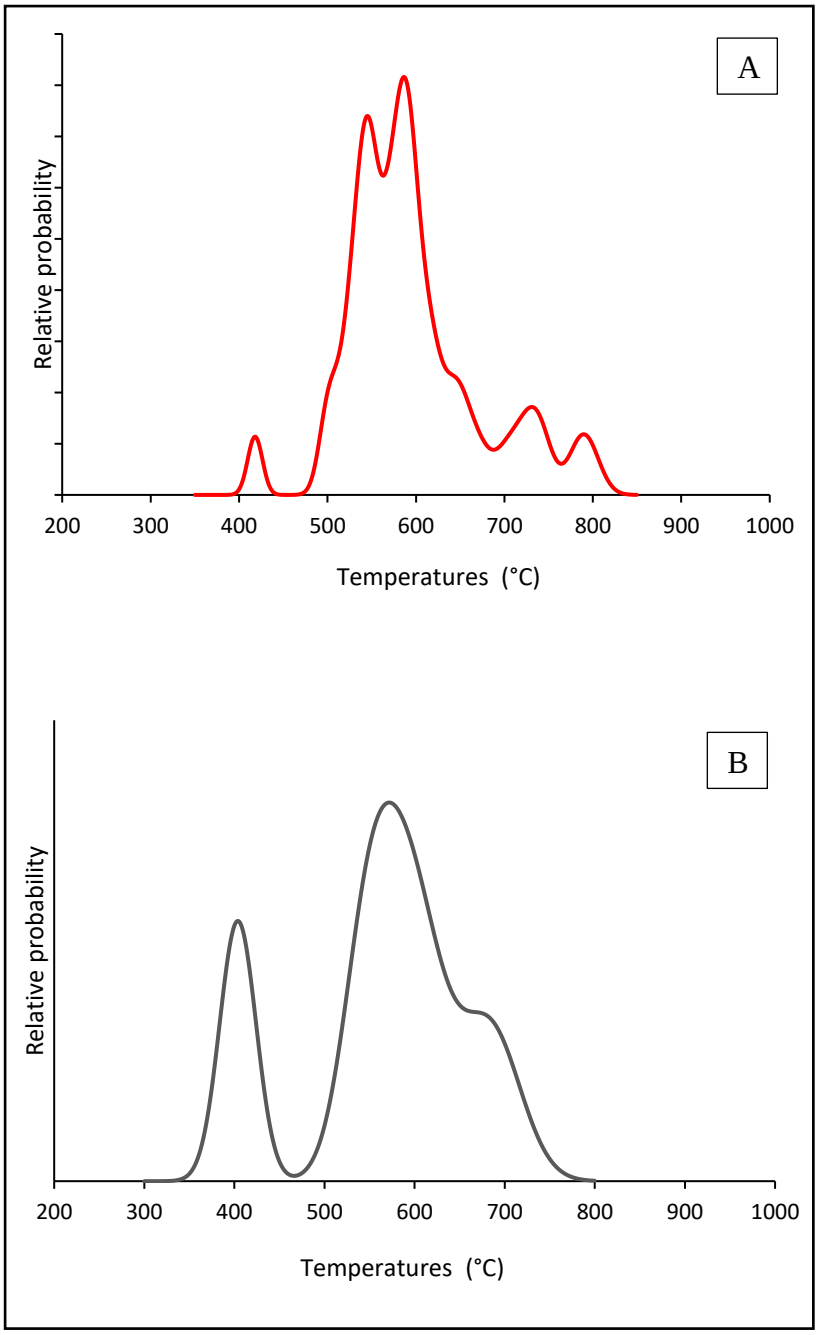

Fig. 35. Rutile crystallization temperature of IB (A) and BK (B) crystals obtained using the Zr-in geotermomether of Watson et al. (2006) plotted against its relative probability.

Finally, the data suggest that the rutiles have been crystallized mainly in amphibolite-eclogite facies and only a minority in greenschist and granulite facies. All the basins share sources with high Nb content suggesting a metapelitic-felsic nature, while JB, IB and partially BK seem to share metamafic source rocks that could derive from an ophiolitic suite. BK is poorly represented in the metamafic suite probably due the small number of crystals analyzed. These lithologies can be easily found all

together in an ophiolitic suite. Furthermore, only few rutiles with high Ta content have been recognized in BK and JB, possibly suggesting a pegmatite origin. Even though, the main groups of temperature are similar for the three basins, the difference ratio of the highest peaks suggest that the source rock are similar but located in different areas. A different path of the source supply is suggested also by the presence of the peak at 931°C only in the JB temperature distribution pattern, testifying the participation of this source only for the Julian basin.

Zircon

The Adriatic Basins have been active during the Dinaric uplift, in particular JB deposition lasted from the Maastrichtian to the Middle Paleocene, while BK, IB and ZB have been filled during the Eocene. This variance in age deposition could led to a difference in zircon age-distribution, as well as its chemistry, suggesting a multiple sources system supply. Furthermore, the basins are located in an area that covers about 600 km^2, in which there is a strong variance in lithotypes, influencing in turn the mineralogy of the sediments.

Generally, the zircon geochemistry suggests mainly a magmatic origin for the studied crystals, but hydrothermal and metamorphic signatures are also present. Their crystallization ages span from the Late Cretaceous ($^{206}Pb/^{238}U_{age}$ ZB=81±4 Ma) to the Archean ($^{207}Pb/^{207}Pb_{age}$ JB=3127±27 Ma), without the presence of Cenozoic crystals. Following the Besoulova et al. (2002) classification, most of the crystals show granitoid origin, while doleritic, basaltic, carbonatitic and syenitic-monzonitic are subordinates. Furthermore, most of the crystals show continental affinity overlapping the post-collision granitoids area, and plot in the magmatic arc array suggesting that the source could have been involved in an active and or past subductions (Grimes et al., 2015).

>750 M.y. and the Greenville Orogeny

This period of time comprehends the Greenvillle orogeny (980-1250 Ma) and the zircons that have registered older geodynamic events that now are hardly recognizable in the field. The best way to better understand the provenance of these crystals is to link them to the remnants of ancient terranes, which most of the times correspond to the cratons. The Adria plate during his "life" has always been between the Laurasia and African (or Gorndwana) continents, so it is natural to compare the zircon age obtained in this work with the literature data of these two. In particular, the most interesting terranes are those that contains cratons and could be divided in provenance provinces. The most suited assemblages for this purpose are the Laurussia, which Stephan et al. (2019 a,b) divided in Baltica and Peri-Laurentia provinces, Avalonia and West- and East African-Arabian provinces, which comprehend the northern Peri-Gondwana terranes. The zircon age spectra of the period considered is diagnostic of each of these provinces (Stephan et al., 2019a), and it is easily recognizable. The Avalonian province is characterized by the zircon supply from both West African and Amazon cratons together with Laurussia material, but only after its separation from Gondwana, while West and East African provinces are supposed to be fed by two different fans that collected the sediments only in part from the named cratons, but also from the Neo-Proterozoic orogeny that border the cratons (Stephan et al. 2019a, and reference therein).

In the studied basins Meso-, Paleo-Proterozoic and Archean zircons are present, but in different proportion. Archean is well represented only in BK, while Paleo- and Neo-Proterozoic ages are present with a significant number of crystals in all the basins, and in particular in JB and BK. On the contrary, Meso-Proterozoic ages have been rarely found, with the exception of JB, suggesting an affinity with one of the African provinces (Stephan et al., 2019a). The difference between the two regards mainly the presence of a significant number of zircon relative to the Greenville event, together with the "Sardic event" and ~800 Ma peaks. Other features that it is possible to take in consideration are the 2.5–2.7 Ga, 2.1 Ga (Eburnean) and 1.9–2.0 Ga peaks (Garfunkel, 2015; Stephan et al., 2019).

The age distribution spectra in fig. xxx show that all the samples display a distinctive peak for the Greenville orogeny, the one at ~800 Ma (JB=810, BK=850, B=868, and ZB=880) and the subordinate one at 1.9 Ga, while the Sardic event is properly registered only by JB, BK and ZB at around 460 Ma. The small peaks at 2.1 and 2.6 Ga are displayed by JB-BK and JB-BK-IB, respectively. In agreement with Stephan et al. (2019a) the siliciclastic material in the studied basins could be related to the East African-Arabian province. The small differences in peak position and their relative presence do not change the general affinity of the basins, but probably can be due to the changing of the supply pattern as well as the difference in number of zircons analyzed.

Most of the zircon relatives to this period of time show granitoid features, in particular GR70 and GR65, while GR75 crystals are present only in the Neo-Proterozoic in the Zadar Basin. Metamorphic and doleritic zircon are also present in JB and BK in Proterozoic ages, but not in the Archean, while carbonatitic affinity have been found in Paleoproterozoic in JB, BK and IB. Such old carbonatite is hard to find and recognize because old carbonatite are often characterized by recrystallization and share broad chemical similarities with metamorphosed sedimentary lithologies. However, Archean-Paleoproterozoic carbonatite complexes have been reported in South Africa (Phalaborwa Complex; Erikkson, 1984) and Algeria (In Ouzzal granulitic terrane, Western Hoggar; Ouzeghane et al., 2003). This last is considered as part of the Saharan Metacraton (e.g. Meinhold et al., 2011), which is comprised in the East African-Arabian province, strengthening the idea that the oldest part of the zircon population derives from this part of Africa. The distribution of common protoliths in most of the basin suggests the idea of a similar ancient source, which have been incorporated and reworked several times during the ages. The little differences are inferred to the change in the supply patterns probably due to the geodynamic evolution of the area.

550-750 M.y. – Cadomian Cycle and Pan African Event

Neo-Proterozoic and Early Palaeozoic times witness an important paleogeografic reconfinguration related to the Pannotia supercontinent break-up and the opening of the Iapetus and Paleo-Asian oceans (Hajná et al., 2018 and reference therein). These important tectonomagmatic events produced extensive magmatic and metamorphic basements, which are mostly covered, preventing a direct input from these. However, recycled material eroded in past ages could be a potential source for Cadomian and Pan African zircons. The two coeval cycles reflect different geodynamical environments that developed asynchronous, making possible the affinity discrimination through the study of age zircon distribution.

The Cadomian Cycle represent a series of geotecnic events that comprehend subduction, sediment accretion and arc magmatism occurred at the north-western edge of the Gondwana at the periphery of the West African Craton (Linnermann et al.,2014 and reference therein). It is generally accepted that it is the result of Andean-type subduction involving Avalonia, Armorica and Iberia terranes, and in some places continued until the Cambrian (Hajná et al., 2017). The resulting orogeny is better preserved and now outcropping mainly in the Armorican Massif, but it is possible to find it also in the Iberian and Bohemian Massifs. In these last, it is also preserved several Ediacaran basins that show zircon ages that span from the Neo-Proterozoic to the Meso-Archean, with a strong affinity with the West African Craton features (Linnermann et al, 2014).

The Pan African Cycle comprehend several not synchronous geodynamics events that register the continental collisions and amalgamation of the West and East Gondwana. The accretion of the super continent led to the formation of a series of mobile belts and orogenies that are located in Africa, South America and Australia (e.g. Rino et al., 2008). The constitution of this huge supercontinent is occurred in two main phases, the pre 600 Ma East African Orogeny and the 570-500 Ma Kuunga-Malagasy Orogeny (Vermeesh et al., 2009 and reference therein).

In the studied samples, Cryogenian and Ediacaran zircons are low in number and generally define small peaks in all the basins that most of these are composed by one or two age data. In particular, in

Cryogenian only JB show one peak at 710 Ma, while JB, IB and ZB display one at ~680 Ma and JB, BK and IB one at ~650 Ma. Similar age peaks have been found in the Hammamat Group that is considered to register the change from compressive to extensive regimes. The group consists of a sequence of immature, clastic sedimentary rocks that crops out in the central-northern part of the Eastern Desert of Egypt. The authors suggest that the peaks testify a significant volume of igneous rocks that have been actively eroded probably during the Ediacaran (Wilde & Youssef, 2002). Furthermore, Garfunkel (2015) indicate these two ages as the probable time of the two main collisions that led to the formation of West and North Africa Arabia.

In Ediacaran JB, BK and IB show a peak at ~600 Ma (Ediacaran) while only JB and IB at ~560 Ma, similarly to those registered in the northern Arabian-Nubian Shield where volcanic and sedimentary series overlie metamorphosed granites not older than 630 Ma containing clasts of older members.

The data obtained for the detrital zircons are in agreement with those found in several sedimentary lithologies located mainly in the north and north-east African territories, which testify the East-Cadomian affinity.

The chemistry of the zircons suggests a granitoid affinity and in particular GR60 and GR70, no GR75 have been found, pointing out for a common provenance for the Ediacaran and Cryogenian crystals. The data are in agreement with Wilde & Youssef (2002), which suggest large granitoid bodies as sources for the crystals with such ages.

550-390 M.y Late Pan African-Caledonian phase

During the Cambrian (late Pan-African cycle), the northern Gondwana area is characterized by a series of mini-continents separated by deep basins that received a huge sedimentary input from the south, which constituted the inner part of the continent (Avigad et al., 2003). During the formation of Pangea these microplates welded together as a consequence of the collision between Gondwana and Laurasia. This huge event led to the developing of the Variscan orogeny, which in his basement have incorporated part of the previous oceanic floors that were filled by the inner Gondwana sediments. As a consequence, the pre-Variscan basements of the territories that were part of the north Gondwana "archipelago" show Cadomian arc and North-African affinities (Schaltegger et al., 2009).

In particular, Cambrian–Ordovician meta-igneous rocks of the Central Western Carpathian basement have been dated and related to north Gondwana hinterland (Putiš et al. 2008a, 2009; Vozarova et al. 2017). The authors individuated two main magmatic phases, the first occurred between 525 and 470 Ma and a second between 480 and 440 Ma. Similarly, in the Romanian Carpathians basement orthogneiss and metagranite zircon suggest an extensional environment origin and northeastern Gondwana margin derivation (Balintoni et al., 2009).

In the Austro-Alpine, the Silvretta Nappe is presumed to date the local formation of Cambrian oceanic crust (532 Ma; Müller et al., 1996) and together with several other coeval oceanic intrusions of the Central Alps (mean age 495 Ma) are considered to have been located off the northern margin of the Gondwana (Müller et al., 1996, and reference therein). Ordovician plutonic suites have been compared by Zurbriggen (2015) observing some common features (e.g. large volumes, sheet-like concordant bodies; presence of continental xenoliths, mainly potassium dominated, peralluminuos granitic to granodioritic), suggesting that the pre-Mesozoic crust of the Alps was mainly generated in the Ordovician by the cratonization of subduction–accretion complexes and related forearc magmatism that occurred along peri-Gondwanan territories.

A possible Adria Plate basement has been found in the Venetian Region at a depth of 4711m. The observed granodiorite shows a whole rock K/Ar age of 446 ± 18 Ma and zircon concordant U/Pb ages

of 461-463 Ma, confirming the Ordovician age for the granodiorite emplacement (Meli & Sassi , 2003 and reference therein). Notably, 460 Ma is registered in many territories related to the East African-Arabian province and referred as “Sardic Phase”, which is a series of magmatic-metamorphic events (440-460 Ma) that is related to a major rifting event that is considered to have had a role in the fragmentation of the northern Gondwana. Furthermore, the rock shows an Rb/Sr isochron age of 263 ± 13 Ma that testify a reopening of the Rb/Sr system during Late Permian. The presence of small metasedimentary enclaves in the granodiorite suggest an anatectic origin, while the geochemistry indicate a volcanic-arc or (syn- to late) collisional affinity (Meli & Sassi, 2003).

However, considering Cambrian and Ordovician times a further distinction between West and East Gondwana affinities is possible. In the northern part of Gondwana, the magmatism occurred differently, in the East African-Arabian Zircon Province Ordovician pulses predominate, while two Cambrian events (525 and 500 Ma) characterize the West African Zircon Province, Late Cambrian-Early Ordovician events happened in both in Provinces (Stephan et al., 2019b).

In the studied basins**,** Cambrian and Ordovician zircon are quite scarce, in particular regarding the oldest period. Two Cambrian peaks, commons for all the basins show ~500 and ~460 Ma, while IB show two more peaks at ~470 and ~480 Ma, strenghten the idea of a East African derivation. On the contrary ZB have another small peak at 523 Ma, suggesting a mixed East-West African source. The common Cambrian peaks among all the basins are similar to the volcanic phases suggested by Vozarova et al. (2017) for the Southern Gemericum Basement, which consider the first peak developed upon the Neoproterozoic cratonic basement, while the second represents the reactivation of the Cambrian magmatic arc with possible extension and crustal melting. On the contrary, Müller et al. (1996 and reference therein) consider the Sardic Event event as the one that consumed the “Silvretta Nappe” oceanic crust through plate convergence. Taking in account that North and South Gemericum show Avalonian and West-African province affinities (Vozarova et al., 2017) and the similarities among the Cambrian peaks, it mast takes in account the Western Carpathians as possible source.

Other minor peaks have been found in IB-BK at ~429 Ma, IB-JB at ~415, and only in JB and IB one at 446 and 414 Ma respectively, which are comparable to those found in the metamorphic complexes in the Slavonian Mts. (Croatia, Tisza Unit), which show similar monazite Th/U age (444±19, 428±25 and 417 Ma; Balen et al., 2006; 2015; Horvàth et al., 2010). Notably, Middle Ordovician ages have been found also in Southern Alps where extension regime granite-rhyolite magmatism is widespread (Sassi and Spiess 1993). Furthermore, some comparable age metasediements have been found in Cima d'Asta 446 ± 13 Ma, Scisti di Edolo 459 ± 66 Ma, the Serie dei Laghi ortogneisses 446 ± 5 Ma (Zajzon et al., 2011 and reference therein).

Cambrian and Ordovician zircons show several rock affinities, but the most represented are GR70 Cambrian: IB, BK, ZB Ordovician: all), GR65 (Cambrian: JB and ZB; Ordovician: JB, BK and ZB) and MET (Cambrian: JB, IB and ZB Ordovician: JB and BK). SYE (Cambrian: BK; Ordovician ZB) crystals is also present in both the Periods, while GR75 (BK) and DOL (JB) have been found in Ordovician. In Silurian only few GR70 (all the basins) and GR65 (JB and IB) are present. The data suggest an important diversification in zircon suppliers in Cambrian and Ordovician times that support the idea that in those times magmatism-metamorphic events occurred extensively. Furthermore, this wide zircon speciation is in agreement with the idea that the inherited Middle-Europe basement could be a remnant of ancient floors that have been filled by transported Inner-Gondwanan zircons. The small number of Silurian zircons found suggest a stop of crustal accretion during the Period in the Northern Gondwana, while the Mid-German Crystalline zone (Laurussia affinity) registers island arc activity due to the initial closure of the Rheic Ocean (Kroner & Romer, 2013). GR70 and GR65 seem to be the most common zircon sources, being present in all three Periods, the first is found in almost all basins and suggest a common source, while the second is always present in JB but no in the other basins probably due to small local difference in supply-area. Early Devonian (420-390 Ma) zircon are mainly present in IB, BK and ZB, generally showing granitoids affinity. However, JB zircons are also present, in particular only as GR65 and GR70.

390- 250 Ma- Variscan

The Variscan orogeny is the result of the Gondwana-Laurasia collision during Late Paleozoic, the cycle started with the opening of the Palaeotethys and lasted until the end of Carboniferous (Spiess et al., 2010). Nowadays Variscan crust mainly crops out in central and western Europe as well as in north-western Africa (e.g. Algeria and Morocco). Furthermore, younger orogeny such as Alps, Carpathians, Balkanides and Hellenides have locally overprinted and inherited parts of Variscan crust that records the past influences (Kroner & Romer, 2013 and references therein).

Following Kroner & Romer (2013) the Variscan cycle is composed by three sequential events dated ~390, ~360 and ~340 Ma, interpreted as three different subduction zones. While, Spiess et al. (2010) suggest that the first collision between Galatian and Hanseatic terranes (ribbon-like continents detached from Gondwana and Laurussia, respectively) occurred diachronously from 350 Ma (Silvretta eclogites and Ötzal basement) to ~330 Ma (high pressure association of Ulten area). This is in agreement with the observation of Stephan et al. (2019b) which consider the start of the East African-Arabian zircon province Variscan Cycle not before the Late Devonian.

The northeastern Adria basins detrital zircon register the first subductive event at ~390 Ma suggested by Kromer & Romer (2013), while IB (368 Ma) and BK-JB (333 and 332 Ma) show zircon age peaks comparable with the second and third phases, respectively.

Early Devonian peak showed by IB-BK-ZB at ~390 Ma could be related to the final closure of Rheic and Paleotethys that have been registered in NW-Iberia and in the Eo-Variscan event in the Carpathians (Haas et al., 2020 and reference therein). The authors observed this peak in the Silbersberg Fm and has been associated with one at ~511 Ma (present in our samples also). These two are absent in Alps, but present in Veporicum Fm., suggesting a Carpathian affinity (Haas et al., 2020).

Ages similar to the second and third phase are shown by the granitoids that crop out in the Outer Western Carpathians (353-356 Ma; Buda et al., 2004), Mecsek Mts. (Hungary; 354 ± 5 and 339 ± 10 Ma; Klötzli et al., 2004) in the southern Tisza-plate and in the South Bohemian granodiorite (Klötzli & Parrish, 1996; Buda, 2004). Furthermore, the last the authors found also inherited zircons that belonged to the Pan-African cycle (623 ± 22 Ma) suggesting the incorporation of old Cadomian crust and point out an age of ~353 Ma for the first lower-crustal magma-forming event and an age comparable to the third Variscan phase of 338 ± 2 Ma for the intrusion of the pluton (Klötzli & Parrish, 1996).

However, JB shows also a minor peak at 346 Ma, which is comparable to the second subductive phase but not directly related. West Carpathians S-type granites are largely widespread in Slovakia and Hungary and show comparable intrusion ages, zircon U-Pb datings point out ages between 345 ± 11 (Veporic Unit, Klàlova Hola type; Gaab et al., 2005). Furthermore, Burda et al. (2013) suggest a prolonged granite crystallization for the High Tatre complex that lasted between 350 and 337 Ma, with a maximum at about 345 Ma. Regarding the Central Alps, in the Tauern window the oldest sequence of lavas and tuffs have been date, showing ages of ~343 ± 6 Ma (Eichorn et al., 2000).

A second magmatic pulse, from felsic to intermediate explosive is characterized by the presence of lavas, tuff and tufites intercalated with basic products and dated 300 ± 5 Ma (Eichorn et al., 2000). This last is slightly younger than the peak of JB, BKB and IB found at ~310 Ma, which is comprised to the age of I-type suite intrusion in inner Western Carpathians (303-314 Ma; Buda et al., 2004). Granodioritic-tonalitic rocks are characterized by intrusion ages that span from 303 ±2 (Sihla tonalite; Bibikova et al., 1990) to 314 ± 4 (High Tatra tonalite; Poller & Todt 2000).

All the basins show peaks at ~280 M.y. which correspond to tan important volcanic activity in the Southern Alps (Berra et al., 2015). In particular, the Serie dei Laghi show a crystallization age that span from 276 ± 8 to 277 ± 7 Ma, the Athesian Volcanic Group formed in a span of about 10 Ma from ~275 to ~285 Ma (Shaltegger & Brack, 2007; Marocchi et al., 2008 and reference therein) and

andesite in the Dolomites with ages of 290 ± 3 and 279 ± 3 Ma (Visonà et al., 2007). The Southalpine magmatism emplacement may be related to an extensional tectonic phase. This have been associated to post-collisional collapse of the Variscides, strike-slip movements occurred along the southern limit of this orogeny or the hypothetical Permian transformation from Pangea-B to Pangea-A (Shaltegger & Brack, 2007 and reference therein). These could be considered the first trastensional movements of the Periadriatic Line that will be reactivated several times in the Successive Periods (e.g. Triassic). In Austroalpine, these Early Permian magmatisms are coeval to the third magmatic pulse recognize in the Tauern window by Eichorn et al. (2000), which is composed by felsic tuffs emplaced at 279 ± 7 Ma. In Central Western Carpathian Zone, the fine microaplitic Hrončok Granite show a U/Pb zircon age of 278 ± 1, while along the Balaton Line felsic magma intruded the Variscan basement, forming granite, granodiorite and quartz diorite (Velence Mts. zircon U/Pb age 274±1.7; Buda et al., 2004). In the Tisza Terrane Gyűrűfű Rhyolite is a rather monotonous complex of lava flow alternating with ignimbrites, which whole rock Rb-Sr age is 277±45 Ma (Balogh & Kovách 1973).

Julian Basin Late Permian peak show an age at ~264 M.y., similar to the age of acid volcanic rocks fount in the Central-Western Carpathians. In particular, for the Infratatric Inovec Nappe the U/Pb SIMS zircon analyses indicate a crystallization age that spans from 267 to 262 M.y. (Putiš et al., 2016), which is compatible with Turčok (262 ± 4 M.y.), Hrončok: (267 ± 2 M.y.) and Upohlav (264 ± 3 M.y.) granites (Uher et al., 2010). Similarly, in the Pannonian Basin zircon U/Pb analyses gave slightly younger ages for the Battonya–Pusztaföldvár volcanics (~260 Ma), and coeval ones for Transdanubia and Kelebia areas (267–264 Ma; Szemerédi et al., 2019). Notably, Permian siliciclastic rocks are missing in the neighbouring Tatric pre-Mesozoic basement (West Carpathians), including the overlying north-Tatric Panská Javorina Nappe in the Považský Inovec Mountains (Putiš et al., 2016).

Devonian zircons are well represented in BK and IB while ZB and JB count few crystals.These have been crystallized for the major part in granitoids, in particular zircon from all the basin show GR70

affinities while GR65 and GR 75 are present in JB-BK-IB and BK-ZB, respectively. One doleritic crystal can be found onluy in BK. Carboniferous zircons are present in JB-BK-IB in which GR65 and GR70 are the most representatitive compositions, while SYE is shown only by BK and DOL cystal by JB. Pemian crystals are present in all the basins and GR70 zircons are the most abundant. DOL zircons are represented in JB-BK- IB and GR65 by JB-BK. Only BK have GR75 and SYE crystals, while ZB show MET zircon.

250-80 M.y. Mesozoic-Dinaric Cycle

In Triassic times Julian basin show three close peaks with ages of 232, 220, 210 Ma, while BK, IB and ZB show only one peak at 231, 246 and 241 Ma, respectively. In the Northern Adria Plate two main Triassic magmatism have been reported, the first occurred around 235 Ma and a second at ~220 Ma.. These events take part mainly near the Periadriactic/Balaton line and together with a Permian one (cited in the previous chapter) coul be related to the first transtensional events that led to the break-up of the Pangea (De Min et al., in review). The two volcanic moments are widely reported in literature and comprehend felsic and mafic volcanics, in the Bükk Mts. (Downes et al., 1990; Haas et al., 2000), in the Velence Mts. (Benkò, 2008 and reference therein) Transdanubian Range (Dunkl et al., 2019), Dinarides (Neubauer et al., 2014; Pamić, 1984), Karawanke Mts. (Eisenkappel; Dunkl et al., 2019), Dolomites (De Min et al., in review), Southern-Western Alps (Cassinis et al., 2008; Zanetti et al., 2013).

Particular interesting ages and possible supply-areas are represented by the Eisenkappel granitic intrusion (234.1 ± 2.5 and $231.2 + 5.8 - 2.2$ Ma; Dunkl et al., 2019), the volcanoclastic-volcanic formations of Bakony Mts. and Buda Hills (229±1 and 238±1 Ma; Dunkl et al., 2019), Szabadbattyán andesite vein (210±4 Ma; Bagdaszarjan, 1989; 213±13 Ma, Balogh et al., 1973; 214±49 Ma), the andesitic plutons of Gorski Kotar (~242 Ma; Palinkaš et al 2010) and Fužine (233.7±1.5; Neubauer et al., 2014).

Triassic Period is represented by the most number of different zircon hostrock affinities, which in any case are all magmatic. The major part of the crystals show granitoids features, in particular all the basin show GR65 zircons, while IB-BK GR70 and GR65 compositions are present too. CARB, SYE and DOL affinities are present only in the BK zircons, while in JB one BAS crystal is present as well. The chemistry of the zircon suggest that BK sources are the most diversified, receiving crystals with several different magmatic affinities, most of these are shared by IB, suggesting similar supply areas for the two. Furthermore, JB show an enigmatic and intriguing “carbonatitic” zircon, because no

Triassic carbonatites is known in the possible provenance areas. However, this kind of magmatic rocks are often related with lamprophyres and alkaline-basalts, litologies that have been found both in S. Alps, NW Dinarides and Tisza Plate.

JB is the only basin where a Jurassic crystal is represented (180 Ma).. Middle Jurassic felsic rocks are quite rare in the Perimediterranean and Central Europe regions, generally plutonic and volcanic occurrences are related to the ophiolitic obduction in Dinarides, Carphatians and Rhodopes and dated between 165 to 140 Ma. However, some Early Jurassic granitoids show ages comparable to that found in JB, in particular Malé Karpaty Mountains in Western Carpathians (Slovakia) show concordant ages of 177 ± 2 Ma, while metarhyolite show a K-Ar age of 187 ± 52 Ma. (Igal basement, central Hungary; Arkài et al., 1991) and Rubiku granite a zircon age of 169 ± 2 (Central Albania; Kryza & Beqiraj; 2014), that could be related to a still poorly known Paleo-Alpine thermal event (Kohút et al., 2009). Mikes et al. (2009) found a similar peak in the Late Cretaceous Vranduk Fm. (Bosnian Flysch), but it partially overlap the population that form a larger one at 152 M.y. deriving from the near Dinaric Ophiolites. The authors suggest that from Early to Late Jurassic coeval anatectic and mantle-derived production of melts occurred during the intra-oceanic subduction of the Neotethys occurred in the Dinarides.

The Jurassic zircon shows a doleritic affinity, that have been found in the Kalnik mountains (185 ± 6 and 189 ±7; Pamič et al., 2002 and reference therein) and the Jurassic Szarvasko complex in the Bükk Mts. (Downes et al., 1990).

Late Cretaceous is indicated by several authors as the time where continent-continent collision Adria and Tisza-Dacia occurred with the consequent closing of the Sava remnant ocean (e.g. Ustaszweski et al., 2010; Balen et al., 2017; Schneider et al., 2019). Cretaceous zircons are present in BKB, IB and ZB, but no in JB, suggesting two different zircon sources. The three basins show age peaks at 87 M.y. (BKB), 98 M.y. (IB) and 82 M.y. (ZB).

Rhyolite pebbles found at the base of Santonian-Campanian- Maastrichtian geological column have been dated using La-ICPMS analyses on zircon and give ages between 88 ± 2 to 86 ±1 M.y. (Balen et al., 2017). These could be related to red colored hematite-bearing granite from Mt. Požeška Gora and albite rhyolite from Rupnica that gives crystallization temperatures between 840−950°C, showing characteristics of post-orogenic rocks and similar ages (~82 Ma for the Rupnica rhyolite and ~86 Ma for the Mt. Požeška Gora granite; Schneider et al., 2019). These acidic rocks have been related to a local transition from compression to extension occurred in the Sava zone, indicated as Europe-Adria suture zone (Balen et al., 2017; Schneider et al., 2019). In the Central Alps the magmatic protolith on an amphibolite shows ~93 Ma and is related to the Valais oceanic domain (Liati et al., 2003). Late cretaceous dolerite have been found in North-Kozara (Hungary; Ustaszewski et al., 2010) and Medvednica Mts. (Pamič et al., 2002 and reference therein) as part of ophiolitic bodies.

However, another possible source of Mesozoic zircon could be the old protolith of the Pohorje eclogitic-gneisses. In fact this Miocenic metamorphic complex show zircons with rims age between 86±2 and 92±1 M.a, while the cores between 238±3 and 286±10 (Janák et al., 2009). However, their Th/U ratio is generally minor than 0.01 for both these ages. Such low ratio testifies their metamorphic affinity, contrasting with the data obtained for the here studied zircons.

The chemistry of the Cretaceous zircon do not show any particular correlation among the basins. In fact syenitic crystals are found in BK-ZB, doleritic in ZB-IB, GR65 in BK-IN and GR75 only in BK, suggesting that the crystlas could derive from areas with rather coeval felsic-intermediate magmatism or a single area with rocks differently evolved.

Geochronological Comparisons

It is interesting to compare the detrital zircon geochronology with coeval sedimentary basin located in the Dinarides. In particular, the coeval Bosnian Flysch basin has been often suggested to compose a single big trough with JB. Detrital zircon of the coeval Ugar (Fig. 35 B, D, F, H) and slightly older Vranduk formations (Bosnian flysch basin; Serbia) have been studied by Mikes et al. (2008; 2009) and compared with the Dinaride Ophiolitic Zone mèlange (DOZ). The data of the Vranduk Frm. displayed in the age distribution pattern (Mikes et al., 2009) suggest an important Jurassic and Triassic input. The first is represented by two peaks, the main at 152 ± 10 and a secondary at 185 ± 15 Ma, while the second is composed by a single important peak at 244 ± 15 Ma. Similarly, the Ugar formation do not show any Cretaceous zircon (Fig. 35 B, D, F, H), while differ from the first because of the presence of one small Jurassic peak at ~165 Ma and two Triassic ones, placed at ~215 and ~235 Ma (Mikes et al., 2008). Among the studied basins only JB hold one comparable Jurassic peak (180 ± 3 Ma; composed by a single zircon data) with the Vranduk Fm. while Triassic data sensibily differ. On the contrary, JB and Ugar Fm. do not show similarities between Jurassic population, but share common Triassic. BK, IB and ZB show Cretaceous peaks (not present in the Bosnian Flysch and JB) but no Jurassic ones. Furthermore, BK share a common Triassic population with JB and Ugar Fm., while IB and ZB are more like the Vranduk one.

Finally, as evidenced by the data, it is possible to suggest that the northeastern Adria and Bosnian Flysch Basins do not formed a single wide body, but rather they were two separated basins, which have been supplied with similar material that come from different areas.

Unfortunately, in literature other works focusing on Late Cretaceous- Eocene flysch formations in neighbouring areas present only zircon fission track data (e.g. Spiegel et al., 2000; Dunkl et al., 2009; Lužar Obeiter et al., 2012) and no direct comparison could be made.

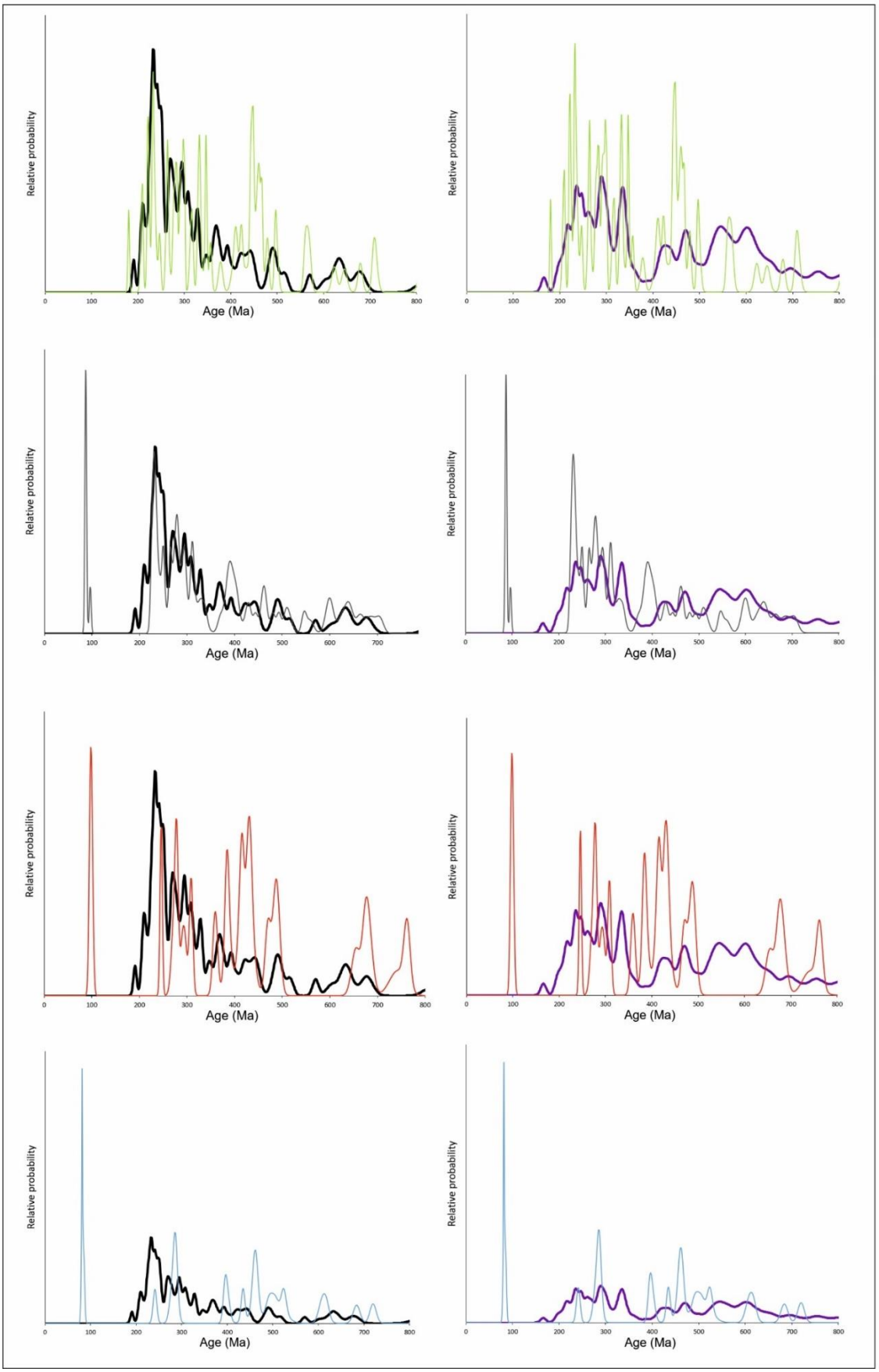

Fig. 35. In the left column (A, C, E and G) the comparisons among the DOZ (Mikes et al., 2008; black line) and the studied basins (A=JB vs DOZ, C= BK vs DOZ, E=IB vs DOZ and G=ZB vs DOZ). The right column shows the comparisons among the studied basins and the Ugar Formation (Mikes et al., 2008; purple line; B=JB vs Ugar frm., D= BK vs Ugar frm., F=IB vs Ugar frm. and H=ZB vs Ugar frm.).

Possible Provenances

Previous studies on the heavy minerals of these basins (e.g. Lenaz et al., 2001; 2003; 2008) suggest that the source of the siliciclastic sediment, mainly composed by metasediments, granitoids, amphibolites and high grade metabasites, probably are located in the outer and inner Dinarides. However, in this work it has taken in consideration also the Southernalps, Austroalpine, Slavonian Mts., Transdanubian and Carpathian areas.

The garnets studied in JB-BK-IB show similar B-/C- type population ratio but slightly different Bi vs Bii distribution. JB and IB show a little preference for Bi-type crystals in comparison with Bii ones, while BK show a strong preference for the first. The two populations could be derived from granitoids metasediments, if they fall entirely in the Bi field, or amphibolite-facies metasediements (Bii). The third largest population show metamorphic affinity, while small number of garnets formed in high grade granulite-facies metasediments, charnokites or intermediate-acidic igneous rocks, metasomatic rocks, very low grade metabasic rocks, or from ultrahigh temperature metamorphosed calc-silicate granulites. The trace elements indicate for Bi- and Bii-types both feldspar-bearing and feldspar free protoliths, furthermore that Bi-type suffered prograde and retrograde metamorphic events.

The rutile chemistry partially agrees, showing that the crystals mainly derive by metapelites (or felsic protoliths) that underwent amphibolitic-facies like metamorphic conditions (crystallization temperature between 500-650 °C). However, the studied basins show differences that regards the rutile-protoliths, in particular JB show more metamorphic-like crystals than IB (and BK), but not significant differences in crystallization temperatures. These could suggest that the crystals have been formed in one main large event that acted incorporating several kind of lithotypes with different affinities, or that the rutiles crystallized in two similar metamorphic events (at least) that occurred in different areas. Otherwise, part of the population could be derived from an older siliciclastic sediment, so it may be occurred similar metamorphic events in different times. Furthermore, the Nb-Ta-Zr ternary diagram points out that possible rutiles sources are composed by micaschist, quartzites and

amphibolites that undergo prograde and retrograde metamorphism, as well as metabasalts, metagabbros, granulite, gabbros and pegmatite (Fig. 33).

Many of the cited lithologies could be present in ophiolitic mélanges, for this reason ophiolites could be a probable source for garnet and rutile. A second option is that the crystals could derive by an older reworked sedimentary unit which have been eroded during the uplift of the Dinarides.

In the Central Europe and Mediterranean Region there are several ophiolitic bodies that testify the intense geodynamic evolution of the area. Ophiolitic suites are scarcely present in Western Carpathians (e.g.Ivan & Méres, 2012; Faryad et al., 2005; Mikuš & Spišiak, 2007) and Alps (e.g. Missoni & Gawlich, 2011; Giobbi-Mancini et al., 2003; Rubatto et al., 1998; Liati et al., 2005), while are much more abundant in the Dinarides, in which two main members compose the Dinaride Ophiolite Zone (DOZ) and the Vardar Zone sensu lato (VZ; Mikes et al., 2008; Pamic et al., 2002; Saccani et al., 2011).

The DOZ is dated Jurassic-Early Cretaceous age, it is mainly composed by shaly-silty matrix embedding fragments of several kind of rocks (i.e. gabbro, diabase, basalts and litharenites) that could be locally different and by areas in which the normal undisturbed ophiolite sequence is preserved. The mineral assemblage, the chemistry of the rutile-garnet-zircon-spinel litharenites are similar to those of the studied basins. On the contrary the DOZ and northeaster Adria Flysch basins zircon age patterns differ, JB show a Jurassic peak younger than the DOZ one, while BK-IB-ZB show no Jurassic data, but Cretaceous crystals are present (Mikes et al., 2008; Fig. 35 A, C, E, G).

Considering the differences among the studied basins, it is possible to suggest that these shares only part of the sources, and that there must be a change of supply material and area between the Maastrichtian to the Eocene. In agreement with previuos studies conducted by Lenaz et al., (e.g. 2000, 20003, 2005, 2008 and 2018) and Lenaz & Princivalle (2002) the founding of pigeonites only in Late Eocenic strata could suggest that this change could have been occurred during the Middle Eocene. However, the garnet B-/C- type population ratio and the general crystallization temperature of rutile do not change, supporting the idea that the main kind of source should have been remained the same.

The mafic minerals present in all the basins have mainly ophiolitic affinities and the zircon geochronology show good similarities with the DOZ mélange (Fig. 35A, C, E, G; studied by Mikes et al. 2008), supporting the fact that a possible supplier could be this branch of ophiolites. However, the rare Jurassic zircons found in the studied basins, as well as in the DOZ, shows different age of crystallization. The zircon found in JB is Toarcian, while the DOZ (Mikes et al., 2008) shows Sinemurian age, implying that the Dinaric ophiolite sources of the basins must be partly different. BK, IB and ZB do not show Jurassic crystals but Cretaceous ones (Fig. 35A, C, E, G), suggesting that the DOZ could not be the supplier of the younger basins neither. However, recently, the Kalnik Unit ophilite (Croatia) has been considered as the remnant of an oceanic realm called Repno Ocean (Slovenec et al., 2010) that lasted from the Early Ladinian to the Midle Cretaceous. Taking in account that the starting of the oceanic closure started during the Middle Jurassic (Slovenec et al., 2010), it appears that the geodynamic evolution of the ophiolites are quite similar to those of the DOZ. Thus, in according to several authors (e.g. Schmid et al., 2008; Ustaszweski et al., 2010) it is possible to consider these mélanges related to the closure of the Vardar Ocean and put inserted in the Western Vardar Ophiolitic Unit. Jurassic dolerites have been found in the Jurassic Szarvasko complex in the Bükk Mts. (Downes et al., 1990) and in Kalnik mountains (185 ± 6 and 189 ±7; Pamič et al., 2002 and reference therein), showing a good agreement with the Jurassic zircon age found in JB.

A study conducted by Ustaszewski et al. (2009) pointed out that Adria, Tisza and Dacia Mega-Unit were small independent micro-plates unitll the Early-Maastrichtian and only during the latest Cretaceous the final collision occurred. During the subduction of the Dinarides underneath the Tisza-Dacia Mega Unit a bimodal continental-arc magmatism formed, now located in the Sava zone. These have been dated from rhyolite pebbles fould at the base of Santonian-Campanian- Maastrichtian geological column (88 ± 2 to 86 ±1 M.y.; Balen et al., 2017), Rupnica rhyolite (~82 Ma for the Rupnica rhyolite and ~86 Ma for the Mt. Požeška Gora granite; Schneider et al., 2019) and Late Cretaceous dolerite have been found in North-Kozara (Hungary; Ustaszewski et al., 2010), Medvednica Mts. (Pamič et al., 2002 and reference therein) and Ivanščica Mts. as part of ophiolittic

bodies (Lugović et al., 2015). These appear quite coeherent with the Cretaceous zircon found in BK, IB and ZB.

Finally, the data support an ophiolitic provenance of the siliciclastic detritus of the flysch basins. The mineralogy and geochronological data of JB support the idea that the Western Vardar Ophiolitic Unit is the main supplier, and that the detritus could derive by the northwesternmost branch of the Vardar Ocean (Repno Domain) located in the Kalnik Mts. area (Internal Dinarides, Croatia). Zircon age data suggest a change in the supply catchment-system that have occurred during the Middle Eocene. The new source of detritus could be located in the Sava Zone, where extended Cretaceous bimodal magmatism occurred during the subduction of the Dinarides underneath the Tisza-Dacia Mega Unit (Ustaszweski et al., 2010) and extended ophiolites crops out.

Conclusions

In this work garnet, rutile and zircon chemistry together with zircon geochronology of the Late Cretaceous-Eocene basins located at the northeastern part of Adria plate have been investigated. The basins are supposed to have been formed during the uplift of the Dinarides and filled with the material formed during their erosion. The conclusions can be reassumed in several points:

1. Detrital garnets generally show a higher B-type affinity and secondary a C-type one, suggesting a derivation from sources amphibolitic facies and granitoid metasediments and subordinate metamafic rocks.
2. Constant B-/C- type population ratio suggests that the detritus source remained similar from the Maastrichtian to the Late Eocene and that local differences are minimal.
3. Garnets REE suggest that Bi- and Bii-type are formed by both feldspar-bearing and feldspar-free protoliths, while only Bi points out both prograde and retrograde features.
4. Detrital rutile geochemistry have differences among the basins. In JB crystal populations with metamafic and metapelitic affinity are similar (45% and 55%, respectively), while BK and IB rutiles show 100% and 89% metapelitic features, suggesting a difference in source among the JB and BK-IB.
5. The Zr-in-rutile geothermometer suggested by Watson et al. (2006), resulted more reliable for provenance studies than the one by Zack et al. (2004).
6. Most of the rutiles in JB, BK and IB show amphibolite-eclogite facies crystallization temperatures of (80%, 93%, and 80%, respectively). The basins show a broad similarity with the temperature obtained for the DOZ formation rutiles, while a detailed approach show that the peaks of JB and IB built with isoplot differ, suggesting a slightly different source catchment-system.
7. The here suggested Zr-Nb-Ta ternary diagram classified efficaciously the rutiles, suggesting that the primary source of the metapelitic (felsic) affinity crystals are felsic micaschist and quartzites and secondary amphibolites, while the metamorphic (metamafic) ones show mafic

amphibolites, metagabbro and metabasalt features. Few crystals derive from gabbro and pegmatites.

8. The zircon chemistry showed that GR65 is its main source, followed by GR70 and GR75. Secondly are metamorphic, monzonitic-syenitic and doleritic showing similar populations, and rare carbonatitic and basaltic crystals occur.
9. The chemical diagrams testify that more than 95 % of the total magmatic crystals show Continental affinities (Grimes et al., 2015).
10. In-situ zircon U/Pb geochronology show a common East African-Arabian affinity for the oldest population of the basin, while the Mesozoic peaks show a difference in supply among the Maastrichtian basin JB (no Cretaceous but Jurassic crystals) and the Eocenic BK, IB and ZB (Cretaceous but no Jurassic zircon). These differences support the idea that during the Middle Eocene a change in the catchment supply sytem occurred, and that the JB recycled material is not the source of the younger BK, IB and ZB.
11. In-situ zircon U/Pb geochronologic data support the idea that coeval Julian and Bosnian flysch basins were separated during the Maastrichtian.
12. Broad similarities in the age distribution pattern among the studied basins and the DOZ suggest that part of the siliciclastic detritus could derive by the same ophiolitic formation located in a northwestern area. In particular, the presence of Jurassic dolerites within the Kalnik Mts. area that show comparable age with JB data support this idea. Regarding the Cretaceous zircon, the most probable area resides in the Sava zone (e.g. Pozeska Gora).

References

Albarello D. Mantovani E. Babbucci D. Tamburelli C., 1995. Africa-Eurasia kinematics: main constraints and uncertainties, Tectonophysics , 243, 25–36.

Anderson, H. and Jackson, J., 1987. Active tectonics of the Adriatic Region. Geophysical Journal of the Royal Astronomical Society, 91, 937-983.

Árkai, P., Lantai, C., Fórizs, I., and Lelkes-Felvári, G., 1991. Diagenesis and low-temperature metamorphism in a tectonic link between the Dinarides and the Western Carpathians: the basement of the Igal (Central Hungarian) Unit. Acta Geologica Hungarica, 34, 81–100.

Aubouin, J., 1973. Des tectoniques superposées et de leur signification par rapport aux modèles géophysiques: l'exemple des Dinarides; paléotectonique, tectonique, tarditectonique, néotectonique (In French). Bullettin de la Société Géologique de France, 15, 426-460.

Avigad, D., Kolodner, K., McWilliams, M., Persing, H and Weissbrod, T, 2003. Origin of northern Gondwana Cambrian sandstone revealed by detrital zircon SHRIMP dating. Geology, 31, 227-230.

Babić, L. and Zupanič, J., 1976. Sediments and paleogeography of the globotruncana calcarata zone (upper cretaceous) in banija and kordun, central Croatia. Geoloski Vjesn., 29, 49-73.

Babić, L. and Zupanič, J., 1996. Coastal Dinaric Flysch Belt: Paleotransport model for the Pazin Basin and the role of a foreland uplift. Natura Croatica, 5, 317-327.

Babić, L. and Zupanič, J., 2008. Evolution of a river-fed foreland basin fill: the North Dalmatian Flysch revisited (Eocene, Outer Dinarides). Natura Croatica, 17, 357-374.

Babić, L., Hernitz Kučenjak, M., Ćorić, S. and Zupanić, J., 2007. The Middle Eocene age of the supposed Late Oligocene sediments in the flysch of the Pazin basin (Istria, Outer Dinarides). Natura Croatica, 16, 83-103.

Bagdaszarjan, G. P., 1989. Velencei-hegységi minták radiometrikus koradatai. — Kézirat, Magyar Állami Földtani Intézet.

Balen, D., Horváth, P., Tomljenović, B., Finger, F., Humer B., Pamić, J. and Árkai, P., 2006. A record of pre-Variscan Barrovian regional metamorphism in the eastern part of the Slavonian Mountains (NE Croatia). Mineralogy and Petrology, 87, 143-162.

Balen, D., Massonne, H. J. and Petrineca, Z., 2015. Collision-related Early Paleozoic evolution of a crustal fragment from the northern Gondwana margin (Slavonian Mountains, Tisia Mega-Unit, Croatia): Reconstruction of the P–T path, timing and paleotectonic implications. Lithos, 232, 211-228.

Balen, D., Schneider, P., Massone, H.-J., Opitz, J., Putiš, M., Luptàkovà, J. and Petrinec, Z., 2017. Zircon grains in A-type granite and their inclusions as recorder of upper mantle conditions in the Croatian segment of the Late Cretaceous collisional zone between Europe and Adria. In: Book of abstracts, (Eds.: Nasdala, L.,Broska, I. & Novák. M.). CAM-2017, Conference on Accessory Minerals, Beĉ.

Balintoni, I., Balica, C., Ducea, M. N., Chen, F., Hann, H. P. and Şabliovschi, V., 2009. Late Cambrian–Early Ordovician Gondwanan terranes in the Romanian Carpathians: A zircon U–Pb provenance study. Gondwana Research, 16, 119-133.

Balogh, K., Colantoni, P., Guerrera, F., Majer, V., Ravasz-Baranyai, L., Renzulli, A., Veneri, F. and Alberini, C., 1994. The medium-grained gabbro of the Jabuka Islet ("Scoglio del Pomo", Adriatic Sea). Giornale di Geologia, ser. 3a, 56/2, 13–25, Bologna.

Balogh, Kad. & Kovach, Á. 1973. Determination of the Battonya quartz porphyries age by Rb/Sr method. ATOMKI Közl. 15, 4, 245—249 (in Hungarian, English summary).ù

Battaglia M., Murray M. H., Serpelloni E. and Bürgmann R., 2004. The Adriatic region: An independent microplate within the Africa-Eurasia collision zone. Geophysical Research Letters, 31, p. L09605.

Belousova, E. A., Griffin, W. L., O'Reilly, S. Y. and Fisher, N. I., 2002. Igneous zircon: trace element composition as an indicator of source rock type. Contributions to Mineralogy and Petrology, 143, 602–622.

Benac, Č., Juračić, M., Matičec, D., Ružić, I. and Pikelj, K., 2013. Fluviokarst and classical karst: Examples from the Dinarics (Krk Island, Northern Adriatic, Croatia). Geomorphology, 184, 64-73.

Benkò, Z., 2008. Reconstruction of Multi-Phase fluid flow history and tectonic evolution in a Variscan Ggranite intrusion (Velence Mts., Hungary). Ph. D Thesis.

Bernardini F., De Min A., Demarchi G., Montagnari Kokelj E., Velušček A. and Komšo D., 2009. Shaft-hole axes from Slovenia and northwestern Croatia: a first archaeometric study on artefacts manufactured from meta-dolerites. Archaeometry, 51, 894-912.

Berra, F., Tiepolo, M., Caironi, V. and Siletto, G. B., 2015. U–Pb zircon geochronology of volcanic deposits from the Permian basin of the Orobic Alps (Southern Alps, Lombardy): chronostratigraphic and geological implications. Geological Magazine, 152, 429-443.

Bibikova, E.V., Korikovsky, S.P., Putiš, M., Broska, I., Goltzman, Y.V. and Arakeljants, M.M., 1990. U-Pb, Rb-Sr and K-Ar dating of Sihla tonalites of the Vepor pluton (Western Carpathians Mts.). Geologica Carpathica, 41, 427–436.

Bonazzi, A., Catani, G., Tunis, G., 1996. Clay mineral assemblages of the eastern Southern Alps flysch units (NE Italy, SW Slovenia, W Croatia). Memorie Società Geologica Italiana, 51, 929-947 (In Italian).

Bortolotti, V. and Principi, G., 2005. Tethyan ophiolites and Pangea break-up. The Island Arc, 14, 442-470.

Boynton, W.V., 1984. Geochemistry of the rare earth elements: meteorite studies. Red. P. Henderson, Elsevier.

Bracciali, L., Parrish, R. R., Horstwood, M. S. A., Condon, D. J. and Najman, Y., 2013. U-Pb La-(MC)-ICP-MS dating of rutile: New reference materials and applications to sedimentary provenance. Chemical Geology, 347, 82-101.

Brenan, J.M., Shaw, H.F., Phinney, D.L. and Ryerson, F.J., 1994. Rutile–aqueous fluid partitioning of Nb, Ta, Hf, Zr, U and Th: implications for high field strength element depletions in island-arc basalts. Earth Planetary Science Letters, 128, 327-339.

Buda, G., Koller F. and Ulrych, J., 2004. Petrochemistry of Variscan granitoids of Central Europe: Correlation of Variscan granitoids of the Tisia and Pelsonia Terranes with granitoids of the Moldanubicum, Western Carpathian and Southern Alps. A review: Part I. Acta Geologica Hungarica, 47, 117–138.

Burda, J., Gaweda, A. and Klötzly, U., 2013. Geochronology and petrogenesis of granitoid rocks from the Goryczkowa Unit, Tatra Mountains (Central Western Carpathians). Geologica Carpathica, 64, 419-435.

Bušer, S., 1987. Development of the Dinaric and the Julian carbonate platforms and the intermediate Slovenian basin (NW Yugoslavia). Memorie della Società Geologica Italiana, 40, 313-320.

Carminati, E. and Doglioni, C., 2012. Alps vs. Apennines: the paradigm of a tectonically asymmetric Earth. Earth-Science Reviews, 112, 67-96.

Cassinis, G., Ronchi, A., Gretter, N., and Durand, M., 2008. The Val Daone Conglomerate: a Middle Permian key unit from the Central Southern Alps (western Trentino, Italy), and regional stratigraphic implications. Bollettino della Società Geologica Italiana, 127, 519-532.

Cave, B. J., Stepanov, S., Craw, D., Large, R. R., Halpin, J. A. and Thompson, J., 2015. Release of trace elements through the sub-greenschist facies breakdown of detrital rutile to metamorphic titanite in the Otago Schist, New Zealand. The Canadian Mineralogist, 53, 379-400.

Channell J.E.T., D'Argenio B. and Horvath F. 1979. Adria, the African promontory in Mesozoic Mediterranean paleogeography. Earth Science Reviews 15, 213–292.

Channell, J.E.T. and Horváth, F., 1976. The African/Adriatic promontory as a paleogeographical premise for Alpine orogeny and plate movements in the Carpatho-Balkan region. Tectonophysics, 35, 71-101.

Channell, J.E.T., 1992. Paleomagnetic data from Umbria (Italy): implications for the rotation of Adria and Mesozoic apparent polar wander paths. Tectonophysics, 216, 365-378.

Cousin, M., 1972. Ésquisse géologique des confins italo-yougoslaves; leur place dans les Dinarides et les Alpes méridionales (In French). Bullettin de la Société Géologique de France, 12, 1034-1047.

Csontos, L. and Vörös, A., 2004. Mesozoic plate tectonic reconstruction of the Carpathian region. Palaeogeography, Palaeoclimatology, Palaeoecology, 210, 1-56.

De Min, A., Rosset, A., Tunis, G., Tosone, A., Kocmann, C. and Lenaz, D., 2007. Igneous rock clasts from the Bovec Maastrichtian flysch (Slovenia): petrology and geodynamic aspects. Geologica Carpathica, 58, 169-179.

De Min, A., Princivalle, F. and Lenaz, D., 2014. Geochemistry of the Late Mesozoic - Early Cenozoic turbidites from the NE part of the Adria microplate. Periodico di mineralogia, 83, 141-158.

De Min, A., Velicogna, M., Ziberna, L., Marzoli, A., Chiaradia, M. and Alberti, A. in review. Triassic Magmatism in Southern Alps as an Early Phase of Pangea Break-up. Submitted to Geological Magazine.

Dercourt, J., Zonenshain, L.P., Ricou, L.E., Kazmin, V.G., Le Pichon, X., Knipper, A.L., Grandjacquet, C., Sbortshikov, I.M., Geyssant, J., Lepvrier, C., Pechersky, D.H., Boulin, J., Sibuet, J.-C., Savostin, L.A., Sorokhtin, O., Westphal, M., Bazhenov, M.L., Lauer, J.P. & Biju-Duval, B., 1986. Geological evolution of the Tethys belt from the Atlantic to the Pamirs since the Lias. Tectonophysics, 123: 241-315.

Downes, H., Árkai, G. and Thirlwall, M. F., 1990. Petrology and geochemistry of Mesozoic igneous rocks, Bükk Mountains, Hungary. Lithos, 24, 201-215.

Dunkl I, Frisch W, Kuhlemann J and Brügel A., 2009. Pebble population dating as an additional tool for provenance studies—examples from the Eastern Alps. Geological Society London Special Publications, 324, 125–140.

Dunkl, I., Farics, E., Józsa, S., Lukács, R., Haas, J. and Budai, T., 2019. Traces of Carnian volcanic activity in the Transdanubian Range, Hungary. International Journal of Earth Sciences, 108, 1451-1466.

Eichhorn, R., Loth, G., Höll, R., Finger F., Schermaier A. and Kennedy A., 2000. Multistage Variscan magmatism in the central Tauern Window (Austria) unveiled by U/Pb SHRIMP zircon data. Contributions to Mineralogy and Petrology, 139, 418-435.

Eriksson, S. C., 1984. Age of carbonatite and phoscorite magmatism of the Phalaborwa Complex (South Africa). Chemical Geology, 46, 291-299.

Faryad, S.W., Spišiak, J., Horváth, P., Hovorka, D., Dianiška, I. and Jósza, S., 2005. Petrological and geochemical features of the Meliata mafic rocks from the sutured Triassic oceanic basin, Western Carpathians. Ofioliti, 30, 27–35.

Franke, W., Cocks, L. R. M. and Torsvik, T. H.., 2017. The Palaeozoic Variscan oceans revisited. Gondwana Research, 48, 257-284.

Gaab, A. S., Poller, U., Janák, M., Kohút, M. and Todt, W., 2005. Zircon U–Pb geochronology and isotopic characterization for the pre-Mesozoic basement of the Northern Veporic Unit (Central Western Carpathians, Slovakia). Schweizerische Mineralogische und Petrographische Mitteilungen 85, 69–88.

Gao, X. Y., Zheng, Y. F., Xia, X. P. and Chena, Y. X., 2014. U–Pb ages and trace elements of metamorphic rutile from ultrahigh-pressure quartzite in the Sulu orogeny. Geochimica et Cosmochimica Acta, 143, 87-114.

Garfunkel Z., 2015. The relations between Gondwana and the adjacent peripheral Cadomian domain—constrains on the origin, history, and paleogeography of the peripheral domain. Gondwana Research, 28, 1257-1281.

Giobbi-Mancini et al., 2003;

Golonka J., 2004. Plate tectonic evolution of the southern margin of Eurasia in the Mesozoic and Cenozoic. Tectonopysics, 381, 235-273.

Gregoric, M., Caffau, M., Lenaz, D. and De Min, A., 1998. Late Maastrichtian- ?Paleocene unaltered glassy microspherules at Padriciano (Trieste Karst, NE Italy): a preliminary report. Razprave SAZU, 39, 211– 233.

Grimes, C. B., John, B. E, Kelemen, P. B., Mazdab, F. K., Wooden, J. L., Cheadle, M. J, Hanghøj, K. and Schwartz, J. J., 2007. Trace element chemistry of zircons from oceanic crust: A method for distinguishing detrital zircon provenance. Geology, 35, 643-646.

Grimes, C. B., John, B. E., Cheadle, M. J., Mazdab, F. K., Wooden, J. L.,Swapp, S. and Schwartz, J. J., 2009. On the occurrence, trace element geochemistry, and crystallization history of zircon from in situ ocean lithosphere. Contributions to Mineralogy and Petrology, 158, 757–783.

Grimes, C. B., Wooden, J. L., Cheadle, M. J and John, B. E, 2015. “Fingerprinting” tectono-magmatic provenance using trace elements in igneous zircon. Contributions to Mineralogy and Petrology, 158, 757–783.

Haas, J., Mioč, P., Pamić, J., Tomljenović, B., Árkai, P., Bérczi-Makk, A., Koroknai, B., Kovács, S. and Rálisch-Felgenhauer, E., 2000. Complex structural pattern of the Alpine–Dinaridic–Pannonian triple junction. International Journal of Earth Sciences, 89, 377–389.

Haas, I., Eichinger, S., Haller, D., Fritz, H., Nievoll, J., Mandl, M., Hippler, D. and Hauzenberger, C., 2020. Gondwana fragments in the Eastern Alps: A travel story from U/Pb zircon data. Gondwana Research, 77, 204-222.

Hajná, J., Žáka, J. and Dörrb W., 2017. Time scales and mechanisms of growth of active margins of Gondwana: A model based on detrital zircon ages from the Neoproterozoic to Cambrian Blovice accretionary complex, Bohemian Massif. Gondwana Research, 42, 63-83.

Hajná, J., Žáka, J., Dörrb, W., Kachlík, V. and Sláma, J., 2018. New constraints from detrital zircon ages on prolonged, multiphase transition from the Cadomian accretionary orogen to a passive margin of Gondwana. Precambrian Research, 317, 159-178.

Hart, E., Storey, C., Bruand, E., Shertl, H. P. and Alexander, B. D., 2016. Mineral inclusions in rutile: A novel recorder of HP-UHP metamorphism. Earth and Planetary Science Letters, 446, 137-148.

Hart, N. R., Stockli, D. F. and Hayman, N. W., 2016. Provenance evolution during progressive rifting and hyperextension using bedrock and detrital zircon U-Pb geochronology, Mauléon Basin, western Pyrenees. Geosphere, 12, 1116-1186.

Heimann, A., Spry, P. G., Teale, G. S., Conor, G. H. H. and Pearson, N. J., 2011. The composition of garnet in garnet-rich rocks in the southern Proterozoic Curnamona Province, Australia: an indicator of the premetamorphic physicochemical conditions of formation. Mineralogy and Petrology, 101, 49-74.

Hoffman, J. E., Münker, C., Næraa, T., Rosing, M. T., Herwartz, D., Garbe-Schönberg, D. and Svahnberg, H., 2011. Mechanisms of Archean crust formation inferred from high-precision HFSE systematics in TTGs. Geochimica et Cosmochimica acta, 75, 4157-4178.

Horváth, P., Balen, D., Finger, F., Tomljenović, B. and Krenn, E., 2010. Contrasting P–T–t paths from the basement of the Tisia Unit (Slavonian Mts., NE Croatia): Application of quantitative phase diagrams and monazite age dating. Lithos, 117, 269-282.

Hoskin, P. W. O. and Shaltegger, U., 2003. The Composition of Zircon and Igneous and Metamorphic Petrogenesis. Reviews in Mineralogy and Geochemistry, 53, 27-62.

Hoskin, P. W. O., 2005. Trace-element composition of hydrothermal zircon and the alteration of Hadean zircon from the Jack Hills, Australia. Geochimica et Cosmochimica Acta, 69, 3, 637–648.

Hrvatović, H., 1999. Geološki Vodić Kroz Bosnu I Hercegovinu (In Serbian). Geological Survey of Bosnia and Herzegovina, Sarajevo, 203.

Ivan, P. and Méres, S., 2012. The Zlatnik group – Variscan ophiolites on the northern border of the Gemeric Superunit (Western Carpathians). Mineralia Slovaka, 44, 39-56.

Janák, M., Cornell, D., Froitzheim, N., De Hoog, J. C.M., Broska, I., Vrabec, M. and Hurai, V., 2009. Eclogite-hosting metapelites from the Pohorje Mountains (Eastern Alps): P-T evolution, zircon geochronology and tectonic implications. European Journal of Mineralogy, 21, 1191-1212.

John, T., Klemd, R., Klemme, S., Pfänder, J.A., Hoffmann, J.E. and Gao, J., 2011. Nb-Ta fractionation by partial melting at the titantite-rutile transition. Contributions to Mineraleralogy and Petrolology, 161, 35–45.

Kalfoun, F., Ionov, D. and Merleta, C., 2002. HFSE residence and Nb/Ta ratios in metasomatised, rutile-bearing mantle peridotites. Earth and Planetary Science Letters, 199, 49-65.

Kamenetsky, V., Crawford, A. J. and Meffre, S., 2001. Factors controlling chemistry of magmatic spinel: an empirical study of associated olivine, Cr-spinel and melt inclusions from primitive rocks. Journal of Petrology, 42, 655–71.

Kirkland, C. L., Smithies, R. H., Taylor, R. J. M., Evans, N., and McDonald, B., 2015. Zircon Th/U ratios in magmatic environs. Lithos, 212, 397–414.

Klemme, S., Prowatke, S., Hametner, K. and Günther, D., 2005. Partitioning of trace elements between rutile and silicate melts: Implications for subduction zones. Geochimica et Cosmochimica Acta, 69, 2361-2371.

Klötzli, U. S., Buda, G. and Skiöld, T., 2004. Zircon typology, geochronology and whole rock Sr–Nd isotope systematics of the Mecsek Mountain granitoids in the Tisia Terrane (Hungary). Mineralogy and Petrology, 81,113–134.

Klötzli, U.S. and Parrish, R.R., 1996. Zircon U–Pb and Pb–Pb geochronology of the Rastenberg granodiorite, South Bohemian Massif, Austria. Mineralogy and Petrology, 58, 197–214.

Kohút, M., Uher, P., Putiš, M., Ondrejka, M., Sergeev, S., Larionov, A. and Paderin, I., 2009. SHRIMP U–Th–Pb zircon dating of the granitoid massifs in the Malé Karpaty Mountains (Western Carpathians): evidence of Meso-Variscan successive S- to I-type granitic magmatism. Geologica Carpathica, 60, 345-350.

Konrad-Schmolke, M., Zack, T., O'Brien, P. J. and Jacob, D., 2008. Major- and rare-earth-element modelling in garnet along eclogite P-T paths, examples from the Western Gneiss Region, Norway. Earth and Planetary Science Letters, 272, 488-498.

Korbar, T., 2009. Orogenic evolution of the External Dinarides in the NE Adriatic region: a model constrained by tectonostratigraphy of Upper Cretaceous to Paleogene carbonates. Earth-Science Reviews, 96, 296–312.

Kováč, M., Plašienka, D., Soták, J., Vojtko, R., Oszczypko, N., Less, G., Ćosović, V., Fügenschuh, B. and Králiková, S., 2016. Paleogene palaeogeography and basin evolution of the Western Carpathians, Northern Pannonian domain and adjoining areas. Global and Planetary Change, 140, 9–27.

Kroner, U. and Romer, R. L., 2013. Two plates-Many subduction zones: The Variscan orogeny reconsidered. Gondwana Research, 24, 298-329.

Kryza, R. and Beqiraj, A., 2014. Palaeoproterozoic (1.83 Ga) zircons in a Bajocian (169 Ma) granite within a Middle Jurassic ophiolite (Rubiku, central Albania): a challenge for geodynamic models. International Journal of Earth Sciences (Geol Rundsch), 103, 607-625.

Lenaz, D., 2008. Detrital pyroxenes in the Eocene flysch of the Istrian Basin (Slovenia, Croatia). Geologica Acta, 6, 259-266.

Lenaz, D. and Princivalle, F., 1996. Crystal-chemistry of detrital chromites in sandstones from Trieste (NE Italy). Neues Jahrbuch fur Mineralogy Monatshefte, 9, 59-67.

Lenaz, D. and Princivalle, F., 2002. Detrital high pressure - low temperature minerals in Lower Eocene deep-sea turbidites of the Julian Alps (NE Italy). Periodico di Mineralogia, 71, 127-135.

Lenaz, D. and Princivalle, F., 2005. The crystal chemistry of detrital chromian spinel from the southeastern Alps and Outer Dinarides: the discrimination of the supplies from areas of similar tectonic settings?. The Canadian Mineralogist, 43, 1305-1314.

Lenaz, D., Kamenetsky, V. S., Crawford, A. J. and Princivalle, F., 2000. Melt inclusion in detrital spinel from SE Alps (Italy-Slovenia): a new approach to provenance studies of sedimentary basins. Contributions to Mineralogy and Petrology, 139, 748-758.

Lenaz D., Kamenetsky, V. S. and Princivalle, F., 2003. Cr-spinel supply in the Brkini, Istrian and Krk Island flysch basins (Slovenia, Italy and Croatia). Geological magazine, 140, 335-342.

Lenaz, D., and F. Princivalle (2005), Crystal chemistry of detrital chromian spinel from the southeastern Alps and Outer Dinarides: The discrimination of supplies from areas of similar tectonic setting?, *Can. Mineral*., 43, 1305-1314.

Lenaz, D., A. Alberti, G. Tunis, and F. Princivalle (2001), Heavy mineral association and its paleogeographic implications in the Eocene Brkini Flysch Basin (Slovenia), *Geol. Carpath*., 52, 239-245.

Lenaz D., Mazzoli C., Velicogna M. and Princivalle F., 2018. Trace and Rare Earth Elements chemistry of detrital garnets in the SE Alps and Outer Dinarides flysch basins: An important tool to better define the source areas of sandstones. Marine and Petroleum Geology, 98, 653-661.

Liati, A., Gebauer, D and Fanning, C. M., 2003. The youngest basic oceanic magmatism in the Alps (Late Cretaceous; Chiavenna unit, Central Alps): geochronological constraints and geodynamic significance. Contributions to Mineralogy and Petrology, 146, 144-158.

Liati, A., Froitzheim, N. and Fanning, C. M., 2005. Jurassic ophiolites within the Valais domain of the Western and Central Apls: geochronological evidence for re-rifting of oceanic crust. Contributions to Mineralogy and Petrology, 149, 446-461.

Lin, J., Liu, Y., Yang, Y. and Hu, Z., 2016. Calibration and correction of LA-ICP-MS and LA-MC-ICP-MS analyses for element contents and isotopic ratios. Solid Earth Sciences, 1, 5-27.

Linnemann, U., Pereira, F., Jeffries, T. E., Drost, K. and Gerdes, A., 2008. The Cadomian Orogeny and the opening of the Rheic Ocean: The diacrony of geotectonic processes constrained by LA-ICP-MS U–Pb zircon dating (Ossa-Morena and Saxo-Thuringian Zones, Iberian and Bohemian Massifs). Tectonophysics, 461, 21-43.

Linnemann, U., Ouzegane, K., Drareni, A., Hofmann, M., Becker, S., Gärtner, A. and Sagawe, A., 2011. Sands of West Gondwana: An archive of secular magmatism and plate interactions — A case study from the Cambro-Ordovician section of the Tassili Ouan Ahaggar (Algerian Sahara) using U–Pb–LA-ICP-MS detrital zircon ages. Lithos, 123, 188-203.

Linnermann U., Gerdes A., Hofmann M. and Marko L., 2014. The Cadomian Orogen: Neoproterozoic to Early Cambrian crustal growth and orogenic zoning along the periphery of the West African Craton-Constraints from the U-Pb zircon ages and Hf isotopes (Schwarzburg Antiform, Germany). Precambrian Research, 244, 326-278.

Longerich, H. P., Jackson, S. E. and Günther, D., 1996. Inter-laboratory note. Laser ablation inductively coupled plasma mass spectrometric transient signal data acquisition and analyte concentration calculation. Journal of Analytical Atomic Spectrometry, 11, 899-904.

Ludwig, K. R., 2003. Mathematical–Statistical Treatment of Data and Errors for ^{230}Th/U Geochronology. Reviews in Mineralogy and Chemistry, 52, 631-656.

Lugović, B., Slovenec, D., Schuster, R., Schwarz, W. H. and Horvat, M., 2015. Petrology, geochemistry and tectono-magmatic affinity of gabbroic olistoliths from the ophiolite mélange in the NW Dinaric-Vardar ophiolite zone (Mts. Kalnik and Ivanščica, North Croatia). Geologia Croatica, 68, 25-49.

Luvizotto. G. L. and Zack, T., 2009. Nb and Zr behavior in rutile during high-grade metamorphism and retrogression: An example from the Ivrea–Verbano Zone. Chemical Geology, 261, 303–317.

Luvizotto, G. L., Zack, T., Triebold, S. and von Eynatten, H., 2009. Rutile occurrence and trace element behavior in medium-grade metasedimentary rocks: example from the Erzgebirge, Germany. Mineralogy and Petrology, 97, 233–249.

Lužar-Oberiter, B., Mikes, T., von Eynatten, H. and Babić, L., 2009. Ophiolitic detritus in Cretaceous clastic formations of the Dinarides (NW Croatia): evidence from Cr-spinel chemistry. International Journal of Earth Science, 98, 1097-1108.

Lužar-Oberiter, B., Mikes, T., Dunkl, I., Babić, L. and von Eynatten, H., 2012. Provenance of Cretaceous synorogenic sediments from the NW Dinarides (Croatia). Swiss Journal of Geosciences, 105, 377-399.

Maffione M. and D.J.J. van Hinsbergen, 2018. Reconstructing plate boundaries in the Jurassic Neo-Tethys from the East and West Vardar Ophiolites (Greece and Serbia). Tectonics, 37, 858-887.

Magaš, D., 2000. Contribution to the knowledge of the geographical characteristics of the Pag Island. Geoadria, 5, 5- 48.

Magdalenić, Z., 1972. Sedimentologija Fliskih naslaga srednje Istre (Sedimentology of Central Istrian Flysch deposits). Acta Geologica Zagreb 7, 71–100.

Malaroda, R., 1947. Arenarie eoceniche della regione di Trieste. Bollettino Società Adriatica di Scienze Naturali, 43, 90–112.

Mancktelow, N. S., Stöckli, D. F., Grollimund, B., Müller, W., Fügenschuh, B., Viola, G., Seward, D. and Villa, I. M., 2001. The DAV and Periadriatic fault systems in the Eastern Alps south of the Tauern window. International Journal of Earth Sciences, 90, 593–622.

Mange, M. A. and Morton, A. C., 2007. Geochemistry of heavy minerals. In: M.A. Mange, D.T. Wright (Eds.), Heavy Minerals in Use, 58, Developments in sedimentology, 345-391.

Mantovani, E., Viti, M., Cenni, N., Babbucci, D. and Tamburelli, C., 2015. Present Velocity Field in the Italian Region by GPS Data: Geodynamic/Tectonic Implications. International Journal of Geosciences, 6, 1285-1316.

Marianač et al., 1991).

Marinčić, S., Šparica, M., Tunis, G. and Uchman, A., 1996. The Eocene Flysch deposits of the Istrian Peninsula in Croatia and Slovenia region: stratigraphic, sedimentological and ichnological analysis Annales, 9, 139-156.

Marjanac, T. and Marjanac, L., 1991. Shallow-marine clastic Paleogene on the Island of Rab (northern Adriatic). Dolomieu Conference on Carbonate Platforms and Dolomitization, Ortisei.

Marjanac, T. and Marjanac, L., 2007. Sequence stratigraphy of Eocene incised valley clastics and associated sediments, Island of Rab, northern Adriatic Sea, Croatia. Facies, 53, 493–508.

Marocchi, M., Morelli, C, Mair, V, Klötzli, U. and Bargossi, G. M., 2008. Evolution of Large Silicic Magma Systems: New U-Pb Zircon Data on the NW Permian Athesian Volcanic Group (Southern Alps, Italy). The Journal of Geology, 116, 480-498.

Márton, E., Ćosović, V., Moro, A. and Zvocak, S., 2008. The motion of Adria during the Late Jurassic and Cretaceous: new paleomagnetic results from stable Istria Tectonophysics, 454, 44-53.

Márton, E., Zampieri, D., Grandesso, P., Ćosović, V. and Moro, A., 2010. New Cretaceous paleomagnetic results from the foreland of the Southern Alps and the refined apparent polar wander path for stable Adria. Tectonophysics, 480, 57-72.

Márton E., Zampieri, D., Ćosović, V., Moro, A. and Drobne, K., 2017. Apparent polar wander path for Adria extended by new Jurassic paleomagnetic results from its stable core: Tectonic implications. Tectonophysics, 700–701, 1-18.

Márton et al. 2019

Matte, P., 2001. The Variscan collage and orogeny (480–290 Ma) and the tectonic definition of the Armorica microplate: a review. Terra Nova, 13, 122-128.

McKay, M.P., Jackson, W. and Hessler, A.M., 201. Tectonic stress regime recorded by zircon Th/U. Gondwana Research, 57, 1-9.

Meinhold G., 2010. Rutile and its applications in earth sciences. Earth-Science Reviews, 102, 1-28.

Meinhold, G., Morton, A. C., Fanning, M., Frei, D., Howard, J. P., Phillips, R. J., Strogen, D. and Whitham, G., 2011. Evidence from detrital zircon for recycling of Mesoproterozoic and

Neoproterozoic crust recorded in Paleozoic and Mesozoic sandstones of southern Libya. Earth and Planetary Science Letters, 312, 164-175.

Meli, S. and Sassi, R., 2003. The «Venice Granodiorite»: constraints on the «Caledonian» and Variscan events in the Alpine domain. Rendiconti Lincei, 14, 179-204.

Meyer, M., John, T., Brandt, S. and Klemd, R., 2011. Trace element composition of rutile and the application of Zr-in-rutile thermometry to UHT metamorphism (Epupa Complex, NW Namibia). Lithos, 126, 388-401.

Mikes et al., 2008b

Mikes, T., Christ, D., Petri, R., Dunkl, I., Frei, D., Baldi-Beke, M., Reitner, J., Wemmer, K., Hrvatović, H. and von Eynatten, H., 2008a. Provenance of the Bosnian Flysch. Swiss Journal of Geosciences 101, Supplement 1, S31–S54.

Mikes, T., Dunkl, I., von Eynatten, H., Báldi-Beke, M. and Kázmer, M., 2008b. Calcareous nannofossil age constraints on Miocene flysch sedimentation in the Outer Dinarides (Slovenia, Croatia, Bosnia-Hercegovina and Montenegro). In: Siegesmund, S., Fügenschuh, B. & Froitzheim, N. (Eds.): Tectonic aspects of the Alpine-Dinaride-Carpathian System, Geological Society London Special Publications, 298, 335–363.

Mikes, T, Baresel, B., Kronz, A., Frei, D., Dunkl, I., Tolosana-Delgado, R. and von Eynatten, H., 2009. Jurassic granitoid magmatism in the Dinaride Neotethys: geochronological constraints from detrital minerals. Terranova, 21, 495-506.

Miklavič, B. and Rožič, B., 2008. The onset of Maastrichtian basinal sedimentation on Mt. Matajur, NW Slovenia. Materials and Geoenvironment, 55, 199-214.

Mikuš, T. and Spišiak, J., 2007. Chemical composition and alteration of Cr-spinels from Meliata and Penninic serpentinized peridotites (Western Carpathians and Eastern Alps). Geological Quarterly, 51, 257–270.

Milovanović, D., 1984. Petrology of low-grade metamorphic rocks of the middle part of the Drina-Ivanjica Palaeozoic (in Serbian with English summary). Glasnik Prirodnjačkog Muzeja u Beogradu (Ser. A), 39, 13-139.

Missoni, S. and Gawlich, J., 2011. Evidence for Jurassic subduction from the Northern Calcareous Alps (Berchtesgaden; Austroalpine, Germany). Interantional Journal of Earth Sciences, 100, 1605–1631.

Morishita T., Ishida Y., Arai S. and Shirasaka M., 2005. Determination of multiple trace element compositions in thin (< 30 μm) layers of NIST SRM 614 and 616 using laser ablation ICP-MS Geostandard and Geoanalytical Research, 29, 107-122.

Morton, A. C., Hallsworth, C. R. and Chalton, B., 2004. Garnet composition in Scottish and Norwegian basement terrains: a framework for interpretation of North Sea sandstone provenance Marine and Petroleum Geoscience, 21, 393-410.

Müller, B., Schaltegger, U., Klötzli, U. and Flisch, M., 1996. Early Cambrian oceanic plagiogranite in the Silvretta Nappe, eastern Alps: geochemical, zircon U-Pb and Rb-Sr data from garnet-hornblende-plagioclase gneisses. Geologische Rundschau, 85, 822-831.

Münker et al., 2003).

Muttoni, G., Kent, D. V., Garzanti, E., Brack, P., Abrahamsen, N. and Gaetani, M., 2003. Early Permian Pangea “B” to Late Permian Pangea “A”. Earth and Planetary Science Letters, 215, 379-394.

Muttoni, G., Gaetani, M., Kent, D. V., Sciunnach, D., Angiolini, L., Berra, F., Garzanti, E., Mattei, M. and Zanchi, A., 2009. Opening of the Neo-Tethys Ocean and the Pangea B to Pangea A transformation during the Permian. GeoArabia, 14, 17-48.

Neubauer, F., Liu, X., Borojević Šoštarić, S., Heberer, B. and Dong, Y., 2014. U-Pb zircon data of Middle-Upper Triassic magmatism in Southern Alps and NW Dinarides: Implications for the Southeast Mediterranean tectonics. In Buletini i Shkencave Gjeologjike, Ionescu, C.; Christofides,

G.; Uta, A.; Beqiraj Goga, E. ; Marku, S. (ur.).Tirana, Albanija, 2014. str. 1-1 (predavanje, međunarodna recenzija, sažetak, znanstveni)

Ogata, K., Festa, A., Pini, G. A., Pogačnik, Z., and Lucente, C. C., 2019. Substrate deformation and incorporation in sedimentary mélanges (olistostromes): Examples from the northern Apennines (Italy) and northwestern Dinarides (Slovenia). Gondwana Research, 74, 101-125.

Orehek, S., 1972. Eocensli fliš Pivške Kotline in Brkinov: 7. Kongres Geolog. SFRJ, Predavanija, 252-270.

Orehek, S., 1991. Palaeotransport of SW Slovenian Fysch. Field Trip Guidebook. IGCP Project 286 - Early Paleoegene Benthos, 2nd Meeting Postojna, 27-31.

Ouzegane, K., Kienast, J. R., Bendaoud, A, and Drareni, A., 2003. A review of Archean and Paleoproterozoic evolution of the In Ouzzal granulitic terrane (western Hoggar, Algeria). Journal of African Earth Science, 37, 207-227.

Palinkaš, L. A., Borojević Šoštarić, S. and Strmić Palinkaš, S., 2008. Metallogeny of the Northwestern and Central Dinarides and Southern Tisia. Ore Geology Reviews, 34, 501-520.

Palinkaš, L. A., Borojević Šoštarić, S., Strmić Palinkaš, S. and Crnjaković, M., 2010. Volcanoes in the Adriatic Sea: Permo-Triassic Magmatism on the Adriatic-Dinaridic Carbonate Platform: IMA2010 Field Trip Guide HR1.

Palinkaš, L. A., Šoštarić, S. B. and Palinkaš, S. S., 2008. Metallogeny of the Northwestern and Central Dinarides and Southern Tisia. Ore Geology Reviews, 34, 501-520.

Pamić, J., 1984. Triassic magmatism of the Dinarides in Yugoslavia. Tectonophysics, 109, 273-277, 281-307.

Pamić, J., Scavnicar, S. and Medijmorec, S., 1973. Mineral assemblages of amphibolites associated with alpine-type ultramafics in the Dinaride Ophiolite Zone (Yugoslavia). Journal of Petrolology, 14, 133-157.

Pamić, J., Gušić, I. and Jelaska, V., 1998. Geodynamic evolution of the Central Dinarides. Tectonophysics, 297, 251–268.

Pamić, J., Tomljenović, B and Balen, D., 2002. Geodynamic and petrogenetic evolution of Alpine

Pavšič, J. and Peckmann, J., 1996. Stratigraphy and sedimentology of the Piran flysch area (Slovenia). Annales, 9, 123-138.

Pearce N.J.G., Perkins W.T., Westgate J.A., Gorton M.P., Jackson S.E., Neal C.R. and Chenery S.P. 1997. A compilation of new and published major and trace element data for NIST SRM 610 and NIST SRM 612 glass reference materials Geostandards Newsletter, 21, 115-144.

Pereira, I., Storey, C., Darling, J., Lana, C., and Alkmim, A. R., 2019. Two billion years of evolution enclosed in hydrothermal rutile: Recycling of the São Francisco Craton Crust and constraints on gold remobilisation processes. Gondwana Research, 68, 69-92.

Petrelli M., Laeger K. and Perugin D., 2016a. High spatial resolution trace element determination of geological samples by laser ablation quadrupole plasma mass spectrometry: implications for glass analysis in volcanic products. Geoscience Journal, 20, 851-863.

Petrelli M., Morgavi D., Vetere F. and Perugini D., 2016. Elemental imaging and petro-volcanological applications of an improved laser ablation inductively coupled quadrupole plasma mass spectrometry. Periodico di Mineralogia, 85, 25-39.

Pirini, C, Tunis, G. and Venturini, S. 1986. Biostratigrafia e paleogeografía dell'area sud-occidentale dell'anticlinale M. Mia—M. Mataiur (Prealpi Giule). Rivista Italiana di Paleontologia e Stratigrafia, 92, 327-382.

Placer, L., Vrabec, M., Celarc, B., 2010. The bases for understanding of the NW Dinarides and Istria Peninsula tectonics. Geologija, 53, 55–86.

Poller, U. and Todt, W., 2000. U-Pb single zircon data of granitoids from the High Tatra Mountains (Slovakia): implications for the geodynamic evolution. Trans. Roy. Soc. Edin-Earth, 91, 235—243.

Putiš M., Ivan P., Kohút M., Spišiak J., Siman P., Radvanec M., Uher P., Sergeev S., Larionov A., Méres Š., Demko R., 2009. Meta-igneous rocks of the West-Carpathian basement, Slovakia: indicators of Early Paleozoic extension and shortening events. Bulletin de la Société Géologique de France, 180, 461-471.

Putiš, M., Sergeev, S., Ondrejka, M., Larionov, A., Iman, P., Spisiak, J., Uher, P. and Paderin, I., 2008a. Cambrian-Ordovician metaigneous rocks associated with Cadomian fragments in the West-Carpathian basement dated by SHRIMP on zircons: a record from the Gondwana active margin setting. Geologica Carphatica, 59, 3-18.

Putiš, M., Li J., Ružička, P., Ling, X. and Nemec O., 2016. U/Pb SIMS zircon dating of a rhyolite intercalation in Permian siliciclastics as well as a rhyodacite dyke in micaschists (Infratatricum, W. Carpathians). Mineralia Slovaca, 48, 135-144.

Rino, S., Kon, Y., Sato, W., Maruyama, S., Santosh, M. and Zhao, D., 2008. The Greenvillian and Pan-African orogens: World's largest orogenies through geologic time, and their implications on the origin of superplume. Gondwana Research, 14, 51–72.

Rosenbaum G and Lister G. S., 2005. The Western Alps from the Jurassic to Oligocene: spatio-temporal constraints and evolutionary reconstructions. Earth-Science Reviews, 69, 281-306.

Rosenbaum G., Lister G. S. and Duboz C., 2002. Relative motions of Africa, Iberia and Europe during Alpine orogeny. Tectonophysics, 359, 117-129.

Rosenbaum G., Lister G. S. and Duboz C., 2004. The Mesozoic and Cenozoic motion of Adria (central Mediterranean): a review of constraints and limitations. Geodinamica Acta, 17, 125–139.

Rosset A., De Mina A., Marques L. S.,.Macambira M.J.B., Ernesto M., Renne P. R. and Piccirillo E. m., 2007. Genesis and geodynamic significance of Mesoproterozoic and Early Cretaceous tholeiitic dyke swarms from the São Francisco craton (Brazil). 24, 69-92.

Rožič, B., 2005. Albian – Cenomanian resedimented limestone in the lower flyschoid formation of the Mt. Mrzli vrh area (Tolmin region, NW Slovenia). Geologija, 48, 193-210.

Rubatto, D., 2002. Zircon trace element geochemistry: partitioning with garnet and the link between U–Pb ages and metamorphism. Chemical Geology, 184, 123–138.

Rubatto, D., Gebauer, D. and Fanning, M., 1998. Jurassic formation and Eocene subduction of the Zermatt–Saas-Fee ophiolites: implications for the geodynamic evolution of the Central and Western Alps. Contributions to Mineralogy and Petrology, 132, 269-287.

Rubatto, D., 2017. Zircon: The Metamorphic Mineral. Reviews in Mineralogy and Geochemistry, 83, 261-295.

Rudnick, R. L., Barth, M., Horn, I. and McDonough, W. F., 2000. Rutile-Bearing Refractory Eclogites: Missing Link Between Continents and Depleted Mantle. Science, 287, 278-281.

Saccani, E., Beccaluva, L., Photiades, A. and Zeda, O., 2011. Petrogenesis and tectono-magmatic significance of basalts and mantle peridotites from the Albanian–Greek ophiolites and sub-ophiolitic mélanges. New constraints for the Triassic–Jurassic evolution of the Neo-Tethys in the Dinaride sector. Lithos, 124, 227-242.

Sassi F. P. and Spiess R., 1993. The South-Alpine Metamorphic Basement in the Eastern Alps. In: von Raumer, J.F., Neubauer, F. (eds) Pre-Mesozoic Geology in the Alps. Springer, Berlin, Heidelberg.

Schaltegger, U., Brack, P., Ovtcharova, M., Peytcheva, I., Schoene, B., Stracke, A., Marocchi, M. and Bargossi, G. M., 2009. Zircon and titanite recording 1.5 million years of magma accretion, crystallization and initial cooling in a composite pluton (southern Adamello batholith, northern Italy). Earth and Planetary Science Letters, 286, 208-218.

Schettino, A. and Turco, E., 2009. Breakup of Pangaea and plate kinematics of the central Atlantic and Atlas regions. Geophysical Journal International, 178, 1078–1097.

Schettino, A. and Turco, E., 2011. Tectonic history of the western Tethys since the Late Triassic. Geological Society of American Bulletin, 123, 89-105.

Schmid, S. M., Aebli, H. R., Heller, F. and Zingg, A., 1989. The role of the Periadriatic Line in the tectonic evolution of the Alps. Geological Society, London, Special Publications, 45, 153-171.

Schmid, S. M., Bernoulli, D., Fügenschuh, B., Matenco, L., Schefer, S., Schuster, R., Tischler, M. and Ustaszewski, K., 2008. The Alpine-Carpathian-Dinaridic orogenic system: correlation and evolution of tectonic units. Swiss Journal of Geosciences, 101, 139-183.

Schmid, S. M., Fügenschuh, B., Kounov, A., Matenco, L., Nievergelt, P., Oberhänsli, R., Pleuger, J., Schefer, S., Schuster, R., Tomljenović, B., Ustaszewski, K., and van Hinsbergend, D. J. J., 2019. Tectonic units of the Alpine collision zone between Eastern Alps and western Turkey. Gondwana Research, in print.

Schmidt, A., Weyer, S., John, T. and Brey, G. P., 2009. HFSE systematics of rutile-bearing eclogites: new insights into subduction zone processes and implications for the Earth's HFSE budget. Geochimica et Cosmochimica Acta, 73, 455-468.

Schmidt et al. (2008),

Schneider, P., Balen, D., Massone, H.-J.and Opitz, J., 2019. Cretaceous rift-related magmatism in the suture zone of Adria microplate and European plate (Slavonian Mts., Croatia). Zbornik recenzovanych abstraktov a prispevkov / Ondrejka, Martin, Fridrichova, Jana - Bratislava, 50-53.

Schulz, B., Klemd, R. and Brätz, H., 2006. Host rock compositional controls on zircon trace element signatures in metabasites from the Austroalpine basement. Geochimica et Cosmochimica Acta, 70, 697–710.

Schwandt, C. S., Papike, J. J., Shearer, C. K. and Brearley ,A. J., 1993. A SIMS investigation of REE chemistry of garnet in garnetite associated with the Broken Hill Pb-Zn-Ag orebodies, Australia. Canadian Mineralogist, 31, 371-379.

Şengün, F., 2017. Zr-in-rutile thermometry of eclogites from the Karakaya Complex in NW Turkey: Implications for rutile growth during subduction zone metamorphism. Chemie der Erde, 77, 95-104.

Şengün, F. and Zack, T., 2016. Trace element composition of rutile and Zr-in-rutile thermometry in meta-ophiolitic rocks from the Kazdağ Massif, NW Turkey. Mineralogy and Petrology, 110, 547–560.

Şengün, F., Zack, T. and Topuz, G., 2017. Rutile geochemistry and thermometry of eclogites and associated garnet-mica schists in the Biga Peninsula, NW Turkey. Geochemistry, 77, 503-515.

Shaltegger & Brack, 2007;

Slovenec, D.A., Lugović, B. and Vlahović, I., 2010. Geochemistry, petrology and tectonomagmatic significance of basaltic rocks from the ophiolite mélange at the NW External-Internal Dinarides junction (Croatia). Geologica Carpathica, 61, 273–294.

Smythe, D. J., Schulze, D. J. and Brenan, J. M., 2008. Rutile as a kimberlite indicator mineral: minor and trace element geochemistry. 9th International Conference, Extended Abstract, No. 9IKC-A-00193.

Sölva, H., Grasemann, B., Thöni, M., Thiede, R. and Habler, G., 2015. The Schneeberg Normal Fault Zone: Normal faulting associated with Cretaceous SE-directed extrusion in the Eastern Alps (Italy/Austria). Tectonophysics, 401, 143-166.

Spiegel, C., Kuhlemann, J., Dunkl, I., Frisch, W., von Eynatten, H., and Balogh, K., 2000. The erosion history of the Central Alps: Evidence from zircon fission track data of the foreland basin sediments. Terra Nova, 12, 163–170.

Spiess, R., Cesare, B., Mazzoli, C., Sassi, R. and Sassi, F. P., 2010. The crystalline basement of the Adria microplate in the eastern Alps: a review of the palaeostructural evolution from the Neoproterozoic to the Cenozoic. Rendiconti Lincei, 21, S31-S50.

Stampfli, G. M. and Hochard, C., 2009. Plate tectonics of the Alpine realm. Geological Society, London, Special Publications, 89-111.

Stampfli, G. M. and Kozur, H. W., 2006. Europe from the Variscan to the Alpine cycles. Chapter in Geological Society London Memoirs.

Stampfli, G. M., von Raumer, J. F. and Borel, G., 2002. The Paleozoic evolution of pre-Variscan terranes: From Gondwana to the Variscan collision. In: Martínez Catalán, J. R., Hatcher, R. D. Jr.,

Arenas, R., Díaz Garcia, F. (eds) Variscan-Appalachian dynamics: the building of the Late Paleozoic basement. Geological Society of America Special Paper 364, 263–280.

Stampfli, G. M., Hochard, C. and von Raumer, J. F., 2006. Reconstructing the Palaeozoic Gondwana margin and its redistribution: new aspects: Geophys Res Abstr, 8, EGU06–A-02708.

Stampfli, G. M., Hochard, C., Vérard, C., Wilhem, C. and von Raumer, J., 2013. The geodynamics of Pangea formation. Tectonophysics, 593, 1–19.

Stampfli, G. M., 2000. Tethyan Oceans. Geological Society, London, Special Publications, 173, 1-23.

Stampfli, G. M, Mosar J., Favre P., Pillevuit A. and Vannay J. C., 2001. Permo-Mesozoic evolution of the western Tethyan realm: the Neotethys/East-Mediterranean connection. Mémoire du Museum National d'Histoire Naturelle, 186, 51-108.

Stefani, C., Fellin, M. G., Zattin, M., Zuffa, G. G., Dalmonte, C., Mancin, N. and Zanferrari, A., 2007. Provenance and Paleogeographic Evolution in a Multi-Source Foreland: The Cenozoic Venetian–Friulian Basin (NE Italy). Journal of Sedimentary Research, 77, 867-887.

Stepanov, A. S. and Hermann, J., 2013. Fractionation of Nb and Ta by biotite and phengite: Implications for the “missing Nb paradox”. Geology, 41, 303-306.

Stephan et al. (2019 a,b)

Stephan, T., Kroner, U. and Romer, R. L., 2019. The pre-orogenic detrital zircon record of the Peri-Gondwanan crust. Geological Magazine, 156, 281-307.

Stephan, T., Kroner, U., Romer, R. L. and Rösel, D., 2019. From a bipartite Gondwanan shelf to an arcuate Variscan belt: The Early Paleozoic evolution of northern Peri-Gondwana. Earth-Science Reviews, 192, 491-512.

Stern, G. and Wagreich, M., 2013. Provenance of the Upper Cretaceous to Eocene Gosau Group around and beneath the Vienna Basin (Austria and Slovakia). Swiss Journal of Geosciences, 106, 505-527.

Szemerédi, M., Lukács, R., Varga I. A., Dunkl, I., Józsa, S., Tatu, M., Pál-Molnár, M., Szepesi, J., Guillong, M., Szakmány, G. and Harangi,S. , 2019. Permian felsic volcanic rocks in the Pannonian Basin (Hungary): new petrographic, geochemical, and geochronological results. International Journal of Earth Sciences, 1-25.

Tari, V., 2002. Evolution of the Norther and Western Dinarides: a Tecnonostratigraphic approach. EGU Stephan Mueller Special Publication series, 1, 223-236.

Tari et al., 2000).

Tugend, J., Chamot-Rooke, N., Arsenikos, S., Blanpied, C. and Frizon de Lamotte, D., 2019. Geology of the Ionian Basin and Margins: A Key to the East Mediterranean Geodynamics. Tectonics, 38, 2668-2702.

Tunis, G. and Uchmann, A., 1996. Trace fossils and facies changes in Cretaceous-Eocene flysch deposits of the Julian Prealps (Italy and Slovenia): Consequences of regional and world-wide changes. Ichnos, 4, 169-190.

Tunis, G., and Venturini, S. 1984. Stratigrafia e sedimentologia del flysch Maastrichtiano-Paleocenico del Friuli orientale. Gortania, 6, 5-58.

Tunis, G. and Venturini, S., 1992. Evolution of the Southern Margin of the Julian Basin with Emphasis on the Megabeds and Turbidites Seqence of the Southern Julian Prealps (NE Italy). Geologia Croatica, 45, 127-150.

Tunis, G. and Venturini, S., 1996. L'Eocene delle Prealpi Carniche, dell'Altipiano di Brkini e dell'Istria: precisazioni biostratigrafiche e paleoambientali. Natura Nascosta, 13, 40-49.

Uher, P., Putiš, M., Ondrejka, M., Kohut, M. and Sergeev, S., 2010. Postorogénne granity typu A v Západných Karpatoch – nové výsledky datovania zirkónu metódou SHRIMP. Abstract, 7th annual seminary of Slovak Geological Society.

Ustaszewski, K., Kounov, A., Schmid, S. M., Schaltegger, U., Krenn, E., Frank, W. and Fügenschuh, B., 2010. Evolution of the Adria-Europe plate boundary in the northern Dinarides: from continent-continent collision to back-arc extension. Tectonics, 29, TC6017.

Ustaszewski, K., Schmid, S. M., Lugović, B., Schuster, R., Schaltegger, U., Bernoulli, D., Hottinger, L., Kounov, A., Fügenschuh, B. and Schefer, S., 2009. Late Cretaceous intra-oceanic magmatism in the internal Dinarides (northern Bosnia and Herzegovina): implications for the collision of the Adriatic and European plates. Lithos, 108, 106-125.

Ustawezski et al (in print)

van Achterbergh et al. (2001)

Velić, J., Malvić, T., Cvetković, M. and Velić, I., 2015. Stratigraphy and petroleum geology of the Croatian part of the Adriatic basin. Journal of Petroleum Geology, 38, 281-300.

Venturini, S., and Tunis, G. 1991. La composizione dei conglomerati cenozoici del Friuli: dati preliminary. Studi Geologici Camerti, Special Issue, CROP 1/1A, 285-295.

Venturini, S., and Tunis, G. 1991. Nuovi dati stratigrafici, paleoambientali e tettonici sul Flysch di Cormons (Friuli orientale). Gortania, 13, 5-30.

Vermeesch, P., Avigad, D. and McWilliams, M., 2009. 500 My of thermal history elucidated by multi-method detrital thermochronology of North Gondwana Cambrian sandstone (Eilat area, Israel). Geological Society of America Bulletin, 121, 1204-1216.

Visonà, D., Fioretti, A. M., Poli, M. E., Zanferrari, A. and Fanning, M., 2007. U-Pb SHRIMP zircon dating of andesite from the Dolomite area (NE Italy): geochronological evidence for the early onset of Permian Volcanism in the eastern part of the Southern Alps. Swiss Journal of Geosciences, 100, 313-324.

Vlahović, I., Tišljar, J. T., Velić, I. and Matičec, D., 2005. Evolution of the Adriatic Carbonate Platform: Palaeogeography, main events and depositional dynamics. Palaeogeography, Palaeoclimatology, Palaeoecology, 220, 333– 360.

Vlahović, I., Mandic, O., Meinjek, E., Bergant, S., Cosovic, V., De Leeuw, A., Enos, P., Hrvatovic, H., Maticec, D., Miksa, G., Nemec, W., Pavelic, D., Pencinger, V., Velic, I and Vranikovic, A., 2012. Marine to continental depositional systems of Outer Dinarides foreland and intra-montane basins

(Eocene-Miocene, Croatia and Bosnia-Herzegovina). Field Trip Guide 29th IAS Meeting of Sedimentology Schladming/Austria.

Vozárová, A., Rodionov, N., Šarinová, K. and Presnyakov, S., 2017. New zircon ages on the Cambrian–Ordovician volcanism of the Southern Gemericum basement (Western Carpathians, Slovakia): SHRIMP dating, geochemistry and provenance. International Journal of Earth Sciences, 106, 2147-2170.

Wasser et al., 2008).

Watson, E. B., Wark, D. A. and Thomas, J. B., 2006. Crystallization thermometers for zircon and rutile. Contributions to Mineralogy and Petrology, 151, 471–488.

Wiesender, H. 1960. Petrographie und Petrologie dereozanen Flyschsandsteine. Verhandlungen der Geologischen Bundesanstalt, 166-171.

Wilde, S. and Youssef, K., 2002. A re-evaluation of the origin and setting of the Late Precambrian Hammamat Group based on SHRIMP U–Pb dating of detrital zircons from Gebel Umm Tawat, North Eastern Desert, Egypt. Journal of the Geological Society, 159, 595-604.

Woletz, G. 1960. Schwermineralvergesellschaftungen ausostalpinen Sedimentationsbecken der Kreidezeit. Geologische Rundschau, 56, 308–20.

Wortmann, U. G., Weissert, H., Funk, H. and Hauck, J. 2001. Alpine plate kinematics revisited: the Adria problem. Tectonics, 20, 134–147.

Xiong, X.L., Adam, J. and Green, T.H., 2005. Rutile stability and rutile/melt HFSE partitioning during partial melting of hydrous basalt: Implications for TTG genesis. Chemical Geology, 218, 339-359.

Yakymchuk, C., Kirkland, C.L. and Clark, C., 2018. Th/U ratios in metamorphic zircon. Journal of Metamorphic Geology, 36, 715-737.

Zack, T. and Kooijman, E., 2017. Petrology and Geochronology of Rutile. Reviews in Mineralogy & Geochemistry, 83, 443-467.

Zack, T., Moraes, R. and Kronz, A., 2004. Temperature dependence of Zr in rutile: empirical calibration of a rutile thermometer. Contributions to Mineralogy and Petrology, 148, 471-488.

Zajzon, N., Szabó, Z., Gábor Weiszburg, T. and Jeffries, T. E., 2011. Multiple provenance of detrital zircons from the Permian–Triassic boundary in the Bükk Mts., Hungary. International Journal of Earth Sciences, 100, 125-138.

Zanetti, A., Mazzucchelli, M., Sinigoi, S., Giovanardi, T., Peressini, G., Fanning, M., 2013. SHRIMP U-Pb ZirconTriassic Intrusion Age of the Finero Mafic Complex (Ivrea-Verbano Zone, Western Alps) and its Geodynamic Implications. Journal of Petrology,54, 2235-2265.

Zheng, Y. F., Gao, X. Y., Chen, R. X. and Gao, T., 2011. Zr-in-rutile thermometry of eclogite in the Dabie orogen: Constraints on rutile growth during continental subduction-zone metamorphism. Journal of Asian Earth Sciences, 40, 427-451.

Živkovic, S. and Glumac, B., 2007. Paleoenvironmental reconstruction of the Middle Eocene Trieste-Pazin basin (Croatia) from benthic foraminiferal assemblages. Micropaleontology, 53, 285-310.

Zurbriggen, R., 2015. Ordovician orogeny in the Alps: A reappraisal. International Journal of Earth Sciences, 104, 335–350.

Appendices

Garnets

Major and traces elements

Garnets Major-Trace	Al	Li	Mg	Si	P	Ca	Sc	Ti	V	Cr	Mn	Fe	Co	Ni	Cu
JB-1-1	1.02E+08	11.4	8700	185800	15.5	37510	385.6	494	29.6	95	23490	234000	13.33	-1	0.36
JB-1-2	1.09E+08	11.3	14050	180600	67.8	13370	209	312	48.2	55.9	57700	220000	19.5	-1.19	0.37
JB-1-3	9.51E+07	11.2	15520	185100	16.6	37000	87.5	124.3	65.8	167.2	17890	240000	28.6	0.7	0.19
JB-1-4	1.03E+08	11.7	39700	194000	29.6	61200	53.3	351	134.6	169.5	6710	175000	49.2	1.2	0.37
JB-1-5	9.75E+07	11.3	17760	187500	18.9	17370	184.8	100.3	308	2.47	12530	268000	12.77	-0.94	0.29
JB-1-6	1.04E+08	11.6	44300	194500	34.2	49900	55.9	406	211.5	128.6	4200	193000	70.6	3.9	0.26
JB-1-7	1.02E+08	12.2	71500	201300	51.6	49100	56.5	296.6	45.2	201.3	2421	124000	65.6	9	0.33
JB-1-8	9.62E+07	11.3	11010	186800	13.2	69600	37.3	466	128.3	5.9	14130	227000	14.78	-1.81	0.16
JB-1-9	1.08E+08	11.3	8760	180200	9.9	65400	45.7	496	112.8	0.99	19040	214000	16.98	-0.6	0.2
JB-1-10	1.04E+08	11.4	7320	179900	15.6	72700	65.3	660	174.4	2.59	14780	224000	18.35	-1.1	0.03
JB-1-11	9.94E+07	11.2	9150	187400	37.5	15600	335	214.8	29.05	33.4	17590	282000	12.25	-1.32	-0.06
JB-1-12	1.00E+08	11.8	41600	191300	43.8	72000	58.4	305.2	115.6	333	4860	163000	46.4	2.3	0.2
JB-1-13	9.44E+07	11.1	10820	182300	930	7920	75.3	32.3	12.23	0.52	49200	260000	9.87	0.39	0.26
JB-1-14	9.75E+07	11.5	22620	186400	15.3	35460	107.6	98.5	73.7	97.8	6370	233000	8.4	-0.28	0.05
JB-1-15	9.62E+07	11.3	18330	181100	362	11020	178.3	28.9	69	144.6	23880	247000	12.48	0.1	0.01
JB-1-16	9.47E+07	11.7	51500	195900	46	52000	65.2	463	239.8	234.5	3834	158000	60.4	7	0.08
JB-1-17	9.30E+07	11.3	15460	185300	29.4	18150	172.8	138.8	35.4	37.6	1606	278000	21.03	-0.32	0.07
JB-1-18	9.78E+07	11.9	49500	194700	67.5	63900	34.2	470	122.3	134.5	6970	143000	58.3	7.4	0.18
JB-1-19	9.93E+07	11.4	15180	185300	36.1	29010	105.4	428	31.07	16.5	1829	262000	15.47	-0.25	-0.05
JB-1-20	9.35E+07	11.1	10980	183300	1205	6860	62.5	67.3	6.62	0.6	45800	255000	9.45	-0.68	0.24
JB-1-21	9.32E+07	11.4	15480	186000	66.7	11990	23.9	121.1	32.6	64.6	803	293000	37.8	0.5	1.33
JB-1-22	9.44E+07	11.7	50220	197100	23.6	56100	61.1	478	199.5	163	4630	163000	58.3	4.28	0.09
JB-1-23	9.37E+07	11.1	6950	186900	30	17630	63.2	469	75.5	71.7	53200	242000	20.3	-0.2	0.11

JB-1-24	9.64E+07	11.3	18800	183900	231	12910	144.9	15.5	55.2	105.5	13670	256000	14.91	-0.3	-0.18
JB-1-25	9.43E+07	11.4	21160	190600	236	12210	88.1	1165	129.1	122.7	17170	263000	35.9	2.77	0.27
JB-1-26	9.78E+07	11.2	5080	183300	14.8	45400	51.9	442	92.8	107.7	12200	245000	11.34	-1.2	0.11
JB-1-27	9.58E+07	11.3	18340	187100	22	23100	199.9	1440	42.3	66.6	45200	211000	44.7	-0.4	0.81
JB-1-28	8.95E+07	11.5	27200	193600	240	22660	90.8	46.5	46.4	114.2	8260	261000	19	-0.7	-0.11
JB-14-1	9.51E+07	11.5	30680	192600	44.7	25750	77.6	262	55	88.3	1325	235000	48.2	0.85	0.4
JB-14-2	9.79E+07	11.6	25950	190200	14.6	30120	81.1	80	32.7	58.6	7190	236000	19.13	0.5	-0.04
JB-14-3	8.64E+07	11.4	23120	191900	41.8	27900	65.9	880	126	113.6	44100	215000	22.7	0.5	0.52
JB-14-4	8.33E+07	11.2	12140	189000	26.5	40200	104.6	568	172.8	148	4350	266000	9.24	-2.1	0.21
JB-14-5	9.25E+07	11.3	12600	186700	19.4	56100	137.3	312	84.1	76.3	8640	229000	11.12	-0.7	0.23
JB-14-6	9.59E+07	11.2	2806	184700	13.3	49300	111.1	532	87.6	118.4	69800	182000	4.09	-1.3	0.18
JB-14-7	9.67E+07	11.3	5630	187300	16.6	50400	41.3	508	85.8	69.2	27900	223000	9.32	-1.3	0.12
JB-14-8	9.78E+07	11.6	47700	196100	19.4	48100	54.9	412	137.9	339	5120	183000	60.2	3	0.11
JB-17-1	9.68E+07	11.4	8110	183000	7.9	74400	86.2	480	88.9	91.4	6150	223000	13.69	-1.12	0.03
JB-17-2	9.47E+07	11.3	12340	184800	13.4	63800	73.2	2420	94.1	168	5220	227000	29.8	-1.24	0.33
JB-17-3	9.80E+07	11.4	14750	186300	3.5	31200	89.1	295	44	72.7	16200	243000	21.44	0.09	0.27
JB-17-4	9.39E+07	11.4	7530	182700	10.1	47000	12.48	386	45	5.23	35400	220000	8.94	-1	-0.01
JB-17-5	9.08E+07	11.4	8900	186200	13.6	43400	64	262	130.2	110	26800	236000	19.22	-0.9	0.07
JB-17-6	1.04E+08	11.5	27540	181300	55.2	14460	147.4	45.1	40.1	64.6	10630	233000	23.1	-0.08	-0.01
JB-17-7	9.57E+07	11.7	30200	189400	79.5	29700	27.2	382	36	39.2	2984	240000	52.2	1	0.13
JB-17-8	9.88E+07	11.3	4920	181400	10.3	37570	23.18	450	80.5	32.6	1031	262000	4.79	-0.16	-0.08
JB-17-9	9.41E+07	11.2	1888	181400	13.7	68700	37.3	1080	11.79	4.5	62000	164000	3.25	-0.39	0
JB-17	9.38E+07	11.5	12450	188200	18.3	65600	6.3	464	39.2	0.21	15540	203000	14.41	-0.24	0.02
JB-17-10	8.95E+07	10.9	8530	183800	24.9	20550	1.48	221.4	2.64	0.46	146000	148000	1.8	-0.75	0.16
JB-17-11	8.87E+07	11.6	30690	193200	99.9	7150	200.5	183.1	102.3	148	10380	249000	28.1	0.06	0.08
JB-17-12	8.70E+07	11.3	13850	196000	32.9	7700	74.3	35	0.86	1	66900	234000	15.65	-0.88	1.25
JB-17-13	9.29E+07	11.1	7650	181100	420	12130	59.5	486	104.1	47.6	99800	205000	1.85	-0.25	0.07
JB-17-14	8.85E+07	11.4	18210	194900	118	15690	162	54	87.3	140.1	17290	242000	21.64	0.3	0.04
JB-17-15	9.12E+07	11.5	23150	187300	68.7	27990	33.63	660	33.8	43.8	8900	240000	18.66	-0.5	0.27
JB-17-16	9.18E+07	11.3	11210	185900	19.8	19450	16.01	51.4	25.1	50.2	6580	259000	8.78	0.1	-0.05

JB-17-17	9.20E+07	11.4	18290	188500	18	57400	121	321	66.1	136.3	4510	223000	48	-0.2	0.02
JB-17-18	9.22E+07	11.6	43160	190300	73.1	36860	73.6	443	176.5	125.9	6340	195000	51.2	-0.85	0.32
JB-17-19	7.30E+07	11.5	25180	234300	31	26600	17.3	2010	109	377	15480	216000	21	3.4	0.17
JB-17-20	9.20E+07	11.3	16920	188900	18.3	18190	308.2	340	186.1	29.1	15360	260000	19.24	0.17	0.13
JB-17-21	9.59E+07	11.5	40170	195900	33	45000	60.8	490	241.4	32.9	4250	200000	65.7	3	0.52
JB-20-1	9.17E+07	11.4	13670	188100	73.4	11460	117.1	255	30.95	32	12710	274000	21.46	0	0.1
JB-20-2	9.72E+07	11.3	11520	189600	22.6	56400	81.7	476	72.8	6.16	9790	220000	6.12	-1.6	0.05
JB-20-3	9.20E+07	11.4	21190	193000	238.2	5660	276.8	40.8	74.3	133.6	38700	236000	15.02	-0.1	0.13
JB-20-4	8.99E+07	11.3	6110	190200	10.4	40510	188.8	236	40	81.3	22560	251000	19.76	-1.5	0.02
JB-20-4	9.06E+07	11.3	13570	197200	27.3	32400	147.8	410	66.8	68.9	28850	236000	15.15	1.2	0.16
JB-20-5	9.25E+07	11.4	21320	194200	161.8	4260	61.8	12.5	15.37	27.8	2289	267000	26.94	0.6	0.24
JB-20-6	9.21E+07	11.2	7480	186900	13.4	32800	109.3	472	62.8	69.9	75600	199000	12.67	0.5	0.08
JB-20-7	9.16E+07	11.5	19760	190300	23	35580	87.1	324	67.7	55.2	5810	246000	18.25	-0.2	0.1
JB-20-8	8.92E+07	11.5	24000	191900	61.5	10580	161.3	28.2	33.4	69.5	14080	246000	22.79	-0.1	0.02
JB-20-9	9.12E+07	11.3	22650	190800	42.5	14390	54.2	65.4	30.2	59.4	3570	261000	46.1	1.1	0.1
JB-20-10	9.52E+07	11.2	9150	190500	21.2	63100	201.3	1950	134.5	146.9	7100	217000	10.72	0.3	0.2
JB-20-11	9.08E+07	11.5	21700	189100	22.8	38100	44.8	316	45.6	105.9	872	231000	20.08	-1.1	0.16
JB-20-12	9.37E+07	11.1	6210	181900	32.4	27100	204.7	255	28.8	45.3	10390	255000	10.11	0.1	-0.05
JB-20-13	9.19E+07	11.4	26920	190700	19	22400	95.1	31.9	19.5	91.9	5500	237000	27.7	-0.41	-0.15
JB-20-14	9.11E+07	11.3	13190	188200	20.8	21350	127.4	148	254	65.4	64300	213000	26.4	-1.1	0.11
JB-20-15	9.17E+07	11.2	16730	190500	20.1	12340	180.2	32.3	77.9	114.8	19930	240000	20.4	0.3	0.04
JB-23-1	8.64E+07	11.4	18680	188200	86.6	10660	70.3	199	29.2	68	3380	275000	26.5	0.07	0.12
JB-23-2	9.16E+07	11.4	14240	189700	41.5	29800	122.7	460	43.7	87.8	3980	255000	26.7	-0.1	0.09
JB-23-3	9.07E+07	11.4	33010	189300	18.6	65000	55.1	342	195.4	4.8	3660	181000	35.54	0.7	0.11
JB-23-4	1.08E+08	11.3	12760	180000	111	52200	42.4	370	107.5	151.1	10270	219000	13.71	-1	0.2
JB-23-5	8.81E+07	11.8	43390	203000	40.5	60100	51.7	413	157.1	166.7	4340	176000	56.1	2.3	0.04
JB-23-6	9.10E+07	11.7	53200	195200	37.3	67170	51.8	895	101.9	828	4470	136000	58.3	11.3	0.15
JB-23-7	9.06E+07	11.8	42510	198300	62.3	71600	67.2	530	137.5	145	5840	159000	39.1	1.3	0.25
JB-23-8	8.97E+07	11.7	56400	197600	97.9	35600	73.9	456	198.5	177.8	3930	174000	53.1	0	0.16
JB-23-9	9.25E+07	11.9	41530	197600	37.4	76500	62.4	518	134.3	22.9	5590	158000	53.1	2.5	0.07

JB-23-10	9.38E+07	12	40590	199300	28	70900	65.5	443	89.5	156.5	5130	155000	50.2	0.9	0.13
JB-23-11	9.06E+07	11.7	36670	198600	23.6	67000	47.4	533	235.1	43.1	5280	175000	67.1	4	0.04
JB-23-12	8.91E+07	11.2	16400	185000	38.9	57000	81.4	373	48.7	142.6	5390	210000	30.4	0	-0.08
JB-23-13	9.07E+07	11.4	18080	190500	27.1	9030	43.4	20.9	24.38	187	26180	252000	22.8	-1.7	-0.04
JB-23-14	8.93E+07	11.2	6340	186300	26.7	27840	167.1	445	44	66.1	20430	251000	15.45	-0.6	-0.13
JB-23-15	8.95E+07	12	47630	206100	45.6	68700	58.9	331	129.6	491	3370	149000	55.9	3.65	0.51
JB-23-16	9.14E+07	11.2	7900	189200	21	37300	131	883	45.3	91.6	52300	193000	5.85	-0.3	0.19
JB-23-17	9.01E+07	11.9	44090	197700	46.8	61000	57.5	405	114.7	225	6120	159000	37.8	0.3	0.78
JB-23-18	9.79E+07	11.5	12260	186800	11.1	59700	46.2	315	52.8	137	5210	225000	13.9	-0.7	-0.04
JB-23-19	8.94E+07	11.6	44400	199800	55.1	44300	67.8	467	186.1	48.4	4385	179000	61	3.4	0.15
JB-23-20	9.29E+07	11.7	4820	193700	11.6	81800	74.8	499	99.3	16.9	1860	214000	8.6	-0.6	1.41
JB-23-21	1.09E+08	11.7	43300	188800	41	48500	59.7	252	161.6	190.6	3600	178000	65	2.1	0.61
JB-23-22	1.04E+08	11.2	8570	183200	36	60600	71.6	690	81.6	95.8	10640	219000	4.87	-0.8	0.26
JB-23-23	8.94E+07	11.8	43450	206800	28.9	42740	66.2	190.6	120.6	16.1	3929	187000	65.4	1.6	0.25
JB-23-24	7.15E+07	11.7	37700	203000	46	68200	36.3	720	107	34	5640	150000	44.2	-1.7	0.26
JB-23-25	8.90E+07	11.6	41530	199400	25.3	53300	55	434	242.8	173.2	4290	185000	66.4	2.4	0.04
JB-23-26	9.51E+07	11.5	46360	191200	32.1	54700	58.4	467	210.9	25.6	4596	166000	60.9	1.66	4.23
JB-23-27	8.99E+07	11.2	11290	194900	261.8	5650	143.9	322.3	42.9	62.1	67100	237000	8.25	-0.2	0.2
JB-23-28	8.73E+07	11.7	50090	207300	102.7	36480	76.5	441	181.1	51.2	6200	187000	45.9	-0.2	0.19
JB-23-29	9.38E+07	11.7	25320	202200	20.4	27100	125	136	54.2	134.9	6810	234000	15.07	-1.4	0.58
JB-25-1	9.29E+07	11.2	8590	201100	87.5	9720	185.1	329	71	67.6	75600	212000	9.84	-0.7	0.06
JB-25-2	8.85E+07	11.7	45050	205100	60.3	42410	61.4	359.5	210.8	41.8	5400	199000	64.2	1.5	0.19
JB-25-3	8.70E+07	11.7	43040	204000	54	55500	74.5	369	175	287	4330	186000	45.7	0.4	-0.02
JB-25-4	9.07E+07	11.4	9220	184800	14.3	60300	26.08	578	62.5	79.7	3880	242000	5.94	-0.6	1.71
JB-25-5	7.26E+07	11.3	7530	234400	41	58100	70.7	3510	132.5	88.4	27660	203000	20.7	-0.2	-0.01
JB-26-1	8.79E+07	11.8	54630	203400	118.3	35210	81.3	295	122.9	43.5	4130	175000	37.8	-0.8	0.27
JB-26-2	8.94E+07	11.4	34820	194600	32.1	61900	61	443	179.5	259.6	4346	177000	54.4	2.9	0.3
JB-26-3	8.89E+07	11.5	43960	198500	41.8	41470	60.8	371	210.2	93	4250	181000	55.9	-0.2	0.18
JB-26-4	9.08E+07	11.1	22540	192100	26.1	66400	45.6	496	162.8	16.9	19350	181000	27.5	-0.55	-0.02
JB-26-5	9.16E+07	11.3	10810	182400	48	13720	149.4	260	33.34	65.2	6760	272000	19.8	-0.6	-0.05

JB-26-6	8.69E+07	11.7	43140	196800	39.5	48000	65.3	371	184	209	3800	185000	71.7	3.1	0.23
JB-26-7	8.90E+07	11.8	44600	199900	30.3	67400	69.1	467	147.4	27.7	5490	154000	54	4.6	-0.03
JB-26-8	8.44E+07	11.2	7800	185200	26	35200	219	388	46.4	25.1	16690	241000	16.4	0.1	0.37
JB-26-9	8.63E+07	11.7	37960	198000	40.2	61400	54.5	486	156.1	253	4390	175000	44.8	1	1.19
JB-26-10	8.85E+07	11.5	41070	197100	80.9	42200	60.1	314	158.3	58.9	3890	196000	62	-0.1	0.25

Table 1a. Major and trace elements of JB detrital garnets, determined in situ by electron probe analyses.

	Zn	Ga	Ge	As	Rb	Sr	Y	Zr	Nb	Sn	Ba	Hf	Ta	Pb	Th	U
JB-1-1	55.5	7.2	19.3	0.23	0.18	0.175	504	0.97	0.342	0.33	0.048	0.041	0.133	1.06	0.0091	0.048
JB-1-2	49.1	7.4	19.7	1.5	0.02	-0.038	170	8.39	3.93	1.15	-0.064	0.205	0.57	0.097	0.044	0.246
JB-1-3	43.6	8.02	6.1	0.14	-0.004	0.026	230	1.43	0.018	0.43	-0.107	0.022	0.005	0.0073	-4E-06	-2.2E-06
JB-1-4	64.6	6.07	5.13	-0.044	-0.031	-0.008	62.2	4.51	-0.0059	0.27	-0.044	0.103	-0.0051	0.026	0.0021	-2.1E-06
JB-1-5	64.6	14.59	10.6	0.36	0.06	0.061	223	0.427	0	0.27	0.003	0.0038	-0.0069	0.031	-3.9E-06	0.0032
JB-1-6	58.1	9.41	4.82	0	0.017	0.02	71.5	3.67	-0.003	0.2	0.044	0.021	0.0005	0.034	0.0009	-2E-06
JB-1-7	59.1	5.87	2.37	0.06	-0.051	-0.075	12.9	3.78	0.001	0.189	0.04	0.093	-0.0039	0.018	-4E-06	-2.2E-06
JB-1-8	46.2	9.73	7.57	0.15	0.049	0.019	149.9	2.39	-0.0051	0.242	-0.047	0.033	-0.0002	0.0018	-3.9E-06	-2.1E-06
JB-1-9	30.4	5.54	6.72	0.24	0.02	0.092	127.2	1.39	0.014	0.17	0.003	0.012	-0.0007	0.022	-3.5E-06	-1.9E-06
JB-1-10	27.1	5.51	5.93	0.13	-0.031	0.008	52.5	1.66	0.025	0.136	0.18	0.0043	0.0054	0.017	-3.6E-06	-1.9E-06
JB-1-11	29.9	4.97	9.15	0.072	0.151	0.035	785	0.82	0	0.42	-0.011	0.02	0.014	0.023	-3.7E-06	0.0124
JB-1-12	44.2	6.76	4.24	0.083	0.067	0.011	81.5	4.87	-0.01433	0.119	-0.079	0.098	-0.0018	0.0037	-3.9E-06	-2.1E-06
JB-1-13	96.7	32.7	43.7	0.13	-0.023	0.086	133.4	6.51	0.149	2.93	0.002	0.519	1.422	0.027	-3.8E-06	0.058
JB-1-14	54.1	5.13	11.57	0.043	0.015	0.01	86.3	2.55	0.013	0.154	0.005	0.026	-0.0028	0.022	-3.8E-06	-2.1E-06
JB-1-15	54.8	11.55	10.63	0.32	0.131	-0.008	264.2	8.95	0.006	0.128	-0.066	0.268	0.0039	0.024	-3.8E-06	0.0078
JB-1-16	75.2	8.6	3.32	0.18	0.005	0.057	60.9	4.23	0	0.11	0.06	0.045	0.006	0.011	-4E-06	-2.2E-06
JB-1-17	76.5	5.17	15.2	0.09	0.18	0.09	1057	1.13	0.067	0.43	0.049	0.032	0.03	0.022	0.0011	0.028
JB-1-18	60.7	6.13	3.23	0.15	-0.128	-0.013	13.5	9.36	-0.003	0.17	0.15	0.181	-0.0022	0.009	0.0025	-2.2E-06
JB-1-19	76.1	8.1	17.8	0.05	-0.021	-0.033	124	2.67	0.089	0.8	0.07	0.046	0.072	0.02	-3.6E-06	0.0055
JB-1-20	94.7	43.5	21.4	0.35	-0.022	-0.064	37.3	5.63	0.6	7.31	0.078	0.68	2.08	0.023	-3.8E-06	0.108
JB-1-21	10.2	4.46	13.2	0.06	-0.034	0.018	14.39	4.85	-0.0029	0.84	0.048	0.094	-0.0025	0.254	-3.9E-06	0.0026
JB-1-22	56.8	7.23	4.69	0.01	0.003	-0.01	66.2	6.24	0.0002	0.136	-0.01	0.068	-0.0048	0.014	-3.9E-06	-2.2E-06
JB-1-23	28.3	8.51	49.1	0.77	0.15	0.038	333	1.78	0.284	1.65	0.11	0.062	0.12	0.17	0.036	0.101
JB-1-24	51.6	12.72	11.3	-0.03	0.165	0.061	289	4.71	0.007	0.13	0.09	0.33	-0.0008	0.021	0.0153	-2.1E-06
JB-1-25	110.1	16.66	10	0.2	0.072	0.035	416	112	0.041	0.15	0.039	1.99	0.017	0.02	0.027	0.036
JB-1-26	39.2	5.99	11.4	0.01	0.01	-0.009	48.9	1.48	0.096	0.52	0.019	-8.9E-05	0.039	0.043	0.0017	-2.1E-06
JB-1-27	36.7	6.79	16.8	1.54	0.171	0.19	779	33	8.7	0.73	0.57	0.81	0.64	0.185	0.102	0.99
JB-1-28	24.1	7.78	11.7	0.1	-0.06	0.24	313	30.2	0.078	0.58	0.14	0.76	0.025	0.029	0.052	0.35
JB-14-1	140.2	7.27	9.9	0.03	0.017	0.044	102.2	3.99	-0.0094	0.349	-0.03	0.035	0.01	0.0023	-3.8E-06	0.0124

JB-14-2	80.9	5.74	7.81	0.2	-0.067	0.008	127	1.25	0.155	0.15	0.018	0.03	0.0091	0.082	-3.7E-06	-2.1E-06
JB-14-3	165.9	11.1	21.3	4	0.24	0.4	49.6	13.3	11.3	3.98	1.07	0.52	1.45	0.098	0.078	0.098
JB-14-4	24	9.1	6.4	0.12	-0.18	-0.043	54.8	5.4	-0.0114	3.79	-0.074	0.137	-0.0019	0.026	-4.1E-06	0.084
JB-14-5	89.7	6.31	8.3	0.02	0.01	0.066	144.5	1.13	0.014	0.28	-0.017	0.018	-0.0028	0.019	-3.8E-06	-2.2E-06
JB-14-6	32.8	7.32	23.2	0	-0.008	0.068	99.8	0.89	1.1	0.96	-0.013	0.026	0.296	0.064	0.0015	0.094
JB-14-7	35.5	7.01	21.6	0.1	-0.06	-0.015	35.8	1.97	0.151	0.57	0.012	0.055	0.096	0.029	-3.6E-06	-2.1E-06
JB-14-8	55.4	8.01	6.6	0.08	0.041	0.043	78.1	6.21	0.002	0.24	0.1	0.096	0.0031	0.011	-3.7E-06	-2.1E-06
JB-17-1	90.8	6.65	11.59	0.008	0.038	0.009	87.4	1.28	0.044	0.27	-0.036	0.03	0.0079	0.019	-3.6E-06	-2.1E-06
JB-17-2	36.4	7.56	3.81	0.22	-0.041	0.3	52.2	7.2	0.66	0.45	-0.011	0.111	0.048	0.048	-3.7E-06	0.0044
JB-17-3	89.4	6.46	19.4	0.96	2.53	0.143	159.9	62	1.34	0.48	1.15	1.9	0.229	0.57	0.32	0.75
JB-17-4	34.5	6.21	9.36	0.05	0.08	0.122	17.7	1.04	0.166	0.101	0.2	0.023	0.03	0.016	-3.7E-06	-2.2E-06
JB-17-5	27.8	6.9	7.48	0.09	-0.02	0.083	97.2	0.8	-0.0039	0.171	-0.05	-8.8E-05	0.0078	0.017	-3.8E-06	-2.2E-06
JB-17-6	102.2	5.2	9.1	0.08	0.045	0.049	283	7.9	0.017	0.21	-0.068	0.15	0.014	0.052	-3.4E-06	0.0059
JB-17-7	163.4	6.7	5.29	0.05	0.07	0.009	24.6	12.49	-0.001	0.28	-0.022	0.23	0.0085	0.018	-3.7E-06	0.021
JB-17-8	62.5	9.06	4.63	0.16	0.006	0.04	3.52	1.58	0.054	0.59	0.05	0.066	0.021	0.019	-3.4E-06	0.0038
JB-17-9	22.5	9.25	12.2	0.37	0.049	61	63.2	29.9	1.06	0.62	0.042	0.93	0.095	3.97	2.57	0.454
JB-17	42.5	8.41	5.09	0.14	0.041	0.033	37.2	2.45	-0.002	0.19	-0.005	0.036	0.0019	0.012	-3.7E-06	-2.2E-06
JB-17-10	10.34	5.63	11.5	0.108	-0.035	0.047	8.5	4.08	1.91	3.54	-0.083	0.114	0.54	0.015	-3.6E-06	0.143
JB-17-11	112.4	12.58	10.8	-0.01	0.332	0.173	1214	16.6	0.009	0.12	-0.023	0.392	-0.0006	0.0045	-3.9E-06	0.014
JB-17-12	88.9	23.6	25.6	0.14	0.24	0.11	1137	7.77	5.37	2.81	0.16	0.79	1.1	0.192	0.0065	0.299
JB-17-13	32.4	10.05	39	4.11	0.011	0.79	182.3	15.6	1.004	1.84	0.03	0.43	0.278	0.124	0.393	1.29
JB-17-14	53.7	8.06	18.2	0.25	0.55	4.9	408	0.88	0.059	0.198	2.8	0.036	0.034	0.105	0.029	0.037
JB-17-15	65.3	8.26	6.15	0.2	0.007	0.028	113.1	42.6	0.013	0.36	0	1.15	0.023	0.03	0.158	0.86
JB-17-16	47.6	4.6	13.5	0.04	0.24	0.064	2043	0.66	0.0007	0.179	0.15	0.024	0.019	0.009	-3.7E-06	-2.2E-06
JB-17-17	53.5	6.01	4.2	-0.086	-0.113	-0.045	62.4	1.02	-0.003	0.142	-0.048	0.016	0.019	0.076	-3.7E-06	-2.3E-06
JB-17-18	70.4	12.12	3.07	0.02	0.02	-0.037	120	9.2	-0.0049	0.158	-0.017	0.111	0.014	0.0014	-3.8E-06	-2.3E-06
JB-17-19	21.9	10.9	1.3	0.66	0.04	21.4	8.7	20	2.72	0.38	1.8	0.61	0.224	2.09	0.119	0.094
JB-17-20	47.1	10.73	17.3	0.83	0.216	0.077	375	2.22	0.227	0.9	-0.024	0.062	0.051	0.04	-3.6E-06	0.047
JB-17-21	42.5	11.4	4.79	0.16	-0.006	0.057	108.4	7.65	0.001	0.164	0.04	0.151	0.0039	0.247	-3.6E-06	-2.2E-06
JB-20-1	9.7	5.04	9.9	0.05	0.159	0.077	598	2.56	0.058	0.28	-0.088	0.027	0.022	0.069	0.002	0.064

JB-20-2	46.3	8.14	6.1	-0.046	0.069	0.033	157.1	1.6	-0.0089	0.34	-0.117	0.022	0.0006	0.035	-3.4E-06	-2.1E-06
JB-20-3	82.9	10.32	14.7	0.04	0.12	0.132	321	8.32	0.001	0.016	-0.017	0.21	0.011	0.022	-3.7E-06	0.0016
JB-20-4	34	6.12	27.1	0.99	0.042	0.141	169.2	4.3	0.022	0.35	-0.077	0.07	0.0141	0.134	-3.7E-06	0.0083
JB-20-4	61.3	7.87	13.2	0.02	0.089	0.036	263	0.83	0.89	0.312	0.04	-8.2E-05	0.061	0.099	0.0114	0.032
JB-20-5	83.4	4.97	9.4	0.08	0.067	0.013	66.9	1.24	-0.003	0.13	0.02	0.053	0.004	0.017	-3.6E-06	-2.3E-06
JB-20-6	48	6.75	13.4	0.55	0.04	0.028	37.1	2.82	0.522	1.07	-0.038	0.075	0.166	0.111	0.018	0.063
JB-20-7	39.1	8.24	7.65	0.24	0.085	0.055	88.5	3.3	-0.0104	0.065	-0.123	0.04	0.022	0.031	-3.6E-06	-2.3E-06
JB-20-8	71.6	6.85	15	0.09	0.13	0.092	405	2.83	0.004	0.046	-0.01	0.091	0.0046	0.0062	-3.7E-06	0.0068
JB-20-9	55.1	5.7	15.7	0.21	0.253	0.011	730	1.43	0.013	0.36	-0.045	0.021	0.013	0.039	-3.6E-06	0.0043
JB-20-10	13.42	7.56	3.13	0.12	0.16	0.41	114.4	2.64	0.37	0.208	-0.082	0.06	0.035	0.022	-3.3E-06	0.023
JB-20-11	96.7	6.02	8.36	0.05	0.05	0.038	172.5	2.31	0.024	0.13	0.033	0.066	0.0143	0.0059	-3.6E-06	-2.3E-06
JB-20-12	88.5	5.91	21.9	0.1	0.014	0.033	133.6	1.71	0.191	0.57	0.08	0.015	0.086	0.019	-3.4E-06	0.022
JB-20-13	77.1	5.45	14.2	-0.01	0.011	0.033	171	0.69	-0.0108	0.103	-0.035	-7.7E-05	0.0068	0.036	-3.6E-06	-2.3E-06
JB-20-14	80	10.7	14	0.06	0.03	0.061	321	4.29	0.005	0.75	-0.013	0.13	0.013	0.067	-3.6E-06	0.023
JB-20-15	47.7	9.73	12.7	0.13	0.113	0.031	362	1.27	-0.0026	0.25	-0.005	0.017	0.033	0.019	0.0015	0.0116
JB-23-1	35.1	6.01	17	0.14	-0.01	0.129	14	3.05	0.006	0.43	0.01	0.025	0.0033	-0.0005	-3.8E-06	0.016
JB-23-2	85.2	7.38	10.45	0.14	0.09	0.185	262	4.15	0.51	0.82	0.011	0.099	0.127	2.6	-3.5E-06	0.033
JB-23-3	40	15.09	2.66	0.01	-0.04	0.023	82.8	1.38	0.001	0.082	0.021	0.009	0.017	0.03	-3.6E-06	-2.3E-06
JB-23-4	50.5	4.89	7.6	0.01	-0.03	0.07	50.6	0.626	0.034	0.07	0.03	-6.2E-05	0.022	0.047	0.009	0.027
JB-23-5	60.6	6.34	4.06	-0.111	0.1	-0.033	71.8	6.93	-0.002	0.21	-0.117	0.109	0.01	0.023	0.0106	0.0012
JB-23-6	32.3	7.03	3.22	0.03	-0.01	0.022	23.68	11.05	-0.0062	0.161	-0.052	0.195	0.0081	0.0022	-3.6E-06	-2.4E-06
JB-23-7	46.1	6.77	2.96	0.15	-0.05	0.006	80.1	17.09	-0.001	0.094	0.01	0.266	0.012	0.0019	-3.7E-06	-2.4E-06
JB-23-8	74.3	10.79	2.76	0.15	0	0.017	65.8	11.38	-0.001	0.14	-0.062	0.182	0.0017	0.017	-3.6E-06	-2.4E-06
JB-23-9	93.1	6.95	3.73	0.13	-0.032	0.034	45.6	6.18	-0.0067	0.12	-0.05	0.087	0.012	0.036	-3.6E-06	-2.4E-06
JB-23-10	47.3	4.83	3.09	-0.052	-0.038	0.022	50.4	3.31	-0.0077	0.1	-0.096	0.05	0.0041	0.054	-3.6E-06	-2.4E-06
JB-23-11	51.1	10.17	5.73	0.1	0.03	0.048	115	6.38	-0.0027	0.045	-0.034	0.064	0.0007	0.013	-3.6E-06	-2.4E-06
JB-23-12	31.3	6.21	3.7	0.03	-0.032	0.021	56	1.25	-0.0064	0.19	-0.067	0.0048	-0.0019	0.013	-3.5E-06	-2.3E-06
JB-23-13	74.5	6.63	24.8	-0.03	0.53	0.392	1124	1.12	-0.003	0.22	-0.109	-7.2E-05	0.007	0.011	-3.6E-06	-2.3E-06
JB-23-14	49.6	7.17	30.5	0.67	0.067	-0.05	95.8	3.18	0.298	1.33	-0.019	0.086	0.157	0.014	-3.5E-06	0.064
JB-23-15	74.6	7.32	2.69	0.11	0.023	-0.041	55.4	6.88	-0.002	0.2	0.1	0.117	-0.0014	0.104	-3.7E-06	-2.5E-06

JB-23-16	156	5.94	7.34	-0.04	-0.02	0.005	124.6	0.89	2.06	0.48	-0.074	0.008	0.161	0.041	-3.5E-06	0.0085
JB-23-17	78.8	7.72	4.74	0.09	-0.002	0.018	121.7	8.2	-0.0141	0.115	0.01	0.135	-0.0025	0.096	-3.7E-06	-2.5E-06
JB-23-18	47.5	6.14	16.7	0.29	0.01	0.029	112.2	1.32	0.023	0.28	0.03	0.072	-0.00604	0.29	-3.2E-06	-2.2E-06
JB-23-19	53.3	10.49	4.18	0.18	0	0.012	155.4	8.3	0.01	0.213	0.02	0.179	0.0023	0.0069	-3.6E-06	-2.4E-06
JB-23-20	28.7	9.25	6.9	0.01	-0.079	0.04	133.3	5	0.004	0.24	-0.017	0.142	0.0023	0.66	0.0026	0.0049
JB-23-21	59	8.44	3.1	0.14	0.06	0.05	78	3.72	0.023	0.14	-0.01	0.071	-0.003	0.152	0.015	-2E-06
JB-23-22	44.6	7.8	6.5	0.07	-0.15	0.068	84.3	1.48	0.012	0.33	-0.025	-5.6E-05	-0.00611	0.11	0.051	-2E-06
JB-23-23	32.6	8.32	5.56	0.09	0.054	0.08	98.8	9.6	0.007	0.18	-0.071	0.087	0.0027	0.014	-3.6E-06	0.0011
JB-23-24	33.4	4.41	3.3	-0.08	-0.08	-0.12	17.92	12.4	-0.0179	0.04	0.21	0.69	0.04	0.043	-4.2E-06	-2.8E-06
JB-23-25	54.5	10.9	3.72	0.17	-0.004	0.044	84.5	5.94	0.007	0.128	0.06	0.102	0.011	0.02	-3.5E-06	-2.4E-06
JB-23-26	86.2	9.32	3.47	-0.019	0.032	0.018	81.5	8.28	-0.0043	0.13	0.027	0.131	0.0002	0.324	-3.3E-06	-2.3E-06
JB-23-27	34.7	7.6	16	1.38	0.453	0.36	940	8.02	0.164	1.25	0.04	0.242	0.102	0.038	0.0017	0.288
JB-23-28	115.1	11.63	3.35	0.04	0.057	0.098	222	8.69	-0.001	0.2	-0.027	0.139	0.0055	0.021	-3.6E-06	-2.5E-06
JB-23-29	64.7	6.59	9.05	0.16	0.13	0.19	183.4	2.65	0.23	0.28	0.12	0.039	0.016	0.261	-3.4E-06	0.013
JB-25-1	43.4	8.37	24.5	2.53	0.18	0.14	1018	31.6	0.514	1.17	0.19	0.9	0.21	0.118	0.408	1.16
JB-25-2	79.1	12.3	3.34	0.13	-0.01	-0.014	87.9	5.59	0.014	0.22	0.04	0.076	-0.0083	0.022	-3.6E-06	-2.5E-06
JB-25-3	66.3	9.65	2.4	0.17	-0.018	0.017	120.3	7.11	0.007	0.1	-0.033	0.151	0.007	0.04	-3.6E-06	-2.5E-06
JB-25-4	63	5.54	11.3	0.01	-0.028	0.003	48.4	2.23	0.044	0.45	0.032	0.012	0.028	0.288	-3.4E-06	-2.4E-06
JB-25-5	77.8	6.75	7.1	0.66	0.1	0.37	172.5	179	8.9	0.82	0.14	5.5	0.617	0.57	1.82	2.17
JB-26-1	68.7	9.18	2.94	0.03	0.005	0.016	92.4	6.69	-0.014	0.17	-0.025	0.13	-0.0021	0.028	-3.6E-06	-2.5E-06
JB-26-2	32.6	8.62	4.95	0.19	-0.005	0.022	147.3	5.62	-0.0056	0.158	-0.056	0.064	0.023	0.026	-3.5E-06	-2.4E-06
JB-26-3	64	10.38	5.06	-0.025	-0.015	-0.004	90.1	6.88	-0.003	0.101	0.029	0.104	-0.001	0.035	-3.5E-06	-2.5E-06
JB-26-4	159	8.33	4.04	0.08	-0.036	0.079	94.3	4.67	-0.0069	0.11	-0.022	0.051	-0.0005	0.036	-3.3E-06	-2.3E-06
JB-26-5	43.8	5.54	16.1	0.19	0.029	-0.028	119.7	2.65	0.098	0.77	0.015	0.056	0.038	0.046	-3.3E-06	0.034
JB-26-6	74.6	9.85	2.66	0.26	0.03	0.024	89.3	5.9	-0.0082	0.16	0.07	0.1	-0.0075	0.028	-3.6E-06	-2.6E-06
JB-26-7	69.5	7.75	4.42	0.07	0.06	0.062	77.1	6.25	-0.001	0.1	0.003	0.114	-0.0084	0.03	-3.6E-06	-2.6E-06
JB-26-8	76.2	6.72	18.7	0.09	-0.1	0.033	262	1.63	0.417	0.8	0.1	0.015	0.099	0.08	-3.5E-06	0.0069
JB-26-9	55.7	8.16	4.58	-0.01	-0.089	0.064	117.4	7.87	0.005	0.16	0.04	0.167	-0.0037	0.328	-3.6E-06	-2.5E-06
JB-26-10	49.5	10.5	2.95	-0.07	-0.06	0.022	89.4	5.64	-0.0053	0.05	-0.064	0.153	0.002	0.0076	-3.5E-06	-2.5E-06

Table 1b. Major and trace elements of JB detrital garnets, determined in situ by electron probe analyses.

Garnets Major-Trace	Al	Li	Mg	Si	P	Ca	Sc	Ti	V	Cr	Mn	Fe	Co	Ni	Cu
BK-JAP-1	1.12E+08	11.4	28000	183900	141.1	12010	238.3	882	171.2	101.3	17810	251000	42.4	4.9	0.23
BK-JAP-2	1.14E+08	11.3	15430	179700	75.9	20300	109.1	409	58.4	23.3	26680	239000	13.63	-0.01	0.34
BK-JAP-3	1.12E+08	11.5	30940	184400	41.8	14870	172	180.9	132.7	581	9170	235000	35.3	0	0.25
BK-JAP-4	1.06E+08	11.1	10960	187300	213.4	10310	333.3	805	54.4	18.2	24380	262000	15.21	0.27	0.21
BK-JAP-5	1.04E+08	11.3	15730	193500	67	21460	93.1	318	82.2	44.4	29760	239000	13.48	-0.32	0.14
BK-JAP-6	1.09E+08	11.4	19910	183700	229	9740	172.5	204.9	82.2	114.2	12350	252000	31.3	0.74	0
BK-JAP-7	1.19E+08	11.3	15910	178300	1060	19200	176.3	292	113.9	216.8	53300	220000	21.57	1.1	0.22
BK-JAP-8	1.09E+08	11.3	21270	188000	183.7	11950	88.2	966	98	25.8	11260	256000	38	1.94	0.86
BK-JAP-9	1.12E+08	11.4	18570	185000	100	11900	77.3	245.1	94.9	35.3	17460	248000	27	1.19	0.21
BK-JAP-10	1.07E+08	11.5	26210	191400	162.3	11990	195	825	159.2	98.3	16600	259000	41.8	3.27	0.16
BK-JAP500-1	1.08E+08	11.5	25070	187500	153.9	13000	183.8	921	178.1	104	16450	248000	37.5	3.57	0.2
BK-JAP500-2	1.06E+08	11.4	26800	186600	91.9	10890	258.7	457	94.2	3.31	19900	247000	32.1	0.43	0.25
BK-JAP500-3	1.12E+08	11.3	15550	185000	230	10500	60.3	1113	73	23.5	16060	267000	29.7	2.1	0.17
BK-JAP500-4	1.09E+08	11.3	20600	185400	147.9	10820	9.16	547	110.2	26.5	8430	264000	39.1	1.25	0.26
BK-JAP500-5	1.08E+08	11.3	21770	183800	167	12480	209	620	71.7	5.8	23010	247000	27.25	1.38	0.14
BK-JAP500-6	1.11E+08	11.4	24610	183400	231.4	12330	32.48	800	199.4	49.7	13050	254000	50.3	1.15	0.29
BK-JAP500-7	1.05E+08	11.6	25950	190000	205.5	10240	424.1	434	196.8	85.5	19910	254000	35.14	3.78	0.29
BK-JAP500-8	1.08E+08	11.2	16010	180200	292	12110	85.9	1387	42.1	6.8	14970	275000	29.07	1.97	0.09
BK-JAP500-9	1.04E+08	11.6	28460	188500	121.6	10920	173.7	323	115.8	27.3	21530	247000	35.84	2.5	0.32
BK-JAP500-10	1.08E+08	11.4	26600	184500	149.3	11960	129.5	708	139.2	51.1	15750	251000	43.7	3.8	0.17
BK-JAP500-11	1.08E+08	11.4	24360	181200	153.9	11790	104.2	735	97.3	31.8	13810	253000	36.4	3.26	0.04
BK-JAP500-12	1.09E+08	11.1	1733	177100	17.8	45900	30.36	467	20.3	16.5	13530	254000	1.92	-0.01	0.02
BK-JAP500-13	1.05E+08	11.5	24380	184500	122.3	13120	319	444	136.1	119.7	21170	243000	31.04	2.72	0.26
BK-JAP500-14	1.03E+08	11.2	11520	183100	81.1	12260	110.9	810	80.9	14.3	32850	263000	18.77	0.73	0.24
BK-JAP500-15	1.05E+08	11.4	26700	185100	157.4	11780	136.7	757	130.5	64.4	16290	257000	38.1	2.95	0.21
BK-JAP500-16	1.06E+08	11.3	23710	179900	68.4	10200	140.4	242.8	166.4	122.8	15570	237000	35.1	2.69	0.16
BK-JAP500-17	1.04E+08	11.5	24820	182300	136.9	10530	283.5	294.6	88.4	17.7	22810	234000	25.13	0.93	0.28

BK-JAP500-18	1.02E+08	11.5	28200	186600	122.6	10480	274.7	262.9	200.9	218.2	20440	235000	34.9	3.22	0.21
BK-JAP500-19	1.01E+08	11.4	22920	187700	174	12150	71.6	918	119.5	42.3	11950	247000	40	3.79	0.13
BK-JAP500-20	1.02E+08	11.3	18180	185800	184.8	10760	61.9	783	51.3	14.4	11510	262000	31.17	1.63	0.07
BK-JAP500-21	9.77E+07	11.4	25390	191900	185.3	12690	100.3	985	130	43.9	13740	255000	42.3	3.69	0.4
BK-TATRE-1	9.95E+07	11.3	23590	189200	172.2	11770	67.3	830	109.8	45.5	11470	248000	39.2	3.71	0.06
BK-TATRE-2	9.96E+07	11.2	15620	189500	77.4	21770	68.9	622	40.8	7.7	17650	247000	13.99	0.04	0.16
BK-TATRE-3	1.07E+08	11.4	19650	191900	17.4	51100	87.3	163.3	23.83	73.5	15550	210000	94.3	0.95	0.95
BK-TATRE-4	1.08E+08	11.3	22200	184100	76	32000	17.9	1700	50	34.4	7630	238000	20.4	1.9	0.27
BK-TATRE-5	1.05E+08	11.3	17800	186200	45.3	27200	148	889	56.7	16.2	16840	249000	16.81	0.06	0.34
BK-TATRE-6	1.02E+08	11.5	14960	187800	18.7	26590	111.1	353	46.2	39.1	15330	254000	19.99	0.94	2.07
BK-TATRE-7	1.03E+08	11.8	48290	198200	105.9	40400	69.7	2950	119.1	44	7340	189000	35.8	-0.9	0.53
Nova-1	1.02E+08	11.3	21460	186100	73.5	18200	77.4	410	62.4	20.1	17620	252000	20.34	0.38	0.09
Nova -2	1.04E+08	11.4	24420	192000	244	13840	90.2	1201	123.4	17	13110	260000	40.7	3.1	-0.06
Nova -3	1.03E+08	11.3	9220	188300	66.6	26180	131.2	647	12.76	2.57	18860	270000	8.63	-0.57	0.09
Nova -4	9.53E+07	11.2	11450	190700	19.7	9000	133	24.3	64.6	232.7	92000	212000	15.43	-0.6	-0.01
Nova -5	1.02E+08	11.5	27180	189400	194	14620	44.4	930	140.9	17.1	16190	241000	61.8	9.7	0.1
Nova -6	1.08E+08	11.4	21160	178500	80.1	11000	288.3	210.1	80.7	33.8	25360	248000	24.72	1.25	0.15
Nova -7	1.00E+08	11.2	17830	185300	74.3	13830	113.5	271	39.1	42.4	9210	269000	18.58	-0.3	-0.07
Nova -8	1.03E+08	11.2	28970	186600	88.8	14460	29	237.3	35.2	80.3	5190	245000	35.6	0	0.11
Nova -9	8.78E+07	11.4	11000	191100	28.1	28900	124	9800	53	120	12460	253000	7.66	0.6	0.59
Nova -10	1.02E+08	11.3	7400	190300	25.9	19910	91.4	180.2	29	106.4	14970	278000	6.09	-0.53	0
Nova -11	9.56E+07	11.3	3749	185800	15	50300	155.1	615	48.8	89.9	1585	264000	11.77	-0.3	0.07
Nova -12	9.97E+07	12	54500	199300	57.9	37220	58.5	168.9	65.9	2.3	1801	180000	77.7	-1	0.53
Nova -13	9.99E+07	11.3	5920	187100	16.7	61500	161.3	1200	120.2	98.1	55400	199000	3.71	-0.02	0.11
Nova -14	1.02E+08	11.5	14750	187300	29.1	42600	38.3	525	80.2	172.3	5900	244000	15.22	-0.87	0.21
Nova -15	1.02E+08	11.6	26630	190000	77	32470	11.35	753	3.89	0.63	10480	227000	19.86	-0.7	1.09
Nova -16	1.12E+08	11.3	16340	178600	89	11990	175	149	39.1	75.4	12090	274000	21.3	0.5	0.54
Nova -16	1.01E+08	11.4	12780	185700	19.9	53700	38.6	612	46.54	63.1	8640	226000	4.28	-0.69	0.17
Nova -17	1.11E+08	11.2	4070	177200	13.9	50500	221.1	463	57.3	93.4	28710	230000	6.69	-1	0.17
Nova -18	9.88E+07	11.2	7590	181400	17.5	41100	193.7	382	192.2	6.3	5010	256000	12.01	-0.65	-0.09

Nova -19	1.02E+08	11.7	24140	187300	22.7	44400	8.98	194.2	21.27	6.4	17570	214000	7.5	-0.29	0.3
Nova -20	9.92E+07	11.5	25060	187800	26.8	21390	147.2	57.9	52.5	69.6	4580	253000	41.8	0.4	0.06
Nova -21	1.00E+08	11.3	5160	181600	20.5	38690	287.7	590	54.6	79.3	64700	214000	7.97	-0.14	-0.07
Nova -22	9.92E+07	11.4	19240	185600	43.3	32250	152.5	420	116.2	115.4	9320	241000	8.92	1.27	0.51
Nova -23	9.05E+07	11.5	21420	191400	90.4	8740	137.4	22.5	46.6	46.9	18180	264000	21.55	-0.7	0.19
Nova -24	9.83E+07	11.5	15190	189600	17.6	45900	36.13	385	54.4	42.8	17690	226000	8.75	-0.41	0.22

Table 2a. Major and trace elements of BK detrital garnets, determined in situ by electron probe analyses.

	Zn	Ga	Ge	As	Rb	Sr	Y	Zr	Nb	Sn	Ba	Hf	Ta	Pb	Th	U
BK-JAP-1	97.3	14.48	8.98	0.1	0.57	0.19	1009	160.6	0.026	0.196	0.02	2.34	0.006	0.043	0.0021	0.0103
BK-JAP-2	87.4	13.93	11.13	0.07	0.585	0.353	1751	33	0.029	0.13	0.021	0.8	0.014	0.015	0.0022	0.033
BK-JAP-3	80.9	10.68	7.44	0.1	0.063	0.003	263	16.18	0.027	0.016	-0.071	0.479	-0.0042	0.02	-4E-06	0.0114
BK-JAP-4	117.8	22.47	11.68	0.31	0.241	0.119	1203	46.9	0.057	0.099	0.09	1.05	0.066	0.0026	-4.1E-06	0.035
BK-JAP-5	86.5	13.32	12.2	0.16	0.72	0.438	2001	27.2	0.003	0.17	-0.133	0.498	-0.0021	0.0086	0.0011	0.031
BK-JAP-6	97.8	9.98	13.28	0.03	0.155	0.075	840	43.8	0.011	0.096	0	0.79	0.0023	0.007	0.001	0.027
BK-JAP-7	73.3	9.88	10.31	0.32	-0.036	0.57	72.4	99	0.008	0.48	0.05	2.91	0.004	0.141	0.146	0.495
BK-JAP-8	131.7	15.2	7.84	0.063	0.058	0.069	213	124.8	0.015	0.22	0.15	1.97	0.003	0.167	0.0033	0.038
BK-JAP-9	98.1	14.3	9.7	0.07	0.087	0.051	695	39	0.007	0.12	-0.053	0.73	-0.0021	0.012	-4E-06	-1.8E-06
BK-JAP-10	114.3	14.77	9.2	0.03	0.2	0.08	797	117.3	-0.0032	0.051	0.08	1.87	-0.0003	0.008	-4.2E-06	0.0114
BK-JAP500-1	110.8	15.28	8.59	0.11	0.254	0.16	857	121.1	-0.0025	0.24	0.13	1.83	0.004	0.015	-4.1E-06	0.015
BK-JAP500-2	50.7	15.47	14.66	0.1	0.53	0.042	2230	129.5	-0.0069	0.199	-0.01	1.9	-0.0055	0.009	-4.2E-06	0.0056
BK-JAP500-3	121.3	18.3	8.8	0.12	-0.003	0.077	28.5	48.6	0.075	0.16	0.065	1.58	0.044	0.013	-3.9E-06	0.038
BK-JAP500-4	160.9	15.06	7.47	0.07	-0.002	0.02	20.7	75.5	0.01	0.107	0.15	1.3	-0.0004	0.0056	-4.1E-06	0.0036
BK-JAP500-5	83.7	14.9	10.36	0.11	0.29	2.8	1313	107.6	0.008	0.14	0.06	1.84	0.0037	0.041	-4E-06	0.02
BK-JAP500-6	109.5	14.89	7.54	0.16	0.062	0.042	97.4	142.2	0.009	0.1	-0.024	2.23	-0.0006	0.0089	0.0035	0.047
BK-JAP500-7	56.5	10.59	12.7	0.02	0.541	0.271	1810	117.1	-0.0041	0.102	-0.023	1.51	0.009	0.0079	-4.3E-06	0.0042
BK-JAP500-8	132	20.76	9	0.09	0.029	0.071	337.6	121.4	0.059	0.138	0.16	2.5	0.037	0.0075	0.0084	0.079

BK-JAP500-9	86.4	10.36	8.64	0.1	0.141	0.138	813	74.7	0.016	0.16	-0.003	1.27	-0.0012	-0.001	-4.2E-06	0.0043
BK-JAP500-10	101.4	13.32	9.2	0.11	0.081	0.09	551	118.9	0.006	0.14	0.05	1.82	-0.0008	0.0057	0.0044	0.0118
BK-JAP500-11	85	14.66	8.93	0.35	0.021	0.031	201.2	95.8	0.013	0.116	0.06	1.83	0.0095	0.0061	-4E-06	0.023
BK-JAP500-12	32.8	12.39	25.6	0.2	0.004	-0.023	84.2	1.17	0.044	1.38	0.12	0.021	0.013	0.019	-3.9E-06	-1.8E-06
BK-JAP500-13	95.5	13.23	9.42	0.14	0.331	0.181	1164	68.1	0.023	0.102	0.13	1.29	0.018	0.009	0.0045	0.016
BK-JAP500-14	84.5	24.4	14.31	0.26	0.87	0.27	4570	28.6	0.007	0.181	-0.064	0.75	0.016	0.0035	-4.1E-06	0.0163
BK-JAP500-15	102.3	13.33	8.67	0.17	0.094	0.107	551	106.8	0.009	0.088	-0.057	1.78	0.0071	0.016	-4.1E-06	0.0089
BK-JAP500-16	86.4	11.9	13.13	-0.041	0.307	0.087	1497	52.7	0.012	0.15	0.15	1.03	-0.0002	0.028	-4E-06	-1.9E-06
BK-JAP500-17	90.1	11.68	11.15	0.09	0.386	0.118	1368	62.5	0.001	0.125	-0.036	1.14	0.006	0.008	-4.1E-06	-2E-06
BK-JAP500-18	46.4	10.07	8.22	0.14	0.179	0.176	760	51.5	0.009	0.042	-0.02	0.97	-0.0005	0.0102	-4.2E-06	-2E-06
BK-JAP500-19	127.8	14.23	8.44	0.21	0.121	0.029	295	125.7	0.024	0.125	-0.111	2	0.014	0.021	-4.2E-06	0.013
BK-JAP500-20	143.9	14.94	7.89	0.11	0.04	0.031	129.9	90.5	0.002	0.076	0.05	1.75	-0.0029	0.016	0.0019	0.023
BK-JAP500-21	117.4	14.58	9.3	0.09	0.09	0.101	455	140.8	0.017	0.11	-0.02	2.1	0.009	0.011	-4.3E-06	0.019
BK-TATRE-1	122.6	14.06	8.87	0.16	0.116	0.035	201.2	108	0.0035	0.139	-0.02	1.67	0.013	0.0017	0.0022	0.0155
BK-TATRE-2	95.5	14.62	8.8	0.35	0.13	0.114	808	46.1	0.021	0.148	-0.01	0.8	0.02	0.06	0.0024	0.033
BK-TATRE-3	66.8	2.36	5.52	0.04	-0.004	0.018	34.4	1.03	-0.001	0.074	-0.089	0.007	-0.0041	0.198	-3.9E-06	-1.9E-06
BK-TATRE-4	117	10.8	6.25	-0.07	0.027	-0.018	105	62.4	0.037	0.11	0.13	0.84	0.031	0.043	0.0072	0.015
BK-TATRE-5	89.1	13.59	10.1	0.2	0.3	0.158	1097	41.1	0.015	0.122	0.07	0.63	0.0092	0.113	0.0082	0.029
BK-TATRE-6	102.6	5.85	23.2	0.09	0.219	0.113	39	4.34	3.7	1.28	0.14	0.063	0.166	0.212	0.034	0.035
BK-TATRE-7	63.4	11.11	5.49	0.12	-0.026	0.038	193	73.4	0.023	0.17	-0.034	1.23	0.006	0.012	0.0056	0.038
Nova-1	85.7	12.53	7.46	0.02	0.08	0.03	731	24.1	0.007	0.072	0.04	0.46	0.0079	0.02	0.0039	0.018
Nova -2	71.3	13.8	8.49	0.3	-0.06	0.034	186.3	166.4	0.016	0.073	-0.044	2.58	0.014	0.011	0.0065	0.023
Nova -3	116.1	15.72	10.13	0.26	0.074	0.051	587	35.1	0.104	0.11	-0.024	0.99	0.076	0.007	0.001	0.064
Nova -4	43.3	14.2	30.8	-0.014	0.06	0.13	189.2	5.6	0.013	0.19	0.04	0.15	0.0037	0.02	-4.2E-06	0.015
Nova -5	81.2	16.19	6.53	0.04	0.066	4.6	214.1	218.3	0.003	0.021	1.1	3.49	-0.0031	0.147	0.0099	0.03
Nova -6	99	16.29	14.61	0.035	0.69	0.326	2392	33.6	0.005	0.143	-0.084	0.669	-0.0004	0.016	-3.8E-06	0.0023
Nova -7	76.8	6.87	21.6	0.15	-0.001	0.085	224	2.68	0.79	1.2	-0.11	0.052	0.127	0.038	0.0012	0.105
Nova -8	112.8	6.17	6.17	-0.013	0.006	-0.022	15.89	5.43	0.002	0.21	-0.05	0.088	0.009	0.0026	-3.9E-06	0.0105
Nova -9	64.6	6	22.2	0.72	-0.02	0.09	399	3.7	22.6	0.64	-0.08	0.19	2.27	0.152	0.242	0.54
Nova -10	51	4.96	13.2	0.084	0.01	0.021	224.3	1.12	-0.0045	0.35	0.07	0.041	0.0016	0.031	-4E-06	0.0191

Nova -11	77.9	7.29	11.5	0.12	0.038	-0.045	230	5.1	0.103	1	0.05	0.142	0.04	-0.0009	-4.1E-06	0.045
Nova -12	145.5	6.95	2.57	0.67	-0.048	0.068	98.3	2.55	0.015	0.128	0.14	0.074	0.0019	0.059	-4.2E-06	0.0016
Nova -13	29	7.84	15.3	0.21	0.051	0.091	131.3	1.75	1.02	0.54	-0.038	0.043	0.094	0.058	0.0011	0.0028
Nova -14	51.2	7.91	7.46	0.22	0.096	0.038	56.9	3.43	0.076	0.26	-0.077	0.126	0.014	0.014	-3.9E-06	0.0022
Nova -15	35.3	9.65	2.49	-0.009	0.067	0.05	61	21.67	0.028	0.173	-0.052	0.246	-0.0044	0.191	0.0026	0.0073
Nova -16	76.2	6.77	28.1	0.28	-0.07	0.03	184	2.61	0.39	1.32	0	0.099	0.073	0.24	0.014	0.079
Nova -16	33.6	6.48	12.53	0.14	0.083	-0.005	31.9	2.83	-0.0004	0.21	0.026	0.051	-0.0031	0.52	-3.9E-06	0.0011
Nova -17	25	6.06	20.3	0.18	0.03	0.057	317	0.88	0.159	0.79	-0.02	-8.9E-05	0.116	0.08	0.0031	-1.8E-06
Nova -18	33.5	8.3	13	0.12	-0.028	-0.015	201.1	1.31	0.028	0.4	0	0.036	0.013	0.011	-3.9E-06	-2E-06
Nova -19	163.1	4.22	3.61	0.23	0.28	0.027	291	3.78	0.006	0.14	0.26	0.077	0.014	0.35	0.0038	-2E-06
Nova -20	157	6.57	12.76	0.21	0.088	-0.049	367.6	1.44	-0.0123	0.43	0.01	0.028	0.0088	0.0088	-3.9E-06	0.0067
Nova -21	23.6	7.1	9.2	0.06	0.054	0.026	182.4	0.518	0.33	0.69	0	0.013	0.031	0.027	0.0025	0.0187
Nova -22	21.6	10.1	11.41	0.36	0.65	0.111	792	2.94	0.137	0.61	0.28	0.047	0.009	0.3	0.119	0.022
Nova -23	58.2	7.48	10.9	0.21	0.13	0.113	251	4.65	0.019	0.3	0.19	0.147	-0.00861	-0.00087	0.0048	0.0076
Nova -24	38.5	5.76	10.7	0.15	0.106	0.028	367	2.27	0.012	0.19	-0.03	0.028	-0.0023	0.0073	0.0046	-2.1E-06

Table 2b. Major and trace elements of BK detrital garnets, determined in situ by electron probe analyses.

IB Garnet Major and Trace	Al	Li	Mg	Si	P	Ca	Sc	Ti	V	Cr	Mn	Fe	Co	Ni	Cu
Cont-1	1.45E+08	11.2	20370	181200	327	12820	209.6	1595	82.5	10.2	19250	237000	26.75	3.16	0.49
Cont -2	1.43E+08	11.1	11060	179500	14.6	47200	122.7	166.2	142.6	87.6	8330	247000	11.62	0.11	-0.003
Cont -3	1.43E+08	11.4	25040	181000	241	13030	136.4	982	172.7	26.2	16290	250000	42.6	4.32	0.11
Cont -4	1.43E+08	11.8	37220	194000	49.4	27620	96.9	87.4	78.3	75	10820	226000	47.9	0.24	0.09
Cont -5	1.39E+08	11.4	17200	184600	99	7420	150.9	60.8	72.4	73.5	10870	280000	46.6	0.53	0.2
ZAULE-1	1.30E+08	11.2	19800	191000	28.3	19180	87.8	9620	56.3	64.7	64200	214000	21.3	0.42	0.53
ZAULE-2	1.57E+08	11.1	6360	179300	60	9180	112.2	642	48.6	3.32	88900	218000	4.81	0.06	0.39
ZAULE-3	1.42E+08	11.8	40740	196500	89.9	11060	138.4	332.3	745	372	22870	242000	81.9	7.09	0.14
ZAULE-4	1.54E+08	13.2	131.4	184800	80	152000	3.94	679	454	-0.38	115.6	82500	1.76	-0.64	0.09

ZAULE-5	1.42E+08	11.3	7490	186400	19.6	30460	35.9	425	70.3	44.4	52400	240000	11.16	-0.27	0.06
ZAULE-6	1.38E+08	11.2	16790	184700	65.3	42660	36.87	1823	61.6	13.8	15270	234000	14.03	0.2	0.12
ZAULE-7	1.42E+08	11.5	13040	181200	42.7	25340	102.9	253	24.12	51	17670	256000	6.15	-0.21	0.04
ZAULE-8	1.56E+08	11.6	31500	181800	41.2	38100	61.7	220.6	50.5	31.1	1854	231000	77	1.22	1.52
ZAULE-9	1.38E+08	11.5	27350	187700	54.8	9340	112.6	12.6	44.5	116.1	26210	243000	34.3	0.45	0.34
ZAULE-10	1.41E+08	11.6	29890	186700	32.5	53800	38.2	236	70.6	11.2	3198	211000	43.9	-0.23	0.13
ZAULE-11	1.40E+08	11.4	5060	180000	21.9	58800	49.4	1227	60.2	60.5	46300	206000	17.86	-0.19	-0.06
ZAULE-12	1.48E+08	11.6	21240	187000	24.1	51800	58.8	300.5	100.3	149.6	5100	223000	40.7	0.16	-0.01
BER-1	1.37E+08	11.3	2150	181600	101.6	148600	7.69	876	269.1	23.5	1936	114000	3.36	7.09	0.79
BER-2	1.36E+08	11.2	8710	181700	51.2	15570	65.4	341	55.4	60.6	64000	227000	16.83	2.12	-0.07
BER-3	1.07E+08	9.7	5800	187200	380	223100	3.13	2139	98	10.3	10820	59000	1.12	19.3	1.29
BER-4	1.35E+08	10.8	3275	180100	2	51300	45.2	594	52.5	0.28	100000	172000	4.22	-0.03	0.01
BER-5	1.38E+08	11.3	29460	180400	33.1	9430	165.5	30.7	36.39	31.4	29380	241000	47.9	0.55	1.35
BER-6	1.34E+08	11.3	13490	177400	15.1	33130	78.6	359.8	70.1	14.1	14910	248000	20.82	-0.3	0.13
BER-7	1.32E+08	11.4	23700	183600	52.8	43400	21.59	1773	45.07	25.7	8000	224000	19.61	-0.02	0.23
BER-8	1.32E+08	11.3	12620	179300	113.9	35800	71.4	672	100.7	86.8	26290	232000	6.07	1.22	0.24
BER-9	1.32E+08	11.7	23380	185400	25.6	50300	137.5	321	66.3	47.1	10920	224000	46.2	1.45	0.35
BER-10	1.33E+08	11.4	18800	176200	24.4	19220	78.6	33.9	56	68.6	23830	238000	19.92	-0.44	0.19
BER-11	1.36E+08	11.1	360	164200	34.9	144200	15.94	214	390.1	3.91	648	104000	0.93	1.28	0.17
BER-12	1.34E+08	11.3	3750	177900	10.5	60100	120.2	507	75.3	37.1	16400	244000	8.88	-0.5	-0.092
BER-13	1.35E+08	12	60600	189700	95.1	7290	70.2	306.6	166.3	249.1	2583	211000	17.41	-0.42	0.17
BER-14	1.28E+08	11.3	15740	174100	61.5	21340	113.1	486	61.5	23.3	27000	262000	13.74	-0.3	0.19
BER-15	1.28E+08	11.3	18890	179700	30.1	16020	997	178.4	149.2	172.1	47900	233000	19.04	1.22	0.45
BER-16	1.16E+08	11.4	24110	185900	202	12820	91.6	1092	129.4	37.1	12610	248000	41.2	3.37	0.07
BER-17	1.17E+08	11.5	28860	187000	172.1	12040	115.2	923	140.6	49.5	17120	255000	37.84	3.12	0.33
BER-20	1.38E+08	11.4	17310	187100	18.8	55300	81.8	338	87.1	181	7130	210000	34.7	-0.5	0.44
BER-21	1.14E+08	11.4	24890	189900	81.2	21640	133	831	68.9	57	11890	252000	19.51	-0.04	0.08
BER-22	1.20E+08	11.3	21320	180200	132.7	11090	26.45	465	138.2	45.2	15600	261000	25.29	1.27	0.11
BER-23	1.11E+08	11.2	15590	186000	69.3	29870	148.9	1211	47.8	12	15650	238000	14.38	0.67	0.19
BER-24	1.28E+08	11.4	17700	187300	27.7	26400	130.5	125.2	63.3	143.4	14730	237000	23.6	0.61	0.02

BER-25	1.19E+08	11.3	20600	181600	480	4770	192.9	36	24.12	61.5	13520	260000	31.42	-0.59	0.12
BER-26	1.21E+08	11.4	19070	183100	60.6	24470	116.3	716	88.2	25.3	16670	231000	15.98	0.54	0.29
BER-27	1.17E+08	11.4	17220	190400	25.1	42600	67.9	522	81.4	336.6	9830	241000	24.77	-0.25	0.09
KRK-1	1.17E+08	11.3	21380	184900	91.9	18540	99.9	941	62.6	18.9	18720	253000	20.42	0.35	0.12
KRK-2	1.15E+08	11.4	20460	189900	55.9	24890	97.3	835	103.3	64.4	18550	254000	17.42	0.24	0.13
KRK-3	1.15E+08	11.4	15620	186900	66.6	22210	84.2	514	16.1	0.64	20250	262000	14.43	0.43	0.16
KRK-5	1.14E+08	11.6	25420	189700	146.9	8860	202.9	100.3	153.9	301.1	14510	268000	21.78	0.39	0.01
KRK-6	1.20E+08	11.2	15530	180600	201.1	10760	217.4	984	43.7	4.56	18300	282000	24.91	0.3	0.07
KRK-7	1.12E+08	11	2751	183700	20.7	40300	168.4	664	74.7	127.9	94800	183000	9.9	-0.27	0.14
KRK-8	1.15E+08	11.4	20780	192000	112.7	11720	64.4	220.2	115	66.2	16830	261000	35.47	1.87	0.2
KRK-9	1.13E+08	11.2	15560	182400	294	10930	113.5	1319	31.4	9.9	33960	260000	15.47	0.51	0.06
KRK-11	1.10E+08	11.4	26940	190700	110.7	10590	232	348.1	110.4	110.2	20460	245000	33.7	2.98	0.08
KRK-12	1.12E+08	11.5	23910	188800	317	3730	139.6	16	9.31	0.62	31330	267000	18.83	0.1	0.22
KRK-13	1.11E+08	11.3	18010	185200	425	6610	152.7	301.2	48.1	56.2	5340	297000	28.63	0.5	0.07
KRK-14	1.15E+08	11.2	8610	177600	66.5	23560	132.6	515	18.11	14.1	19510	271000	8.43	-0.94	0.1
KRK-15	1.08E+08	11	1871	184800	24.8	21920	50.7	677	340.3	100.7	159000	142000	3.08	-0.36	0.54
KRK-16	1.12E+08	11.4	22060	183400	180	11900	478	954	71.9	8.55	27090	244000	22.96	1.02	0.18
KRK-17	1.12E+08	11.4	19110	183500	118.7	13100	328.5	903	81	25.1	27410	246000	21.24	1.9	0.66
KRK-18	1.16E+08	11.4	17600	180700	59.9	22030	110.5	229.7	30.77	30.9	3417	258000	21.36	0.38	0.25
KRK-19	1.11E+08	11.6	27630	188100	84.2	10930	639	321	109.6	98	26220	240000	29.6	1.7	0.19
RAB-1	1.12E+08	11.3	23800	181600	158.4	11710	79	800	94.1	19.7	11970	258000	39.5	3.51	0.06
RAB-2	1.13E+08	11.4	23530	179500	181	12060	217.7	659	236	255	17580	251000	44.86	3.42	0.001
RAB-3	1.13E+08	11.5	26110	184800	165.4	12240	93.7	823	119.9	45.1	15490	255000	35.8	4.07	0.14
RAB-4	1.11E+08	11.4	23130	180100	150.8	11890	272.6	717	152.1	90.3	25350	235000	26.53	1.92	0.15
RAB-5	9.84E+07	11.2	9420	181200	14.1	36300	114.8	281	45.1	112.3	61300	212000	25	0.2	0.15
RAB-7	1.11E+08	11.4	26750	179900	155.4	11690	287.9	419	155.2	87.1	17370	240000	38.88	2.9	0.17
RAB-8	1.09E+08	11.2	24520	176300	155.5	11560	82.3	809	119.1	46.6	12300	246000	39.38	3.27	0.01
RAB-9	1.10E+08	11.3	21780	181700	235	12970	51.9	1216	85.6	9.9	12940	260000	40.96	2.98	0.13

Table 3a. Major and elements of IB detrital garnets, determined in situ by electron probe analyses.

	Zn	Ga	Ge	As	Rb	Sr	Y	Zr	Nb	Sn	Ba	Hf	Ta	Pb	Th	U
Cont-1	102.2	16.54	8.22	0.43	1.41	0.306	1728	322	0.032	0.169	0.25	4.42	0.023	0.047	0.026	0.045
Cont -2	115.8	18.86	9.49	0.16	0.196	0.06	488	2.09	0.008	0.4	-0.03	0.114	-0.0019	0.0039	-3.5E-06	-1.2E-06
Cont -3	95.5	14.76	7.49	0.33	0.236	0.119	706	229.3	0.0126	0.111	-0.03	3.44	0.0041	0.02	0.0095	0.035
Cont -4	50.2	5.41	5.11	0.11	0.023	-0.033	47.3	4.34	0.0019	0.169	0.04	0.115	-0.0029	0.035	-3.7E-06	0.0019
Cont -5	101.4	7.4	15.79	0.01	0.277	-0.01	416.7	3.73	0.0061	0.22	0.01	0.147	0	0.109	0.0053	0.023
ZAULE-1	24	6.55	28.3	1.83	0.297	0.64	191.2	3.51	29.1	3.29	0.11	0.246	2.23	0.5	0.235	1.57
ZAULE-2	41	14.31	15.7	0.1	0.6	0.19	1173	9.05	0.019	1.54	0.19	0.29	0.054	0.083	0.0034	0.053
ZAULE-3	131.9	11.86	9.42	0.19	0.099	0.092	214.7	41	0.0087	0.113	0.01	0.8	-0.0009	0.023	0.0006	0.0089
ZAULE-4	0.42	112.1	7.8	2.06	0.4	402	343	32.3	0.01	1.02	1.2	1.87	0	0.079	2.24	12.8
ZAULE-5	39.1	6.69	25.8	0.22	0.008	0.011	31.8	0.41	0.139	0.88	-0.06	0.011	0.071	0.0136	-3.5E-06	0.039
ZAULE-6	96.1	11.4	7.51	0.4	0.17	0.02	339	43.4	0.37	0.367	-0.07	0.76	0.065	0.0074	0.0057	0.05
ZAULE-7	32.4	4.82	9.68	0.11	0.081	-0.013	126	1.22	0.037	0.444	-0.1	0.019	0.0039	0.033	0.0029	0.048
ZAULE-8	113.9	4.99	3	0.08	0.149	-0.061	37.3	2.1	0.005	0.204	0.17	0.053	0.0044	0.191	0.0017	0.0013
ZAULE-9	51.6	7.13	13.97	0.13	0.081	-0.027	133.4	1.7	-0.0038	0.084	-0.01	0.053	-0.0005	0.043	-3.7E-06	0.0135
ZAULE-10	149.6	5.14	3.76	0.033	0.011	-0.004	47.4	1.88	0.0033	0.2	-0.11	0.03	0.0024	0.029	-3.6E-06	-1.4E-06
ZAULE-11	26.2	6.86	13.5	0.06	-0.015	0.043	44.1	12.6	3.25	0.78	0.04	0.4	0.241	0.073	0.046	0.087
ZAULE-12	54.3	7.72	3.8	-0.002	0.007	0.018	48.6	1.04	0.0015	0.208	0	0.012	0.0047	0.0089	-3.5E-06	0.0006
BER-1	28.5	42.3	2.96	1.68	0.136	174.1	16.62	14.01	0.109	0.51	6.22	0.456	0.021	6.54	0.215	0.04
BER-2	7.1	6.68	15.52	-0.134	0.032	0.026	256.4	6.15	0.244	0.81	-0.06	0.129	0.089	0.025	-3.6E-06	0.058
BER-3	31.6	23.74	2.61	19	5.22	21	11.8	18.4	8.31	3.77	9.2	0.52	0.223	2.23	1.84	1.84
BER-4	154.1	7.8	11.85	0.03	0.055	0.116	63.7	0.606	0.129	4.66	0.06	0.046	0.054	0.015	-3.5E-06	-1.3E-06
BER-5	98.9	7.24	20.5	0.4	0.042	0.033	196.6	3.34	0.015	0.212	0.12	0.07	0.0026	0.02	-3.6E-06	-1.4E-06
BER-6	30.2	5.72	12.41	0.3	-0.001	0.024	53.1	1.45	0.051	0.527	-0.17	0.048	0.0173	0.049	0.0031	0.0346
BER-7	103.5	10.7	6.51	0.22	0.071	-0.02	98.6	53.4	0.029	0.15	-0.05	0.687	0.0065	0.015	0.0058	0.042
BER-8	81.4	9.14	15.76	3.05	0.075	0.17	87.2	20.44	1.314	1.39	0.08	0.471	0.358	0.2	0.081	0.559
BER-9	105.6	5.96	6.07	0.22	0.105	0.01	269.6	148	0.0025	0.261	-0.01	4.44	-0.00639	0.043	0.134	0.207
BER-10	11.7	5.74	7.66	0.06	0.066	-0.07	106.8	1.61	0.0034	0.269	-0.08	0.03	0.0085	0.043	0.0053	0.035

BER-11	14.11	44.6	17.33	2.63	0.074	370	59	24.2	0.043	0.572	14.37	1.07	-0.0026	15.23	0.484	0.169
BER-12	24.3	7.06	19.72	0.21	0.061	0.026	60.7	0.71	0.03	0.199	0.13	0.01	0.0049	0.012	-3.7E-06	-1.4E-06
BER-13	137.9	12.74	4.47	0.26	0.033	-0.047	113.4	40.7	0.014	0.183	-0.01	0.89	-0.0016	0.011	-3.9E-06	0.029
BER-14	90.5	12.03	9.44	0.15	0.322	0.14	1208	26.5	0.051	0.148	0.05	0.56	0.031	0.077	0.029	0.04
BER-15	48.7	18.2	14.41	0.08	0.99	0.41	2880	16.99	0.014	0.059	-0.186	0.409	0.005	0.039	0.018	0.0035
BER-16	120.5	13.67	7.86	0.18	0.138	0.07	365	157.5	0.009	0.156	-0.1	2.49	0.0017	0.0011	0.0012	0.037
BER-17	77.1	13.85	7.94	0.21	0.18	0.005	575	131.2	0.029	0.176	-0.01	2.01	-0.0059	0.016	-4.2E-06	0.0088
BER-20	35.8	6.22	3.63	0.03	0.1	0.17	64.3	1.41	-0.004	0.28	0.13	0.043	0.003	0.131	0.0036	-1.4E-06
BER-21	98.5	11.22	8.64	0.12	0.245	0.026	808	49.4	0.008	0.153	-0.01	0.83	0.014	0.016	-4.3E-06	0.023
BER-22	123.7	12.44	7.48	0.14	-0.034	-0.035	221.9	57	0.014	0.134	0.05	0.97	-0.0008	0.0009	-4E-06	0.0032
BER-23	87.3	14.6	10.03	0.44	0.487	0.174	1471	64.6	0.041	0.15	-0.01	0.91	0.012	0.008	0.0009	0.039
BER-24	47.9	6.68	8.3	0.41	0.201	0.143	440	1.78	0.022	0.12	-0.09	0.089	0.012	0.011	-3.8E-06	0.009
BER-25	81.5	4.56	8.68	0.05	0.011	-0.013	28.79	1.49	0.003	0.39	0.08	0.062	0.0048	0.031	-4.1E-06	0.031
BER-26	81.5	11.77	9	0.15	0.247	0.081	932	28.4	0.007	0.241	-0.06	0.468	0.019	0.0057	0.02	0.031
BER-27	55.3	6.76	9.44	0.11	0.01	-0.01	24.7	4.05	0.54	0.56	-0.08	0.104	0.043	0.0042	0.0038	0.017
KRK-1	88.1	12.24	8.99	0.1	0.375	0.28	1398	38.57	0.014	0.147	-0.05	0.67	0.005	0.015	0.0059	0.033
KRK-2	90.2	12.04	9.35	0.19	0.399	0.146	1003	26.91	0.0005	0.143	-0.05	0.409	0.0068	0.0084	-4.2E-06	0.0186
KRK-3	97.4	12.92	7.88	0.44	0.158	0.04	467	34.5	0.013	0.102	0.02	0.478	0.029	0.018	-4.2E-06	0.0234
KRK-5	63.6	9.24	7.08	-0.05	0.055	0.055	309.9	13.88	-0.006	0.141	0.05	0.332	0.011	0.008	-4.3E-06	-1.8E-06
KRK-6	140.7	19.04	10	-0.01	0.133	0.033	863	60.2	0.022	0.065	-0.03	1.31	0.024	0.014	-3.9E-06	0.033
KRK-7	23	8.13	36.9	0.36	0.197	0.28	346.5	2.05	0.591	1.4	0.09	0.077	0.158	0.022	-4.1E-06	0.0019
KRK-8	107.8	15.43	11.35	0.08	0.088	0.064	1057	37.34	0.004	0.171	-0.03	0.81	0.006	0.0072	-4.1E-06	0.0028
KRK-9	88.7	18.86	5.45	0.23	0.204	0.096	717	107.2	0.04	0.122	0.05	2.18	0.025	0.0052	0.017	0.042
KRK-11	95.1	12.44	12.58	0.08	0.46	0.077	1779	85.1	-0.0041	0.083	-0.05	1.34	0.003	0.0041	-4.3E-06	-1.8E-06
KRK-12	81.1	12.12	30.3	0.08	-0.014	-0.018	157.1	3.41	0.0024	0.25	0.084	0.121	0.013	0.0077	-4.3E-06	0.0063
KRK-13	116.5	6.54	11.58	0.12	0.038	0.063	232.9	2.6	-0.0058	0.91	-0.03	0.064	-0.0065	0.0076	-4.2E-06	0.083
KRK-14	113.7	15.18	9.32	0.38	0.2	-0.004	609	29.7	0.052	0.23	0.01	0.805	0.051	0.0105	0.001	0.039
KRK-15	30.3	12.79	78.4	1.19	0.031	0.056	32.43	1.64	2.75	3.55	0.12	0.043	0.418	0.241	-4.2E-06	0.207
KRK-16	92.4	18.53	14.02	0.27	0.78	0.41	2590	138.6	0.017	0.12	0.04	2.25	0.01	0.01	0.0049	0.0071
KRK-17	99	19.4	14.35	0.18	1.2	0.43	3290	84.1	0.024	0.194	0.01	1.58	0.014	0.229	0.0079	0.036

KRK-18	128.3	6.13	11.29	0.2	0.08	0.064	369	1.88	0.013	0.5	0.04	0.063	-0.0016	0.031	-4.1E-06	0.028
KRK-19	85.3	12.45	13.7	0.08	0.74	0.362	1766	66.7	0.004	0.16	0.01	1.03	-0.0062	0.009	-4.3E-06	0.0041
RAB-1	117.6	14.45	8.7	0.2	-0.038	0.003	202.7	100.2	0.016	0.175	-0.01	1.8	-0.0005	0.0009	-4.1E-06	0.0168
RAB-2	93.4	13.34	9.39	0.13	0.337	0.142	830	151	0.017	0.095	0.11	2.62	0.004	0.032	0.0204	0.02
RAB-3	54.4	14.67	7.94	0.11	-0.023	0.039	244.9	105.9	0.021	0.198	0.03	1.74	0.0009	0.012	-4.1E-06	0.0153
RAB-4	77.9	16.63	11.83	0.03	0.66	0.219	2238	120.9	0.009	0.079	0.05	1.9	-0.0032	0.011	-4.1E-06	0.0162
RAB-5	48.4	7.38	35	-0.01	0.157	0.18	220.5	16.2	0.01	0.58	0.1	0.38	0.022	0.022	-4.5E-06	0.014
RAB-7	91.1	13.74	8.88	0.08	0.401	0.309	1029	114.8	0.002	0.142	0.07	1.95	-0.0019	-0.00108	0.0008	0.0178
RAB-8	106.6	13.68	8.56	-0.017	0.066	0.017	339.5	112.8	0.011	0.22	-0.01	2.04	-0.0011	0.019	0.0027	0.022
RAB-9	113.4	16.93	7.55	0.29	-0.004	0.004	197.5	183.9	0.041	0.18	-0.05	3.25	0.013	0.0017	0.0141	0.049

Table 3b. Major and trace elements of IB detrital garnets, determined in situ by electron probe analyses.

Rare Earth Elements

JB Garnet REE	^{139}La	^{140}Ce	141Pr	^{146}Nd	^{147}Sm	^{153}Eu	^{157}Gd	^{159}Tb	^{163}Dy	^{165}Ho	^{166}Er	^{169}Tm	^{173}Yb	^{175}Lu
JB-1-1	0.013	0.024	0.003	0.053	0.147	0.113	3.68	2.98	47.8	16.4	62.2	11.42	86	11.95
JB-1-2	0.005	0.05	0.019	0.35	1.57	0.68	6.69	1.89	20.2	6.86	29.1	5.88	51.7	8.23
JB-1-3	-0.002	-0.0029	0.0029	0.131	0.75	0.581	6.91	2.96	31	7.15	19.8	2.81	21	2.85
JB-1-4	-0.001	0.055	0.047	0.88	1.69	1.08	5.46	1.111	8.68	2.38	9.27	1.73	14.8	2.57
JB-1-5	0.005	-0.0024	0.0115	0.163	1.05	0.342	7.99	3.3	32.1	7.91	24.7	3.5	25.1	3.77
JB-1-6	0.015	0.051	0.038	0.75	1.38	1.051	4.83	1.186	10.54	2.93	9.64	1.499	10.53	1.51
JB-1-7	0.009	0.024	0.0191	0.336	0.389	0.375	1.41	0.314	2.44	0.536	1.422	0.197	1.48	0.22
JB-1-8	-0.0078	-0.0008	0.0023	0.052	0.371	0.371	3.16	1.401	16.28	4.97	18.07	2.9	21.8	3.69
JB-1-9	0.0089	0.0034	-0.0027	0.005	0.048	0.115	1.23	0.702	10.86	4.05	15.19	2.34	15.29	2.18
JB-1-10	-0.0025	0.0005	-0.0023	-0.0154	0.025	0.042	0.345	0.265	4.86	1.843	7.65	1.315	9.76	1.391
JB-1-11	-0.0045	0.0068	0.0003	0.181	1.73	2.13	38	17.15	153.8	33	87.2	10.6	63.2	8.66

JB-1-12	0.001	-0.003	-0.0001	0.035	0.133	0.09	1.12	0.598	9.11	3.03	9.74	1.315	8.27	1.163
JB-1-13	0.014	0.033	0.017	0.145	0.432	0.051	2.13	1.164	14.34	4.06	13.95	2.38	16.79	2.07
JB-1-14	0.001	-0.0055	0.0025	0.014	0.38	0.269	4.48	2.304	20.39	3	5.87	0.711	4.74	0.695
JB-1-15	-0.0071	-0.0017	0.0021	0.043	0.303	0.069	2.56	1.591	26.88	9.2	35.2	6.22	44.8	6.04
JB-1-16	-0.0032	0.027	0.0106	0.54	0.96	0.664	2.72	0.739	7.92	2.254	7.31	1.098	7.48	1.074
JB-1-17	0.0041	0.0046	-0.0013	0.253	1.78	1.91	33	17.87	187.9	41	105	14.35	93.7	13.47
JB-1-18	-0.0083	0.055	0.029	0.57	1.02	0.524	1.9	0.31	2.19	0.478	1.23	0.204	1.54	0.235
JB-1-19	-0.0066	0.0051	0.0053	0.151	1.46	1.32	16.49	5.34	33.46	4.84	9.73	1.017	5.44	0.669
JB-1-20	-0.0002	-0.0009	0.0028	0.061	0.26	0.047	1.23	0.503	4.81	1.041	2.83	0.419	2.4	0.237
JB-1-21	0.0008	0.0015	0.0149	0.336	2.83	1.76	13.77	1.91	5.83	0.534	0.82	0.082	0.652	0.092
JB-1-22	0.0024	0.07	0.041	0.84	1.76	1.06	5.52	1.158	9.51	2.4	8.81	1.728	15.2	2.68
JB-1-23	0.007	0.025	0.0159	0.476	3.14	1.94	16.1	4.73	40.4	9.3	34	6.9	62	9.9
JB-1-24	0.005	0.0026	0.0061	0.065	0.33	0.089	3.17	1.99	31.6	10.79	40.3	6.52	46.6	6.55
JB-1-25	0.076	0.486	0.224	5.93	18.64	1.32	67.6	13.21	81	14.67	36.9	5.1	33.5	5.1
JB-1-26	0.001	0.007	0.0004	0.072	0.416	0.395	3.86	1.109	8.17	1.76	4.59	0.65	4.59	0.705
JB-1-27	0.029	0.043	0.014	0.15	0.304	0.29	6.35	4.69	83.6	28.6	89.8	11.6	72.4	9.67
JB-1-28	-0.001	0.014	-0.0024	0.042	0.67	0.594	7.98	3.83	43.8	10.74	30.7	4.1	24.5	3.35
JB-14-1	0.0015	0.016	0.0118	0.438	3.27	2.64	28.1	5.66	26.7	3.99	9.03	1.053	6.86	1.003
JB-14-2	0.0008	0.0021	0.0027	0.113	0.79	0.529	9.74	3.65	25.8	4.65	11.36	1.584	11.02	1.89
JB-14-3	0.019	0.183	0.049	1.23	3.09	0.91	6.16	1.21	7.33	1.63	6.38	1.31	11.53	1.9
JB-14-4	-0.007	0.009	-0.0033	0.45	2.61	2.74	12.3	1.84	10.5	2.07	5.82	0.936	6.55	1.23
JB-14-5	0.006	-0.002	-0.006	0.01	0.274	0.275	4	2.18	24.5	6.12	17.3	2.33	15.3	2.11
JB-14-6	0	0.0018	-0.0012	0.01	0.356	1.24	8.35	2.51	18.7	3.58	10.18	1.46	9.64	1.38
JB-14-7	-0.0012	-0.0004	-0.0003	-0.014	0.117	0.08	0.94	0.362	4.25	1.073	3.69	0.544	3.76	0.53
JB-14-8	0.004	0.042	0.041	0.571	1.22	1	5.28	1.254	10.4	2.94	13.12	2.65	23.9	4.3
JB-17-1	-0.0023	0.0002	-0.0026	0.015	0.027	0.064	0.85	0.578	9.57	2.91	8.77	1.12	6.67	0.882
JB-17-2	0.015	0.119	0.053	0.35	0.5	0.287	2.36	0.81	8.34	2.02	6.26	0.901	6.1	0.805
JB-17-3	0.013	0.058	0.0071	0.095	0.54	0.42	6.27	2.65	22	4.51	12.31	1.62	10.63	1.47
JB-17-4	0.002	-0.0042	-0.0043	-0.006	0.141	0.151	1.42	0.513	3.65	0.524	1.15	0.135	0.97	0.094
JB-17-5	-0.0054	0.0018	0.009	0.105	0.84	0.91	7.26	2.22	17.2	3.34	8.15	0.936	5.38	0.699

JB-17-6	-0.003	0.03	0.005	0.205	1.47	0.54	14.7	5.92	51.1	10.74	29.7	4.12	27.9	3.87
JB-17-7	0.006	0.016	0.0261	0.81	4.41	2.95	22.6	2.81	7.99	0.903	1.94	0.277	1.97	0.368
JB-17-8	0.0005	0.009	-0.0016	0.007	0.45	1.21	1.99	0.326	1.11	0.11	0.173	0.0039	0.049	0.0014
JB-17-9	5.27	10.3	1.19	5.17	1.29	0.47	1.6	0.334	3.82	1.95	14.21	4.47	52	9.41
JB-17	-0.0022	0.0041	-0.0019	-0.0164	0.088	0.132	0.55	0.245	3.35	1.122	4.4	0.792	7.18	1.191
JB-17-10	-0.001	0.037	0.044	1.49	3.25	1.29	5.55	0.478	1.55	0.17	0.256	0.024	0.078	0.0209
JB-17-11	-0.0079	0.023	0.044	0.85	3.91	0.097	27.36	11.73	143.4	43.6	142.4	20.78	131.4	16.49
JB-17-12	0.0052	0.025	0.0015	0.123	2.25	0.034	48.2	17.44	157.9	34	90.4	12.7	88.1	11.81
JB-17-13	0.217	0.8	0.194	3.48	12.31	3.38	51.6	8.33	39	5.66	11.28	1.223	7.12	0.882
JB-17-14	0.055	0.2	0.025	0.31	0.54	0.136	5.31	3.25	47.4	14.46	53.9	10.49	102.3	21.4
JB-17-15	0.003	0.024	0.0152	0.52	3.08	2.57	15.23	3.19	21.1	4	10.82	1.336	8.64	1.035
JB-17-16	-0.0023	0.0012	-0.0002	0.053	0.58	0.609	12.73	10.82	199.9	68.7	196.7	22.54	116.8	12.26
JB-17-17	0.006	0.029	0.0033	0.05	0.275	0.321	3.16	1.148	10.47	2.39	6.74	0.882	6.22	1.042
JB-17-18	0.016	0.126	0.072	1.27	2.44	1.5	9.8	2.61	21.11	4.52	10.83	1.224	6.55	0.75
JB-17-19	0.059	0.099	0.015	0.29	0.88	1.53	1.73	0.236	1.6	0.322	0.75	0.092	0.86	0.134
JB-17-20	0.0014	0.043	0.032	0.72	2.43	0.165	12.23	3.97	42.8	13.09	51.2	8.51	67.9	10.4
JB-17-21	0.0069	0.102	0.07	1.26	2.62	1.46	8.8	2.11	17.25	4.13	12.07	1.78	12.84	1.92
JB-20-1	-0.0028	0.0154	0.0089	0.292	2.75	2.48	28.4	10.48	94.7	22.5	68.5	9.73	62.8	8.62
JB-20-2	-0.0049	0.0015	-0.0015	0.005	-0.0364	0.024	0.39	0.271	8.32	5.21	30.3	6.32	50.3	8.11
JB-20-3	0.0021	0.006	0.0005	0.047	0.308	0.071	3.28	2	32.4	12.95	57.9	11.41	95.4	15.32
JB-20-4	-0.002	-0.0049	-0.0013	0.045	0.19	0.185	2.92	2.168	28.62	6.63	16.51	2.173	13.4	1.71
JB-20-4	0.007	0.021	0.0049	0.01	0.142	0.115	3.22	2	31.7	11.29	40.9	6.02	38.6	5.07
JB-20-5	0.003	-0.0019	-0.0031	0.013	0.074	0.165	1.27	0.687	9.52	2.83	7.79	0.912	4.92	0.6
JB-20-6	0.0086	0.0069	0.0017	0.035	0.32	0.225	2.61	0.738	6.1	1.297	3.41	0.518	3.67	0.508
JB-20-7	0.001	0.003	0.003	0.131	0.66	0.415	8.04	3.24	22	3.29	6.42	0.704	3.93	0.514
JB-20-8	0.011	0.0015	0.0021	0.154	0.5	0.105	4.49	2.68	40.6	15.36	59.1	9.26	63.2	9.03
JB-20-9	0.002	0.002	0.0058	0.25	2.39	2.12	27.8	12.6	124.4	29.2	80.6	9.45	47.3	4.79
JB-20-10	0.022	0.132	0.04	0.38	0.62	0.505	4	1.344	14.2	4.4	14.6	2.27	16.5	2.48
JB-20-11	0.003	0.0023	0.002	0.2	0.99	1.15	11.31	3.61	29.4	6.17	16.27	2.1	12.67	1.775
JB-20-12	0.0062	0.0001	-0.0009	0.136	1.49	1.26	14.12	3.34	23.5	5.23	14	2.04	13.12	1.733

JB-20-13	-0.001	-0.0014	-0.0038	0.021	0.33	0.411	5.8	3.38	31.1	6.1	14.8	1.84	12.2	1.54
JB-20-14	-0.0059	0.016	0.0114	0.532	3.78	0.258	32.8	8.71	60.6	11.06	27.4	3.39	21.8	2.9
JB-20-15	-0.0047	0.0016	-0.0006	0.094	0.4	0.1	4.04	2.35	37.5	12.36	45	7.52	52.7	7.19
JB-23-1	0.008	0	0.0047	0.23	1.84	1.56	8.33	0.993	3.42	0.506	1.56	0.26	2.84	0.486
JB-23-2	-0.0016	0.008	-0.0003	0.217	1.43	0.94	10.81	2.8	26.1	8.66	40.2	8.95	87.9	15.45
JB-23-3	0.0035	0.0097	0.0074	0.101	0.82	0.917	7.27	2.14	16.98	3.47	8.73	1.116	6.94	0.826
JB-23-4	0.011	0.057	0.007	0.067	-0.011	0.033	0.24	0.288	5.73	1.84	4.63	0.56	2.68	0.298
JB-23-5	0.004	0.061	0.036	0.87	1.96	1.24	6.33	1.371	10.27	2.69	9.39	1.419	9.51	1.261
JB-23-6	0.007	0.0236	0.018	0.078	0.099	0.086	0.57	0.226	3.11	0.941	3.1	0.506	3.5	0.533
JB-23-7	0.0072	-0.0025	0.0065	0.036	0.374	0.26	2.45	0.978	11.34	3.28	9.34	1.292	8.39	1.227
JB-23-8	-0.0044	0.059	0.036	0.81	1.83	1.036	6.88	1.593	11.92	2.5	6.28	0.704	3.67	0.396
JB-23-9	0.009	0.083	0.064	0.88	1.17	0.683	2.13	0.612	6.58	1.779	5.21	0.638	4.28	0.549
JB-23-10	-0.0044	-0.0005	-0.0017	0.025	0.057	0.084	0.53	0.284	5.08	1.836	6.36	1.066	7.97	1.318
JB-23-11	0.011	0.108	0.073	1.55	2.75	1.42	6.15	1.172	12.8	4.42	15.9	2.5	17.2	2.54
JB-23-12	0.0017	-0.0029	-0.0012	0.03	0.398	0.632	4.29	1.66	12.17	2.11	4.9	0.6	3.73	0.547
JB-23-13	0.005	-0.0001	-0.0013	0.096	0.309	0.073	5.85	5.49	121.8	54.2	246	46.3	370	52.5
JB-23-14	0.001	0.0115	0.0141	0.422	2.56	1.65	13.4	2.36	15.89	3.04	8.88	1.281	9.23	1.38
JB-23-15	-0.002	0.0043	-0.0004	0.008	0.23	0.145	1.14	0.566	7.42	2.05	5.63	0.654	3.74	0.467
JB-23-16	-0.001	-0.011	0.0009	0.097	0.97	0.639	9.01	3.21	24.5	4.25	9.96	1.26	7.77	1.097
JB-23-17	0.003	0.058	0.033	0.67	1.26	0.926	5.81	1.91	19.2	4.4	11.49	1.42	8.54	1.043
JB-23-18	-0.001	0.012	-0.00633	0.039	0.182	0.177	1.78	1.34	17.8	4.66	9.86	1.14	5.75	0.67
JB-23-19	-0.006	0.073	0.064	1.1	2.2	1.218	7.94	2.213	21.92	5.92	18.49	2.634	17.65	2.27
JB-23-20	0.006	0.006	-0.0023	0.052	0.165	0.076	1.01	0.74	12.9	4.44	11.98	1.21	5.5	0.537
JB-23-21	0.035	0.068	0.052	0.86	1.66	1.33	7.12	1.71	13.16	3.01	7.51	1.11	7.2	1.13
JB-23-22	0.105	0.17	0.033	0.17	0.117	0.139	1.9	0.916	11.46	3.02	9.16	1.306	9.5	1.181
JB-23-23	0.019	0.078	0.047	0.87	2.17	1.37	7.48	1.82	14.93	3.63	13.1	2.71	27	6.11
JB-23-24	0.013	-0.002	-0.00807	0.03	-0.0428	0.003	0.284	0.17	1.78	0.54	2.45	0.48	4.3	0.82
JB-23-25	0.0017	0.101	0.064	1.28	2.51	1.469	8.08	1.673	13.39	3.14	9.66	1.468	11.03	1.64
JB-23-26	0.0029	0.079	0.06	1.21	2.16	1.357	6.33	1.355	11	3.204	10.27	1.34	8.42	1.021
JB-23-27	-0.001	0.019	0.012	0.333	1.31	1.07	13.57	7.03	109	40.3	180.7	39.3	370	61.5

JB-23-28	-0.001	0.091	0.075	1.28	2.58	1.55	10.72	3.04	30.6	8.42	26.7	3.92	26.6	3.46
JB-23-29	0.009	0.019	0.0067	0.054	0.54	0.486	6.3	3.12	31	6.63	17.6	2.23	13.41	1.8
JB-25-1	0.009	0.077	0.049	1.28	6.2	1.96	50.9	16.21	144.7	34.5	99.7	13.26	86.6	11.4
JB-25-2	0	0.058	0.041	0.95	2.35	1.28	7.98	1.89	15	3.38	9.22	1.185	6.94	0.842
JB-25-3	-0.0058	0.059	0.049	0.82	1.69	1.019	7.33	2.17	21.2	4.82	12.74	1.7	10.2	1.229
JB-25-4	-0.01	-0.0094	-0.0011	0.005	0.06	0.049	0.65	0.345	5.71	1.69	5.4	0.775	4.65	0.515
JB-25-5	0.222	0.52	0.05	0.25	0.46	0.347	3.71	1.8	24.5	6.61	20.1	2.9	19.4	2.79
JB-26-1	0.002	0.036	0.035	0.49	1.26	0.89	5.88	1.77	15.32	3.51	9.3	1.224	7.18	0.85
JB-26-2	0.006	0.094	0.064	1	1.82	1.205	6.73	2.2	21.43	5.85	16.87	2.36	16.47	2.39
JB-26-3	0.0066	0.046	0.033	1	2.14	1.35	8.58	2.16	16.53	3.49	9.11	1.21	7.4	0.929
JB-26-4	0.018	0.181	0.112	1.32	1.04	0.447	2.78	0.828	10.22	3.39	13.1	2.39	21.6	4.02
JB-26-5	-0.0048	0.013	0.0119	0.379	3.88	3.01	40.6	12.37	54.2	5.57	9.59	1.122	7.5	1.14
JB-26-6	-0.008	0.069	0.059	0.98	2	1.18	7.83	1.99	17.3	3.66	8.99	1.04	6.04	0.707
JB-26-7	0.005	0.097	0.067	1.07	2.12	1.03	5.01	1.08	10.3	2.81	11.13	1.8	13.23	1.92
JB-26-8	-0.003	-0.0024	0.0098	0.137	1.44	1.41	17.9	7.4	59.9	9.26	17.1	1.95	11.39	1.501
JB-26-9	-0.0026	0.086	0.038	0.69	1.42	0.982	5.45	1.76	17.8	4.58	13.61	1.68	11.1	1.436
JB-26-10	0.015	0.081	0.047	1.05	2.3	1.32	7.76	2.04	15.58	3.36	8.82	1.24	7.9	1.097

Table 4. Chemical analyses of the Rare Earth elements of JB detrital garnets, determined in situ by LA-ICPMS.

BK Garnet REE	^{139}La	^{140}Ce	^{141}Pr	^{146}Nd	^{147}Sm	^{153}Eu	^{157}Gd	^{159}Tb	^{163}Dy	^{165}Ho	^{166}Er	^{169}Tm	^{173}Yb	^{175}Lu
BK-JAP-1	0.0036	0.168	0.119	2.53	7.85	0.953	42.1	13.21	141.5	41.1	146.7	24.5	191	29.3
BK-JAP-2	-0.0025	0.16	0.181	4.06	15.01	0.839	78.3	24.3	243	70.4	252	42.8	335	51
BK-JAP-3	0.0039	0.093	0.094	2.47	8.76	0.356	33.2	6.76	48.1	9.89	28.3	4.05	30.1	4.34
BK-JAP-4	0.0138	0.108	0.115	2.73	13.44	1.508	81.7	24.01	201.7	41.7	111.9	15.44	101.4	13.75
BK-JAP-5	0.016	0.14	0.133	3.56	12.44	0.751	70.6	23.4	253	75.5	283	48.7	389	59.9
BK-JAP-6	0.006	0.0211	0.0131	0.433	2.2	0.425	21.87	9.81	115.3	30.7	87	11.51	72.4	8.55
BK-JAP-7	2.81	8.6	1.41	8.6	9.36	0.767	28.56	4.66	20.88	2.14	3.75	0.371	2.29	0.279
BK-JAP-8	0.003	0.235	0.199	4.69	14.9	1.69	54.9	10.45	56.9	7	11.88	1.167	5.79	0.681

BK-JAP-9	-0.0012	0.118	0.082	2.27	9.21	1.12	76.1	25.7	192	21.9	23.4	1.355	4.59	0.392
BK-JAP-10	-0.0061	0.159	0.107	2.64	8.66	1.052	45.3	13.24	126.2	31.5	97.7	14.08	91.4	12.61
BK-JAP500-1	-0.004	0.205	0.14	3.47	10.72	1.286	54.3	14.31	130.5	32.1	107.9	17.09	125.5	18.99
BK-JAP500-2	-0.003	0.097	0.056	1.5	5.92	0.91	62.4	27.1	344	86.9	205.1	18.18	74	5.52
BK-JAP500-3	0.0015	0.094	0.099	2.46	10.31	1.38	21.8	2.44	8.24	1.02	1.99	0.255	1.34	0.13
BK-JAP500-4	0.015	0.202	0.16	4.25	12.66	1.43	44.2	6.06	13.37	0.638	0.747	0.065	0.51	0.078
BK-JAP500-5	0.014	0.162	0.14	3.21	10.85	1.2	77.9	26.03	227	45.8	113.8	13.53	79	9.34
BK-JAP500-6	0.011	0.322	0.227	5.63	15.19	1.13	44.4	7.21	30.59	3.2	5.01	0.499	2.68	0.366
BK-JAP500-7	0	0.071	0.064	1.1	4.81	0.412	52.8	21.53	250.5	69.5	237.9	35.6	262.6	38.39
BK-JAP500-8	0.007	0.31	0.276	6.52	21.11	2.08	79.8	15.82	86.4	11.39	21.67	2.141	11.5	1.305
BK-JAP500-9	0.005	0.104	0.056	1.33	4.42	0.591	31.9	11.57	120.2	30.75	91.4	12.38	77.4	9.29
BK-JAP500-10	0.004	0.188	0.121	2.9	8.27	1.089	39.3	10.73	93.9	21.35	59.4	7.84	48.7	6.4
BK-JAP500-11	0.012	0.194	0.167	3.94	13.37	1.61	52.2	10.21	55.1	7.21	13.08	1.384	7.94	1.002
BK-JAP500-12	-0.0052	0.0095	0.0055	0.16	1.28	2.02	14.27	3.41	20.4	3.13	6.76	0.777	4.89	0.653
BK-JAP500-13	-0.0012	0.166	0.108	2.5	7.32	0.852	38.8	12.52	144	43.9	167.9	28.52	217	33.4
BK-JAP500-14	0.007	0.106	0.106	2.93	15.77	1.76	142.3	61.2	689	163.2	423	50.09	278.6	30.09
BK-JAP500-15	0.004	0.177	0.125	3.02	9.02	1.108	42.8	11.56	96.2	21.06	56.6	6.97	43.5	5.64
BK-JAP500-16	0.005	0.062	0.06	1.11	4.41	0.507	45.8	19.98	231.8	56.8	139.8	14.39	66.5	6.23
BK-JAP500-17	-0.0016	0.054	0.05	1.18	4.18	0.441	42.2	18.19	206.1	50.9	147.9	19.53	127.4	17.11
BK-JAP500-18	0.004	0.089	0.047	1.44	4.25	0.497	26.8	8.76	99.4	28.7	105.6	17.62	141.1	22.33
BK-JAP500-19	0.0013	0.212	0.17	4.11	12.06	1.55	49.9	10.88	67.8	10.47	20.15	2.13	10.36	1.195
BK-JAP500-20	0.001	0.176	0.154	3.62	13.31	1.769	50.6	9.49	41.5	4.24	6.13	0.571	3.19	0.374
BK-JAP500-21	-0.001	0.198	0.164	3.57	10.3	1.308	50.1	12.19	89.4	16.38	39	4.48	25.3	2.87
BK-TATRE-1	-0.004	0.177	0.174	4.02	12.52	1.44	48.3	9.8	53.9	6.85	11.6	1.169	6.45	0.772
BK-TATRE-2	0.004	0.258	0.319	7.78	22.5	1.6	88.1	21.28	156.4	29.4	71.8	9.23	58.9	7.47
BK-TATRE-3	-0.0063	0.006	-0.0025	0.001	0.017	-0.002	0.075	0.065	1.8	1.068	7.84	2.16	22.9	4.17
BK-TATRE-4	0.013	0.236	0.173	3.29	6.8	1.26	15.5	2.61	16	3.23	9.6	1.52	11.7	1.74
BK-TATRE-5	0.026	0.449	0.374	8.04	19.5	1.81	82	21.5	180.9	39.6	105.9	13.69	84.9	10.75
BK-TATRE-6	0.046	0.11	0.033	0.51	1.26	0.792	10.17	2.52	11.92	1.452	2.59	0.273	1.53	0.187
BK-TATRE-7	0.0083	0.267	0.158	2.89	4.59	1.145	14.2	3.51	30.1	7.26	21.97	3.19	22.23	3.34

Nova-1	0.009	0.252	0.196	4.33	12.55	0.63	54.6	15.06	123.8	26.6	68	8.61	52.4	5.92
Nova -2	0.008	0.291	0.223	5.04	15	1.5	49.7	9.18	48.1	6.7	13.97	1.631	10.08	1.392
Nova -3	0.009	0.46	0.402	9.14	26.5	1.99	92.5	19.65	121.8	19.77	44.7	5.27	33.9	4.32
Nova -4	0.013	0.0033	0.001	0.186	1.91	0.142	11.75	3.7	31.2	6.94	21.6	3.35	25.4	3.49
Nova -5	0.159	0.649	0.273	5.28	12.89	1.64	48	9.43	52.7	7.69	14.56	1.538	7.65	0.9
Nova -6	0.003	0.058	0.037	0.92	4.13	0.532	44.5	21.96	309	101	326	44	245	26.5
Nova -7	-0.0031	0.023	0.0305	0.8	5.32	3.41	34.2	8.94	56	9.57	21	2.21	11.16	1.201
Nova -8	-0.0086	0.0078	0.0105	0.396	2.61	2.14	14.9	1.83	5.43	0.573	1.11	0.192	1.46	0.275
Nova -9	0.287	0.73	0.068	0.35	1.23	1.13	16.2	8.1	76.4	15.2	35.1	4.15	24.5	3
Nova -10	0.0063	0.0008	0.0011	0.177	2.21	2.33	32	10.97	65.5	8.87	16.35	1.61	9.64	1.147
Nova -11	0.007	0.007	0.0089	0.118	1.07	0.882	13.2	5.22	45.5	9.85	28.5	4.49	31.4	5.07
Nova -12	-0.0054	-0.0029	0.0006	0.076	0.62	0.644	3.8	1.361	13.93	3.96	12.09	1.72	11.56	1.594
Nova -13	-0.005	0.006	0.0027	0.009	0.1	0.03	0.296	0.337	7.25	4.2	25.1	5.4	49.4	7.81
Nova -14	-0.0021	-0.0067	0.0072	0.07	1.05	1.196	9.81	2.53	14.49	2.19	4.08	0.417	2.07	0.222
Nova -15	0.01	0.098	0.071	1.51	3.59	3.99	11.89	2.12	12.4	2.22	5.97	0.903	5.91	0.9
Nova -16	-0.004	0.049	0.023	0.34	2.7	2.28	20	5.32	36.7	5.69	11.56	1.46	8.83	1.22
Nova -16	-0.0004	0.002	-0.0021	0.042	0.322	0.293	3.27	0.983	7.04	1.014	1.73	0.156	0.95	0.151
Nova -17	-0.0037	0.013	0.0007	0.08	0.35	0.406	6.07	4.2	50.7	11.04	27.58	3.69	24.54	3.5
Nova -18	-0.007	0.0049	0.0046	0.063	1	1.29	16.64	6.47	46.9	8.42	19.99	2.352	13.3	1.667
Nova -19	0.045	0.053	0.018	0.138	0.092	0.042	0.86	0.694	15.36	8.33	45.9	9.49	82.5	11.03
Nova -20	0.009	0.01	0.0024	0.158	1.15	0.77	12.5	5.64	57.1	14.03	42.2	5.79	37.2	5.01
Nova -21	-0.0041	-0.0016	0.0041	0.066	0.625	0.542	4.92	2.463	25.66	6.52	18.94	2.961	20.71	2.95
Nova -22	0.241	0.269	0.064	0.51	0.85	0.404	13.22	7.49	95.8	28.49	93.1	12.79	79.5	12.29
Nova -23	0.015	0.007	0.0024	0.05	0.46	0.115	3.83	2.38	31.5	9.55	34.2	5.82	42.7	6.9
Nova -24	0.001	-0.0008	-0.0005	0.022	0.265	0.624	4.72	2.89	42.9	12.78	42.9	6.46	46.4	6.76

Table 5. Chemical analyses of the Rare Earth elements of BK detrital garnets, determined in situ by LA-ICPMS.

IB Garnet REE	^{139}La	^{140}Ce	^{141}Pr	^{146}Nd	^{147}Sm	^{153}Eu	^{157}Gd	^{159}Tb	^{163}Dy	^{165}Ho	^{166}Er	^{169}Tm	^{173}Yb	^{175}Lu
Cont-1	0.031	0.244	0.178	4.23	13.79	1.378	93.6	29.8	281.5	64.9	172.9	21.83	123.8	14.78
Cont -2	-0.0035	0.027	0.0379	1.19	5.54	1.18	34.48	9.25	78.2	18.51	57.6	8.84	65.3	10.38
Cont -3	-0.0001	0.273	0.19	4.6	11.91	1.362	55.5	14.32	118.8	27.02	73.8	9.72	60.4	7.82
Cont -4	-0.0069	0.041	0.0158	0.287	0.443	0.304	1.44	0.459	5.11	1.796	6.97	1.187	9.93	1.404
Cont -5	-0.0076	0.0162	0.003	0.299	1.29	0.078	9.2	4.13	52.9	15.7	55.4	8.31	60.4	8.91
ZAULE-1	0.237	0.55	0.065	0.35	0.69	0.83	13.24	4.9	36.3	6.08	14	1.79	10.57	1.392
ZAULE-2	0.0067	0.0146	0.0143	0.91	5.13	1.247	40.6	16.22	173.5	42.7	135.5	20.8	152.1	20.54
ZAULE-3	0.013	0.202	0.105	2.18	5.18	0.494	19.19	4.47	36.5	8.28	21.4	2.59	14.62	1.61
ZAULE-4	71.3	153	20	107	40	245	67.8	10.8	66.2	12.8	31.1	3.53	22.8	4.02
ZAULE-5	-0.0014	-0.0029	0.0014	0.213	2.11	1.75	9.95	1.54	7.36	1.047	2.4	0.31	2	0.274
ZAULE-6	0.004	0.165	0.136	2.74	6.35	2.262	22.32	5.45	48.3	12.38	40.7	6.71	52.8	8.74
ZAULE-7	-0.0025	0.0065	0.0058	0.193	1.89	1.49	13.99	3.64	23.3	4.47	12.09	1.7	11.92	1.858
ZAULE-8	0.009	0.012	0.0005	0.1	0.69	0.819	5.42	1.339	8	1.512	3.41	0.425	2.35	0.366
ZAULE-9	-0.002	0	0.0018	0.026	0.274	0.088	4.89	2.43	22.4	5.14	14.84	2.123	15.01	2.33
ZAULE-10	0.009	-0.0014	0.0049	0.073	0.262	0.439	4.56	1.72	11.47	1.767	3.52	0.36	2.41	0.365
ZAULE-11	-0.0112	0.0029	0.0026	0.049	0.272	0.204	2.36	0.866	7.05	1.452	3.99	0.569	4.21	0.65
ZAULE-12	-0.0058	-0.004	0.0056	0.13	0.79	0.858	5.15	1.273	9.18	1.879	5.52	0.761	4.95	0.782
BER-1	75.8	152	10.62	27.3	2.89	2.68	2.39	0.354	2.22	0.453	1.352	0.202	1.33	0.221
BER-2	0.006	0.0015	0.0052	0.327	2.78	1.872	18.33	5.32	41.2	7.51	17.47	2.018	11.8	1.395
BER-3	6.08	16	2.59	11.6	2.51	1.39	2.49	0.39	2.2	0.493	1.26	0.169	1.2	0.144
BER-4	-0.0012	0.0001	-0.0013	0.017	-0.006	0.009	0.095	0.082	2.45	1.986	17.13	5.33	62	13.28
BER-5	0.0051	0.0036	0.0056	0.066	0.572	0.484	9.59	4.07	38.1	7.97	21.27	2.812	18.8	2.65
BER-6	-0.0019	0.008	0.0052	0.17	2.21	1.837	15.64	2.691	12.22	1.727	3.49	0.398	2.03	0.23
BER-7	0.0081	0.424	0.259	4.95	7.69	1.94	18.4	3.37	19.85	3.463	8.54	1.062	7.14	0.976
BER-8	0.123	0.27	0.06	1.05	3.53	2.303	8.84	2.034	15.16	3.35	10.39	1.552	11.69	1.663
BER-9	-0.003	0.0023	-0.0013	0.056	0.47	0.708	5.88	3.61	43.8	10.59	28.8	3.4	21.3	3.09
BER-10	0.0018	0.0113	0.0078	0.129	1.01	0.647	10.36	3.35	23.18	3.88	8.7	1.141	7.41	0.968

BER-11	116.2	239.4	17.18	44.4	7.09	2.58	7.61	1.402	10.01	2.16	5.89	0.789	4.99	0.589
BER-12	0.017	-0.0025	0.004	0.003	0.066	0.062	0.89	0.675	9.06	2.457	5.93	0.698	4.18	0.547
BER-13	0.004	0.226	0.263	6.04	12.66	0.17	26.91	4.36	24.35	4.23	10.82	1.522	10.89	1.614
BER-14	0.077	0.356	0.232	4.61	15.67	0.907	75.5	21.7	190.2	45.6	130.7	18.6	128.6	17.2
BER-15	0.044	0.209	0.101	1.95	7.47	0.998	75.5	34.8	413	112.7	320	43.7	329	57.3
BER-16	0.0023	0.235	0.167	4.43	11.86	1.44	51.6	11.9	76.5	13.13	27.76	2.88	15.64	1.778
BER-17	0.003	0.183	0.117	2.95	9.81	1.178	48.6	12.85	103	21.65	55.5	6.54	38.6	4.65
BER-20	0	-0.003	0.0032	-0.014	0.07	0.054	0.91	0.56	8.54	2.53	6.81	0.917	4.9	0.677
BER-21	0.031	0.371	0.292	6.29	14.54	1.145	56.9	15.11	125.3	30.09	91.1	12.99	92.6	13.42
BER-22	0.0016	0.129	0.107	2.35	8.18	0.981	49.3	13.62	79.9	7.15	5.81	0.293	1.26	0.174
BER-23	0.028	0.632	0.505	10.22	24.31	1.89	95.3	25.22	220	54.5	175.8	26.95	198.6	30.34
BER-24	0.02	0.027	0.0189	0.43	1.24	0.125	10.63	4.74	55.6	16.88	60	9.53	68.2	11.39
BER-25	-0.0004	-0.0007	-0.0013	0.054	0.171	0.267	3.53	1.395	8.11	1.239	3.06	0.472	4.28	0.83
BER-26	0.071	0.427	0.288	6.2	16.26	0.948	66.9	17.78	146	33.7	100.3	13.8	97.6	13.62
BER-27	0.01	0.0089	0.0099	0.142	0.85	0.595	6.54	1.488	7.02	0.81	1.38	0.138	0.647	0.09
KRK-1	0.011	0.258	0.221	4.8	14.07	0.596	63.4	19.58	186.1	52.8	186.9	29.73	234.7	35.59
KRK-2	0.022	0.308	0.255	6.05	16.52	0.959	69.1	18.65	159.1	39.22	119.1	17.74	130.6	19.98
KRK-3	0.016	0.358	0.303	7.46	21.52	1.45	77.7	17.13	100.6	16.3	31.4	3.24	16.9	1.71
KRK-5	-0.004	0.013	0.0225	0.495	1.89	0.156	11.58	4.04	43.2	11.53	38.2	5.56	39.6	5.44
KRK-6	0.003	0.138	0.139	3.46	14.86	1.67	79.8	22.11	161	30.57	72.3	8.36	48.8	5.64
KRK-7	0.015	-0.0096	-0.0044	0.012	0.155	0.116	1.32	0.966	20.76	10.4	63	17.08	191.8	35.7
KRK-8	0.006	0.07	0.055	1.55	6.06	0.622	59.9	23.34	217.2	38.7	61.6	4.16	13.78	0.751
KRK-9	0.039	0.327	0.207	5.16	15.36	1.61	62.5	16.63	127.8	26.71	76.8	10.62	75.1	8.92
KRK-11	0.011	0.072	0.046	1.28	4.31	0.567	43.2	19.06	239.1	71.3	203.6	23.39	118.7	11.32
KRK-12	-0.0046	0.003	0.0025	0.096	0.393	0.039	2.29	1.511	18.12	3.72	10.04	1.625	11.5	1.169
KRK-13	0.012	0.0001	0.0028	0.152	1.27	1.06	12.78	5.48	51.2	10.2	21.27	2.114	12.14	1.8
KRK-14	0.024	0.343	0.313	6.97	21.77	1.628	86.8	20.05	128.3	21.49	48.1	5.77	34.4	4.38
KRK-15	0.0058	0.031	0.028	0.92	3.8	6.57	10.34	1.352	6.74	1.162	3.31	0.599	5.3	0.932
KRK-16	0.0022	0.158	0.119	2.8	10.27	1.035	79.5	32	362	104.9	332	50.1	339	48.2
KRK-17	0.004	0.169	0.151	3.67	15.04	1.62	114.4	43.9	485	132.9	434	66.3	471	67.4

KRK-18	0.001	0.0127	0.0103	0.229	2.23	2.17	24.4	8.98	73.4	14.89	38.9	4.77	27.4	2.91
KRK-19	0.006	0.06	0.049	1.05	3.12	0.43	27.33	13.25	190.3	72.4	305.8	54	439	69.7
RAB-1	0.008	0.181	0.176	3.76	12.42	1.51	48.9	10.09	55.7	7.24	11.79	1.007	4.78	0.491
RAB-2	0.037	0.303	0.167	3.21	9.02	1.081	43.3	12.37	119.6	33.8	118.5	19.6	152.7	24.1
RAB-3	-0.0028	0.192	0.17	4.12	13.02	1.54	51.6	10.66	62.3	8.78	16.16	1.666	9.09	1.117
RAB-4	0.009	0.105	0.091	2.11	7.35	0.949	63.5	26.18	314.6	88.4	259.8	34.88	206.2	24.95
RAB-5	0.011	-0.0141	-0.0056	-0.004	0.069	0.012	0.41	0.552	12.71	7.09	32.1	4.46	26.6	3.07
RAB-7	0.001	0.14	0.113	2.51	7.31	0.972	40.5	12.93	140.7	42	149.6	24.81	186.6	28.46
RAB-8	0.008	0.177	0.152	3.73	11.11	1.404	51	11.48	77.2	12.86	26.38	2.853	15.78	1.918
RAB-9	0.005	0.321	0.289	6.96	19.28	2.08	66.4	11.81	60.6	7.04	10.09	0.852	3.7	0.398

Table 6. Chemical analyses of the Rare Earth elements of IB detrital garnets, determined in situ by LA-ICPMS.

Rutile

Major and Trace elements

JB Rutile	^{24}Mg	^{27}Al	^{51}V	^{53}Cr	^{90}Zr	^{93}Nb	^{178}Hf	^{181}Ta	^{182}W	^{184}W	T (°C) Zack	T (°C) Watson
1_1	82.5	36.5	654	992	327.2	518	28.8	24.9	0.42	0.68	730	650
1_2	350	660	1922	1383	216	1010	22.2	73.4	354	355	677	616
1_3	92	72	1200	154.2	46.9	1394	3.03	87.1	122.2	121.8	482	513
1_4	106	230	1383	527	90.8	1775	4.64	150.2	135.2	136.8	566	554
10_1	107	313	768	369	180	3850	7.6	308	331	321	654	603
13_1	86.6	18.2	2237	364	320.7	228.7	11.06	8.28	23.2	22.1	727	648
13_2	2460	8900	855	783	505	975	19.5	36.1	66.6	70.1	785	687
13_3	1340	7100	186	47	30	507	0.96	45	10.5	10.2	425	487
13_4	160	680	285	54	2.34	881	0.22	72	164	172	99	366
13_5	85.7	53.8	1030	896	56.8	439	1.88	24.1	33.5	32.4	506	524
13_6	162	920	1860	1288	115.2	1237	5.64	116.1	71.2	72.1	597	571
16_1	82.8	122.2	1969	718	92.4	1203	10.99	71.7	5.05	4.82	568	556
16_10	83.3	126	2426	481	135.9	260	5.88	7.1	6.4	6.7	618	582
16_11	83.1	87	1394	688	72.2	2069	3.88	152	118	119	537	540
16_12	87.4	55	1956	821	4474	5650	256.8	236.7		0.37	1064	932
16_13	84.5	84	779	517	110.4	2678	6.1	264	77	78	591	568
16_14	577	1180	1067	251	123.1	2256	6.15	92.7	189.7	195.4	605	575
16_15	119	1060	861	570	68.1	1982	4.17	146.9	83.1	80.1	529	536
16_16	183	284	723	111.7	310	3406	10.6	217.7	295	299	723	645
16_17	83.3	54.9	2480	2349	639.6	2526	27.7	151.5	117.2	120.8	816	709
16_18	85.1	16.6	1134	1091	49	227.6	2.63	16.33	22.3	21.7	487	515
16_19	89.2	125	1014	334	268	941	12.7	74.9	300	305	705	633
16_2	111	702	1177	356	1007	579	24.2	22.7	141	143	874	753
16_3	3100	21700	491	154	18.2	618	0.66	75.4	77.1	76.3	361	460
16_4	93.8	353	1245	711	105.9	3160	4.62	156	256	262	586	565

16_5	173	1690	1363	552	221.5	118.1	8.89	6.78	47.1	49.6	680	618
16_6	88.2	94.3	547.3	54.4	467	1820	38.1	149	347	359	776	680
16_7	377	1100	1011	389	115	3230	5.69	189	201	202	596	571
16_8	83.7	55.3	1649	469	59.3	93.3	3.05	6.95	4.72	4.11	512	527
16_9	836	4340	71.7	240.4	26	1813	1.07	157.8	240.6	242.5	406	479
17_1	82.1	24.2	625	1134	109.5	281.3	4.38	19.89	120.3	121.6	590	567
17_2	82.2	43.2	1350	292	36.8	1300	2.24	78	76	78	451	498
17_3	83.6	43.7	260.9	126.3	21.87	605	1.5	66.4	0.93	1.3	384	470
17_4	83.8	199	2055	1466	251.3	322.9	12.22	21.83	32.4	33.2	696	628
17_5	82.7	545	576.5	355.7	172.4	5544	16.76	684	272.2	275.8	648	599
17_6	169	1530	1504	476	1222	590.6	31.4	39.9	13.1	13	898	773
17_7	83.7	66.3	991	384	130	135.4	5.98	7.34	13.72	14.1	612	579
21_1	85	127.8	1256	117.9	172.6	171.2	6.01	9.33	8.99	9.1	648	600
21_10	275	840	1403	571	68.5	1605	3.4	124.5	444	453	530	536
21_11	82.5	53	1332	400	88.6	3240	4.64	228	150	142	563	553
21_12	82.5	20.5	805	678	47.2	3780	2.48	245	18.7	18.6	483	513
21_13	83.6	29.9	779	796	156.5	187.3	7.55	12.08	274	277	636	592
21_14	90.4	148	696	408	37	3036	2.18	238	144.8	148.3	451	499
21_15	85.5	594	984	478	58.8	1873	2.65	165.5	187.3	183.6	511	527
21_16	116	453	318	11.5	47.9	3970	6.13	115.9	29.3	27.3	484	514
21_17	82.6	93.6	950	124	39.7	4770	3.53	282	152	157	460	503
21_18	154	550	1454	326	59.6	1289	3.22	111.7	87.4	86.4	512	527
21_19	90.7	678	5440	272	477.6	318	24.1	18.8	18.5	18.4	778	682
21_2	83.5	33.6	717	390	209.8	3359	10.88	441	237.3	236.1	673	614
21_20	84.2	181.4	886	370	67	1919	3.49	171.2	127.4	125.6	527	535
21_21	87.9	88	2335	1815	402.2	1691	18.32	93.5	360	367	756	667
21_22	84.7		4366	1827	1071	1826	54.2	159.5	251	249	882	759
21_23	82.9	69.1	1120	938	565	2827	28.1	247	395	401	800	697
21_3	84.8	67	1710	808	62.6	1852	3.06	144	66.8	67.3	519	530
21_4	1370	7800	1057	67	537	281	12.2	24	97.2	93.7	793	692

21_5	1180	990	2090	3030	18.2	2280	1	74	38.8	39	361	460
21_6	1360	6230	1839	632	53	1350	2.14	47.4	146	141.3	497	520
21_7	90	910	924	140	49	324	2.36	15.96	257	247	487	515
21_8	4000	4200	769	270	67.3	523	4.13	25	112	114.2	528	535
21_9	88.2	143	1785	7.4	180	232.9	11.21	14.32	4.05	3.54	654	603
26_1	203	290	1769	1839	56	731	3.12	45.7	22.4	22.6	504	524
26_2	86.5	77	771	307	69	1389	2.48	121.3	7.9	7.8	531	537
26_3	83.4	43.5	1154	15.6	166.3	662	8.87	18.36	21.1	21.4	644	597
26_4	83.3	63.9	1099	110.8	199.2	264.1	7.6	10.4	1.21	1.28	667	610
26_5	147	220	715	1035	224	1886	8	135.5	4.66	5.38	682	619
26_6	83.5	87.8	1519	2142	746	117.3	20.7	7.35	52.5	52.4	835	723
5_1	300	12100	3445	2683	157	1890	7.07	114.9	66.5	63.4	636	593
5_2	131	86	797	69.2	389.3	382.5	16.45	22.13	91.4	92.5	752	664
5_3	460	24100	880	54.7	11.75	503	0.54	52.6	33.7	35.7	305	438
5_4	620	2600	1343	298	228	715	11	28.4	265	259	684	621
5_5	640	1040	2345	517	225	1963	10.87	55.4	199.2	202.8	682	620
5_6	95	542	2006	445	1163	2631	48	206.5	259	257.3	892	768
5_7	83.5	50.7	1360	458	71.9	251.7	4.02	18.96	9.83	9.03	536	539
5_8	266	718	991	531	781	2887	49.1	121	125.4	129.7	841	728
5_9	81.4	27.4	3045	1381	9.49	2128	2.47	230.6	278	340	278	427
CL_1	104.5	279	504	369	69.8	4240	3.96	112	196.4	192.5	533	537
CL_2	374	830	821	170	97.9	147.7	5.2	11.6	115.3	115.9	576	560
CL_3	577	16500	1115	324	15.7	964	0.8	137.6	82.2	82	342	452
Nimis1_1	90	118	1274	299	146	5360	9	502	216	221	627	587
Nimis1_2	84.1	232	517.9	105.6	188	4204	12.65	2409	272.2	270.4	659	606
Nimis1_3	84.7	383	519	104.1	185.6	4202	12.55	2427	270.8	266.6	658	605
Nimis1_4	349	1020	1806	43.6	507	56.3	9.3	3.82	0.62	0.97	786	687
Nimis1_5	99.4	186	158.8	58	0.91	600	0.056	39.3	16.3	17.8	-22	331
Nimis4_1	81.2	44.6	432	723	366	732	15	44.9	86	50.1	744	659
Nimis4_2	81.7	14.4	1492	1233	205	290.3	5.62	20	3.59	3.26	670	612

Nimis4_3	89.5	102	1006	347	112.9	1884	5.46	136.7	144.3	144.4	594	569

Table 7. Chemical analyses of Major and Trace elements of JB detrital rutiles, determined in situ by LA-ICPMS and the crystallization temperature obtained using the Zr-in rutile geothermomether suggested by Watson et al. (2006) and Zack et al. (2004).

BK Rutile	^{24}Mg	^{27}Al	^{51}V	^{53}Cr	^{90}Zr	^{93}Nb	^{178}Hf	^{181}Ta	^{182}W	T (°C) Zack	T (°C) Watson
Nova1	93.9	22.2	1489	13	125	2493	4.36	477	90.4	607	576
Nova2	113.6	33.5	296	199	197.7	2770	8.7	45.8	1278	666	610
Nova3	138	390	753	158	482	1730	15.7	34.2	773	780	683
Nova4	104.5	230	1011	410	78.4	1279	3.66	560	98.5	547	545
Nova5	106	182	160	41.8	5.7	2970	0.39	160.4	39	212	404

Table 8. Chemical analyses of Major and Trace elements of BK detrital rutiles, determined in situ by LA-ICPMS and the crystallization temperature obtained using the Zr-in rutile geothermomether suggested by Watson et al. (2006) and Zack et al. (2004).

IB Rutile	^{24}Mg	^{27}Al	^{51}V	^{53}Cr	^{90}Zr	^{93}Nb	^{178}Hf	^{181}Ta	^{182}W	T (°C) Zack	T (°C) Watson
IB1	116.6	430	420.6	899	590	1426	24.5	88.4	87.8	805	701
IB2	105	112	892	262	78.2	1370	9.4	146	44.4	547	545
IB3	96.9	101.2	1128	260	1388	985	65.9	55.6	15.7	915	787
IB4	170	230	1161	452	148	957		0.026	0.25	629	588
IB5	93.9	246	1370	318	170.8	487.3	7.39	33.9	16.67	647	599
IB6	82.9	88.2	888	175.3	85.2	1676	4.76	93.9	37	558	550
IB7	90.6	230	1459	818	148.1	2150	7.2	187.7	239	629	588
IB8	106.9	185	1640	102.6	105.3	700	6.33	49.1	41.4	585	564
IB9	115	43.7	935	180	80.4	161.3	2.85	13.63	1.5	551	546
IB10	82	92	1710	2779	887	1796	40	139.9	903	857	740
IB11	93	160	2381	75.1	225	873	8.59	57	102	682	620
IB12	86.4	31.1	1045	1732	427.2	1888	18.9	23.7	50.4	764	672

IB13	80.1	195.8	2093	89.2	1467	165.9	39.5	7.46	0.83	922	793
IB14	82.7	70.4	2183	73.7	154.9	1253	8.73	50.7	16.2	634	592
IB15	86.8	74	1577	935	62.8	950	3.74	55.9	60.7	519	531
IB16	88.7	810	1562	450	86.1	3334	4.91	269.9	87.9	559	551
IB17	86	50.4	1536	717	119.8	1385	7.19	94	96.9	602	573
IB18	83.9	15.4	1270		106.7	77.9	4.56	5.62	2.05	587	565
IB19	83.2	56	930	896	41.7	1549	2.34	129.2	93.2	467	506
IB20	98.9	500	1430	409	77.3	3860	4.89	320	161.1	546	544
IB21	82.4	98	1784	111.8	127	208.5	2.66	15.21	23.61	609	577
IB22	96.2	186	1278	235	36.6	980	1.95	72.7	172	450	498
IB23	84.1	131.3	1873	1087	288.5	7350	14.66	455	398	714	639
rab1	97	178.2	733	346	160	1700	9.6	153.6	144	639	594
rab1	101.7	497	547	38.3	105.4	3500	7.91	404	248.3	585	565
rab1	570	15100	730	201	7.8	462	0.68	14.1	79	253	418
baska	101.6	125	1139	1023	128.1	2380	8.95	186	270	610	578
baska	132	450	940	819	138.9	2170	7.29	74.3	214	621	584
krkv3	95.2	86	1796	695	725	159.4	21.65	10.89	0.22	832	720
krkv3	96.9	15	781	1734	51	1560	3.09	71	118	492	518
krkv3	94.7	103	2181	499	849	199	26.5	16.25	7.39	852	736
krkv3	100.5	194.1	2020	411	156	2340	10.2	207	312	635	592
krkv3	290	370	678	52.7	64.3	1470	6.7	102	118.7	522	532
krkv3	98.6	148	1009	363	146.8	1656	7.28	38.2	157.5	628	588
rab2	97.1	22.1	842	1077	58.7	2364	2.82	54.6	130.1	510	526
rab2	93.6	142	2054	608	312.4	2820	14.9	195	251.9	724	646
rab3	99.4	92.4	1150	352	202.8	2088	8.1	131.1	108.4	669	612
rab5	179	1370	444	19.2	190	9180	8.9	849	155	661	607
rab6	101.4	105.3	1869	442	347.7	1587	19	147.6	97.3	738	655
rab6	101.4	100	1878	338.6457	78.7	1677	3.27	90.1	24.2	548	545
rab6	105.6	26.6	584	29.4	72.4	2310	2.7	75.8	184	537	540
rab6	91.6	44.5	1244	481	230	832	10.4	27.2	167.3	685	621

Table 9. Chemical analyses of Major and Trace elements of IB detrital rutiles, determined in situ by LA-ICPMS and the crystallization temperature obtained using the Zr-in rutile geothermomether suggested by Watson et al. (2006) and Zack et al. (2004).

Zircon

Trace elements

JB Zircon Trace		^{31}P	^{47}Ti	^{49}Ti	^{88}Sr	^{89}Y	^{93}Nb	^{178}Hf	^{181}Ta	^{208}Pb	^{232}Th	^{238}U
1-1	GR65	158.00	927.00		0.30	740.00	8.30	12150.00	3.71	5.01	96.00	265.00
1-10	MET	544.00	944.00	6.10	0.26	1040.00	1.20	12700.00	0.77	4.95	28.50	468.00
1-11	GR65	264.00	965.00	7.70	0.43	832.00	1.38	8870.00	0.54	1.23	28.80	49.30
1-12	GR70-75	1302.00	1046.00	8.10	0.59	3120.00	1.28	13460.00	1.06	5.00	65.70	447.00
1-13	GR65	316.00	980.00		0.29	898.00	6.50	9920.00	2.57	12.14	84.40	151.20
1-14	GR65	179.00	1022.00	17.40	0.22	883.00	1.58	9390.00	0.75	3.58	48.20	86.90
1-15	GR65	287.00	1071.00	4.50	0.46	732.00	2.68	11370.00	0.90	3.26	60.80	56.60
1-16	GR65	226.00	1045.00	10.50	0.30	777.00	1.97	11380.00	1.08	2.43	112.00	248.90
1-17	GR65	600.00	904.00	4.70	0.41	526.00	1.67	10040.00	1.09	3.29	130.60	259.00
1-18	BAS	253.00	841.00	10.20	0.33	1430.00	1.78	6290.00	0.63	7.23	260.70	191.40
1-19	GR65	182.00	950.00	8.20	0.60	1080.00	1.70	9010.00	0.76	4.40	128.00	258.00
1-2	CARB	226.00	970.00	15.00	0.27	147.00	0.84	11870.00	0.63	60.40	286.00	844.00
1-20	GR65	933.00	889.00	6.80	0.53	2220.00	1.18	12460.00	0.87	5.09	73.80	729.00
1-21	GR65	113.00	958.00		0.32	1050.00	6.20	10870.00	1.89	7.80	323.00	897.00
1-22	GR65	151.00	966.00	4.90	0.30	670.00	0.76	12510.00	0.44	2.82	48.90	140.00
1-23	GR65	161.00	898.00	5.20	0.20	369.00	2.47	10720.00	1.38	21.12	108.80	103.20
1-24	GR65	242.00	889.00	4.60	0.25	759.00	1.28	10450.00	0.76	2.35	109.00	369.00
1-25	GR65	198.00	927.00	9.40	0.36	594.00	1.57	9910.00	0.69	22.20	106.60	166.50
1-26	GR65	123.00	889.00	4.20	0.18	352.90	0.99	9010.00	0.63	2.80	60.70	182.80
1-27	GR65	261.00	882.00	3.70	0.22	770.00	0.99	9860.00	0.56	2.95	102.00	183.00
1-28	GR65	385.00	926.00	23.10	2.99	1138.00	2.42	11560.00	1.58	3.76	152.30	322.60
1-3	GR65	183.00	990.00	9.00	0.25	545.00	2.86	11210.00	1.52	9.08	54.00	154.30
1-4	GR65	296.00	1095.00	7.60	0.29	1080.00	1.96	9950.00	0.70	0.77	41.10	95.50
1-5	GR65	293.00	904.00	4.40	0.36	1282.00	6.39	11390.00	2.91	18.06	584.00	881.00
1-6	GR70-75	600.00	1105.00	8.70	1.09	1600.00	3.38	11860.00	2.62	7.51	305.00	482.00
1-7	GR65	208.00	1043.00		0.27	930.00	3.70	10150.00	1.31	4.62	184.00	262.00
1-8	GR65	126.00	1033.00	7.10	0.24	517.00	1.37	9830.00	0.73	0.79	41.20	94.00

1-9	CARB	53.00	940.00	14.00	0.25	158.60	1.12	11030.00	0.78	16.69	73.70	162.90
10-1	GR65	550.00	1077.00	5.60	1.01	973.00	1.48	10660.00	0.78	1.79	69.00	148.00
10-2	GR70-75	265.00	1121.00	5.90	0.47	2010.00	3.17	10400.00	1.17	5.80	283.00	300.00
13-1	GR70-75	1240.00	1250.00		0.51	3170.00	2.58	13940.00	1.69	7.90	254.00	896.00
13-2	GR65	209.00	1190.00	8.20	0.45	731.00	2.87	11720.00	1.44	15.40	89.00	166.00
13-3	GR70-75	1690.00	1206.00	13.70	1.09	4390.00	2.25	13810.00	1.25	4.15	133.00	708.00
13-4	DOL	186.00	899.00	6.40	0.20	583.00	1.40	8110.00	0.53	2.21	78.80	73.10
16-1	GR65	234.00	1191.00	12.90	0.80	880.00	2.12	10990.00	1.19	27.90	202.00	372.00
16-2	GR65		1270.00		0.12	238.00	2.31	8850.00	0.97	0.80	19.30	94.00
16-3	GR65	518.00	1129.00	6.70	0.38	1180.00	1.57	12880.00	1.30	1.61	52.00	434.00
16-4	MET	2090.00	1160.00		1.35	6000.00	2.34	16540.00	1.51	1.63	64.90	1146.00
16-5	GR65	397.00	1142.00		0.49	1040.00	4.31	12600.00	1.66	4.80	110.00	341.00
16-6	GR65	118.00	1229.00		0.67	819.00	2.76	13400.00	2.06	34.00	175.00	410.00
17-1	GR65	246.00	1034.00	9.00	0.27	776.00	2.61	11080.00	1.59	4.35	105.80	288.00
17-2	GR65	523.00	981.00	8.40	0.35	785.00	1.97	12980.00	1.64	5.10	39.20	399.00
17-3	GR65	145.00	963.00	17.40	0.19	414.00	2.47	9020.00	0.98	3.03	17.75	26.60
17-4	GR65	64.00	1142.00		0.43	239.00	1.71	12870.00	1.21	13.60	89.50	654.00
17-5	GR65	172.00	1042.00	12.70	0.22	795.00	2.41	10800.00	1.15	28.40	134.80	169.30
17-6	DOL	332.00	854.00	7.60	0.16	920.00	1.40	8450.00	0.59	3.13	64.20	146.00
21-1	GR70-75	1354.00	1018.00	7.50	0.40	2960.00	1.65	12430.00	1.14	1.34	36.00	324.00
21-2	MET	1850.00	1158.00	7.70	0.63	4180.00	1.59	14170.00	0.97	1.37	35.20	422.00
21-3	GR65	297.00	991.00	6.50	0.28	1145.00	1.29	10180.00	0.77	3.82	128.00	239.00
21-4	GR65	427.00	1081.00	16.90	0.31	871.00	1.38	10190.00	0.71	1.57	41.30	105.00
21-5	GR70-75	770.00	1151.00	14.20	0.48	1862.00	1.59	13190.00	0.87	4.94	68.50	174.00
21-6	GR70-75	1120.00	1200.00	12.20	0.68	2950.00	1.54	13320.00	1.07	1.07	30.40	235.00
21-7	MET	720.00	1072.00	7.90	0.42	1420.00	2.32	13780.00	1.64	1.17	19.80	520.00
21-8	GR65	205.00	1161.00		0.34	805.00	3.61	10970.00	1.28	13.20	76.00	83.70
21-9	GR65	133.00	1080.00		0.27	550.00	2.00	13420.00	1.61	4.29	95.00	448.00
26-1	GR65	460.00	935.00		0.36	410.00	2.08	10360.00	1.02	9.06	162.00	263.00
26-2	GR65	222.00	1098.00	16.60	0.38	1121.00	3.02	10270.00	1.38	19.40	140.50	95.20
26-3	GR65	468.00	1266.00	17.90	0.39	1740.00	3.75	11390.00	2.22	7.00	290.00	820.00
26-4	MET	301.00	1118.00	7.30	0.24	342.00	1.74	13570.00	1.29	2.53	31.80	503.00

26-5	GR65	118.00	913.00	7.40	0.57	1634.00	3.77	11420.00	2.25	32.20	209.00	498.00
26-6	GR65	198.00	983.00	6.90	0.38	1081.00	1.74	9790.00	0.95	3.65	133.60	227.60
5-1	DOL	336.00	861.00	27.90	0.74	1660.00	2.47	6980.00	0.76	17.40	75.70	101.60
5-10	GR65	243.00	856.00	12.00	0.25	1206.00	1.01	9090.00	0.54	18.00	136.00	179.90
5-11	GR70-75	288.00	911.00		0.46	1921.00	10.25	11600.00	6.77	15.00	560.00	1740.00
5-12	DOL	136.00	916.00	12.90	0.25	806.00	2.16	6700.00	1.18	1.92	109.00	167.70
5-2	GR65	203.00	986.00		0.38	1130.00	3.79	12650.00	2.17	7.40	261.00	811.00
5-3	DOL	227.00	1101.00	8.60	0.33	810.00	1.98	8370.00	0.83	2.35	79.30	154.00
5-4	GR65	639.00	992.00	6.10	0.29	1551.00	2.63	10810.00	0.94	3.93	69.90	127.00
5-5	GR65	347.00	1036.00	22.90	5.49	1750.00	4.08	11800.00	2.15	12.66	487.00	1067.00
5-6	MET	579.00	1048.00	5.10	0.40	996.00	1.14	12830.00	0.83	0.71	14.20	252.00
5-7	GR65	603.00	873.00	21.30	1.18	993.00	4.23	11020.00	1.27	28.60	285.00	471.00
5-8	GR70-75	1130.00	994.00	13.00	0.35	2720.00	1.27	9700.00	0.66	2.00	40.50	138.00
5-9	GR70-75	1754.00	857.00	9.90	0.68	4050.00	1.60	11190.00	1.11	6.84	74.00	461.00
Cl-2	GR65	234.00	1050.00	27.00	0.71	670.00	2.09	10370.00	0.51	9.80	54.70	66.10
Cl-1	GR65	187.00	942.00	26.00	3.60	1890.00	6.20	10990.00	1.74	38.80	783.00	627.00
Nim1-1	BAS	131.00	982.00		0.24	1500.00	4.95	6770.00	1.36	6.29	93.00	138.70
Nim1-10	DOL	239.00	867.00	8.00	0.18	964.00	2.28	7770.00	0.94	1.69	69.60	175.70
Nim1-11	GR65	388.00	878.00	4.30	0.34	875.00	4.61	11750.00	2.61	5.84	56.60	198.60
Nim1-2	GR65	172.00	1044.00	15.10	0.23	556.00	4.10	9670.00	1.53	5.40	33.80	65.70
Nim1-3	GR65	176.00	1222.00	9.30	0.31	1174.00	4.21	12730.00	1.98	7.71	105.00	269.00
Nim1-4	GR65	196.00	1211.00	8.10	0.30	1620.00	12.70	10710.00	3.67	4.30	148.00	279.00
Nim1-5	DOL	159.00	984.00	7.40	0.25	622.00	3.01	8020.00	1.16	3.39	116.50	202.00
Nim1-6	GR65	406.00	976.00	6.00	0.58	1291.00	2.67	9820.00	1.61	6.65	149.00	469.00
Nim1-6b	GR65	230.00	985.00	14.90	0.45	1132.00	1.74	9420.00	0.86	6.85	178.60	343.00
Nim1-7	GR65	503.00	969.00	10.10	0.31	1579.00	3.51	8990.00	1.59	17.00	188.00	152.00
Nim1-8	GR65	277.00	1187.00	19.90	0.27	649.00	1.56	9770.00	0.74	6.66	145.90	292.00
Nim1-9	MET	497.00	963.00	7.40	0.20	830.00	1.43	12790.00	0.92	5.34	39.10	648.00
Nim4-1	GR65	301.00	967.00	8.00	1.41	1620.00	3.17	11810.00	1.63	13.80	590.00	765.00
Nim4-2	GR65	700.00	1174.00	6.70	0.51	1510.00	1.70	13680.00	1.47	4.69	68.20	341.00
Nim4-3	GR70-75	582.00	1029.00	6.90	0.28	1669.00	2.44	9360.00	1.20	5.63	152.00	375.00
Nim4-4	GR65	188.00	1002.00	6.00	0.24	914.00	2.67	9740.00	1.34	2.77	142.70	295.00

Nim4-5	GR65	243.00	1067.00	9.70	2.14	1130.00	2.88	11090.00	1.26	2.82	161.00	266.00
Nim4-6	GR65	420.00	873.00	4.20	0.54	579.00	1.54	10650.00	0.82	3.90	53.30	268.50

Table 10. Chemical analyses of Trace elements of JB detrital zircon, determined in situ by LA-ICPMS and the hostrock affinity classification using the tree diagram (short version) suggested by Besoulova et al. (2002).

BK Zircon Trace		^{31}P	^{47}Ti	^{49}Ti	^{88}Sr	^{89}Y	^{93}Nb	^{178}Hf	^{181}Ta	^{208}Pb	^{232}Th	^{238}U
JAP-1	GR70-75	406.00	1513.00	25.30	0.39	2870.00	6.85	10685.00	3.33	25.10	406.00	804.00
JAP-2	GR70-75	776.00	1568.00	35.70	0.53	3110.00	8.98	8400.00	2.57	3.57	141.30	207.30
JAP-3	GR70-75	330.00	1541.00	8.00	0.33	1423.00	2.40	13150.00	1.66	6.86	108.40	229.80
JAP-4	GR70-75	508.00	1561.00	34.80	0.47	1908.00	3.43	10565.00	1.53	3.69	35.60	75.90
JAP-5	GR70-75	519.00	1498.00	28.10	0.46	4000.00	2.86	11770.00	2.07	19.30	856.00	927.00
JAP-6	GR70-75	357.00	1487.00	14.00	0.46	2310.00	6.78	10575.00	3.07	6.41	305.00	400.00
JAP-7	SYE/MON	700.00	1590.00	10.80	0.72	5270.00	6.60	8800.00	2.16	10.00	478.00	772.00
JAP-8	GR70-75	201.00	1485.00	14.00	0.85	2540.00	8.16	10120.00	2.86	24.20	625.00	540.00
JAP-9	GR65	890.00	1473.00	19.70	5.60	1117.00	3.66	9775.00	1.63	6.64	265.00	224.00
JAP-10	MET	1260.00	1503.00	13.30	0.50	2830.00	2.53	14400.00	1.99	1.78	41.00	512.00
JAP-11	CARB	163.00	1450.00	8.20	0.37	538.00	3.86	11500.00	1.89	5.53	253.00	923.00
JAP-12	GR75	600.00	1500.00	29.00	6.00	4960.00	7.80	10050.00	3.49	17.10	840.00	1990.00
JAP-13	GR70-75	371.00	1500.00	13.20	0.87	4240.00	5.30	10810.00	3.19	14.90	753.00	1218.00
JAP-14	GR75	1540.00	1790.00	284.00	37.40	7200.00	12.70	12500.00	3.83	34.90	1125.00	3890.00
JAP-15	GR65	318.00	1490.00	8.40	0.74	988.00	3.10	10900.00	1.91	10.80	443.00	546.00
JAP-16	GR70-75	501.00	1578.00		0.76	2790.00	7.34	11350.00	3.46	11.80	561.00	1136.00
JAP-17	GR70-75	375.00	1508.00	28.90	1.21	2360.00	7.27	10600.00	3.71	7.30	339.00	492.00
JAP-18	GR70-75	344.00	1486.00	16.30	0.73	2000.00	6.54	11200.00	3.54	21.70	1000.00	1420.00
JAP-19	SYE/MON	2590.00	1494.00	24.10	1.14	6660.00	3.42	13205.00	2.61	9.04	143.60	996.00
JAP-20	GR70-75	569.00	1532.00	24.30	2.11	3400.00	7.90	12400.00	3.20	28.50	373.00	910.00
JAP-22	GR70-75	219.00	1601.00		0.44	1320.00	5.50	11500.00	3.34	6.82	344.00	912.00
JAP-23	GR70-75	243.00	1620.00	77.00	1.29	2510.00	3.15	9150.00	1.46	3.98	244.00	472.00
TATRE-1	MET	2690.00	1540.00	10.90	0.74	6770.00	2.66	13750.00	1.94	2.10	48.10	600.00
TATRE-2	GR70-75	1112.00	1530.00	8.60	0.47	3780.00	3.23	10735.00	1.95	72.00	306.00	647.00

TATRE-3	GR65	156.00	1514.00	14.60	0.50	987.00	6.20	11960.00	6.56	77.70	340.00	2413.00
TATRE-4	GR65	286.00	1504.00	20.30	1.15	988.00	4.05	10165.00	1.85	16.60	275.00	339.00
TATRE-5	GR70-75	503.00	1544.00	14.40	0.40	2480.00	6.33	10000.00	2.87	11.46	227.00	432.00
TATRE-6	GR70-75	368.00	1493.00	9.50	0.76	1960.00	5.09	10665.00	2.83	11.69	423.00	1300.00
TATRE-7	GR70-75	770.00	1525.00	8.00	0.81	1773.00	8.20	12150.00	3.99	17.40	84.00	604.00
TATRE-8	GR70-75	526.00	1525.00	10.20	0.58	2480.00	10.69	12050.00	4.62	15.69	413.00	704.00
TATRE-9	GR70-75	327.00	1550.00	20.50	0.57	2150.00	1.93	11300.00	1.13	6.21	191.00	580.00
TATRE-10	GR65	540.00	1475.00		1.60	550.00	2.04	13700.00	1.54	16.30	165.00	560.00
TATRE-11	SYE/MON	2101.00	1529.00	24.10	0.78	5390.00	4.78	12305.00	3.22	38.70	193.00	631.00
TATRE-12	GR65	369.00	1620.00	31.00	1.17	840.00	3.17	9450.00	1.11	68.60	332.00	392.00
TATRE-14	GR75	1450.00	1600.00		0.93	9390.00	13.30	12500.00	6.00	16.20	2200.00	2740.00
TATRE-15	GR75	1560.00	1590.00	14.00	0.88	6220.00	8.48	13550.00	6.35	5.00	643.00	3780.00
TATRE-16	GR65	315.00	1780.00	220.00	0.71	1459.00	5.39	9720.00	2.59	25.60	422.00	386.00
TATRE-17	GR70-75	410.00	1680.00	48.00	0.42	2700.00	4.78	12050.00	3.13	227.00	1020.00	1220.00
TATRE-18	SYE/MON	495.00	1630.00	12.30	0.76	5230.00	6.36	10850.00	3.27	12.90	616.00	979.00
TATRE-19	MET	1104.00	1511.00	14.20	0.57	2560.00	4.10	14850.00	6.50	1.69	35.80	410.00
TATRE-20	GR75	598.00	1624.00	10.20	0.93	4870.00	24.60	11750.00	10.60	10.90	1550.00	3510.00
MISL-1	GR65	402.00	1497.00	16.90	0.26	1231.00	5.08	10645.00	1.92	63.60	236.70	187.60
MISL-16	GR70-75	503.00	1526.00	9.40	0.38	2200.00	9.41	12450.00	5.21	103.50	547.00	737.00
MISL-2	GR75	1012.00	1529.00	11.40	0.61	5320.00	10.52	11525.00	3.95	34.10	779.00	1430.00
MISL-3	GR70-75	1507.00	1487.00	28.50	0.57	3730.00	2.53	12410.00	1.65	12.90	186.00	528.00
MISL-4	GR65	167.00	1498.00	6.10	0.23	1146.00	3.79	11370.00	2.13	2.73	139.70	490.00
MISL-5	GR65	162.00	1481.00		0.32	1300.00	8.11	11870.00	3.62	6.99	332.00	2210.00
MISL-6	GR75	1271.00	1475.00	10.10	1.26	4730.00	17.24	10050.00	7.41	14.70	1860.00	1962.00
MISL-7	GR70-75	1800.00	1515.00	12.60	0.56	4280.00	3.40	12250.00	2.28	37.00	184.00	669.00
MISL-8	SYE/MON	439.00	1475.00	12.10	0.63	4520.00	2.85	9180.00	1.46	14.70	474.00	938.00
MISL-9	GR65	151.00	1488.00	22.00	0.51	800.00	13.00	13400.00	4.70	81.00	426.00	557.00
MISL-12	GR70-75	476.00	1830.00	360.00	1.20	1778.00	5.22	9810.00	2.04	5.15	218.00	288.00
MISL-13	GR70-75	891.00	1592.00	24.00	0.56	2790.00	5.57	14035.00	3.73	12.70	340.00	910.00
MISL-14	GR65	430.00	1597.00	31.00	0.40	1340.00	1.59	12130.00	0.94	4.00	154.00	369.00
MISL-15	GR65	546.00	1637.00	30.00	0.43	1060.00	2.21	12800.00	1.42	4.24	84.50	500.00
NGRAD-1	GR70-75	440.00	1618.00	78.50	0.34	2504.00	2.39	11700.00	1.47	32.60	520.00	580.00

NGRAD-2	GR65	820.00	1540.00	41.10	0.47	935.00	1.98	7480.00	0.71	1.04	41.30	88.70
NGRAD-4	GR70-75	314.00	1660.00		0.47	2120.00	3.62	11800.00	1.77	8.50	280.00	552.00
NGRAD-10	GR65	463.00	1632.00	37.40	1.37	1239.00	3.37	10300.00	1.46	10.77	147.30	262.00
NGRAD-5	SYE/MON	631.00	1525.00	25.80	0.66	5990.00	4.66	9225.00	2.29	6.40	783.00	865.00
NGRAD-6	GR75	1870.00	1494.00	24.10	0.93	12100.00	16.50	9665.00	4.55	36.20	4520.00	2270.00
NGRAD-7	GR70-75	1592.00	1507.00	18.40	0.84	4320.00	4.72	12975.00	4.50	33.90	392.00	1090.00
NGRAD-8	GR65	202.00	1491.00	7.90	0.61	708.00	2.43	12765.00	1.67	7.50	98.70	205.00
NGRAD-9	GR65	494.00	1505.00	16.70	0.43	1223.00	3.08	10780.00	1.46	51.30	200.00	331.00
JAP500-1	GR65	1070.00	1505.00	10.40	0.38	2452.00	4.52	11455.00	2.64	4.11	147.10	200.50
JAP500-2	GR70-75	590.00	1523.00	30.20	0.36	2780.00	4.53	11775.00	3.02	129.50	702.00	1267.00
JAP500-3	GR65	387.00	1440.00	15.90	1.89	820.00	3.42	7750.00	1.22	4.90	93.10	153.40
JAP500-4	GR70-75	407.00	1618.00		1.12	3300.00	3.62	10000.00	1.46	13.00	537.00	1018.00
JAP500-5	GR70-75	890.00	1560.00	163.00	4.11	2240.00	13.70	10350.00	2.76	33.20	248.00	460.00
JAP500-6	GR75	2790.00	1517.00	25.70	1.08	10700.00	10.80	12250.00	6.19	35.60	1490.00	3530.00
BER-1	GR70-75	474.00	1522.00	48.30	1.02	1530.00	3.42	10470.00	1.55	12.80	207.00	315.00
BER-2	GR70-75	556.00	1680.00	43.00	0.57	2000.00	13.90	13450.00	6.91	85.00	408.00	741.00
BER-3	GR70-75	967.00	1542.00	25.40	0.46	4350.00	2.68	11080.00	1.57	11.68	244.00	384.00
BER-4	GR75	1581.00	1464.00	7.20	0.62	4760.00	10.90	12685.00	6.43	15.60	589.00	1940.00
BER-6	GR70-75	462.00	1483.00	22.50	0.50	3840.00	5.80	9515.00	2.78	88.50	424.00	428.00
BER-7	GR65	358.00	1505.00	20.80	0.87	1790.00	6.80	10355.00	3.29	77.40	1450.00	1480.00
BER-8	GR75	804.00	1536.00	50.00	1.55	4450.00	20.40	10220.00	5.40	26.00	628.00	1630.00
BER-9	GR65	485.00	1567.00	17.80	4.10	1630.00	3.99	13350.00	2.71	14.40	196.00	751.00
BER-10	SYE/MON	2860.00	1499.00	25.80	0.76	6560.00	2.43	12760.00	1.55	2.79	64.80	459.00
BER-11	GR70-75	976.00	1481.00	7.10	0.39	3004.00	5.24	13040.00	3.05	11.73	242.00	852.00
BER-12	GR70-75	331.00	1452.00	21.60	0.38	2260.00	20.10	13955.00	11.60	143.10	691.00	3050.00
BER-13	GR75	1430.00	1520.00	109.00	17.60	4680.00	6.70	11000.00	2.52	39.90	706.00	1720.00
BER-14	SYE/MON	1422.00	1631.00	14.90	0.86	8860.00	6.54	10315.00	2.74	22.70	653.00	1038.00
JAP500-9	GR75	990.00	1493.00	24.40	0.73	5010.00	14.78	9745.00	4.32	28.30	1061.00	1394.00
JAP500-10	GR70-75	1400.00	1439.00	9.70	1.71	3640.00	10.24	10945.00	3.22	9.63	279.80	764.00
nov1-core	GR65	561	892		0.264	1240	2.27	10090.00	1.41	2.79	96.2	266
nov1-accresciment	GR70-75	1330	878		0.79	2320	2.89	11580.00	2.89	3.33	123	1010
nov1-rim	GR70-75	1330	938		0.71	3820	4.75	13070.00	4.46	5.04	205	1870

nov2-1accr	GR65	188	880		0.214	445	1.46	8760.00	0.707	3.44	83	194
nov2-2accr	GR65	183	853		0.131	386	1.26	7870.00	0.527	2.07	50.2	143
nov3-	GR65	152	931		0.145	530	3.25	9030.00	2.19	2.58	280	414
nov4-	CARB	99	858		0.145	115.9	1.02	9020.00	0.555	7.6	35.2	107.4
nov5-	GR65	223	892		0.211	1060	1.06	8790.00	0.54	2.21	80	107
nov6-	GR65	228	874		0.192	628	2.33	9580.00	1.47	24.5	112	199
nov7-	DOL	284	930		0.28	897	1.79	8160.00	0.649	1.69	67.6	98
nov8-core	GR65	241	899		0.94	350	1.75	9600.00	0.82	32	510	665
nov8-rim	MET	718	847		0.63	1400	1.19	10960.00	0.791	3.02	39.4	414
nov9-core	GR70-75	488	914		0.311	2370	9.91	10510.00	3.24	12.6	353	972
nov9-rim	GR70-75	227	889		0.311	1490	9.85	10340.00	3.62	9.58	270	1007
nov10-	GR65	1040	984		2.7	799	8.42	9420.00	3.51	3.51	60.8	101
nov11-	GR65	351	888		0.286	1210	4.37	11800.00	3.29	2.75	74	520
nov12-	GR65	167	861		0.164	448	1.36	9680.00	0.627	3.17	69	136
nov13-	GR65	397	930		0.51	932	2.64	8710.00	1.36	75.4	360	702
nov14-	DOL	240	937		0.243	1368	3.91	7920.00	1.07	9.42	158.3	285
nov16-	GR65	200	877		0.125	692	2.7	8710.00	0.97	15.57	84.4	102.6

Table 11. Chemical analyses of Trace elements of BK detrital zircon, determined in situ by LA-ICPMS and the hostrock affinity classification using the tree diagram (short version) suggested by Besoulova et al. (2002).

IB Zircon Trace		^{31}P	^{47}Ti	^{49}Ti	^{88}Sr	^{89}Y	^{93}Nb	^{178}Hf	^{181}Ta	^{208}Pb	^{232}Th	^{238}U
ZAULE-1	GR70-75	399.00	1522.00	24.70	0.56	1950.00	8.43	12800.00	4.12	6.15	112.60	470.00
CONT-1	GR70-75	236.00	1493.00	7.80	0.95	1800.00	6.66	13050.00	4.18	14.30	535.00	890.00
CONT-2	GR70-75	413.00	1442.00	10.10	0.35	3110.00	9.30	10015.00	3.18	17.05	422.00	612.00
CONT-3	GR70-75	751.00	1640.00		0.64	4230.00	19.60	11850.00	6.59	14.00	645.00	1133.00
CONT-4	GR70-75	2200.00	1522.00	17.50	0.70	6490.00	3.85	12115.00	2.23	13.30	382.00	767.00
CONT-5	CARB	576.00	1528.00	65.50	0.60	234.00	2.63	12390.00	1.35	75.10	315.00	429.00
CONT-6	MET	3700.00	1506.00	16.00	1.09	8430.00	2.49	13820.00	1.86	2.92	62.80	840.00
st.vas1	GR65	187.00	1140.00		0.21	762.00	1.56	10310.00	0.62	10.40	186.00	294.00
st.vas2	GR65	324.00	894.00		0.27	850.00	2.07	9090.00	0.97	11.20	101.10	167.00

Pag-1	CARB	91.00	925.00	4.00	0.20	166.30	1.08	11960.00	0.72	2.37	35.03	162.10
Pag-2	GR65	319.00	967.00	19.10	0.30	1062.00	2.81	6930.00	0.88	6.33	94.20	433.00
Pag-3	GR65	361.00	952.00	3.30	0.36	1385.00	3.66	10680.00	2.08	3.96	153.00	546.00
krkv3-1	DOL	229.00	898.00		0.29	1860.00	1.42	8120.00	0.63	2.55	76.10	156.50
krkv3-2	DOL	237.00	888.00		0.26	1180.00	6.43	7380.00	2.41	5.48	613.00	820.00
krkv3-4 core	DOL	206.00	896.00		0.21	1470.00	0.94	8010.00	0.51	4.97	190.00	315.00
krkv3-4-rim	GR65	181.00	925.00		0.41	1100.00	0.95	9500.00	0.57	4.48	158.00	309.00
krkv3-5	DOL	304.00	874.00		0.36	2780.00	6.01	8590.00	3.68	5.53	618.00	739.00
rab6-3	GR65	651.00	854.00		0.22	1387.00	1.15	9930.00	0.71	12.52	59.50	153.30
rab6-4 core	GR65	376.00	902.00		0.18	770.00	1.18	8780.00	0.53	3.52	103.00	205.00
rab6-4 rim	GR65	617.00	905.00		0.30	1340.00	1.49	10760.00	0.92	2.17	63.70	285.00
rab6-5	GR65	442.00	901.00		0.26	1648.00	1.88	9990.00	0.93	5.99	144.40	307.00
rab2-2 core	GR65	419.00	874.00		0.29	1060.00	2.64	10910.00	1.12	18.60	94.00	155.00
rab2-2 1accr	GR70-75	2129.00	834.00		0.83	6100.00	10.72	12840.00	4.46	5.90	147.00	1098.00
rab2-2 rim	GR70-75	641.00	850.00		0.55	1660.00	3.38	10670.00	1.62	2.94	72.00	296.00
rab2-6	GR65	410.00	876.00		1.14	1470.00	2.26	10040.00	0.83	12.73	132.00	192.00
rab1-4 core	GR65	287.00	885.00		0.25	1476.00	5.80	8960.00	2.00	38.60	631.00	960.00
rab1-4 rim	GR70-75	942.00	902.00		0.50	2440.00	2.44	11440.00	1.47	8.36	127.00	627.00
dobrini1	GR65	163.00	920.00		0.19	1015.00	1.21	8620.00	0.38	13.90	196.00	331.00
dobrimi2	GR65	157.50	883.00		0.17	405.00	6.13	9520.00	2.78	5.24	78.90	143.40
baska6	GR65	194.00	876.00		0.17	609.00	1.45	9730.00	0.76	2.39	74.10	235.90
baska7	GR70-75	988.00	946.00		0.36	2410.00	1.54	10370.00	0.90	5.08	109.20	397.00
baska8	GR70-75	1171.00	954.00		0.46	2970.00	1.85	10670.00	1.12	5.26	116.30	451.00
baska9 core	GR70-75	1002.00	872.00		0.96	2160.00	1.48	10540.00	1.00	3.99	69.90	306.00
baska9 rim	GR70-75	832.00	878.00		0.42	1820.00	1.31	9410.00	0.67	3.62	94.00	221.00
baska 14	GR70-75	402.00	860.00		1.10	2510.00	12.90	10520.00	7.30	45.60	595.00	920.00

Table 10. Chemical analyses of Trace elements of JB detrital zircon, determined in situ by LA-ICPMS and the hostrock affinity classification using the tree diagram (short version) suggested by Besoulova et al. (2002).

ZB		^{31}P	^{47}Ti	^{49}Ti	^{88}Sr	^{89}Y	^{93}Nb	^{178}Hf	^{181}Ta	^{208}Pb	^{232}Th	^{238}U
Z0-2	GR65	502.00	1620.00	28.00	1.79	1240.00	5.70	12300.00	2.14	57.00	331.00	570.00
Z1-1	MET	1150.00	1530.00	44.00	0.91	2670.00	25.00	14000.00	42.00	1.40	28.00	1300.00
Z1-2	GR65	349.00	1540.00	21.00	0.88	890.00	3.44	10450.00	2.11	4.77	81.00	530.00
Z1-3	GR65	376.00	1550.00	11.40	0.54	1420.00	3.02	11000.00	2.05	4.39	98.00	412.00
Z2-1	GR70-75	283.00	1580.00	17.00	0.62	1320.00	6.12	11350.00	3.01	18.80	322.00	711.00
Z2-2	GR70-75	909.00	1580.00	23.50	0.62	2430.00	3.94	12950.00	3.24	8.80	218.00	1332.00
Z2-4	MET	566.00	1535.00	56.00	7.50	1520.00	5.82	12050.00	4.55	21.20	148.00	1584.00
Z2-5	GR70-75	1570.00	1530.00	22.30	1.71	3510.00	4.05	13100.00	2.91	4.90	169.00	924.00
Z3-1	SYE/MON	1800.00	1530.00	10.40	1.08	4550.00	3.59	13500.00	2.79	12.90	126.00	868.00
Z3-2	GR75	1430.00	1447.00		0.84	7400.00	23.00	10450.00	10.38	42.00	1099.00	2510.00
Z3-3	GR75	639.00	1390.00	48.00	3.80	4550.00	12.43	7650.00	7.22	84.00	1000.00	1650.00
Z3-4	GR65	720.00	1469.00	22.80	0.81	1510.00	4.54	9850.00	2.64	33.40	178.00	587.00
Z3-5	GR70-75	510.00	1530.00	30.00	5.20	3750.00	13.50	10750.00	6.44	37.10	689.00	1220.00
Z3-6	GR70-75	425.00	1560.00	20.60	0.56	3640.00	7.04	11300.00	2.09	8.30	305.00	701.00
Z3-12	GR70-75	332.00	1590.00	27.00	0.54	2250.00	3.34	11740.00	2.06	4.10	131.00	206.00
Z3-7	GR70-75	755.00	1600.00	63.00	1.86	3240.00	11.60	12700.00	6.45	7.25	920.00	2670.00
Z3-8	SYE/MON	726.00	1520.00		1.03	4800.00	16.20	8250.00	4.83	43.80	756.00	866.00
Z3-9	GR70-75	533.00	1519.00	63.00	0.53	1380.00	3.15	11500.00	3.80	52.20	170.00	1160.00
Z3-10	SYE/MON	908.00	1510.00	8.80	0.76	5530.00	13.30	10300.00	5.56	3.15	386.00	945.00
Z3-11	SYE/MON	444.00	1527.00	21.00	0.85	4690.00	11.30	11100.00	4.41	2.21	294.00	470.00
Z4-1	GR70-75	408.00	1561.00	22.70	0.65	2380.00	3.02	11720.00	1.84	13.70	512.00	855.00
Z4-2	SYE/MON	3040.00	1520.00	40.00	1.18	7680.00	3.48	12850.00	2.42	5.68	128.00	803.00
Z4-3	GR70-75	597.00	1451.00	14.00	0.40	1960.00	4.04	12250.00	2.82	36.10	233.40	713.00
Z4-4	GR65	357.00	1470.00	32.00	0.26	1440.00	3.88	9900.00	2.02	13.10	248.00	297.00
Z4-5	GR65	555.00	1487.00	33.00	0.50	1330.00	3.38	13250.00	2.18	9.96	159.10	714.00
Z4-6	SYE/MON	1200.00	1510.00	10.50	0.76	4630.00	5.34	10800.00	2.49	13.00	293.00	702.00
Z4-7	GR65	314.00	1460.00	9.30	0.87	1300.00	4.55	12650.00	3.05	13.44	181.80	549.00
Z5-1	GR70-75	466.00	1568.00	12.50	0.41	2710.00	10.30	10750.00	7.40	64.80	960.00	1050.00
Z5-2	GR65	234.00	1610.00	13.20	0.49	1400.00	5.00	13200.00	4.40	21.40	213.00	737.00

Z5-3	GR65	284.00	1610.00	12.10	0.48	1254.00	4.91	11950.00	2.83	4.47	195.00	385.00
Z8-1	GR65	360.00	1410.00	15.00	0.75	1140.00	4.20	14200.00	3.10	14.60	165.00	990.00
Z8-2	GR70-75	790.00	1530.00	11.20	0.68	3750.00	13.11	11450.00	4.94	19.50	565.00	1300.00

Table 11. Chemical analyses of Trace elements of ZB detrital zircon, determined in situ by LA-ICPMS and the hostrock affinity classification using the tree diagram (short version) suggested by Besoulova et al. (2002).

Rare Earth Elements

JB Zircon REE	^{139}La	^{140}Ce	^{141}Pr	^{146}Nd	^{147}Sm	^{153}Eu	^{157}Gd	^{159}Tb	^{163}Dy	^{165}Ho	^{166}Er	^{169}Tm	^{173}Yb	^{175}Lu
1-1	0.04	13.10	0.03	0.91	1.85	0.09	12.50	4.72	60.50	24.30	117.00	26.10	248.00	49.80
1-10		0.58	0.05	0.57	2.38	0.03	19.40	7.62	94.10	34.80	147.00	29.40	261.00	50.30
1-11	0.05	10.14	0.08	1.35	3.05	1.36	15.80	5.68	70.00	26.70	127.50	28.00	282.00	61.40
1-12		0.61	0.05	0.75	3.84	0.10	37.40	17.80	255.00	102.10	486.00	104.30	934.00	175.30
1-13	0.02	15.16		0.74	2.47	0.22	16.00	5.86	74.20	29.81	141.50	30.60	290.00	57.90
1-14		3.14	0.13	2.14	4.65	0.46	23.70	7.70	87.40	31.30	132.00	25.30	223.00	42.30
1-15	1.34	33.50	0.43	3.90	4.73	0.67	20.40	6.45	71.70	24.70	104.00	20.66	187.50	36.90
1-16		4.00	0.05	1.02	2.67	0.10	15.70	5.19	66.20	25.90	120.00	24.89	228.90	46.20
1-17	2.40	15.20	0.61	2.81	1.46	0.31	7.91	2.84	36.90	15.94	82.40	20.78	221.50	51.20
1-18	0.11	38.40	0.74	11.05	15.71	7.07	54.90	14.87	143.40	49.50	207.10	41.50	382.00	78.40
1-19	0.33	4.82	0.42	4.30	6.80	1.22	27.70	9.00	104.00	37.60	160.00	32.50	296.00	58.50
1-2	0.12	2.45	0.24	3.17	9.30	0.08	27.80	4.36	25.60	4.91	13.60	2.32	20.50	3.80
1-20	0.09	1.31	0.11	1.24	5.17	0.13	43.60	18.82	216.00	74.50	296.00	57.80	496.00	92.00
1-21	0.04	36.20	0.11	1.24	2.52	1.20	16.60	6.11	76.20	31.70	160.00	38.20	405.00	93.70
1-22		8.13	0.03	0.64	2.01	0.33	13.20	4.66	58.00	22.50	100.90	21.20	198.00	41.10
1-23		18.40	0.03	0.30	1.02	0.18	5.96	2.25	29.10	11.93	58.00	13.50	129.90	27.89
1-24	0.04	2.61	0.08	1.51	2.89	0.40	17.40	5.47	66.90	25.80	116.00	26.10	256.00	55.30
1-25	0.12	11.66	0.07	1.28	2.92	1.25	14.90	4.41	52.90	19.97	92.10	21.14	208.80	44.20
1-26		4.94	0.02	0.40	1.04	0.44	6.03	2.18	26.10	10.79	54.00	12.97	138.10	31.51
1-27		6.47	0.07	0.89	1.94	0.53	11.60	4.55	57.50	24.60	121.00	29.00	293.00	66.80
1-28	0.64	6.58	0.68	4.79	5.99	2.19	27.30	8.94	106.80	40.13	173.50	36.00	330.00	65.40
1-3		14.51	0.20	2.19	3.09	0.77	13.90	4.05	46.80	18.00	79.30	17.17	162.80	34.70
1-4		8.71		0.49	1.56	0.50	13.90	5.33	78.70	34.37	180.90	42.60	428.00	95.40
1-5	0.04	53.20	0.21	3.01	5.69	0.98	28.30	9.45	114.20	43.10	192.00	40.00	368.00	71.30
1-6	3.80	35.60	0.98	5.40	4.12	0.63	24.40	9.15	124.00	51.10	251.00	58.80	603.00	128.90
1-7		38.00	0.07	1.62	3.51	0.85	18.90	6.65	80.30	31.00	145.50	33.00	320.00	67.30
1-8		2.05		0.47	1.51	0.16	8.40	3.33	42.60	16.80	81.40	18.00	180.00	38.30
1-9	0.05	8.96	0.02	0.29	0.43	0.12	2.14	0.77	10.30	4.76	25.40	6.76	76.50	18.60

10-1	2.50	10.40	0.78	3.20	2.87	0.43	15.40	5.47	71.90	31.70	156.00	36.70	371.00	80.40
10-2	0.16	42.80	0.23	4.22	9.40	1.80	44.10	14.70	171.20	69.90	317.00	69.40	665.00	130.80
13-1		2.50		2.10	6.40	0.22	46.50	21.90	292.00	120.00	567.00	131.00	1223.00	217.00
13-2	0.85	22.90	0.35	2.36	3.40	0.44	19.60	5.93	70.60	24.60	115.00	25.00	230.00	45.70
13-3	1.20	4.60	0.41	5.60	10.60	0.38	73.30	32.30	414.00	151.00	646.00	132.00	1200.00	215.00
13-4		12.97	0.12	1.76	3.46	0.71	15.20	4.87	55.70	20.20	89.70	18.10	167.00	34.90
16-1	0.10	18.40	0.42	5.60	7.30	2.00	26.40	7.60	90.00	32.00	139.00	31.60	300.00	62.20
16-2		6.40				0.23	3.21	1.22	16.30	7.00	37.30	8.60	106.00	21.40
16-3		1.17	0.09	1.91	3.50	0.37	23.40	8.20	101.00	41.00	192.00	42.20	455.00	99.00
16-4	0.11	1.30	0.28	3.20	9.90	0.10	95.91	45.20	640.00	204.00	740.00	149.00	1116.00	171.00
16-5	0.02	21.10	0.09	1.02	3.10	0.84	16.80	6.20	83.00	34.00	158.00	37.00	364.00	76.00
16-6	0.06	37.50	0.44	7.20	7.90	1.86	33.70	9.50	94.00	26.50	105.80	22.50	202.00	34.50
17-1	0.08	5.89	0.06	1.04	2.26	0.23	16.40	5.54	69.00	25.80	116.00	24.10	224.00	43.70
17-2	0.02	0.99	0.03	0.54	1.38	0.39	10.60	5.28	68.20	25.80	119.50	26.90	257.00	51.80
17-3		6.12	0.07	1.23	2.00	0.25	11.35	3.34	40.50	14.31	62.60	13.06	115.70	24.05
17-4	0.03	10.47		0.53	0.87	0.26	3.40	1.35	17.70	7.37	37.10	9.41	103.50	24.50
17-5		19.00	0.08	1.27	3.08	0.29	16.60	6.28	70.00	25.80	115.60	24.90	229.00	44.40
17-6		2.77	0.08	1.93	3.65	0.45	20.30	7.20	85.00	32.80	142.00	29.40	260.00	53.30
21-1		0.59	0.06	0.63	3.44	0.11	32.40	15.72	231.00	97.70	468.00	101.10	912.00	174.00
21-2		0.76	0.09	1.77	6.70	0.10	52.00	25.30	356.00	143.00	652.00	140.00	1240.00	229.00
21-3	0.02	12.00	0.21	3.30	5.80	1.65	31.10	10.00	110.00	40.30	177.00	36.80	332.00	65.70
21-4		1.10	0.06	1.17	3.01	0.16	19.30	6.77	80.10	30.40	132.80	27.60	263.00	50.70
21-5		1.87	0.05	2.35	6.00	0.12	36.30	13.10	167.50	65.00	291.00	58.90	555.00	105.40
21-6		0.93	0.04	2.21	6.40		48.80	18.20	276.00	104.00	453.00	96.00	880.00	153.90
21-7		0.85		0.45	1.99	0.08	17.20	9.11	121.00	46.50	188.00	37.40	349.00	63.00
21-8	0.04	30.40	0.20	3.24	5.90	0.49	27.30	8.00	81.60	29.10	117.70	24.20	213.00	40.00
21-9		12.30	0.04	0.70	1.17	0.38	7.40	2.82	39.40	16.90	89.00	22.10	238.00	54.80
26-1	0.21	26.50	0.11	1.19	1.48	0.73	10.00	2.82	32.30	12.00	57.60	14.00	141.00	32.60
26-2	0.04	55.30	0.35	5.70	8.10	1.87	33.80	10.10	110.50	37.90	161.00	32.40	286.00	55.70
26-3	0.02	5.66	0.31	5.10	9.80	0.42	46.50	15.60	167.00	62.70	269.00	54.80	488.00	96.00
26-4		1.40	0.08	1.37	5.90	0.67	31.50	8.48	57.40	12.01	33.40	5.07	39.50	7.89
26-5	0.04	12.81	0.12	2.20	6.26	0.42	33.40	11.61	139.90	55.10	253.80	55.10	489.90	97.60

26-6	0.04	10.30	0.11	1.91	4.19	1.17	22.80	7.24	91.00	35.80	162.50	36.40	349.00	74.50
5-1	0.02	22.20	0.27	4.12	8.90	3.89	44.40	13.30	149.00	54.20	242.00	52.60	497.00	104.20
5-10		16.20	0.22	3.26	6.85	1.01	30.90	9.64	112.10	40.30	175.00	35.10	310.00	60.40
5-11		18.70	0.04	0.68	3.16	0.34	23.90	10.74	145.80	61.20	309.00	71.60	702.00	146.60
5-12	0.17	6.25	0.29	4.06	5.02	0.98	19.20	6.66	75.30	27.00	122.00	25.10	233.00	47.50
5-2		17.10	0.05	1.14	2.57	0.90	17.10	7.20	94.00	37.30	182.00	41.10	407.00	84.80
5-3	1.84	10.00	0.71	4.90	4.09	0.16	19.70	6.46	75.90	29.00	131.10	25.40	239.00	48.00
5-4		15.00	0.09	1.83	5.66	1.69	35.60	11.94	142.50	51.50	224.80	47.80	424.00	83.00
5-5	0.17	31.90	1.54	14.50	17.60	6.37	50.30	16.60	187.00	60.30	248.00	50.00	438.00	80.90
5-6	0.02	1.15		0.40	1.49	0.19	13.50	6.70	87.00	30.10	140.00	32.50	330.00	64.70
5-7	0.52	23.30	0.29	2.70	3.42	1.07	16.80	5.37	71.20	30.20	163.00	41.50	442.00	107.90
5-8	0.19	2.21	0.07	4.00	8.90	0.24	49.80	20.40	269.00	102.00	415.00	88.00	948.00	148.00
5-9	0.03	0.97	0.09	1.69	5.95	0.10	50.90	23.96	333.00	137.20	641.00	135.20	1208.00	228.30
Cl-2	0.02	40.20	0.12	1.45	5.30	0.66	20.90	5.77	61.30	22.80	100.00	20.80	196.00	37.00
Cl-1	0.18	112.00	1.35	16.50	25.20	8.40	81.90	22.80	214.00	66.70	252.00	48.90	413.00	71.30
Nim1-1	1.00	23.90	0.47	4.50	7.13	0.08	38.20	13.17	151.10	54.70	228.30	43.60	360.00	66.20
Nim1-10		6.72	0.05	0.93	2.44	0.65	17.00	6.16	81.00	33.80	158.80	33.40	332.00	68.50
Nim1-11		21.10	0.04	0.75	1.62	0.62	11.70	4.47	64.20	28.20	148.70	36.30	387.00	83.10
Nim1-2		9.82	0.07	1.52	2.90	0.15	14.81	4.65	53.10	20.24	85.00	17.63	157.90	31.36
Nim1-3		16.20	0.11	2.23	5.00	0.20	28.60	10.21	108.20	42.60	178.10	36.90	320.00	58.50
Nim1-4		23.60	0.12	2.67	4.70	0.09	32.90	11.60	146.00	56.60	242.00	48.90	415.00	74.00
Nim1-5		18.50	0.07	1.22	2.42	1.05	11.40	3.83	47.20	19.80	93.70	22.80	229.00	53.70
Nim1-6	0.29	7.26	0.18	1.95	3.51	0.37	18.90	7.56	103.50	43.90	207.90	45.90	427.00	90.10
Nim1-6b		5.29	0.04	1.02	3.01	0.47	20.50	7.72	99.10	39.90	180.50	36.80	339.00	65.70
Nim1-7	0.02	44.40	0.36	5.61	8.50	2.32	41.50	13.40	154.00	55.60	241.00	48.60	432.00	87.90
Nim1-8		6.03	0.15	2.15	4.13	0.55	16.00	5.34	59.00	21.30	89.00	19.70	168.00	31.50
Nim1-9		0.65	0.03	0.76	3.19	0.04	22.90	8.63	88.60	27.10	106.00	20.60	184.00	34.70
Nim4-1	1.70	51.10	0.77	5.80	8.40	2.08	35.40	11.80	146.00	52.50	232.00	49.80	477.00	99.20
Nim4-2		1.68	0.06	1.16	4.05	0.61	37.20	13.00	148.00	51.80	214.00	44.00	405.00	79.00
Nim4-3		5.27	0.09	1.93	4.92	0.48	30.90	11.65	141.10	56.40	259.00	56.20	522.00	108.70
Nim4-4		8.61	0.08	1.83	3.10	0.42	17.60	6.53	79.80	31.60	143.70	30.20	272.90	55.10
Nim4-5	0.03	9.30	0.22	2.90	4.37	1.11	20.30	7.90	96.00	37.70	173.00	36.60	349.00	68.20

Nim4-6	0.04	6.00	0.05	0.60	0.98	0.39	6.33	2.70	41.10	18.60	103.40	27.50	311.00	70.60

Table 12. Chemical analyses of Rare Earth Elements of JB detrital zircon, determined in situ by LA-ICPMS.

BK Zircon REE	^{139}La	^{140}Ce	^{141}Pr	^{146}Nd	^{147}Sm	^{153}Eu	^{157}Gd	^{159}Tb	^{163}Dy	^{165}Ho	^{166}Er	^{169}Tm	^{173}Yb	^{175}Lu
JAP-1	0.29	38.00	0.43	7.68	16.30	1.24	76.90	24.80	281.00	100.50	428.00	86.30	746.00	143.80
JAP-2	0.05	43.90	0.29	4.58	8.41	4.74	42.80	16.90	233.00	99.00	476.00	105.20	1030.00	217.00
JAP-3		21.80	0.05	1.33	4.00	0.88	21.20	7.68	103.70	44.50	229.00	56.80	618.00	147.00
JAP-4	0.03	34.10	0.11	2.26	6.05	1.00	34.70	12.95	165.90	63.60	296.40	62.20	582.00	116.80
JAP-5	0.08	56.60	1.00	16.10	26.10	2.25	110.00	34.20	383.00	137.20	570.00	106.80	897.00	163.50
JAP-6	0.00	24.80	0.18	3.25	8.05	1.28	45.50	16.01	197.00	75.40	340.00	70.90	664.00	133.00
JAP-7	0.34	29.90	1.11	18.00	30.80	5.80	139.00	44.10	510.00	188.00	790.00	151.40	1334.00	260.00
JAP-8	0.04	111.10	0.44	7.35	8.90	3.14	39.50	13.56	168.20	72.90	382.00	94.60	999.00	231.00
JAP-9	3.90	42.00	1.11	6.80	4.59	2.02	24.60	7.65	95.60	34.90	163.00	35.00	332.00	72.40
JAP-10		0.86	0.04	0.55	3.85	0.13	34.30	18.30	244.00	92.00	363.00	67.00	550.00	101.00
JAP-11	0.01	4.57	0.08	2.53	6.48	1.26	28.10	7.27	60.60	16.80	59.00	11.34	93.30	18.92
JAP-12	0.26	22.60	1.51	16.90	30.80	6.30	133.00	42.80	502.00	174.00	696.00	136.00	1170.00	220.00
JAP-13	0.12	39.90	0.45	7.00	14.90	1.96	95.00	32.70	396.00	145.00	644.00	134.00	1180.00	226.00
JAP-14	2.64	84.00	11.90	100.00	103.00	44.90	273.00	90.00	860.00	242.00	930.00	187.00	1670.00	290.00
JAP-15	0.30	40.60	0.34	2.90	2.82	1.59	17.50	5.51	70.00	29.40	147.20	34.80	372.00	88.00
JAP-16	0.66	45.80	0.25	2.60	6.50	1.35	37.40	14.74	200.00	89.00	455.00	114.20	1179.00	254.00
JAP-17	0.12	19.20	0.40	5.60	11.40	1.60	53.80	18.60	230.00	81.00	344.00	72.00	614.00	109.00
JAP-18	0.06	46.40	0.22	2.31	4.29	1.90	28.80	11.40	150.00	61.90	320.00	75.10	804.00	178.00
JAP-19	0.09	1.76	0.16	2.11	8.49	0.41	73.30	36.50	538.00	226.00	1106.00	238.00	2140.00	416.00
JAP-20	0.11	56.00	0.71	6.70	10.60	3.40	51.30	18.95	254.00	105.20	535.00	129.70	1333.00	293.00
JAP-22	0.53	23.10	0.16	0.94	3.50	0.87	25.00	8.60	109.00	46.10	227.00	55.10	541.00	106.40
JAP-23	0.02	11.49	0.33	5.70	10.40	2.55	56.70	20.40	237.00	83.90	360.00	74.20	653.00	123.40
TATRE-1		1.07	0.08	1.72	7.78	0.25	78.90	37.00	546.00	232.00	1097.00	232.00	2060.00	402.00
TATRE-2	0.10	9.04	0.61	9.70	20.70	1.78	114.10	34.20	381.00	133.60	540.00	101.70	866.00	158.80

TATRE-3	0.07	12.73	0.13	1.06	1.97	0.51	9.65	4.05	61.00	28.80	162.60	42.40	453.00	99.50
TATRE-4	0.10	44.80	0.18	2.20	3.97	1.79	19.00	6.18	77.00	30.90	156.00	36.20	382.00	84.20
TATRE-5		29.80	0.12	3.42	8.34	2.47	49.90	17.50	216.00	87.60	398.00	86.70	802.00	166.00
TATRE-6	0.07	25.60	0.35	3.70	7.70	1.84	35.40	12.20	151.00	60.90	302.00	70.70	698.00	153.00
TATRE-7	0.15	19.20	0.21	2.41	3.92	0.90	26.20	10.37	140.50	59.70	301.00	72.50	740.00	155.00
TATRE-8	0.23	58.60	0.23	2.68	7.13	1.27	38.80	14.62	194.00	82.70	405.00	93.50	925.00	197.30
TATRE-9	0.02	12.90	0.11	2.17	6.30	1.16	40.70	15.30	189.00	75.00	329.00	70.00	640.00	126.00
TATRE-10	0.09	21.50	0.27	3.30	3.90	1.80	13.70	4.70	52.00	18.60	83.00	18.40	205.00	49.10
TATRE-11	0.38	6.78	0.37	5.70	12.00	0.30	87.20	34.50	464.00	185.90	845.00	177.20	1581.00	309.00
TATRE-12	0.31	53.50	0.50	5.90	8.60	4.00	34.60	9.90	100.00	31.20	119.00	23.50	218.00	39.30
TATRE-14	0.25	215.00	1.93	42.00	67.00	10.40	277.00	92.00	1010.00	364.00	1530.00	303.00	2830.00	465.00
TATRE-15	0.31	15.56	0.35	4.30	13.90	0.79	92.90	38.90	516.00	206.00	971.00	210.30	1940.00	373.00
TATRE-16	0.09	58.10	0.37	6.17	8.40	2.67	36.60	11.66	134.10	47.70	209.00	44.40	422.00	85.60
TATRE-17	0.08	83.00	1.04	13.83	27.90	3.17	103.00	26.50	282.00	85.00	363.00	74.00	660.00	104.00
TATRE-18	0.06	38.10	0.51	9.10	24.20	2.10	122.00	42.40	489.00	178.00	769.00	150.00	1361.00	256.00
TATRE-19		0.68	0.02	0.80	2.99	0.13	25.10	13.00	193.00	85.80	443.00	102.70	1004.00	199.50
TATRE-20	0.56	78.10	0.46	6.10	15.20	1.82	86.30	32.50	412.00	159.00	751.00	166.00	1550.00	303.00
MISL-1		55.40	0.13	2.52	5.58	1.07	31.30	10.10	116.00	43.10	188.40	37.60	336.00	69.20
MISL-16		79.70	0.12	2.22	6.58	1.23	40.30	14.07	186.00	73.50	348.00	74.30	689.00	144.50
MISL-2		18.40	0.56	11.10	22.70	1.66	127.00	42.50	503.00	188.00	820.00	164.00	1460.00	281.00
MISL-3	0.01	16.10	0.08	1.91	6.71	0.59	58.40	23.80	314.00	124.70	565.00	117.90	1034.00	202.70
MISL-4		6.11	0.06	1.61	4.82	0.74	27.30	9.05	100.40	38.60	174.00	36.30	344.00	69.40
MISL-5	0.03	6.56	0.05	1.68	5.55	0.94	34.40	11.34	123.50	42.00	171.40	34.20	311.00	60.50
MISL-6	2.50	174.00	1.04	13.90	20.60	6.13	100.40	33.70	403.00	153.20	715.00	156.50	1526.00	312.00
MISL-7	0.10	6.90	0.19	4.47	12.20	1.16	81.90	31.20	378.00	148.00	671.00	140.00	1300.00	253.00
MISL-8	0.05	10.60	0.53	8.70	19.50	5.01	110.00	37.30	436.00	162.00	707.00	144.00	1291.00	253.00
MISL-9	0.19	64.70	0.31	2.40	4.60	1.45	14.30	5.40	64.00	26.10	134.00	33.30	370.00	84.00
MISL-12	0.09	22.50	0.21	3.17	6.60	1.87	34.20	12.26	155.80	59.10	275.00	58.70	563.00	116.30
MISL-13	0.01	8.21	0.24	3.40	9.70	0.25	59.50	21.10	253.00	95.00	433.00	85.70	790.00	152.00
MISL-14	0.03	17.80	0.12	2.50	6.60	4.60	50.00	20.00	210.00	50.00	191.00	34.00	306.00	67.70

MISL-15		3.70	0.11	2.57	6.90	0.76	41.80	13.14	120.00	33.90	120.00	22.80	193.00	30.30
NGRAD-1	0.14	39.80	1.41	20.10	25.60	3.60	94.10	26.60	270.00	87.70	345.10	65.60	553.00	103.80
NGRAD-2	4.90	16.60	1.58	9.00	6.56	1.05	27.90	7.89	89.10	33.40	144.60	29.60	268.80	56.60
NGRAD-4	0.03	41.40	0.19	4.10	8.00	1.59	44.30	16.30	188.00	70.30	334.00	75.00	705.00	122.00
NGRAD-10	1.09	46.20	0.56	5.40	9.20	3.23	37.40	10.98	114.80	39.80	175.10	37.40	353.00	71.20
NGRAD-5	0.12	45.80	1.19	19.40	32.20	7.43	163.50	52.60	597.00	213.30	901.00	176.90	1509.00	288.20
NGRAD-6	0.72	365.00	4.56	68.30	97.00	25.80	400.00	118.00	1270.00	438.00	1780.00	353.00	3040.00	572.00
NGRAD-7	0.15	13.00	0.41	6.18	15.70	1.03	93.00	32.40	395.00	150.00	664.00	141.80	1317.00	257.00
NGRAD-8	0.07	20.80	0.15	1.53	1.77	0.87	10.80	4.15	53.00	22.10	117.00	28.60	307.00	68.30
NGRAD-9	0.08	37.40	0.21	2.67	5.96	1.66	29.60	9.61	111.10	40.60	181.60	37.60	351.00	73.50
JAP500-1	0.01	12.58	0.19	3.32	11.50	1.06	70.70	25.70	270.00	82.30	300.00	53.10	418.00	76.50
JAP500-2	0.18	14.21	0.65	10.00	17.80	0.25	80.10	25.50	274.00	97.90	405.00	78.90	672.00	127.30
JAP500-3	1.14	27.80	0.74	7.30	5.50	0.08	23.70	7.40	75.90	28.80	129.10	28.80	282.00	59.50
JAP500-4	0.22	19.90	0.75	9.60	15.50	3.04	79.50	25.70	307.00	114.90	511.00	105.10	1008.00	202.00
JAP500-5	1.57	12.40	0.86	8.20	10.70	2.82	52.40	17.80	209.00	76.40	337.00	70.20	623.00	124.00
JAP500-6	0.01	25.30	0.55	12.70	33.80	0.49	207.00	82.00	1030.00	392.00	1690.00	340.00	2920.00	526.00
JAP500-9	0.12	123.50	0.34	5.98	12.04	3.96	72.10	27.60	382.00	160.70	785.00	178.30	1766.00	379.00
JAP500-10	1.84	57.10	0.60	4.70	6.53	3.00	52.00	20.12	273.00	117.50	579.00	129.60	1284.00	296.50
nov1-core	0.034	4.45	0.046	0.95	2.73	0.052	19.8	8.03	100.5	41.1	192	39.1	358	67.7
nov1-accresciment	3.9	16	1.2	7	4.4	0.064	28.6	12.2	174	76	382	88	820	163
nov1-rim	0.17	3.66	0.113	1.18	4.03	0.072	37.3	19.4	288	129	651	149	1390	273
nov2-1accr	0.052	9.91	0.049	0.55	1.31	0.61	6.2	2.34	31.5	13.3	70.8	17.3	190	48.4
nov2-2accr		7.7	0.022	0.41	1.01	0.482	5.26	1.88	25.4	11.51	62	15.5	181	46.9
nov3-	0.019	12.4	0.162	2.4	2.7	1.44	17.8	5.2	51	19.9	82	16.7	142	28
nov4-		4.82	0.0108	0.18	0.37	0.127	1.73	0.637	7.95	3.29	17.7	4.4	46.3	11.03
nov5-		7.99	0.097	1.84	4.54	0.73	23.4	8.4	96	35.7	155	30.2	268	52.7
nov6-		11.7	0.061	0.72	1.42	0.151	10.8	4.26	50.5	19.5	95	19.7	191	38.4
nov7-	0.27	10.4	0.14	1.5	2.97	1	14.5	5.46	68.7	28.9	140	32.2	324	75.4
nov8-core	2.1	37.5	0.76	5.4	5	0.92	13.6	3.5	34	11.1	48	10.3	99	21.6
nov8-rim	0.32	3.13	0.079	0.64	1.89	0.162	14	6.99	107	45.9	230	53.9	525	108.7

nov9-core	0.044	47.5	0.107	1.77	5.5	2.34	40.2	15.8	203	79.4	370	81.1	755	154.6
nov9-rim	0.077	30.8	0.048	0.83	2.93	1.21	20.1	8.29	111	47.1	232	53.8	538	115
nov10-	41	115	11.4	56	12.7	1.98	26.8	7.29	77.3	28	122.4	25.8	232.3	46.2
nov11-		7.1	0.0115	0.4	1.29	0.173	13.1	6	91	39.3	198	46.1	442	92
nov12-		10.8	0.022	0.56	1.02	0.29	6.1	2.4	33.2	13.5	71	16.2	168	37.7
nov13-	0.47	14.9	0.41	3.81	5.2	0.99	23.7	7.35	81.3	29.6	131	27.9	264	54.2
nov14-	0.049	19	0.255	3.52	7.39	0.262	36.7	11.99	131	48.8	206.1	40.7	365	72.8
nov16-		36.4	0.065	1.44	2.83	0.8	15.6	4.93	58.4	22.7	105.6	23.4	221.4	46.3

Table 12. Chemical analyses of Rare Earth Elements of BK detrital zircon, determined in situ by LA-ICPMS.

IB Zircon REE	^{139}La	^{140}Ce	^{141}Pr	^{146}Nd	^{147}Sm	^{153}Eu	^{157}Gd	^{159}Tb	^{163}Dy	^{165}Ho	^{166}Er	^{169}Tm	^{173}Yb	^{175}Lu
ZAULE-1	0.05	8.66	0.25	4.60	8.90	0.85	47.30	16.10	189.00	68.50	296.00	58.60	507.00	95.90
BER-1	0.19	16.40	0.28	3.23	4.32	1.44	24.60	9.20	118.00	47.40	239.00	57.60	594.00	128.00
BER-2	0.34	114.60	0.46	8.40	14.10	3.75	51.20	16.20	183.00	66.10	318.00	71.50	689.00	147.60
BER-3	0.04	8.00	0.54	9.47	20.70	1.12	114.30	38.20	438.00	156.70	661.00	127.10	1066.00	200.60
BER-4	0.06	11.60	0.15	3.50	10.10	0.40	80.10	31.30	422.00	168.00	762.00	163.00	1467.00	284.00
BER-6	0.23	39.40	1.48	23.00	31.10	3.19	125.50	36.30	394.00	134.80	547.00	103.80	881.00	165.60
BER-7	0.31	138.10	1.24	14.30	18.10	5.31	65.40	17.40	183.00	59.70	246.00	49.90	463.00	90.60
BER-8	0.19	22.50	0.72	8.60	16.00	4.10	84.40	32.30	393.00	149.10	691.00	147.20	1355.00	272.00
BER-9	0.96	23.40	2.13	17.20	16.30	5.60	39.80	14.20	159.00	52.70	235.00	50.30	481.00	98.70
BER-10	0.00	1.19	0.09	2.39	7.50	0.14	68.10	34.10	512.00	220.00	1079.00	227.00	2010.00	384.00
BER-11		9.17	0.08	2.08	5.61	0.20	48.30	19.06	258.40	105.60	502.00	104.40	976.00	197.00
BER-12	0.00	30.40	0.04	0.96	3.81	0.66	25.50	10.62	155.00	69.40	374.00	92.50	990.00	230.00
BER-13	4.90	54.00	3.38	30.60	39.10	17.30	141.00	47.70	490.00	151.00	595.00	121.00	1060.00	196.00
BER-14	0.23	62.30	1.57	32.00	56.70	19.00	241.00	73.30	831.00	295.00	1282.00	268.00	2470.00	472.00
CONT-1	0.09	61.60	0.34	3.30	5.00	1.31	28.50	10.80	140.00	56.60	280.00	63.50	609.00	133.00
CONT-2	0.02	29.30	0.46	7.26	14.80	0.87	85.40	27.30	318.00	115.10	489.00	94.10	807.00	154.10
CONT-3		55.00	0.23	6.20	17.40	0.54	95.00	33.10	410.00	155.70	680.00	128.70	1134.00	211.00

CONT-4	0.06	7.30	0.40	8.20	20.40	0.48	123.00	45.50	575.00	229.00	1010.00	203.00	1740.00	332.00
CONT-5	0.11	6.73	0.62	7.12	11.30	0.38	24.40	4.62	33.40	7.99	23.30	3.91	30.70	5.04
CONT-6	0.06	1.50	0.13	2.63	10.60	0.31	101.00	47.30	689.00	294.00	1430.00	310.00	2860.00	548.00
st.vas1		16.7	0.085	1.26	3.48	1.11	13.4	4.67	56	23.3	112.7	26.6	278	64.1
st.vas2	0.076	13.1	0.078	1.01	2.17	0.53	11.7	4.24	55.2	25.1	135	33.4	350	84.6
Pag_1		4.06		0.071	0.22	0.082	2.04	0.9	11.59	5.11	26.5	6.68	69.6	15.57
Pag_2	0.031	22.73	0.302	4.38	5.65	2.6	23.9	7.5	89.4	33.8	153	32.33	305.3	62.2
Pag_3	0.116	8.61	0.099	1.7	3.16	0.346	22.1	9.15	118.7	48.3	224.1	48.1	451	87.2
krkv3-1	0.038	5.9	0.319	5.38	9.01	2.14	44.9	14.3	166	62.4	280	59.9	556	119.6
krkv3-2	0.031	25.4	0.157	2.32	4.88	1.16	26.2	8.95	104	39.7	175	36.5	332	68
krkv3-4 core	0.028	4.03	0.243	3.81	5.42	1.76	27.3	9.25	118	49.9	235	50.2	461	99
krkv3-4-rim	0.043	3.34	0.182	2.22	3.98	1.49	21	7.4	95	38	179	37.1	338	73.1
krkv3-5	0.035	20.9	0.526	7.8	14.3	2.91	71.3	23.1	262	93	388	78.4	690	130
rab6-3		1.47	0.081	1.35	3.38	0.149	25.7	9.69	119.6	47.5	211.6	42.8	387	77.3
rab6-4 core	0.071	2.49	0.292	4.36	5.8	0.58	23.5	6.9	74	26.1	106	20.5	187	38.1
rab6-4 rim		1.17	0.025	0.61	3.16	0.077	19.7	8.47	114	44.5	207	44.2	399	82
rab6-5	0.011	6.26	0.142	2.65	6.61	0.1	37	13.12	157.3	58.7	253	50.4	441	84.8
rab2-2 core	0.03	13.1	0.128	1.62	3.48	0.92	18.7	6.93	88.2	36.1	160	34.2	330	67
rab2-2 1accr	0.067	7.22	0.084	1.32	6.21	0.432	67.6	33.8	495	212	1013	216	1930	388
rab2-2 rim	0.02	7.26	0.045	0.91	2.6	0.295	22.5	9.9	138	57	263	56.6	514	103
rab2-6	0.32	23.5	0.25	2.51	4.8	1.62	25.8	9.2	118	48.4	229	51.2	499	109
rab1-4 core	1.1	54.2	0.82	9.5	13.8	1.45	57	16.12	164.3	52	202.8	38.1	324	58.8
rab1-4 rim	0.076	4.46	0.095	1.34	3.49	0.164	27.4	12.6	185	78.2	386	84.8	771	152
dobrini1	0.029	26.3	0.417	7.3	13.5	7.21	46	11.7	107.8	34.1	136	26.7	242	48.7
dobrimi2		9.06	0.055	0.99	1.96	0.105	9.51	3.12	36.7	13.95	62.5	12.8	117.5	23.9
baska6	0.02	2.92	0.018	0.5	1.76	0.103	9.73	3.94	48.9	20.1	93.4	19.5	182	36.6
baska7		1.59	0.089	1.98	5.63	0.133	38.5	15.2	203	81.7	381	81.2	727	144
baska8		1.65	0.112	2	6.36	0.183	43.1	17.44	238	99.6	472	101.5	922	184.4
baska9 core	0.04	2.16	0.06	1.13	3.51	0.223	26.3	11.94	170.1	71	341	73.6	679	134.9
baska9 rim	0.061	3.25	0.117	2.26	5.31	0.442	32.7	12.17	158.4	62.3	282	58	528	104.8
baska 14	0.014	34.4	0.156	2.58	5.99	0.465	41.2	15.98	207	83.5	386	82.7	762	153

Table 13. Chemical analyses of Rare Earth Elements of IB detrital zircon, determined in situ by LA-ICPMS.

ZB	^{139}La	^{140}Ce	^{141}Pr	^{146}Nd	^{147}Sm	^{153}Eu	^{157}Gd	^{159}Tb	^{163}Dy	^{165}Ho	^{166}Er	^{169}Tm	^{173}Yb	^{175}Lu
Z0-2	0.18	45.90	0.37	3.20	4.00	1.82	30.10	10.30	143.00	40.90	197.00	39.50	378.00	78.90
Z1-1	0.05	1.00	0.20	1.20	2.40	0.04	18.00	10.10	155.00	80.00	490.00	149.00	1730.00	430.00
Z1-2	0.21	30.00	0.52	5.50	7.90	3.61	30.90	9.40	90.00	30.80	132.00	31.00	370.00	65.00
Z1-3	0.03	3.53	0.15	3.00	5.90	0.73	28.20	9.60	126.00	48.40	217.00	48.30	454.00	93.00
Z2-1	0.06	45.80	0.14	1.59	3.91	1.98	21.80	7.17	92.00	38.90	196.00	50.00	553.00	131.00
Z2-2	0.04	5.98	0.13	3.40	7.70	0.44	54.60	21.80	240.00	78.00	311.00	62.80	531.00	96.00
Z2-4	1.14	18.20	2.48	19.60	19.30	6.77	57.10	17.70	166.00	51.80	189.00	34.80	292.00	56.30
Z2-5	0.06	6.10	0.30	3.50	7.00	2.20	47.40	23.10	306.00	114.70	503.00	109.10	1017.00	193.00
Z3-1	0.11	3.10	0.25	3.90	8.20	0.76	60.50	29.40	385.00	154.00	681.00	139.00	1240.00	244.00
Z3-2	0.06	74.40	0.37	6.70	22.00	2.81	139.00	52.90	685.00	265.00	1183.00	247.00	2230.00	433.00
Z3-3	1.04	55.30	1.82	16.20	25.90	6.10	103.00	35.40	402.00	151.00	690.00	152.00	1370.00	271.00
Z3-4	0.08	39.30	0.37	2.96	10.20	5.90	67.00	20.70	183.00	51.00	188.00	36.60	338.00	67.10
Z3-5	0.54	134.00	2.40	24.20	31.00	10.60	109.00	34.10	363.00	125.00	526.00	104.60	958.00	184.00
Z3-6	0.09	15.90	0.39	5.50	11.10	3.38	76.60	25.90	323.00	129.00	595.00	124.60	1130.00	228.00
Z3-12	0.05	17.20	0.25	4.30	7.90	1.69	57.00	19.20	223.00	81.50	348.00	70.60	645.00	121.00
Z3-7	3.60	45.00	1.60	3.00	9.60	1.85	53.80	23.10	285.00	112.00	507.00	117.00	1130.00	208.00
Z3-8	0.15	65.50	0.27	8.80	17.00	2.21	92.70	33.60	420.00	169.00	783.00	169.00	1515.00	294.00
Z3-9	0.16	9.70	0.40	5.70	5.70	2.00	26.60	8.50	106.00	44.40	225.00	57.80	654.00	150.00
Z3-10	0.13	29.30	0.33	7.20	16.10	1.42	100.70	39.90	495.00	192.00	866.00	177.00	1537.00	282.00
Z3-11	0.08	23.40	0.71	11.80	25.20	4.74	125.80	40.60	461.00	166.00	712.00	142.20	1241.00	227.00
Z4-1	0.08	33.50	0.26	6.10	11.80	2.63	62.20	20.20	223.00	79.50	352.00	73.40	650.00	131.70
Z4-2	0.19	4.20	0.65	8.60	19.20	1.56	116.00	48.60	633.00	258.00	1214.00	261.00	2350.00	446.00
Z4-3	0.04	22.20	0.14	2.10	5.13	0.28	35.80	13.23	171.00	66.80	305.00	65.20	603.00	115.90
Z4-4	0.01	19.50	0.39	5.45	9.70	1.68	44.90	13.70	148.00	50.30	207.00	40.50	344.00	64.70
Z4-5	0.01	7.64	0.10	1.59	4.40	0.63	25.60	10.50	122.00	43.40	187.00	38.40	338.00	65.10
Z4-6	0.04	10.10	0.36	5.25	13.60	1.33	86.90	31.90	401.00	159.50	715.00	145.60	1328.00	264.00
Z4-7	0.70	33.00	0.28	3.20	4.80	1.15	22.20	8.39	102.10	41.10	200.50	47.10	482.00	104.50
Z5-1	0.21	112.00	1.25	18.60	29.40	8.58	119.00	30.30	294.00	94.80	381.00	76.20	671.00	131.50
Z5-2	0.01	18.10	0.09	2.49	4.27	0.56	26.00	10.80	120.00	46.50	217.00	51.00	500.00	89.00
Z5-3		33.40	0.15	1.70	3.58	1.15	21.10	6.92	87.50	37.20	189.50	46.10	491.00	112.10
Z8-1	0.05	23.20	0.08	1.80	3.70	1.61	23.00	7.10	86.00	32.00	152.00	36.00	410.00	104.00

Z8-2	0.04	74.50	0.16	3.53	9.40	3.01	62.90	23.50	307.00	122.00	575.00	128.00	1250.00	266.00

Table 14. Chemical analyses of Rare Earth Elements of ZB detrital zircon, determined in situ by LA-ICPMS.

Geochronologic data

JB Zircon age	$^{207}Pb/^{235}U$	$^{207}Pb/^{235}U$ 2σ	$^{206}Pb/^{238}U$	$^{206}Pb/^{238}U$ 2σ	Rho	$^{207}Pb/^{206}Pb$	$^{207}Pb/^{206}Pb$ 2σ	$^{206}Pb/^{238}U$ age (Ma)	$^{206}Pb/^{238}U$ age 2σ	$^{207}Pb/^{235}U$ age (Ma)	$^{207}Pb/^{235}U$ age 2σ	$^{207}Pb/^{206}Pb$ age (Ma)	$^{207}Pb/^{206}Pb$ age 2σ
1-1	0.2538	0.0091	0.03673	0.00053	0.13	0.0503	0.0018	232.5	3.1	229.9	7.6	191	72
1-10	5.194	0.073	0.3287	0.004	0.45	0.1138	0.0015	1832	18	1853	12	1858	23
1-11	1.476	0.035	0.153	0.0024	0.41	0.0697	0.0015	918	13	917	15	914	43
1-13	1.514	0.041	0.1547	0.0026	0.30	0.0707	0.002	927	14	932	16	926	60
1-14	0.765	0.041	0.0922	0.0017	0.12	0.0601	0.0033	568.6	9.5	567	24	510	110
1-15	0.322	0.012	0.0439	0.0008	0.38	0.0534	0.0019	276.9	4.8	281.7	9.2	309	72
1-16	0.278	0.014	0.03904	0.00083	0.15	0.0519	0.0028	246.8	5	248	11	260	110
1-17	0.332	0.019	0.0443	0.001	0.01	0.0547	0.0034	279.3	6.2	289	14	350	130
1-18	0.239	0.014	0.03313	0.0006	0.24	0.0521	0.0029	210.1	3.6	215	11	220	100
1-19	1.251	0.033	0.134	0.0024	0.63	0.0671	0.0014	810	13	821	15	835	41
1-2	8.97	0.17	0.4347	0.0059	0.90	0.1487	0.0014	2325	25	2330	18	2329	16
1-20	0.3424	0.0064	0.04776	0.00047	0.19	0.05194	0.00098	300.8	2.6	298.5	4.8	270	41
1-21	1.007	0.038	0.1168	0.0019	0.09	0.0633	0.0025	712	11	709	21	662	85
1-22	5.535	0.068	0.3335	0.003	0.38	0.1199	0.0014	1855	13	1903	11	1950	21
1-23	0.2408	0.0089	0.0349	0.00049	0.36	0.0504	0.0018	221.1	2.9	217.8	7.3	194	71
1-24	6.994	0.088	0.3725	0.0033	0.71	0.1356	0.0012	2040	14	2108	11	2170	15
1-25	0.63	0.016	0.08001	0.00089	0.13	0.0573	0.0015	496.1	4.9	495.3	9.6	466	56
1-26	0.345	0.014	0.04687	0.00072	0.15	0.0535	0.0022	295.2	4.2	300	10	301	82
1-27	0.56	0.01	0.07195	0.00076	0.37	0.0565	0.001	447.8	4.2	452.1	6.9	460	39
1-3	5.058	0.077	0.3266	0.0035	0.40	0.1118	0.0016	1821	16	1827	13	1819	26
1-4	0.268	0.022	0.03754	0.00089	0.10	0.053	0.0046	237.5	5.4	238	18	210	150
1-5	0.395	0.014	0.05277	0.00093	0.16	0.0544	0.0019	331.5	5.5	337.8	9.9	370	78
1-6	0.251	0.011	0.03652	0.0005	0.17	0.0498	0.0022	231.2	3	226.3	8.9	168	87
1-7	0.377	0.02	0.0449	0.00076	0.39	0.0612	0.0032	283.1	4.5	327	16	590	110
1-8	0.231	0.018	0.03268	0.00079	0.19	0.0508	0.0039	207.2	4.9	209	15	190	140
1-9	8.8	0.17	0.4302	0.0053	0.69	0.1479	0.0022	2305	22	2313	18	2316	26

10-1	0.3027	0.0098	0.04183	0.00053	0.12	0.0523	0.0017	264.1	3.1	267.2	7.6	269	68
10-2	0.295	0.016	0.04136	0.00079	0.20	0.0518	0.0028	261.2	4.8	262	13	260	110
13-1	0.367	0.015	0.04985	0.001	0.34	0.0534	0.0021	313.6	6	317	11	330	85
13-3	0.5	0.02	0.0659	0.0012	0.28	0.0551	0.0021	411.1	7.4	410	13	389	83
13-4	0.339	0.025	0.04658	0.00096	0.05	0.0531	0.004	293.4	5.8	291	19	240	140
16-1	0.418	0.035	0.054	0.0022	0.04	0.0562	0.0049	339	13	354	25	440	190
16-2	0.493	0.018	0.0652	0.002	0.55	0.0555	0.0018	407	12	406	13	407	73
16-3	0.605	0.028	0.0756	0.003	0.19	0.0584	0.003	469	18	479	18	559	95
16-4	0.551	0.034	0.072	0.0028	0.52	0.0565	0.0032	448	17	443	22	430	120
17-1	0.609	0.024	0.0772	0.0011	0.06	0.0574	0.0024	479.1	6	479	15	445	85
17-2	2.788	0.062	0.2254	0.0033	0.67	0.0899	0.0017	1310	16	1350	17	1415	36
17-3	0.254	0.014	0.03498	0.00077	0.19	0.0532	0.0031	221.6	4.7	229	12	300	120
17-4	4.73	0.14	0.3117	0.0049	0.10	0.1096	0.0036	1748	23	1766	26	1764	61
17-6	0.74	0.023	0.0908	0.0013	0.13	0.0588	0.0018	560.2	7.1	559	13	526	65
17-8	0.557	0.015	0.07128	0.00081	0.20	0.0566	0.0015	443.8	4.5	448.7	9.8	443	58
21-1	0.519	0.013	0.06777	0.001	0.15	0.0552	0.0015	422.6	5.9	423.3	8.9	403	60
21-10	22.15	0.44	0.665	0.011	0.54	0.2412	0.0042	3286	43	3190	19	3127	27
21-2	0.579	0.017	0.0743	0.0011	0.25	0.0565	0.0016	462	6.5	463	11	452	63
21-3	0.389	0.024	0.05256	0.0009	0.17	0.0539	0.0034	330.1	5.3	332	18	300	120
21-4	0.576	0.058	0.0697	0.0034	0.47	0.0603	0.0078	434	20	459	38	540	260
21-5	1.354	0.056	0.1427	0.0039	0.36	0.0686	0.003	859	22	865	24	863	97
21-6	0.565	0.039	0.0732	0.002	0.19	0.0562	0.0039	455	12	451	25	400	140
21-7	0.648	0.018	0.0806	0.0013	0.36	0.0579	0.0015	499.7	7.5	505	11	502	55
21-8	0.89	0.039	0.1053	0.0022	0.07	0.061	0.0028	645	12	642	22	610	100
21-9	0.331	0.02	0.04501	0.00095	0.34	0.0515	0.0027	283.8	5.7	289	15	280	120
26-1	0.848	0.025	0.1015	0.0019	0.25	0.0607	0.0019	623	11	622	14	599	67
26-2	3.38	0.14	0.2618	0.0061	0.18	0.0939	0.0041	1498	31	1489	33	1476	82
26-3	0.381	0.011	0.05311	0.00069	0.20	0.0519	0.0015	333.5	4	327.3	8.2	266	63
26-4	1.648	0.068	0.1616	0.0044	0.14	0.074	0.0034	965	24	987	26	1026	94
26-5	4	0.11	0.2873	0.0098	0.32	0.101	0.0035	1627	49	1633	23	1637	66

26-6	0.335	0.014	0.04614	0.00067	0.08	0.0525	0.0023	290.7	4	291	11	260	84
5-1	6.85	0.12	0.3827	0.005	0.32	0.1298	0.0025	2092	23	2090	16	2087	34
5-10	2.97	0.072	0.2449	0.0031	0.48	0.0883	0.0019	1412	15	1398	19	1391	37
5-11	0.3483	0.0063	0.04734	0.00049	0.45	0.05309	0.00086	298.1	2.7	303.1	4.7	323	36
5-12	0.194	0.011	0.02835	0.00056	0.15	0.0494	0.0027	180.2	3.4	178.3	9.3	150	100
5-2	0.416	0.013	0.05537	0.00073	0.31	0.0543	0.0016	347.4	4.2	352.2	9.2	361	64
5-3	0.436	0.019	0.05675	0.00091	0.03	0.0559	0.0026	356.5	5.6	365	13	391	94
5-4	0.779	0.034	0.0919	0.0017	0.24	0.0613	0.0027	566.4	9.5	581	20	592	93
5-5	0.4055	0.0096	0.05523	0.0006	0.02	0.0533	0.0014	346.5	3.3	344.8	6.9	317	54
5-6	0.57	0.027	0.0734	0.0014	0.14	0.0565	0.0027	456.3	8.4	455	17	430	100
5-8	0.586	0.019	0.0741	0.0012	0.19	0.0576	0.0019	460.5	7.2	466	12	475	73
5-9	1.492	0.022	0.1527	0.0015	0.26	0.0709	0.0011	915.7	7.3	926.6	8.9	941	32
Cl-1	0.928	0.021	0.1111	0.0017	0.01	0.0605	0.0015	679	9.6	665	11	606	52
Cl-2	6.89	0.079	0.3848	0.0034	0.38	0.1294	0.0015	2098	14	2095	10	2083	20
Nim1-1	1.028	0.03	0.1162	0.0015	0.06	0.064	0.002	708.4	8.4	714	15	707	67
Nim1-2	4.27	0.14	0.2786	0.0047	0.12	0.1112	0.004	1583	23	1682	28	1795	66
Nim1-3	1.659	0.038	0.1644	0.0021	0.20	0.0731	0.0018	981	11	990	14	997	50
Nim1-4	0.457	0.03	0.0604	0.0015	0.01	0.0552	0.0038	378.1	9.2	378	21	360	140
Nim1-5	0.35	0.019	0.05045	0.00083	0.16	0.0502	0.0027	317.2	4.9	304	15	190	110
Nim1-6	0.269	0.014	0.03707	0.00064	0.06	0.0531	0.0028	234.6	3.9	239	11	280	100
Nim1-6	0.5924	0.0097	0.07516	0.00072	0.15	0.05707	0.00095	467.1	3.8	471.6	6.2	476	37
Nim1-6r	0.548	0.014	0.07116	0.00087	0.45	0.0559	0.0013	443.1	4.9	442.3	9.1	424	52
Nim1-7	1.65	0.057	0.1643	0.0029	0.25	0.0735	0.0026	980	16	980	22	977	74
Nim1-7	1.66	0.089	0.1679	0.0042	0.15	0.0718	0.0039	1000	23	987	34	940	120
Nim1-8	0.568	0.056	0.0675	0.0035	0.14	0.0606	0.0066	421	21	455	36	580	230
Nim1-9	3.256	0.088	0.2535	0.0044	0.49	0.0926	0.0023	1456	22	1469	21	1475	46
Nim4-1	0.304	0.014	0.0421	0.0011	0.50	0.0528	0.0021	266	6.9	271	11	301	87
Nim4-2	1.487	0.059	0.1531	0.0025	0.07	0.0703	0.0029	918	14	923	24	921	84
Nim4-3	0.555	0.016	0.07203	0.00081	0.13	0.0555	0.0016	448.3	4.5	446	11	399	64
Nim4-4	0.252	0.017	0.0354	0.00081	0.08	0.0519	0.0035	224.2	4.9	226	14	230	130

Nim4-5	0.283	0.045	0.0369	0.0023	0.43	0.0554	0.008	233	14	249	35	340	280
Nim4-6	1.245	0.032	0.1344	0.002	0.31	0.0668	0.0016	813	11	817	14	806	53

Table 15. Isotopic U/Pb age result of the JB concordant detrital zircon, determined in situ by LA-ICPMS.

BK Zircon Age	$^{207}Pb/^{235}U$	$^{207}Pb/^{235}U$ 2σ	$^{206}Pb/^{238}U$	$^{206}Pb/^{238}U$ 2σ	Rho	$^{207}Pb/^{206}Pb$	$^{207}Pb/^{206}Pb$ 2σ	$^{206}Pb/^{238}U$ age (Ma)	$^{206}Pb/^{238}U$ age 2σ	$^{207}Pb/^{235}U$ age (Ma)	$^{207}Pb/^{235}U$ age 2σ	$^{207}Pb/^{206}Pb$ age (Ma)	$^{207}Pb/^{206}Pb$ age 2σ
JAP-1	0.831	0.047	0.1018	0.0033	0.51	0.0602	0.002	616	14	624	15	585	63
JAP-10	0.565	0.038	0.074	0.0024	0.10	0.0561	0.003	451	18	460	11	400	100
JAP-11	0.256	0.019	0.03643	0.0011	0.43	0.049	0.0024	230	11	230.6	5.6	134	88
JAP-13	0.273	0.024	0.0375	0.0017	0.47	0.0522	0.0037	244	17	237.3	9.6	260	140
JAP-14	0.383	0.025	0.0456	0.0023	0.45	0.0602	0.0035	328	12	287	13	560	110
JAP-15	0.271	0.023	0.039	0.0015	0.21	0.0496	0.0034	240	15	246.6	8	170	130
JAP-16	0.306	0.023	0.042	0.0016	0.39	0.0532	0.003	270	14	265.2	8.4	310	110
JAP-17	0.348	0.035	0.0471	0.0017	0.09	0.0537	0.0049	297	23	296.5	8.5	290	170
JAP-18	0.286	0.022	0.0401	0.0013	0.16	0.0506	0.003	253	14	253.1	6.4	200	110
JAP-19	1.422	0.095	0.1413	0.0039	0.38	0.0688	0.0019	894	27	851	16	873	46
JAP-2	0.324	0.049	0.0427	0.0019	0.04	0.0522	0.0073	263	34	269	11	50	230
JAP-20	1.474	0.11	0.1478	0.0042	0.35	0.0686	0.0031	905	31	888	17	830	86
JAP-22	0.266	0.02	0.0376	0.0014	0.29	0.0515	0.0029	241	13	237.6	7.1	230	110
JAP-23	0.257	0.029	0.0364	0.0017	0.33	0.051	0.0052	230	21	230.4	9.9	200	190
JAP-3	0.993	0.077	0.1117	0.0042	0.20	0.0646	0.0042	692	31	682	21	680	130
JAP-4	1.8	0.17	0.1814	0.0072	0.06	0.0685	0.0053	1023	53	1073	34	740	160
JAP-5	0.28	0.018	0.03954	0.0011	0.31	0.0517	0.0024	249.5	9.6	249.9	4.6	241	84
JAP500-1	0.389	0.035	0.0522	0.0018	0.45	0.0509	0.0032	327	21	327.7	9.2	210	120
JAP500-10	0.458	0.034	0.0614	0.0025	0.37	0.0523	0.0025	379	17	384	13	272	91
JAP500-2	5.72	0.37	0.3527	0.011	0.57	0.1136	0.0031	1920	34	1944	44	1845	39
JAP500-3	0.338	0.034	0.0468	0.0016	0.11	0.0503	0.0041	288	22	295	7.8	150	140
JAP500-4	0.392	0.027	0.04188	0.0012	0.47	0.0646	0.0021	336	15	264.4	5.5	744	63
JAP500-5	5.82	0.37	0.3517	0.0096	0.56	0.1154	0.0027	1942	36	1941	32	1878	30

JAP500-6	0.312	0.02	0.0435	0.0015	0.49	0.0517	0.002	277	11	274.2	7.8	256	75
JAP500-7	0.477	0.03	0.0639	0.0028	0.37	0.0554	0.0027	395	13	399	15	370	89
JAP500-8	0.372	0.032	0.0385	0.0016	0.11	0.0704	0.0061	315	19	244.5	8.9	710	160
JAP500-9	0.325	0.019	0.0463	0.0016	0.39	0.0511	0.002	284.6	8.8	291.9	8.1	233	74
JAP-6	0.264	0.023	0.0363	0.0014	0.13	0.052	0.0038	235	15	229.8	7.5	220	130
JAP-7	0.261	0.018	0.03696	0.0012	0.12	0.0511	0.0027	233.7	9.9	233.9	5.7	217	97
JAP-8	0.543	0.04	0.0713	0.0022	0.43	0.0526	0.0025	437	20	444	10	270	88
JAP-9	0.272	0.031	0.0368	0.0017	0.15	0.0547	0.0059	238	23	232.8	9.7	270	190
MISL-1	12.89	0.66	0.527	0.015	0.52	0.1801	0.0048	2667	19	2722	48	2643	34
MISL-10	0.394	0.031	0.0537	0.002	0.19	0.0549	0.0036	335	18	337	10	360	130
MISL-11	0.408	0.066	0.0532	0.0037	0.13	0.0541	0.0096	334	45	333	22	210	300
MISL-12	0.319	0.031	0.0443	0.0015	0.19	0.0535	0.0048	272	18	279.1	7.6	230	140
MISL-13	0.504	0.036	0.065	0.0023	0.29	0.0573	0.0032	412	18	406	12	460	110
MISL-14	0.391	0.045	0.0482	0.0024	0.21	0.0541	0.0049	328	28	303	14	310	170
MISL-2	0.581	0.034	0.0741	0.0026	0.43	0.0582	0.0023	466	14	461	13	507	79
MISL-3	0.828	0.054	0.0978	0.0035	0.33	0.0626	0.003	607	21	601	17	630	96
MISL-4	0.2556	0.015	0.03611	0.0011	0.39	0.0517	0.0018	230.5	6.7	228.6	4.9	252	65
MISL-5	0.25	0.016	0.03551	0.0011	0.14	0.0514	0.0025	225.2	9	224.9	5.2	242	94
MISL-6	0.0918	0.008	0.01346	0.00048	0.34	0.0505	0.0036	89	6.2	86.2	2.6	200	140
MISL-7	7.09	0.42	0.3921	0.012	0.45	0.127	0.0033	2110	28	2128	43	2048	35
MISL-8	0.376	0.026	0.0506	0.0018	0.30	0.0557	0.003	322	14	318.2	9.1	390	110
MISL-9	8.29	0.74	0.426	0.017	0.51	0.1192	0.0034	2266	72	2285	65	1946	44
NGRAD-1	1.013	0.06	0.1159	0.0034	0.32	0.0623	0.0022	705	17	706	15	638	67
NGRAD-2	0.321	0.026	0.0443	0.0016	0.28	0.0528	0.0035	281	16	279.6	8	290	130
NGRAD-3	1.36	0.12	0.1427	0.0055	0.37	0.0705	0.0051	861	44	859	27	860	150
NGRAD-4	0.321	0.034	0.0444	0.0017	0.22	0.0516	0.0048	275	23	279.6	8.7	170	160
NGRAD-5	0.092	0.014	0.01363	0.00063	0.31	0.0465	0.006	92	14	87.3	3.7	70	240
NGRAD-6	0.0895	0.0071	0.01377	0.00048	0.37	0.0459	0.0026	86.7	5.2	88.2	2.5	21	98
NGRAD-7	1.793	0.12	0.1741	0.0072	0.41	0.0729	0.003	1038	30	1034	35	993	77
NGRAD-8	1.618	0.1	0.1668	0.0059	0.64	0.0712	0.0027	973	29	993	27	925	73

NGRAD-9	14.12	1.1	0.542	0.019	0.62	0.1771	0.005	2748	58	2787	64	2615	38
nov10-	0.898	0.059	0.1045	0.0036	0.50	0.0604	0.0034	647	26	640	15	583	99
nov11-	0.489	0.034	0.063	0.0014	0.18	0.0554	0.0038	400	20	393.6	16	370	120
nov12-	0.459	0.026	0.0623	0.0012	0.41	0.0527	0.0027	380	14	389.4	11	302	79
nov13-	12.74	0.5	0.5001	0.01	0.76	0.1798	0.006	2659	17	2613	37	2649	21
nov14-	0.869	0.042	0.104	0.0017	0.23	0.0599	0.0027	632	14	637.6	18	566	68
nov16-	5.16	0.26	0.3347	0.0067	0.47	0.109	0.0047	1843	27	1859	43	1775	44
nov1-rim	0.363	0.017	0.04927	0.00077	0.13	0.0517	0.0023	313.9	7.8	310	8	262	59
nov2-2accr	0.457	0.025	0.06162	0.00099	0.01	0.0546	0.003	380	15	385.4	14	363	96
nov3-	0.0994	0.013	0.0151	0.00062	0.38	0.0471	0.0071	95.6	6.3	96.6	4	60	120
nov5-	0.365	0.025	0.0496	0.00095	0.15	0.0554	0.0036	312	16	312	7	350	120
nov6-	6.73	0.3	0.3846	0.0096	0.34	0.1227	0.005	2074	23	2096	36	1987	43
nov7-	0.263	0.021	0.03671	0.00086	0.17	0.0521	0.004	235	12	232.4	7	230	110
nov8-rim	0.722	0.031	0.0884	0.0011	0.55	0.0583	0.0021	550	12	546	10	533	46
nov9-rim	0.4392	0.019	0.05917	0.00093	0.20	0.0533	0.0021	370.1	5.9	370.5	12	330	43
TATRE-10	1.93	0.15	0.1844	0.0065	0.22	0.0725	0.004	1081	42	1090	29	930	110
TATRE-11	0.648	0.039	0.082	0.0025	0.23	0.0577	0.0025	504	15	508	11	466	83
TATRE-12	13.56	0.96	0.532	0.025	0.73	0.1726	0.0069	2712	49	2743	93	2575	60
TATRE-13	1.809	0.12	0.1764	0.0073	0.66	0.0717	0.0028	1054	32	1046	35	965	71
TATRE-14	0.0916	0.0094	0.0136	0.00062	0.33	0.0494	0.0043	88.8	7.7	87.1	3.6	150	170
TATRE-15	0.0924	0.0081	0.01358	0.00068	0.47	0.0493	0.0035	89.6	6.3	86.9	4	160	140
TATRE-16	0.877	0.066	0.1055	0.0046	0.58	0.0595	0.0029	632	27	646	24	540	100
TATRE-17	11.88	0.66	0.5047	0.014	0.56	0.1668	0.0036	2590	26	2636	41	2520	23
TATRE-18	0.309	0.03	0.0443	0.0022	0.49	0.0486	0.0032	272	20	279	12	120	120
TATRE-2	11.67	0.64	0.496	0.016	0.76	0.169	0.0039	2568	25	2591	53	2543	27
TATRE-3	10.66	0.53	0.4499	0.012	0.64	0.1724	0.0036	2492	13	2392	36	2577	21
TATRE-4	0.937	0.062	0.1085	0.0031	0.22	0.0613	0.003	663	22	664	14	585	93
TATRE-5	0.824	0.065	0.0973	0.0037	0.52	0.0603	0.0034	604	29	598	18	570	110
TATRE-6	0.357	0.021	0.0494	0.0015	0.44	0.0525	0.0019	308.9	9.5	310.7	6.7	283	68
TATRE-8	0.535	0.038	0.0692	0.0022	0.14	0.0556	0.0031	431	19	431	10	390	110

TATRE-9	0.498	0.058	0.0632	0.003	0.10	0.0547	0.0063	413	38	395	16	370	230

Table 16. Isotopic U/Pb age result of the BK concordant detrital zircon, determined in situ by LA-ICPMS.

IB Zircon Age	$^{207}Pb/^{235}U$	$^{207}Pb/^{235}U$ 2σ	$^{206}Pb/^{238}U$	$^{206}Pb/^{238}U$ 2σ	Rho	$^{207}Pb/^{206}Pb$	$^{207}Pb/^{206}Pb$ 2σ	$^{206}Pb/^{238}U$ age (Ma)	$^{206}Pb/^{238}U$ age 2σ	$^{207}Pb/^{235}U$ age (Ma)	$^{207}Pb/^{235}U$ age 2σ	$^{207}Pb/^{206}Pb$ age (Ma)	$^{207}Pb/^{206}Pb$ age 2σ
baska14	1.139	0.053	0.1221	0.0023	0.43	0.0653	0.0027	768	34	742	34	750	120
baska6	0.955	0.047	0.1118	0.0016	0.05	0.0606	0.0028	677	17	682.8	17	599	110
baska7	0.34	0.019	0.04653	0.00074	0.07	0.053	0.0031	295	12	293.1	12	280	45
baska8	0.628	0.033	0.0785	0.0013	0.14	0.0566	0.0028	492	15	487.1	15	440	100
baska9	0.514	0.024	0.0659	0.0011	0.18	0.0579	0.0026	422	13	411.6	13	501	61
BER-1	0.72	0.048	0.0906	0.0031	0.28	0.0574	0.0026	545	19	559	15	470	93
BER-10	0.623	0.036	0.0795	0.0022	0.50	0.0572	0.002	489	13	493.2	9.6	464	63
BER-11	7.21	0.47	0.3828	0.011	0.72	0.1299	0.0028	2127	37	2086	40	2095	23
BER-12	0.973	0.063	0.113	0.0044	0.55	0.0643	0.0026	687	22	690	22	750	74
BER-13	0.493	0.032	0.0639	0.0031	0.30	0.0541	0.0027	406	15	399	18	360	100
BER-2	11.7	1.1	0.466	0.023	0.58	0.165	0.006	2580	76	2452	91	2489	54
BER-3	0.647	0.045	0.0831	0.0028	0.46	0.0554	0.0026	501	20	516	14	387	93
BER-4	0.328	0.026	0.0455	0.0022	0.43	0.0533	0.0033	287	16	287	12	310	120
BER-5	0.315	0.049	0.0423	0.0024	0.03	0.0569	0.0088	265	34	267	14	280	270
BER-6	7.47	0.43	0.404	0.013	0.65	0.1347	0.0041	2160	26	2181	49	2157	48
BER-7	0.8	0.045	0.0975	0.003	0.31	0.0604	0.0021	596	13	600	14	582	65
BER-8	0.574	0.037	0.0746	0.0023	0.34	0.0566	0.0025	458	16	464	11	442	88
BER-9	0.603	0.046	0.0774	0.0022	0.45	0.0535	0.0024	471	21	480.3	9.7	316	85
CONT-1	0.352	0.022	0.0491	0.0015	0.17	0.0532	0.0025	308	11	308.8	7.2	296	100
CONT-2	0.533	0.035	0.0692	0.0023	0.27	0.0569	0.0029	431	17	431	11	430	87
CONT-3	0.319	0.02	0.0441	0.0014	0.42	0.051	0.0017	279.5	9.7	278.4	6.7	234	72
CONT-4	0.463	0.032	0.0614	0.0018	0.40	0.0551	0.0026	383	16	384	8.6	377	100
CONT-5	11.12	0.66	0.4901	0.013	0.62	0.1587	0.0034	2521	29	2568	37	2440	90

CONT-6	0.624	0.044	0.0786	0.0027	0.54	0.0583	0.0026	489	20	488	14	505	59
dobrimi2	1.121	0.049	0.1256	0.0016	0.39	0.064	0.0025	761	13	762	13	729	93
dobrini1	0.2773	0.012	0.03889	0.00041	0.25	0.0521	0.0019	248.1	4.9	245.9	4.9	276	57
krkv3-1	0.462	0.025	0.0619	0.00093	0.09	0.0539	0.0028	383	16	387.1	16	320	100
krkv3-2	0.1029	0.0078	0.01565	0.00027	0.23	0.047	0.0034	98.9	6.2	100.1	6.2	80	100
krkv3-4-rim	0.305	0.021	0.04327	0.00085	0.12	0.0508	0.0032	269	11	273	11	210	68
krkv3-5	0.1074	0.0071	0.01517	0.00034	0.21	0.0506	0.0033	103	5.7	97.1	5.7	180	89
rab1-4 rim	0.596	0.028	0.07563	0.00094	0.20	0.0559	0.0025	474	12	469.9	12	424	86
rab2-2 1accr	0.508	0.022	0.0666	0.0011	0.25	0.0538	0.0022	416.3	8.9	415.8	8.9	345	75
rab2-2 rim	0.539	0.035	0.0698	0.002	0.48	0.0544	0.003	435	19	435	19	370	69
rab2-6	1.361	0.055	0.1443	0.0017	0.35	0.0688	0.0024	870	12	868.7	12	884	75
rab6-3	5.78	0.25	0.3535	0.0073	0.70	0.1147	0.0043	1941	20	1950	20	1870	47
rab6-4 rim	0.418	0.021	0.05735	0.00072	0.28	0.0536	0.0025	353	10	359.4	10	318	130
rab6-5	0.529	0.027	0.0687	0.0018	0.71	0.0552	0.0022	429	13	429	13	398	36
st.vas1	0.915	0.046	0.1069	0.0014	0.27	0.0612	0.0028	659	18	654.7	18	607	48
st.vas2	1.723	0.079	0.1805	0.0037	0.49	0.0698	0.0026	1011	18	1071	18	898	32
ZAULE-1	0.937	0.057	0.1104	0.0033	0.42	0.0608	0.0022	666	18	675	14	587	23

Table 17. Isotopic U/Pb age result of the JB concordant detrital zircon, determined in situ by LA-ICPMS.

ZB	$^{207}Pb/^{235}U$	$^{207}Pb/^{235}U$ 2σ	$^{206}Pb/^{238}U$	$^{206}Pb/^{238}U$ 2σ	Rho	$^{207}Pb/^{206}Pb$	$^{207}Pb/^{206}Pb$ 2σ	$^{206}Pb/^{238}U$ age (Ma)	$^{206}Pb/^{238}U$ age 2σ	$^{207}Pb/^{235}U$ age (Ma)	$^{207}Pb/^{235}U$ age 2σ	$^{207}Pb/^{206}Pb$ age (Ma)	$^{207}Pb/^{206}Pb$ age 2σ
Z0-1	0.329	0.029	0.044	0.002	0.06	0.0556	0.0055	294	22	278	11	380	190
Z0-2	5.62	0.45	0.349	0.016	0.57	0.1144	0.0054	1913	55	1928	67	1860	80
Z1-1	0.881	0.096	0.0843	0.0051	0.44	0.0564	0.0029	647	54	521	29	440	100
Z1-2	0.68	0.15	0.0756	0.007	0.24	0.061	0.011	516	84	469	41	510	360
Z2-1	0.647	0.045	0.0815	0.0029	0.33	0.0584	0.0031	509	22	505	15	520	110
Z2-2	0.939	0.07	0.112	0.0034	0.50	0.0589	0.0027	672	29	684	15	530	91
Z2-3	0.533	0.033	0.0698	0.0019	0.33	0.054	0.0019	432	14	434.8	8.2	358	70
Z2-4	0.352	0.024	0.0455	0.0019	0.78	0.0565	0.0019	305	12	287	10	457	63

Z2-6	0.623	0.037	0.0793	0.0027	0.38	0.0575	0.0023	490	14	492	14	484	77
Z3-1	1.636	0.11	0.1665	0.0058	0.48	0.0714	0.003	981	31	992	26	953	79
Z3-10	0.09	0.012	0.0127	0.00062	0.24	0.0511	0.0061	87	10	81.3	3.6	170	210
Z3-11	0.089	0.014	0.01333	0.00069	0.20	0.0422	0.0054	85	12	85.3	4	-150	200
Z3-2	0.566	0.045	0.0633	0.0018	0.41	0.0585	0.0028	450	22	395.3	8.4	499	88
Z3-3	1.95	0.19	0.1709	0.0054	0.52	0.0711	0.0018	1087	50	1017	23	953	39
Z3-4	5.39	0.38	0.334	0.014	0.77	0.1157	0.0033	1871	43	1856	60	1885	40
Z3-5	0.689	0.04	0.0744	0.0024	0.36	0.0626	0.0023	534	13	462	12	670	68
Z3-6	0.409	0.037	0.0453	0.0021	0.49	0.0564	0.0038	347	23	286	12	440	130
Z3-7	0.0862	0.006	0.01276	0.00036	0.23	0.05	0.0027	83.8	4.2	81.7	1.6	180	100
Z3-8	0.833	0.048	0.0988	0.0032	0.16	0.062	0.0025	614	15	607	15	668	86
Z3-9	21	2.2	0.572	0.027	0.28	0.2103	0.0084	3112	78	2908	99	2913	54
Z4-1	0.33	0.023	0.0454	0.0016	0.40	0.0535	0.0026	288	12	285.9	8.1	319	94
Z4-2	0.563	0.035	0.0743	0.0023	0.36	0.0545	0.0021	451	15	462	11	370	75
Z4-3	3.407	0.17	0.2658	0.0066	0.42	0.0935	0.0024	1505	15	1519	21	1486	36
Z4-4	0.665	0.041	0.0847	0.0025	0.49	0.0557	0.002	514	16	524	11	413	67
Z4-5	0.821	0.046	0.1005	0.0031	0.47	0.0595	0.0019	607	14	617	14	567	60
Z4-6	0.572	0.038	0.0741	0.0026	0.39	0.0571	0.0025	457	16	460	13	464	82
Z4-7	1.418	0.1	0.1475	0.0056	0.61	0.0663	0.0022	889	32	886	27	807	58
Z5-1	1.056	0.067	0.1183	0.0034	0.37	0.0622	0.0018	726	21	720	14	661	50
Z5-2	1.427	0.1	0.1471	0.0058	0.26	0.0704	0.0038	897	31	884	29	920	110
Z5-3	0.293	0.037	0.0382	0.0015	0.17	0.0469	0.0043	257	26	241.5	8	60	170
Z8-1	2.47	0.24	0.1876	0.0063	0.44	0.0725	0.0027	1241	59	1107	28	970	70
Z8-2	0.488	0.029	0.0642	0.0022	0.46	0.0535	0.002	402	12	401	11	339	76
Z8-2	0.488	0.029	0.0642	0.0022	0.46	0.0535	0.002	402	12	401	11	339	76

Table 18. Isotopic U/Pb age result of the JB concordant detrital zircon, determined in situ by LA-ICPMS.